

## Superconducting Contacts for Atomically Precise Graphene Nanoribbons

Bouwmeester, D.

**DOI**

[10.4233/uuid:56ba2302-cde1-441d-a8f1-43ddd458e44c](https://doi.org/10.4233/uuid:56ba2302-cde1-441d-a8f1-43ddd458e44c)

**Publication date**

2024

**Document Version**

Final published version

**Citation (APA)**

Bouwmeester, D. (2024). *Superconducting Contacts for Atomically Precise Graphene Nanoribbons*. [Dissertation (TU Delft), Delft University of Technology]. <https://doi.org/10.4233/uuid:56ba2302-cde1-441d-a8f1-43ddd458e44c>

**Important note**

To cite this publication, please use the final published version (if applicable).  
Please check the document version above.

**Copyright**

Other than for strictly personal use, it is not permitted to download, forward or distribute the text or part of it, without the consent of the author(s) and/or copyright holder(s), unless the work is under an open content license such as Creative Commons.

**Takedown policy**

Please contact us and provide details if you believe this document breaches copyrights.  
We will remove access to the work immediately and investigate your claim.



**Superconducting contacts for atomically  
precise graphene nanoribbons.**



# **Superconducting contacts for atomically precise graphene nanoribbons.**

## **Dissertation**

for the purpose of obtaining the degree of doctor

at Delft University of Technology

by the authority of the Rector Magnificus prof. dr. ir. T.H.J.J. van der Hagen,

Chair of the Board for Doctorates

to be defended publicly on

Tuesday 28, May 2024 at 12:30 o'clock

by

**Damian BOUWMEESTER**

Master of Science in Applied Physics,  
Delft University of Technology, the Netherlands,

born in Leiderdorp, the Netherlands.

This dissertation has been approved by the promotor.

Composition of the doctoral committee:

Rector Magnificus,	chairperson
Prof. Dr. Ir. H. S. J. van der Zant,	Delft University of Technology, promotor
Dr. A. R. Akhmerov,	Delft University of Technology, promotor

*Independent members:*

Prof. Dr. H. Courtois,	Université Grenoble Alpes, institut Neel, France
Prof. Dr. Y. V. Nazarov,	Delft University of Technology
Prof. Dr. M. L. Perrin,	ETH Zurich, Switzerland
Prof. Dr. J. M. van Ruitenbeek,	Leiden University
Dr. G. Borin Barin,	EMPA, Switzerland
Prof. Dr. Y. M. Blanter,	Delft University of Technology, reserve member

This work was supported by the Netherlands Organisation for Scientific Research (NWO/OCW) as part of the Frontiers of Nanoscience program.



# NanoFront



**Keywords:** graphene nanoribbon, superconductivity, SNS junction, Josephson diode, nanotechnology

**Printed by:** Gildeprint

**Cover:** Color map of the differential resistance signature of a superconductor-normal metal-superconductor junction versus in-plane perpendicular magnetic field. Design by Damian Bouwmeester

Copyright © 2024 by D. Bouwmeester

ISBN 978-94-6366-863-7

An electronic version of this dissertation is available at  
<http://repository.tudelft.nl/>.

The associated experimental data for this dissertation are available at  
<http://doi.org/10.4121/0240a853-27a0-47fe-8270-c346f0288580>.

# Contents

<b>Summary</b>	<b>ix</b>
<b>Samenvatting</b>	<b>xi</b>
<b>1 Introduction</b>	<b>1</b>
1.1 Graphene nanoribbons and superconductivity: Why combine them . . . .	2
1.2 Context and theoretical background . . . . .	2
1.2.1 Motivation and scope of the thesis . . . . .	2
1.2.2 Graphene nanoribbons . . . . .	4
1.2.3 Electrical contact to armchair graphene nanoribbons. . . . .	5
1.2.4 Superconductivity . . . . .	6
1.2.5 Superconducting proximity effect and SNS junctions. . . . .	6
1.2.6 Nonreciprocity in SNS junctions . . . . .	9
1.3 Dissertation outline . . . . .	10
<b>2 Theory</b>	<b>11</b>
2.1 Graphene nanoribbons . . . . .	11
2.1.1 Electronic structure . . . . .	11
2.1.2 Magnetism at zigzag edges . . . . .	25
2.1.3 Electronic transport properties of semiconducting graphene nanoribbons . . . . .	25
2.1.4 Interfaces of graphene nanoribbons and metals . . . . .	29
2.1.5 Electronic transport through Schottky barriers . . . . .	31
2.2 Superconductivity . . . . .	31
2.2.1 Critical field of superconductors . . . . .	35
2.2.2 BTK Theory . . . . .	37
2.2.3 Diffusive electronic transport . . . . .	40
2.2.4 Diffusive superconductivity: Proximity effect . . . . .	41
2.2.5 RCSJ model for SNS junctions . . . . .	46
2.2.6 Nonequilibrium superconductivity: charge and branch imbalance . . . . .	48
2.2.7 Nonequilibrium: Finite lifetime effects . . . . .	49
2.2.8 Effect of a Meissner current on SNS junctions . . . . .	50
2.2.9 Eilenberger quasiclassical theory of superconductivity: Finite momentum . . . . .	51
2.2.10 Finite momentum BTK theory . . . . .	53
2.2.11 Linear response kinetic theory of superconductors . . . . .	55
2.2.12 Self-field effects . . . . .	58
<b>3 Fabrication</b>	<b>61</b>
3.1 Design considerations for nanogap electrodes for graphene nanoribbons. . . . .	61

3.2	Design considerations for nanogap electrodes . . . . .	62
3.3	Superconductor - normal metal - superconductor junctions . . . . .	64
3.4	Recipes. . . . .	67
3.4.1	Cleaning of SiO <sub>2</sub> chips prior to processing . . . . .	67
3.4.2	Wide nanogap electrodes. . . . .	67
3.4.3	Cold development CSAR-62 recipe for needlelike nanogap electrodes . . . . .	69
3.4.4	TiPt gate electrodes with HfO <sub>2</sub> gate dielectric . . . . .	70
3.4.5	SNS EMBJ devices: Double angle evaporation . . . . .	71
3.5	Limitations and flaws of fabrication recipes . . . . .	74
3.5.1	Large area gaps: Dog-ears and resist collapse . . . . .	74
3.5.2	Oxides on sputtered MoRe after exposure to (humid) air . . . . .	75
3.5.3	Heating effects during evaporation. . . . .	76
3.5.4	Resist residue . . . . .	78
3.5.5	Metal particles around patterns . . . . .	78
3.5.6	Importance of rinsing procedure after development . . . . .	79
3.6	PMMA membrane-assisted graphene nanoribbon transfer . . . . .	80
3.6.1	Fabrication of PMMA membranes . . . . .	80
3.6.2	GNR transfer using PMMA membranes . . . . .	80
<b>4</b>	<b>MoRe Electrodes with 10 nm Nanogaps for Electrical Contact to Atomically Precise Graphene Nanoribbons</b>	<b>83</b>
4.1	Introduction . . . . .	84
4.2	Discussion . . . . .	91
4.3	Conclusion. . . . .	94
4.4	Appendix . . . . .	95
<b>5</b>	<b>Study of MoRe Interfaces to Ligand-Free Gold Nanoparticles Deposited by Aerosol</b>	<b>105</b>
5.1	Introduction . . . . .	106
5.2	Room temperature characterization . . . . .	107
5.3	Low-temperature characterization . . . . .	110
5.3.1	High-resistance devices . . . . .	111
5.3.2	Low-resistance devices. . . . .	112
5.3.3	Magnetic field dependence of device H9 . . . . .	115
5.3.4	High-bias measurements at 1 T magnetic field . . . . .	117
5.4	Discussion . . . . .	120
5.4.1	Morphology and density of the nanoparticle film. . . . .	120
5.4.2	Room temperature measurements . . . . .	120
5.4.3	BTK analysis. . . . .	120
5.4.4	Sharvin and Maxwell resistance, critical current effects from the MoRe thin film . . . . .	122
5.4.5	Absence of a dissipation-less Josephson current . . . . .	125
5.5	Conclusion. . . . .	125

<b>6 Superconducting Proximity Effect in Constricted Variable Thickness SNS Junctions</b>	<b>127</b>
6.1 Introduction . . . . .	128
6.2 Al/Pd/Al . . . . .	129
6.3 First Nb/Pd/Nb devices . . . . .	133
6.3.1 IV characteristic . . . . .	133
6.3.2 Temperature dependence. . . . .	135
6.3.3 Magnetic field dependence . . . . .	136
6.4 First Nb/Au/Nb devices. . . . .	139
6.5 Final Nb/Au/Nb devices . . . . .	141
6.6 Final Nb/Pd/Nb devices. . . . .	145
6.7 Discussion and Conclusion. . . . .	146
<b>7 Josephson Diode Effect and Nonreciprocal Charge Transport in SNS Junctions</b>	<b>149</b>
7.1 Introduction . . . . .	149
7.2 Methods . . . . .	151
7.3 Results . . . . .	151
7.3.1 Basic characterization . . . . .	151
7.3.2 Josephson diode effect in a magnetic field . . . . .	153
7.3.3 Conductance asymmetry in an atomic point contact . . . . .	156
7.3.4 Resistance dependence . . . . .	156
7.3.5 Asymmetry in Au-based SNS junctions. . . . .	157
7.4 Discussion . . . . .	163
7.4.1 Current symmetries and coordinate symmetries . . . . .	163
7.4.2 Theoretical explanation for diode effects in SNS junctions . . . . .	163
7.4.3 Non-reciprocity at finite bias voltages . . . . .	165
7.5 Conclusion. . . . .	167
7.6 Appendix . . . . .	169
<b>8 Conclusion and outlook</b>	<b>171</b>
<b>References</b>	<b>175</b>
<b>Acknowledgments</b>	<b>189</b>
<b>Curriculum Vitæ</b>	<b>193</b>
<b>List of Publications</b>	<b>195</b>





# Summary

This thesis centers around two topics: graphene nanoribbons (GNRs) and superconductors. The aim of this thesis is to work towards combining these two topics, in order to study how superconducting correlations interact with magnetic correlations within graphene nanoribbons, such as the magnetic edge states present in the zigzag edges of graphene nanoribbons. To introduce superconducting correlations into a graphene nanoribbon, it is important that there is a highly electrically transparent interface between a superconductor and the graphene nanoribbon. This is the main focus of this thesis. In **chapter 1**, I introduce a vision for the interaction of superconductivity with magnetism in graphene nanoribbons. At the basis is the concept of Yu-Shiba-Rusinov (YSR) states, which form when a local magnetic moment interacts with superconductivity. The idea of creating a chain of coupled YSR states is elaborated, which could potentially be created and studied in graphene nanoribbons produced through bottom-up chemical synthesis. After this, more global discussion of graphene nanoribbons, electrical contacts to graphene nanoribbons, superconductivity and the superconducting diode effect (relevant to chapter 7) are given.

In **chapter 2**, the electronic structure and properties of graphene nanoribbons are discussed. A comparison is made with trans-polyacetylene and graphene. A transfer matrix approach is introduced for analytically obtaining the eigenvalues of finite-size graphene nanoribbons, which demonstrates that the tight-binding band structure of graphene nanoribbons can be understood through the Su-Schrieffer-Heeger model. After this, a basic description of different transport mechanisms is given. After this, superconductivity in and out of equilibrium is discussed, with a special focus on the superconducting proximity effect. Finally, the effect of a Meissner current on Andreev reflections at NS interfaces is calculated, which modifies the behavior found by Blonder, Tinkham and Klapwijk (BTK) by introducing nonreciprocity, allowing for different electrical conduction in the forward and backward transport directions.

In **chapter 3**, the fabrication of two types of electrical contacts with nanoscale electrode separations is discussed; so-called nanogap electrodes. Wide nanogap electrodes, with a width of 2  $\mu\text{m}$  and electrode separations of  $\sim 30$  nm are discussed first, after which the fabrication of needle-like nanogap electrodes, with a width of  $\sim 10$  nm and electrode separations of  $\sim 6$  nm is discussed. After the discussion of lithographically defined nanogap electrodes, a fabrication method for electromigration break junctions by means of shadow-mask evaporation in a single vacuum chamber is discussed; This recipe, which requires only a single electron beam write step, enables the production of electromigration break junctions with superconducting niobium patches that introduce superconductivity in the normal metal wire (made of Au or Pd in this thesis). In addition, a list of other fabrication recipes used in this thesis is included. Finally, flaws in fabrication recipes are discussed and a recipe for the substrate transfer of graphene nanoribbons using a Poly(methyl methacry-

late) (PMMA) membrane on a glass slide is introduced.

In **chapter 4**, the electrical contacts between graphene nanoribbons and electrodes made of the superconducting alloy  $\text{Mo}_{0.62}\text{Re}_{0.38}$  are studied in nanogap devices. Devices were found to have a resistance of the order of  $1\text{ G}\Omega$  at room temperature. The temperature dependence of the electrical current versus bias voltage is studied to investigate the transport mechanism. The current at a constant voltage is suppressed as the temperature is decreased, which can be fitted to an activation energy of 60 to 500 meV, depending on the device and electrode geometry. A comparison of MoRe and Pd contacted graphene nanoribbon devices shows that devices made with Pd electrodes can conduct currents that are  $10^4$  larger at the same bias voltage.

In **chapter 5**, the electrical interfaces between MoRe electrodes and aerosol-deposited ligand-free gold nanoparticles are studied by electrical characterization. Interpreting results through the BTK formalism, it is found that MoRe electrodes make electrically transparent interfaces to gold nanoparticles, also confirming the presence of superconductivity in the MoRe nanogap electrodes.

In **chapter 6**, the superconducting proximity effect is studied in electromigrated break junctions with superconducting banks/patches. The wire/constriction part of the break junction is made of Pd, as a contact metal for GNRs, or Au, as a more optimal choice for the proximity effect. Initial devices were made with Al as the superconductor and were found not to be superconducting. Later devices were made with Nb as the superconductor. Several iterations of devices are discussed, leading to a final recipe in which a superconducting gap of  $250\text{ }\mu\text{eV}$  was achieved in a broken constriction. In early iterations, a superconducting diode effect, an asymmetry between the positive and negative critical current, was discovered upon application of an in-plane perpendicular magnetic field. This phenomenon is further studied and explored in chapter 7. By investigating the current versus voltage characteristic, it was furthermore found that the superconducting gap in the electromigrated/broken junctions could be estimated from the behavior of unbroken or partially broken junctions.

In **chapter 7**, the superconducting diode effect is studied in Pd electromigration break junctions with Nb patches. Going beyond the paradigm of the diode effect, which considers the asymmetry in the dissipationless/critical current, the finite bias differential conductance asymmetry and the related excess current/deficit voltage asymmetry are investigated. The deficit voltage and its asymmetry with respect to bias voltage, magnetic field strength and magnetic field direction was studied in the same junction at different junction resistances. It was found that the deficit voltage and its bias and field asymmetry does not depend strongly on junction resistance. An explanation of the asymmetric conductance is given in which the Meissner screening current affects the Andreev reflections at the NS interfaces.

Finally, in chapter **chapter 8** an outlook and the conclusions of this thesis are given.

# Samenvatting

Deze scriptie draait om twee onderwerpen: grafeen-nanoribbons (GNRs) en supergeleiders. Het doel van deze scriptie is om naar de combinatie van deze twee onderwerpen toe te werken, om te bestuderen hoe supergeleidende correlaties interageren met magnetische correlaties binnen grafeen-nanoribbons, zoals de magnetische eindtoestanden aanwezig in de zigzagranden van grafeen-nanoribbons. Om supergeleidende correlaties in een grafeen-nanoribbon te introduceren, is het belangrijk dat er een zeer elektrisch transparante interface is tussen een supergeleider en het grafeen-nanoribbon. Dit is het belangrijkste focuspunt van deze scriptie. In **hoofdstuk 1** introduceer ik een visie op de interactie van supergeleiding met magnetisme in grafeen-nanoribbons. Aan de basis ligt het concept van Yu-Shiba-Rusinov (YSR) toestanden, die ontstaan wanneer een lokaal magnetisch moment interageert met supergeleiding. Het idee van het creëren van een keten van gekoppelde YSR-toestanden wordt uitgewerkt, wat potentieel gerealiseerd en bestudeerd kan worden in grafeen-nanoribbons die zijn geproduceerd door bottom-up chemische synthese. Hierna volgt een meer algemene bespreking van grafeen-nanoribbons, elektrische contacten met grafeen-nanoribbons, supergeleiding en het supergeleidende diode-effect (relevant voor hoofdstuk 7).

In **hoofdstuk 2** worden de elektronische structuur en eigenschappen van grafeen-nanoribbons besproken. Er wordt een vergelijking gemaakt met trans-polyacetyleen en grafeen. Een overdrachtsmatrixbenadering wordt geïntroduceerd om de eigenwaarden van grafeen-nanoribbons van eindige grootte analytisch te verkrijgen, wat aantoont dat de tight-binding bandstructuur van grafeen-nanoribbons begrepen kan worden via het Su-Schrieffer-Heeger-model. Hierna volgt een basisbeschrijving van verschillende transportmechanismen. Vervolgens wordt supergeleiding in en buiten evenwicht besproken, met een speciale focus op het supergeleidende nabijheidseffect. Ten slotte wordt de invloed van een Meissnerstroom op Andreev-reflecties bij NS-raakvlakken berekend, wat het gedrag gevonden door Blonder, Tinkham en Klapwijk (BTK) wijzigt door nonreciprociteit te introduceren, waardoor verschillende elektrische geleiding in de voorwaartse en achterwaartse transportrichtingen mogelijk wordt.

In **hoofdstuk 3** wordt de fabricage van twee soorten elektrische contacten met nanoschaal elektrode-afstanden besproken, zogenaamde nanogap-elektroden. Eerst worden brede nanogap-elektroden besproken, met een breedte van 2  $\mu\text{m}$  en elektrode-afstanden van  $\sim 30$  nm, waarna de fabricage van naaldachtige nanogap-elektroden wordt besproken, met een breedte van  $\sim 10$  nm en elektrode-afstanden van  $\sim 6$  nm. Na de bespreking van lithografisch gedefinieerde nanogap-elektroden wordt een fabricatiemethode voor elektromigratiebreukverbindingen door middel van schaduwmaskerverdamping in een enkele vacuümruimte besproken; Dit recept, dat slechts één elektronenbundel-schrijfstap vereist, maakt de productie van elektromigratiebreukverbindingen met nabije supergeleidende ni-

obiumreservoirs mogelijk die supergeleiding introduceren in de normale metalen draad (gemaakt van Au of Pd in deze scriptie). Bovendien is een lijst van andere fabricagerecepten die in deze scriptie zijn gebruikt, opgenomen. Tot slot worden gebreken in fabricagerecepten besproken en een recept voor de overdracht van substraten van grafeen-nanoribbons met behulp van een Poly(methyl methacrylaat) (PMMA) membraan op een glasplaatje geïntroduceerd.

In **hoofdstuk 4** worden de elektrische contacten tussen grafeen-nanoribbons en elektroden gemaakt van de supergeleidende legering  $\text{Mo}_{0.62}\text{Re}_{0.38}$  bestudeerd in nanogap-apparaten. Apparaten bleken een weerstand van de orde van  $1\text{ G}\Omega$  bij kamertemperatuur te hebben. De temperatuurafhankelijkheid van de elektrische stroom versus de toegepaste spanning wordt bestudeerd om het transportmechanisme te onderzoeken. De stroom bij een constante spanning wordt neemt sterk af naarmate de temperatuur wordt verlaagd, waaraan een activeringsenergie van 60 tot 500 meV kan worden gefit, afhankelijk van het apparaat en de elektrodegeometrie. Een vergelijking van MoRe- en Pd-gecontacteerde grafeen-nanoribbon-apparaten laat zien dat apparaten gemaakt met Pd-elektroden stromen kunnen geleiden die  $10^4$  keer groter zijn bij dezelfde toegepaste spanning.

In **hoofdstuk 5** worden de elektrische interfaces tussen MoRe-elektroden en met aerosol-gedeponeerde ligandvrije goudnanodeeltjes bestudeerd door elektrische karakterisering. Door resultaten te interpreteren met het BTK-formalisme, wordt gevonden dat MoRe-elektroden elektrisch transparante raakpunten vormen met goudnanodeeltjes. Hiermee wordt ook de aanwezigheid van supergeleiding in de MoRe-nanogap-elektroden bevestigd.

In **hoofdstuk 6** wordt het supergeleidende nabijheidseffect bestudeerd in elektromigratiebreukverbindingen met nabije supergeleidende lagen. Het draad/vernuwingsgedeelte van de breukverbinding is gemaakt van Pd, als contactmetaal voor GNRs, of Au, als een meer optimale keuze voor het supergeleidende nabijheidseffect. Initieel werden apparaten gemaakt met Al als supergeleider; Deze bleken niet supergeleidend te zijn. Latere apparaten werden gemaakt met Nb als supergeleider. Verschillende iteraties van apparaten worden besproken, resulterend in een definitief recept waarbij een supergeleidende energiekloof van  $250\mu\text{eV}$  werd bereikt in een gebroken vernauwing. In vroege iteraties werd een supergeleidend diode-effect, een asymmetrie tussen de positieve en negatieve kritische stroom, ontdekt bij toepassing van een in-vlak loodrechte magnetische veld. Dit fenomeen wordt verder bestudeerd en verkend in hoofdstuk 7. Door de stroom versus spanning karakteristiek te onderzoeken, werd bovendien gevonden dat de supergeleidende kloof in de volledig gebroken elektromigratiebreukverbindingen kan worden geschat uit het gedrag van ongebroken of gedeeltelijk gebroken verbindingen.

In **hoofdstuk 7** wordt het supergeleidende diode-effect bestudeerd in Pd-elektromigratiebreukverbindingen met Nb-reservoirs. Verder gaand dan het paradigma van het supergeleidende diode-effect, dat de asymmetrie in de dissiperende/kritische stroom overweegt, worden de asymmetrie in de differentiële geleidbaarheid en de daarmee samenhangende overschotstroom/tekortschieting in spanning onderzocht. De tekortschieting in spanning en diens asymmetrie ten opzichte van de toegepaste spanning, magnetische veldsterkte en magnetische veldrichting werden bestudeerd in dezelfde verbinding bij verschillende

verbindingweerstand. Het werd gevonden dat de tekortschietende spanning en de bijbehorende asymmetrie ten opzichte van de toegepaste spanning en het magnetisch veld niet sterk afhankelijk zijn van de verbindingweerstand. Een verklaring van de asymmetrische geleidbaarheid wordt gegeven waarin de Meissner-afschermingsstroom de Andreev-reflecties bij de NS-interfaces beïnvloedt.

Ten slotte worden in hoofdstuk **hoofdstuk 8** een vooruitblik en de conclusies van deze scriptie gegeven.



# 1

## Introduction

*In this chapter, the context and motivation behind studying graphene nanoribbons with superconducting contact electrodes will be introduced. After this, the relevant background information and theory behind graphene nanoribbons, metal contacts to graphene nanoribbons, superconductivity and superconducting hybrid junctions will be introduced. Finally, the main chapters of the thesis are introduced.*

## 1.1 Graphene nanoribbons and superconductivity: Why combine them

A major motivation behind this thesis was to enable the study of the interaction between a chain of magnetic moments (a spin chain) and superconductivity. The interplay between these two concepts is interesting, as single magnetic moments are known to form localized bound states[1–4] in superconductors and multiple of these bound states could couple to form a band structure[5, 6]. Bottom-up synthesized graphene nanoribbons (GNRs), on the other hand, are produced with atomically precise control over their structure and composition, which allows for making regular spin chains in a conductive material[7]. To study the interaction between these spin chains and superconductivity, electronically transparent electrical contacts to the graphene nanoribbons and superconductivity in the electrical contacts are required. For this reason, this thesis contains studies aimed at making advancements toward highly transparent/conductive superconducting contacts to graphene nanoribbons.

## 1.2 Context and theoretical background

### 1.2.1 Motivation and scope of the thesis

Superconductivity and magnetism are two competing phases of the electronic and magnetic state of matter. On a macroscopic scale, the presence of a magnetic field larger than the critical field ( $H_c$ ) of a superconductor brings the superconductor to the normal state, making it resistive. For magnetic fields smaller than the critical field, a bulk superconductor will instead expel the magnetic field, which is known as the Meissner effect[8]. Above the critical field, superconductivity is suppressed. Thus, the conductive properties of superconductors can be tuned by external (electro)magnetic fields and superconducting circuits can be used as sensitive sensors for magnetic fields.

Recent progress has enabled the study of the interplay of superconductivity and magnetism on the nanoscale. For example, using scanning tunneling microscopy (STM), single magnetic atoms can be placed and probed on superconducting substrates to study the interaction between them and the substrate[9]. In many cases, Yu-Shiba-Rusinov (YSR) bound states are observed in the superconductor, spin polarized electronic excitations that are spatially and energetically localized[1–3]. On these superconducting surfaces, YSR states can be made to interact by moving the magnetic atoms in proximity to each other, creating spin chains. In these spin chains, the YSR states hybridize into bands, with a dispersion relation that depends sensitively on the spacing between magnetic ad-atoms and the Fermi wavelength in the superconducting substrate through the magnetic exchange coupling. Importantly, the electronic degrees of freedom, the YSR states, couple to the magnetic order in the spin chain.

Though such spin chains coupled to superconductors can be realized on surfaces and studied by STM, their properties have not yet been exploited in electronic devices. Potential applications can arise in combinations with field effect transistor (FET) devices, in which it is possible to tune the charge density by an external electric field for a back-gate electrode. A change in charge density slightly changes the Fermi wavelength at the same time, which should change the exchange interaction between the magnetic moments and modulates



the interaction between the YSR states.

As an illustrative example, in the 1D infinite square well of length  $L$ , the allowed wavelength of all eigenstates labeled by indices  $n \geq 0$  is given by  $\lambda_n = \frac{2L}{n}$ . These states are filled up to some maximum  $n_{\max}$ . Adding an extra charge carrier is equivalent to increasing the maximum index to  $n_{\max} + 1$ . As a result, the Fermi wavelength has decreased such that an extra half-wavelength fits in the length  $L$ . At the ends of the chain, the wavefunction at the Fermi energy does not change much, but at the center of the infinite square well, antinodes in the wavefunction change into nodes and vice versa. So, why does this matter for the exchange interactions? The reason why this changes the exchange interactions in the 1D infinite square well is because the carrier electrons, the electrons at the Fermi energy, are responsible for the electronically-mediated exchange interaction. By changing nodes into antinodes or vice versa, the exchange interaction between magnetic moments at the edge and the bulk can be turned on or off. Thus, the exchange interaction changes over the length-scale of the square well.

Neglecting the Fermi wavelength for the moment, dimensionality matters for magnetic order due to electronically-mediated exchange interactions. As opposed to 2D and 3D structures, where inverse area-laws reduce exchange interactions over distance, in 1D the long-distance exchange interaction is significant. In 1D, the exchange interaction decays as  $\frac{1}{r}$ , where  $r$  is the distance between the spins. Thus, when considering a spin chain, the interaction of 1 spin with  $N$  other spins diverges in a logarithmic manner (divergent) as a function of chain length,  $E_0 = \sum_{i=1}^N J_{0i} S_0 S_i \sim J \int_1^N \frac{1}{r} dr \propto \ln(N)$ . The total energy of all interactions scales as  $E_{\text{tot}} \propto JN \ln(N)$ , which can be compared to the entropy term  $TS = k_b T \ln(2^N) = N k_b T \ln(2)$ . The energy term grows faster as  $N$  grows than the entropy term. This suggests that long-range magnetic order can be thermodynamically stable in spin chains in infinitely long ideal 1D conductors for arbitrarily weak exchange interactions.

The interaction of spin chains with long-range magnetic order and superconductivity goes beyond what has so far been studied in STM, as most STM studies are done on surfaces that behave as 3D or 2D conductors, such as Re, Pb and NbSe<sub>2</sub>. To realize this combination experimentally, several approaches are possible. The minimum requirements are the presence of superconductivity and a 1D conductor with localized magnetic sites. The combination of all these properties in a single material would be optimal, but practically difficult to achieve. Thus, another option is to bring a superconductor in contact with a 1D conductor with a built-in spin texture. Such 1D systems can be made in a bottom-up fashion by on-surface chemical synthesis of nano-materials from molecular precursors[10]. In this technique, precursor molecules are polymerized and can be cyclodehydrogenated to form graphene nanostructures. Examples of 1D conductors with built-in spin textures are found in zigzag graphene nanoribbons[11] (ZGNRs), triangulene chains[12] and more generally in zigzag edges and dopants (B,N) in graphene nanoribbons[13, 14]. These are all promising candidates that should be tunable in a field effect transistor, as many are based on graphene-like  $sp^2$  hybridized carbon. With the vision of integrating such nanostructures into field effect transistor devices in the future, this thesis focuses on coupling armchair graphene nanoribbons (AGNRs) made by on-surface bottom-up chemical synthesis to superconducting electrodes.

### 1.2.2 Graphene nanoribbons

Graphene nanoribbons are quasi-1D materials that can be viewed as an intermediate between 1D organic semiconductors (polymers) such as polyacetylene and the 2D material graphene, with edges that look like cis-polyacetylene (armchair edge) or trans-polyacetylene (zigzag edge) and the same bulk structure to that of graphene. The structural analogy can be taken to the point that cis-polyacetylene can be labeled a 2-armchair GNR and trans-polyacetylene a 1-zigzag GNR. The expected properties of graphene nanoribbons thus lie somewhere in-between these two extremes. As such, I briefly introduce the electronic properties of polyacetylene and graphene, starting with their electronic structures and then discussing their electrical properties.

The electronic structure of polyacetylene depends on the atomic structure. In both cis- and trans-polyacetylene, the bond lengths are disproportionate, alternating in length. This alternating bond length makes the Su-Schrieffer-Heeger (SSH) model[15], a tight-binding model with alternating hopping integrals, the simplest model with predictive power for polyacetylene. The main prediction of this model is the presence of a band-gap. Furthermore, if there is a longer bond (smaller hopping integral) at the ends, a localized state is expected to show up there. There is also a difference between the two structures. In trans-polyacetylene moving all bond lengths over by 1 bond results in the same structure (ignoring the ends). Meanwhile, in cis-polyacetylene, the two configurations are not the same and there is an energy cost associated with moving the bonds. This difference means that in undoped trans-polyacetylene it is expected that charges can move much more easily. Experimentally, this is reflected by the electrical conductivities of undoped cis- ( $\sigma = 1.7 \cdot 10^{-9} \text{ S cm}^{-1}$ ) and trans-polyacetylene ( $\sigma = 4.4 \cdot 10^{-5} \text{ S cm}^{-1}$ )[16].

The electronic structure of graphene is intimately related to its structure. The simplest tight-binding band structure of graphene is a honeycomb lattice with equal hopping integrals, with two atoms per primitive unit cell. The honeycomb lattice (and graphene) is famous for exhibiting two Dirac-points. These are points in the band-structure where the dispersion relation becomes linear and particles can behave as-though they are massless Dirac fermions[17]. This also has the consequence that the density of states (DOS) can be zero without the presence of a finite band-gap, at the so-called Dirac points. In the charge-neutral scenario, the chemical potential sits at the energy of the Dirac points, making graphene a semimetal[18]. The electrical conductivity of graphene depends on the mean free path, but it can be as large as  $\sigma = 7.1 \cdot 10^3 \text{ S cm}^{-1}$ [19].

The absence of a band gap in graphene limits its use for field-effect transistors (FETs), as it will remain conductive regardless of the induced charge density[18]. Graphene nanoribbons exhibit an electronic band-structure that can be understood from the band-structure of graphene by making cuts[20]. In the simplest tight-binding scheme, there are 3 families of armchair graphene nanoribbons. Labeling their widths by integers  $p$ , the three families are the small ( $3p + 2$ ), intermediate ( $3p$ ) and large ( $3p + 1$ ) band-gap families. In the simplest approximation, the small band-gap family does not exhibit a band-gap, as a line cuts through the Dirac-point, resulting in a finite density of states at zero energy. Taking into account charging effects and edge reconstructions (similar to the bonds in polyacetylene) significantly modifies the band-gaps, while the shape of the band-structure remains similar. Zigzag graphene nanoribbons, in contrast, exhibit zero-energy flat bands related to

a particular cut through the two Dirac cones. These flat bands are related to edge modes. They are topological in nature and have been related to the end states in the SSH model. In more involved calculations using density functional theory[21, 22] and quantum Monte Carlo[23, 24] approaches, it can be shown that the edges of zigzag GNRs can be spin polarized/ferromagnetic, with an antiferromagnetic exchange interaction between the two edges and a small band-gap in the electronic density of states. The edge states of ZGNRs are of interest for electronics, though because of limited chemical stability of their edges, only STM studies[25] of them have been performed thus far. This is not the case for armchair graphene nanoribbons.

The electrical conductivity of both polyacetylene and graphene has been found to be dependent on doping, with cis-polyacetylene showing an increase by up to 11 orders of magnitude[26], a response that is orders of magnitude larger than that of graphene, which shows up to 3 order of magnitude response [19]. Armchair graphene nanoribbons fit in the middle, with a field-effect-tunable conductance changing over 6 orders of magnitude demonstrated in 9-armchair GNRs[27].

### 1.2.3 Electrical contact to armchair graphene nanoribbons

Since armchair graphene nanoribbons exhibit a band gap in energy, with the chemical potential sitting at the center of the band gap, their intrinsic low-bias conductivity is exclusively related to thermally excited charge carriers. The probability for such a thermal excitation to occur is proportional to the Boltzmann factor  $e^{-\frac{E_{\text{gap}}}{k_B T}}$ . At room temperature, this factor is roughly  $e^{-40}$  for a band gap of 1 eV, growing rapidly when the temperature is decreased. When injection happens from the chemical potential, this is  $e^{-20} \approx 10^{-9}$ . Assuming a single channel model for GNRs with a resonant conductance of  $1G_0$ , this amounts to a room temperature conductance of 0.31 pS per GNR. Evidently, undoped armchair GNRs are poor conductors. Cooling such graphene nanoribbons down to a temperature of a few K, at which superconductivity starts to play a role, will result in an increase in resistance, to the point where it is no longer possible to measure any current through them at low bias voltages.

To improve the electrical conductance of GNRs, it is important that valence and conduction band positions in the GNR can be tuned with respect to the chemical potential, preferably to the point of degenerate doping, where the chemical potential enters the band. Doping can either be achieved by substitution in the precursor or by exposure to alkali metals or halogens, such as K or  $I_2$ . Furthermore, the field effect has been exploited for this purpose. The field effect has the drawback that the metal electrodes used to contact GNRs will also screen the electric field. Thus, while GNRs may be degenerately doped far from the metal, screening will effectively pin the valence and conduction bands close to the metal.

Because of electrostatic screening in FET devices, it is important that the contact metal aligns well to the conduction or valence band. For this purpose, high and low work function,  $\Phi$ , metals can be used to contact the valence and conduction band respectively, as has been shown for carbon nanotubes[28]. Low work function metals are generally prone to oxidation, while high work-function metals[29, 30] tend to be noble metals such as Au ( $\Phi = 5.31$  eV), Pd ( $\Phi = 5.22$  eV) and Pt ( $\Phi = 5.64$  eV) and are preferred due to their chemical

stability. While Pt has a larger work function, Pd is known to result in more charge transfer to graphene and CNTs[31]. This results in larger doping, as a result of which it has become the preferred contact metal for CNT electronics and a promising candidate for GNR-based devices. As for intrinsically superconducting contact metals, Mo ( $\Phi = 4.3 - 4.9$  eV), Re ( $\Phi = 4.72$  eV), MoRe and W ( $\Phi = 4.55$  eV) are known to make good contacts to CNTs. These metals are known to make strong chemical bonds to CNTs, resulting in the formation of metal-carbides at the interfaces.

### 1.2.4 Superconductivity

Superconductivity is an electronic state of matter in which a material loses all electrical resistance below a certain temperature ( $T_c$ ). Furthermore, it exhibits an effect that is known as the Meissner effect, the complete expulsion of magnetic field/perfect diamagnetism[8]. On a microscopic level, conventional superconductors can be microscopically understood on the basis of the Bardeen-Cooper-Schrieffer theory (BCS). In this theory, electrons with equal spin scatter repulsively at the Fermi surface through phonons. Due to these interactions, an effective attractive interaction results, which results in a phase transition with a complex order parameter  $\Delta(r)$  (in a mean-field treatment. In a many-body treatment  $\hat{\Delta}$  is a bosonic quantum field operator.). Associated with this order parameter is a binding energy  $|\Delta|$  per electron. This binding energy results in an energy gap in the quasiparticle excitations, which suppresses thermally excited quasiparticle occupancies

by a factor  $e^{-\frac{|\Delta|}{k_B T}}$  compared to a normal metal. Furthermore, a U(1) (electromagnetic) gauge-covariant phase can be associated with the order parameter. While the global phase is not an observable quantity, phase gradients are associated with superconducting/pair currents and are also responsible for the Meissner effect. Though BCS theory does not accurately describe all superconductors, it makes accurate predictions for conventional superconductors and the observation of a pairing mechanism with a binding energy is nearly universal (although gapless superconducting states do exist[3, 32]). In this thesis, thin films of the conventional superconductors MoRe and Nb are considered. Because of this, a notable deviation from standard BCS theory is that these superconducting films are typically so-called 'dirty' superconducting films. This means that they have a mean electronic free path  $l$  that is smaller than the BCS superconducting coherence length ('clean' limit)  $\xi_{c, \text{clean}} = \frac{\hbar v_F}{\pi |\Delta|}$ , the length-scale associated with the pairing interaction. As a result, the coherence length is smaller, with the dirty coherence length given by the geometric mean  $\xi_{c, \text{dirty}} = \sqrt{\frac{\xi_{c, \text{clean}} l}{3}}$  [33].

### 1.2.5 Superconducting proximity effect and SNS junctions

When a normal (non-superconducting) conductor is brought into electrical contact with a superconductor, pair correlations can delocalize into the normal conductor. This effect, called the superconducting proximity effect, can make the normal metal behave as if it was superconducting itself[34, 35]. This means that the superconducting proximity effect has the potential to be used as a tool to make an optimal contact metal to graphene nanoribbons into a superconducting contact metal. To also induce significant superconducting correlations in GNRs, high interface transparencies are required ( $> 10\%$  electrical

interface transparency), which may only be achievable with certain normal metals, such as Pd. Besides the proximity effect, the opposite effect occurs as well, which is fittingly called the inverse proximity effect. In this effect, electrons from the normal conductor can enter the superconductor and reduce the pair correlations in the superconductor, which reduces and broadens the superconducting gap close (up to a few coherence lengths) to the normal conductor. This also reduces the critical temperature of the superconductor.

The superconducting proximity effect and the inverse effect depend critically on what happens at the interface. If the interface is poorly transparent, quasiparticles will not mix and the effect is small. When the interface is fully transparent, the ratio of charge carriers in the superconductor to the number of charge carriers in the normal metal becomes relevant. If there are significantly more quasiparticles in the normal metal, the proximity effect is weak (and the inverse proximity effect is strong). Vice versa, if there are more superconducting carriers in the mixing region, the proximity effect is strong. The number of carriers crossing the interface also depends on the rate at which electrons move in the material. In thin films, this is described by the electronic diffusion coefficient  $D = \frac{v_F l}{3}$ , where  $v_F$  is the Fermi velocity. Due to the diffusive nature of carriers, electrons delocalize over a distance  $\Delta x^2 = D\Delta t$  in a time span  $\Delta t$ . In a superconductor with characteristic timescale  $\Delta t = \frac{\hbar}{|\Delta|}$ , this leads to a characteristic length-scale equal to the coherence length

for dirty films  $\xi_{c,dirty} = \sqrt{\frac{\hbar D}{|\Delta|}}$ . More generally, in the normal metal at an energy  $E$ , the

characteristic length scale is  $\xi(E) = \sqrt{\frac{\hbar D}{E}}$ . This means that correlations at lower energies will delocalize further into the normal metal. As a result of this, at a distance  $L$  that is far from the interface (in terms of  $\sqrt{\frac{\hbar D}{|\Delta|}}$ ), the energy gap is proportional to the Thouless energy

$E_{Th} = \frac{\hbar D}{L^2}$  [36]. At the interface a proximity parameter can be defined by the ratio of resistance-area products (or just resistances) within the coherence lengths in the normal

and superconducting material  $\gamma = \frac{\rho_S \xi_S}{\rho_N \xi_N} = \frac{D_N^{\frac{1}{2}} N_N}{D_S^{\frac{1}{2}} N_S}$ , with  $\xi_N = \xi(|\Delta|)$ . This shows the large

influence of carrier density (material dependent), as well as the effect of diffusion/grain size (as  $D = \frac{v_F l}{3}$  is proportional to  $l$ ). If the normal metal film thickness  $t$  is smaller than the coherence length, the proximity parameter is smaller by a factor  $\frac{t}{\xi_N}$ . In a similar vein to

the proximity parameter, a parameter related to the interface transparency can be defined by the boundary parameter  $\gamma_B = \frac{R_B}{\rho_N \xi_N}$ , where  $R_B$  is the boundary resistance-area product.

To gain a better understanding of the proximity effect from a practical point of view, it is instructive to compare literature values of metals. In table 1.1, the electronic density of states  $N(E_F)$  (at the Fermi energy) and typical Fermi velocity for electrons in bulk Au, Pd, Al, Mo, Re and Nb are listed<sup>1</sup>. As the mean free path depends on the film structure and deposition method, a single value can not be listed. Typical mean-free paths in evaporated

<sup>1</sup>The density of states values in this table are extracted from the electronic specific heat [37, 38] and the expression

$$C_V = \frac{\pi^2}{3} k_B^2 T N(E_F) [39]$$

Parameters		
Element	Density of states (states nm <sup>-3</sup> eV <sup>-1</sup> )	Fermi Velocity (10 <sup>6</sup> m s <sup>-1</sup> )
Al	34.4	2.03
Au	17.2	1.40
Mo	49.8	-
Nb	222.6	-
Pd	232.4	-
Re	65.9	-

Table 1.1: Density of states and Fermi velocity of selected metals.

thin films are of the order of the grain size ( $\sim 10$  nm). Also, the (free electron) Fermi velocities of Mo, Nb, Pd and Re are not well-defined, as the Fermi surface is fairly anisotropic and consists of multiple electron and hole pockets with different velocities. However, the part of the Fermi surface that is associated with the more localized d orbitals should have a lower Fermi velocity ( $\sim 2.8 \cdot 10^5$  m s<sup>-1</sup> [40]). The Fermi velocity of parts of the Fermi surface that are dominated by the s orbitals, on the other hand, should be similar to the value in gold ( $\sim 1.4 \cdot 10^6$  m s<sup>-1</sup>). From this table it is apparent that there is a large variation in the density of states. Au and Al are the two metals with the smallest DOS and the largest grain size, while the transition metals Pd and Nb have the largest DOS in the table. Combining a metal such as Au with Nb is thus expected to result in a relatively small inverse proximity effect, while combining Pd and Al results in a large inverse proximity effect, which should significantly reduce  $T_c$ . This also indicates that it is significantly more difficult to induce superconducting correlations in Pd than in Au. To efficiently proximitize Pd, a high carrier density superconductor or a thick film of low carrier density superconductor with a large mean-free path is needed. In this thesis, the choice to use e-beam evaporated Nb as a superconductor was made.

The superconducting proximity effect manifests itself in devices in which a small normal metal wire is placed in between superconducting wires, in so-called superconductor - normal metal - superconductor (SNS) junctions. SNS junctions are more generally considered a sub-type of Josephson junctions. These are weak superconducting links that have a smaller critical current than a bulk superconducting wire and can thus act as local superconducting switches. The critical current in SNS junctions depends on their length and resistance. A measure of the quality of a junction at low temperature can be given by the ratio of the product of the critical current and resistance  $I_c R_N$  with respect to the characteristic voltage  $\frac{|A|}{e}$ . In 'long' junctions, where the superconducting coherence length in the normal metal is smaller than the length of the normal metal, the Thouless energy largely determines the  $I_c R_N$  product of the junction, together with the wire resistance. In the opposite 'short' junction limit, where the coherence length is larger, only the superconducting gap and the interface parameters determine the  $I_c R_N$  product. Importantly, the fact that  $I_c R_N$  depends on the Thouless energy and interface parameters means that the degree to which the metal is proximitized can be studied in an SNS junction geometry.

To summarize this section, for SNS junctions the parameters that are important are:

- The proximity parameter  $\gamma$ , through the diffusion coefficients and densities of states.
- The boundary parameter  $\gamma_B$ , through  $R_B$
- The Thouless energy in the normal metal, or  $L$ .
- The film thicknesses  $t_N$  and  $t_S$ , if they are smaller than the coherence length. A thinner normal metal film is better proximitized.
- The critical temperature  $T_c$  of the superconductor, through  $\Delta$ .

The proximity and boundary parameters, as well as the critical temperature are material and fabrication-related parameters, such as thin film structure and the cleanliness and disorder at the interfaces. These are either fixed by the choice of materials or can be improved by modifying the fabrication procedure of devices. In particular, the diffusion coefficient could be improved by increasing grain sizes and thus the mean-free path, while the boundary resistance could potentially be improved by reducing contamination coming from out-gassing of polymer masks[41], understanding alloy formation at thin film interfaces[42] and potentially by using epitaxial growth strategies to reduce disorder. The length and film thicknesses of the normal metal can in principle be controlled precisely by modifying the patterning and metal deposition steps.

In combination with the electromigration technique, I will demonstrate that studying the SNS junction allows for pre-characterizing the proximity effect before breaking the normal metal wire (Au or Pd) to create superconducting contact electrodes for nanoscale objects such as graphene nanoribbons.

### 1.2.6 Nonreciprocity in SNS junctions

A coincidental finding during the study of SNS junctions that will be discussed in this thesis is the discovery of nonreciprocity upon applying a magnetic field on the order of 100 mT in the in-plane direction perpendicular to the current. That is, the critical current in the forward direction  $I_{c+}$  differs from the critical current in the backward direction  $I_{c-}$ .

Such effects have been observed in the 70s and 80s in Josephson junctions (primarily in tunnel junctions), where they were found to be caused by the magnetic field that is created by the bias current itself. This so-called 'self-field effect' is strongly related to the geometry of the device. Another possible origin behind this symmetry breaking is the presence of asymmetry in the resistance, which is possible in tunnel barriers[43]. If  $I_c R_N$  is conserved, then  $I_{c+} = I_{c-} \frac{R_{N-}}{R_{N+}}$ .

Recently, however, studies have observed nonreciprocal superconducting effects that do not match with a self-field effect or an asymmetric barrier effect, such as the superconducting diode effect[44] and the Josephson diode effect[45]. At this point in time, multiple microscopic explanations have been proposed for these effects, some relying on the introduction of finite cooper pair momentum[46], while others rely on a combination of spin/the Zeeman effect and spin-orbit coupling[47–49]. Regardless of the exact mechanism, a common feature across most experiments and theory is the combination of inver-



sion symmetry breaking and time-reversal symmetry breaking. In most experiments, this results in skew-symmetry, such that  $I_{c+}(B) = I_{c-}(-B)$ . In some special cases, it has recently been found that  $I_{c+}(0) \neq I_{c-}(0)$  [50], meaning that there is a Josephson diode effect at zero magnetic field.

In the theory section of this thesis, the finite momentum explanation will be explored a bit more in-depth. In particular, a focus will be placed on the different components that contribute to Cooper pair momentum in current biased SNS junctions with an applied in-plane magnetic field. Furthermore, the relationship between this explanation and the Meissner effect that occurs at the surface of superconductors will be elucidated.

### 1.3 Dissertation outline

The dissertation is divided into 4 main chapters, with supplementary theory, fabrication and conclusion and outlook chapters for the whole thesis. In chapter 2, a more detailed mathematical account of the theory behind graphene nanoribbons electronics as well as superconductivity, the proximity effect and the Josephson diode effect will be given. In chapter 3, the lithographic fabrication of the superconducting nanogap contact electrodes is described, as well as the GNR substrate transfer method onto those devices. Chapter 4 discusses the electrical measurements of 9-AGNRs on MoRe contact electrodes, with a focus on temperature dependence. In chapter 5, the same type of MoRe contact electrodes are characterized by aerosol deposition of ligand-free Au nanoparticles created by spark ablation, demonstrating electrically transparent interfaces by Andreev reflection spectroscopy. Next, in chapter 6, the use of Pd as a superconducting contact metal will be discussed. Measurements of 9-AGNRs on 6 nm Pd nanogap electrodes versus temperature are shown, which show significantly reduced temperature dependence compared to the MoRe devices. Furthermore, the proximity effect in Pd is studied in a constricted variable thickness SNS junction that can be electromigrated to form nanogap electrodes. Finally, in chapter 7, the electrical characteristics of SNS junctions with Au or Pd as the normal metal in the electromigration geometry are studied as a function of magnetic field, which reveals the presence of nonreciprocal superconducting effects, such as the Josephson diode effect. After this there is a discussion of the significance of the results in this thesis and a conclusion.



## 2

## Theory

*In this chapter, a theoretical account will be given of graphene nanoribbons and superconductivity. The band structure of graphene nanoribbons is explained with an emphasis on its relation to the Su-Schrieffer-Heeger model for cis-polyacetylene. A novel analytical calculation, based on the transfer matrix method, is performed for the characteristic polynomial of a graphene nanoribbon, which justifies the Su-Schrieffer-Heeger model picture. A select few transport models for graphene nanoribbons are also elaborated on. For superconductivity, a basic account of Bardeen-Cooper-Schrieffer theory is given, after which Andreev reflections at normal metal-superconductor interfaces, the superconducting proximity effect, and superconductor - normal metal - superconductor Josephson junctions are discussed. Finally, the effect of a non-equilibrium quasiparticle occupancy and momentum resolved effects are discussed. A tight binding model is presented for normal metal -superconductor interfaces in which a Meissner screening current runs parallel to the normal metal - superconductor interface.*

## 2.1 Graphene nanoribbons

### 2.1.1 Electronic structure

The electronic structure of a material is the very basis for understanding its conductive properties. For this reason, in this section the electronic structure of graphene nanoribbons will be discussed.

The electronic structure of graphene nanoribbons is closely related to two 'parent' structures, namely the electronic structure of polyacetylene and that of graphene. In this section the tight-binding structure will be considered. To understand the graphene nanoribbon better, I will first discuss these two structures, before discussing the nanoribbon case. Then for the nanoribbon case, I will introduce the transfer matrix method for finding their electronic band structure. Notably, this method does not rely on a plane wave ansatz[20, 51]. In this approach the electronic structure is found by obtaining a recursion relation for the characteristic polynomial  $\xi(E) = \det(\hat{H} - E\hat{I})$ , parameterizing and then solving for its zeros.

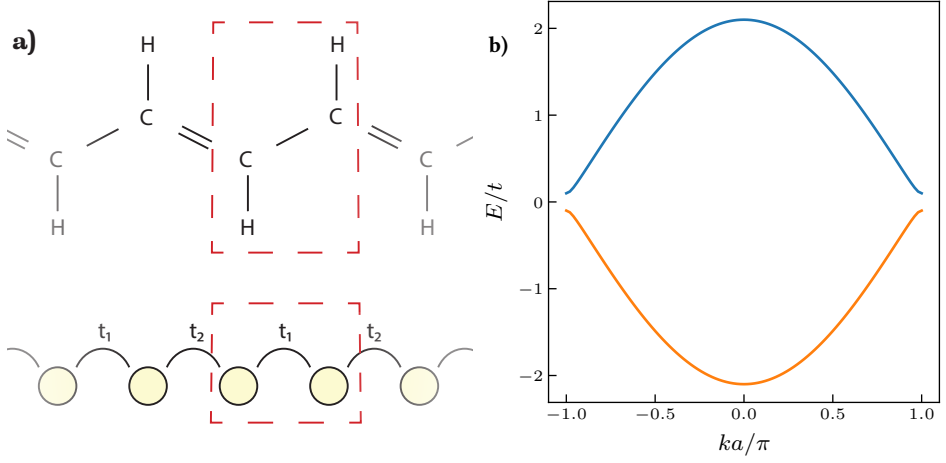


Figure 2.1: a) Schematic structure of trans-polyacetylene and a schematic representation of the related SSH tight binding model. The primitive unit cell is indicated by the dashed red box. b) Band structure of the SSH model for  $t_2 = 1.1t_1 = 1.1t$ .

### Polyacetylene

Polyacetylene is a structure with alternating single and double bonds with different lengths. Electrical conduction happens through the  $\pi$  bonds. The  $p$  orbitals related to conduction can be most simply described by the SSH model, which is illustrated in Figure 2.1a. The electronic structure of this model can be fully described by a hopping energy  $t_1$  and a hopping energy  $t_2$ . One can also include an on-site energy/chemical potential, but this does not affect the dispersion apart from shifting energies. The SSH model is a periodic 1D model with 2 atoms in the primitive unit cell. By Bloch's theorem/translation symmetry, this means that the single particle eigenfunctions are separable and of the form:

$$|\psi\rangle = \sum_j c_j |j\rangle \sum_n e^{ikan} |n\rangle \quad (2.1)$$

Where  $j$  denotes the atom in the unit cell,  $n$  denotes the index of the unit cell,  $c_j$  is the probability amplitude in the unit cell and  $a$  is the spacing between the unit cells.

The Hamiltonian is of the form:

$$\hat{H} = \sum_n t_1(|0, n\rangle\langle 1, n| + |1, n\rangle\langle 0, n|) + t_2(|0, n-1\rangle\langle 1, n| + |1, n\rangle\langle 0, n-1|) \quad (2.2)$$

Applying the Hamiltonian to the wavefunction, we get:

$$\hat{H}|\psi\rangle = (t_1(|0\rangle\langle 1| + |1\rangle\langle 0|) + t_2(e^{ika}|0\rangle\langle 1| + e^{-ika}|1\rangle\langle 0|))|\psi\rangle \quad (2.3)$$

Where the summation over the index  $n$  has been taken. The resulting Hamiltonian only describes the degrees of freedom within the unit cell and has a  $2 \times 2$  matrix representation.

$$\hat{H} = \begin{bmatrix} 0 & t_1 + t_2 e^{ika} \\ t_1 + t_2 e^{-ika} & 0 \end{bmatrix} \quad (2.4)$$

The eigenenergies can be found by solving  $\det(\hat{H} - E\hat{I}) = 0$ . This produces the characteristic equation  $E^2 = (t_1 + t_2 e^{ika})(t_1 + t_2 e^{-ika}) = t_1^2 + t_2^2 + 2t_1 t_2 \cos(ka)$ . This yields two bands:

$$E_{\pm,k} = \pm \sqrt{t_1^2 + t_2^2 + 2t_1 t_2 \cos(ka)} \quad (2.5)$$

These bands are centered around  $k = 0$ . Furthermore, the minimum value of  $E^2$  is  $(t_1 - t_2)^2$ , which results in a band gap of  $2|t_1 - t_2|$  at  $k = \pm \frac{\pi}{a}$ . The resulting dispersion relations are plotted in Figure 2.1b.

Although the dispersion relation does not change by interchanging  $t_1$  and  $t_2$ , the wavefunction amplitude does. For  $k = \frac{\pi}{a}$ , interchanging  $t_1$  and  $t_2$  results in a sign-change in  $\langle 0|\psi\rangle\langle\psi|1\rangle + \langle 1|\psi\rangle\langle\psi|0\rangle = \langle\psi|\hat{X}|\psi\rangle$ , as the hopping element changes sign. The representation of this quantity by the Pauli matrix  $\hat{X}$  indicates that it can be considered as a kind of pseudospin.

In the next section it will be shown that the band structure that can be found for the SSH model is fundamental to not just polyacetylene, but also to graphene and graphene nanoribbons.

## Graphene

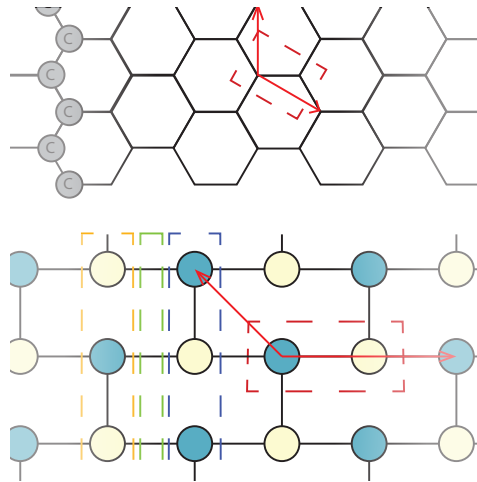


Figure 2.2: Schematic structure of graphene and a schematic representation of the related tight binding model. The primitive unit cell is indicated by the dashed red box.

Graphene has a 2-D lattice, which means it has more electronic degrees of freedom than polyacetylene. Graphene shares the two atoms per primitive unit cell, as illustrated in Figure 2.2. All bonds have equal strength/hopping integral  $t$ , however. Furthermore, graphene is periodic in 2 directions. As has been shown for polyacetylene, this periodicity means that the wavefunction is separable in the form of equation (2.1). The only difference being that in two dimensions, there is periodicity in two spatial dimensions, meaning that the variable  $ka$  becomes  $k_1 a_1 + k_2 a_2$ . In graphene,  $a_1 = a_2 = a$ ,  $k_1 = \frac{1}{2}(-k_x + \sqrt{3}k_y)$  and  $k_2 = \frac{1}{2}(k_x + \sqrt{3}k_y)$ , as defined in the coordinate system in Figure 2.2. The  $2 \times 2$  Hamiltonian that is now found is:

$$\hat{H} = \begin{bmatrix} 0 & t(1 + e^{ik_1 a} + e^{ik_2 a}) \\ t(1 + e^{-ik_1 a} + e^{-ik_2 a}) & 0 \end{bmatrix} \quad (2.6)$$

At this point, writing the Hamiltonian in  $k_x$  and  $k_y$  can be done to illustrate that the electronic structure of graphene can be considered to be SSH-like in the  $k_y$  direction, with differing ratios of  $t_1$  to  $t_2$ .

$$\hat{H} = \begin{bmatrix} 0 & t + 2t \cos(\frac{k_x a}{2}) e^{ik_y \frac{\sqrt{3}}{2} a} \\ t + 2t \cos(\frac{k_x a}{2}) e^{-ik_y \frac{\sqrt{3}}{2} a} & 0 \end{bmatrix} \quad (2.7)$$

Where we may identify  $t_1 = t$  and  $t_2 = 2t \cos(\frac{k_x a}{2})$ . Thus, the SSH-like band structure in the  $y$ -direction depends on the value of  $k_x$ . When  $|t_1| = |t_2|$ , the dispersion relation goes to zero energy. This happens at  $k_x = \frac{2\pi}{3a}$  and  $k_y = \pm \frac{2\pi a}{\sqrt{3}}$ . These are the two unique Dirac points of graphene. Crossing the Dirac point in graphene by varying  $k_x$  is equivalent to flipping the pseudospin defined in the SSH model.

Using the previously obtained solution for the SSH model given by equation (2.5), we find the solution

$$E_{\pm, k_x, k_y} = \pm |t| \sqrt{1 + 4 \cos(\frac{k_x a}{2})^2 + 4 \cos(\frac{k_x a}{2}) \cos(k_y \frac{\sqrt{3}}{2} a)}. \quad (2.8)$$

The positive solution is plotted in Figure 2.3, which shows the hexagonal symmetry of the electronic band structure of graphene. The band approaches zero energy in cones at the Dirac points.

### Graphene nanoribbons

The electronic structure of graphene nanoribbons can be understood in simple terms by considering the previously found band structure for graphene. Since a graphene nanoribbon can theoretically be obtained by cutting out a strip of graphene, the band structure

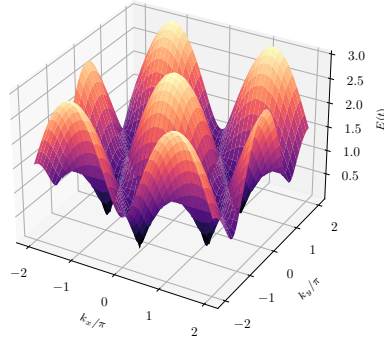


Figure 2.3: Band structure of graphene. For ease of viewing, only the positive energy band is shown.

of graphene nanoribbons can be obtained by transforming this cutting procedure to momentum space. Electronically, this is similar to confining free electrons in 1D to an infinite square well, which yields  $k = \frac{\pi l}{L}$ , with  $l = 1, 2, \dots$ . In the same fashion, a cut in the  $x$ -direction which incorporates  $L$  unit cells in the  $y$ -direction quantizes  $k_y$  into values  $k_y = \frac{\pi l}{a(L+1)}$ , with  $l = 1, 2, \dots, L$  [20]. This is the case of the armchair graphene nanoribbons. These are nanoribbons with edges matching the edge shown in Figure 2.2. The line-cuts in the band structure of graphene yielding the band structure of a 9-atom-wide armchair-edge graphene nanoribbon (9-AGNR) are shown in Figure 2.4a. Note that every atom in the width contributes only half a line-cut. As a result, any armchair graphene nanoribbon with an odd width has a 'half-cut'. The resulting bands from these cuts, plotted in Figure 2.4b, match the tight-binding band structure of a 9-armchair graphene nanoribbon.

Although intuitively correct, making such cuts in the band structure of graphene is not trivial. From the point of view of the SSH model, cutting can make the number of bonds with hopping  $t_1$  unequal to the number of bonds with hopping  $t_2$ . This turns out to always be the case for zigzag-edge graphene nanoribbons, which have a multiple of 2 atoms in the  $y$  direction. As a consequence of this symmetry breaking, the SSH model has 'topological' solutions that appear when cutting the edges. These states only reveal themselves for finite length chains. In the following section a discussion of the finite length SSH model will be given. The solutions can be found by means of an expansion of the characteristic polynomial [52, 53].

### SSH model of finite length

Again, consider the SSH chain, but now with a finite length. In this case, the plane wave solution ansatz no longer holds and the problem is no longer fully separable. Although a solution can still be found by a wave-like ansatz [20], a more direct method of solving will be demonstrated here. To solve for the energies in the tight binding model, the full

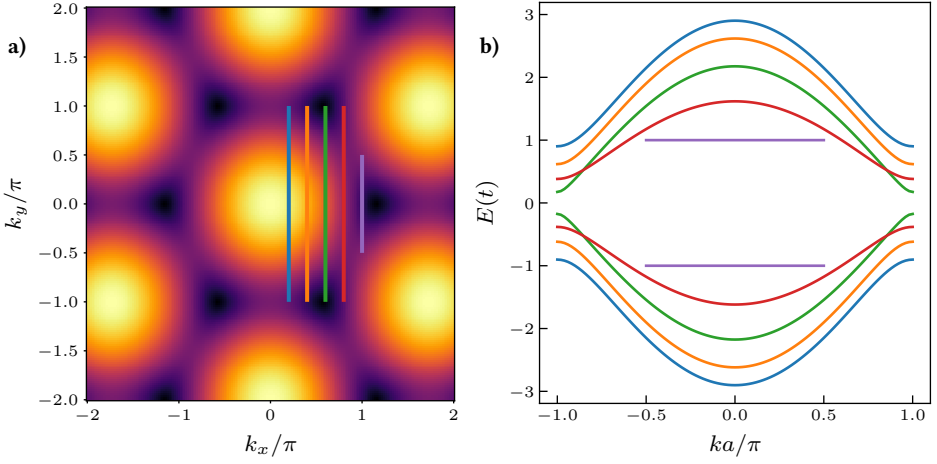


Figure 2.4: Band structure of graphene and GNRs: a) Color map of the band structure of graphene, matching Figure 2.3. The lines represent the locations of the 1D bands of 9-AGNRs. b) Band structure of 9-AGNRs. The colors of the bands match Figure 2.4b

Hamiltonian matrix is considered. Here, I will consider the case where the outer bonds are the same, taken to be  $t_1$ , which is relevant to zigzag edges in graphene nanoribbons. The full Hamiltonian matrix is given by:

$$\hat{H} = \begin{bmatrix} 0 & t_1 & 0 & 0 & \dots & 0 & 0 & 0 & 0 \\ t_1 & 0 & t_2 & 0 & \dots & 0 & 0 & 0 & 0 \\ 0 & t_2 & 0 & t_1 & \dots & 0 & 0 & 0 & 0 \\ 0 & 0 & t_1 & 0 & \dots & 0 & 0 & 0 & 0 \\ \dots & \dots & \dots & \dots & \dots & \dots & \dots & \dots & \dots \\ 0 & 0 & 0 & 0 & \dots & 0 & t_1 & 0 & 0 \\ 0 & 0 & 0 & 0 & \dots & t_1 & 0 & t_2 & 0 \\ 0 & 0 & 0 & 0 & \dots & 0 & t_2 & 0 & t_1 \\ 0 & 0 & 0 & 0 & \dots & 0 & 0 & t_1 & 0 \end{bmatrix} \quad (2.9)$$

This matrix is tridiagonal in form and the model is still periodic/regular in the interior. To solve this model, one can not assume that the wavefunction is separable though, as the boundary sites are missing neighbors. Nevertheless, the regularity of the bulk can be exploited. One way to do this is by using a recursion relation to find an expression for the characteristic polynomial  $\chi(E) = \det(\hat{H} - \lambda E)$  [53]. To do so, consider the characteristic polynomial of a submatrix  $\chi_n(E) = \det(\hat{H}_{1:n,1:n} - E\hat{I})$ , with  $\hat{H}_{1:n,1:n}$  the square submatrix with indices 1 to  $n$ . In this case, let index 1 represent the bottom row and the right-most column. Then  $\chi_1 = \det(0 - E) = E$  and  $\chi_2 = \det\begin{bmatrix} -E & t_1 \\ t_1 & -E \end{bmatrix} = E^2 - t_1^2$ .

The characteristic polynomials are related by the Laplace expansion, which results in re-

current relations when performed in the interior of the SSH Hamiltonian matrix. Taking  $n$  to be an even index, one can find a recurrence relation at an even index,

$$\chi_n = E\chi_{n-1} - t_1^2\chi_{n-2},$$

or at an odd index, giving

$$\chi_{n+1} = E\chi_n - t_2^2\chi_{n-1}.$$

These expressions hold all the way up to  $n = L$ , the length of the full SSH model. Moreover, we can also see that it is possible to include the lower boundary condition by defining  $\chi_0 = 1$  and  $\chi_{-1} = 0$ .

To obtain the characteristic polynomial for the full chain, only the even length components are necessary. To obtain a recursion relation for these, we expand up to  $\chi_{n+2}$ .

$$\chi_{n+2} = E\chi_{n+1} - t_1^2\chi_n.$$

Filling in the expression for  $\chi_{n+1}$  into this equation and using the first equation to express  $\chi_{n-1} = \frac{\chi_n + t_1^2\chi_{n-2}}{E}$ , it is found that:

$$\chi_{n+2} = (E^2 - (t_1^2 + t_2^2))\chi_n - t_1^2 t_2^2 \chi_{n-2}. \quad (2.10)$$

Redefining  $\zeta_n = \frac{1}{(t_1 t_2)^n} \chi_{2n}$ , this expression can be written as:

$$\zeta_{n+1} = \frac{(E^2 - (t_1^2 + t_2^2))}{t_1 t_2} \zeta_n - \zeta_{n-1} \quad (2.11)$$

The new variable  $\zeta_n$  can be seen as a normalized dimensionless version of the characteristic polynomial. The normalization has no impact on the zeros (eigenenergies). The found recursion relation has one parameter, which we call  $\lambda = \frac{(E^2 - (t_1^2 + t_2^2))}{2t_1 t_2}$ . With this parameter defined, the recursion relation takes the form of the generating equation for Chebyshev polynomials:

$$\zeta_{n+1} = 2\lambda(E)\zeta_n - \zeta_{n-1} \quad (2.12)$$

The boundary/initial condition  $\zeta_0$  can be found by computing  $\zeta_1$  and  $\zeta_2$ :

$$\zeta_1 = \frac{\chi_2}{t_1 t_2} = \frac{E^2 - t_1^2}{t_1 t_2} = 2\lambda + \frac{t_2}{t_1} \quad (2.13)$$

and

$$\zeta_2 = \frac{\chi_4}{(t_1 t_2)^2} = \frac{(E^2 - t_1^2)\chi_2 - t_2^2(E^2)}{(t_1 t_2)^2} = \frac{(E^2 - t_1^2 - t_2^2)\chi_2 - t_2^2(E^2 - \chi_2)}{(t_1 t_2)^2} = 2\lambda\zeta_1 - \zeta_0 \quad (2.14)$$

From which it follows that it suffices to take:

$$\zeta_0 = 1 \quad (2.15)$$

2

The initial conditions can be implemented by considering  $\zeta_n$  to be a linear combination of the Chebyshev polynomials of first  $T_n$  and second order  $U_n$ :

$$\zeta_n = AT_n + BU_n. \quad (2.16)$$

Then the boundary conditions are:

$$1 = A + B, \quad (2.17)$$

$$2\lambda + \frac{t_2}{t_1} = (A + 2B)\lambda. \quad (2.18)$$

The solution of this linear system of equations is:

$$A = -\frac{t_2}{t_1\lambda}, \quad (2.19)$$

$$B = 1 - A = \frac{t_1\lambda + t_2}{t_1\lambda}. \quad (2.20)$$

This gives the solution for the characteristic polynomial of the SSH model. To find the band structure, note that the Chebyshev polynomials can be expressed more elegantly by taking  $\lambda = \cos(k)$

This results in:

$$T_n(\cos(k)) = \cos(nk) \quad (2.21)$$

$$U_n(\cos(k)) = \frac{\sin((n+1)k)}{\sin(k)} \quad (2.22)$$

Thus the full expression for the characteristic polynomial is:

$$\zeta_n(\cos(k)) = -\frac{t_2 \cos(nk)}{t_1 \cos(k)} + \frac{t_1 \cos(k) + t_2}{t_1 \cos(k)} \frac{\sin((n+1)k)}{\sin(k)} \quad (2.23)$$

Now, using  $\sin((n+1)k) = \sin(k)\cos(nk) + \sin(nk)\cos(k)$ , we get:

$$\zeta_n(\cos(k)) = \cos(nk) + \left(\cos(k) + \frac{t_2}{t_1}\right) \frac{\sin(nk)}{\sin(k)} \quad (2.24)$$

Multiplying by  $\sin(k)$ , the zeros of this function are given by:

$$0 = \sin((n+1)k) + \frac{t_2}{t_1} \sin(nk) \quad (2.25)$$



or equivalently:

$$\frac{U_{n+1}(k)}{U_n k} = -\frac{t_2}{t_1} \quad (2.26)$$

Where we note that  $\sin(k) = 0$  (e.g.  $k = 0$ ) is not a zero of the characteristic polynomial, as this zero was introduced by a prior multiplication. In general, the solutions can be found by graphical/numerical means. For  $t_2 = 0$ , the solution  $k = \frac{\pi l}{n+1}$  with  $l = 1, 2, 3, \dots, n$  can be found. Likewise, for  $t_1 \rightarrow 0$  we find  $k = \frac{\pi l}{n}$ , with  $l = 1, 2, 3, \dots, n-1$  results. In the latter limit, only  $n-1$  solutions are found (which actually means that two energies are missing). The missing solution can be found by extending  $k$  to the complex plane. In this case, the equation to solve is:

$$(e^{ik(n+1)} - e^{-ik(n+1)}) = -\frac{t_2}{t_1}(e^{ikn} - e^{-ikn}) \quad (2.27)$$

In the large  $n$  limit, for  $k = \pi + i\kappa$ , approximate solutions are

$$e^{\pm\kappa} = \frac{t_2}{t_1} \quad (2.28)$$

Meaning  $\kappa = \pm \ln\left(\frac{t_2}{t_1}\right)$ .

In the special limit that  $t_2 = t_1$ , the solution  $k = \frac{\pi l}{n+\frac{1}{2}}$ , for  $l = 1, 2, 3, \dots, n$  holds.

For any solution, we have:

$$E^2 = t_1^2 + t_2^2 + 2t_1 t_2 \cos(k) \quad (2.29)$$

Which results in

$$E_{\pm, k} = \pm \sqrt{t_1^2 + t_2^2 + 2t_1 t_2 \cos(k)} \quad (2.30)$$

Exactly as was found before, but with a slightly different meaning for the variable  $k$ , which is not explicitly derived from a plane wave approach in this case. Within the plane wave approach, the complex solutions that were found correspond to exponentially growing and decaying waves (with a wave vector of  $k = i\pi \pm \ln\left(\frac{t_2}{t_1}\right)$ ). In the finite-length chain, the normalized states are thus localized at the ends. The energy of these states are:

$$E^2 = t_1^2 + t_2^2 - 2t_1 t_2 \cosh\left(\pm \ln\left(\frac{t_2}{t_1}\right)\right) = t_1^2 + t_2^2 - 2t_1 t_2 \frac{\left(\frac{t_2}{t_1}\right) + \left(\frac{t_1}{t_2}\right)}{2} = 0 \quad (2.31)$$

This reveals that the two states have the same value of  $\lambda$  and are a pair of zero-energy end-states. For small-lengths, the same dispersion relation holds and the eigenvalues can be found numerically/graphically.

Summarizing, the solutions of the finite-length SSH model have been found by an expansion of the characteristic polynomial through a recurrence relation. The result is quantization of  $k_y$ , with the same dispersion relation  $E(k)$ . In the case that  $t_1 < t_2$ , there are 2 solutions for  $ka = i\pi \pm \ln(\frac{t_2}{t_1})$ , which are localized at the ends, decaying at a rate of  $\frac{t_1}{t_2}$ .

### Armchair/zigzag graphene nanoribbon from the bottom up

The same approach for the SSH model can be applied to a whole graphene nanoribbon of finite length and width. Consider again the sketch in Figure 2.2. In this model, we can label the atoms by indices  $x$  (zigzag direction) and  $y$  (armchair direction). Then, in this coordinate system, the tight binding model has the form:

$$H = H_x + H_{y,\text{xodd}} + H_{y,\text{xeven}} \quad (2.32)$$

It can also be seen that any rectangular lattice represents a finite-size graphene nanoribbon.

The Hamiltonian is periodic/regular and has a block-tridiagonal form:

As a result, it can be written in the form:

$$\hat{H} = t \begin{bmatrix} H_1 & -I & 0 & 0 & \dots & 0 & 0 & 0 & 0 \\ -I & H_2 & -I & 0 & \dots & 0 & 0 & 0 & 0 \\ 0 & -I & H_1 & -I & \dots & 0 & 0 & 0 & 0 \\ 0 & 0 & -I & H_2 & \dots & 0 & 0 & 0 & 0 \\ \dots & \dots & \dots & \dots & \dots & \dots & \dots & \dots & \dots \\ 0 & 0 & 0 & 0 & \dots & H_2 & -I & 0 & 0 \\ 0 & 0 & 0 & 0 & \dots & -I & H_1 & -I & 0 \\ 0 & 0 & 0 & 0 & \dots & 0 & -I & H_2 & -I \\ 0 & 0 & 0 & 0 & \dots & 0 & 0 & -I & H_1 \end{bmatrix} \quad (2.33)$$

Where  $H_1 = H_{y,\text{xodd}}$  is the Hamiltonian in  $y$  on the odd rows and is  $H_2 = H_{y,\text{xodd}}$  is the Hamiltonian in  $y$  on the even rows.

Furthermore, the odd and even hamiltonians are expressed as:

$$\hat{H}_1 = \begin{bmatrix} 0 & -1 & 0 & 0 & \dots & 0 & 0 & 0 & 0 \\ -1 & 0 & 0 & 0 & \dots & 0 & 0 & 0 & 0 \\ 0 & 0 & 0 & -1 & \dots & 0 & 0 & 0 & 0 \\ 0 & 0 & -1 & 0 & \dots & 0 & 0 & 0 & 0 \\ \dots & \dots & \dots & \dots & \dots & \dots & \dots & \dots & \dots \\ 0 & 0 & 0 & 0 & \dots & 0 & -1 & 0 & 0 \\ 0 & 0 & 0 & 0 & \dots & -1 & 0 & 0 & 0 \\ 0 & 0 & 0 & 0 & \dots & 0 & 0 & 0 & -1 \\ 0 & 0 & 0 & 0 & \dots & 0 & 0 & -1 & 0 \end{bmatrix} \quad (2.34)$$

$$\hat{H}_2 = \begin{bmatrix} 0 & 0 & 0 & 0 & \dots & 0 & 0 & 0 & 0 \\ 0 & 0 & -1 & 0 & \dots & 0 & 0 & 0 & 0 \\ 0 & -1 & 0 & 0 & \dots & 0 & 0 & 0 & 0 \\ 0 & 0 & 0 & 0 & \dots & 0 & 0 & 0 & 0 \\ \dots & \dots & \dots & \dots & \dots & \dots & \dots & \dots & \dots \\ 0 & 0 & 0 & 0 & \dots & 0 & 0 & 0 & 0 \\ 0 & 0 & 0 & 0 & \dots & 0 & 0 & -1 & 0 \\ 0 & 0 & 0 & 0 & \dots & 0 & -1 & 0 & 0 \\ 0 & 0 & 0 & 0 & \dots & 0 & 0 & 0 & 0 \end{bmatrix} \quad (2.35)$$

2

After division by  $t$ , the normalized characteristic polynomial can be expressed as:

$$\chi(\lambda) = \det\left(\left(\lambda I - \frac{1}{t}H\right)\right) = \det(M(\lambda)) = \det\left(\begin{bmatrix} A_1 & I & 0 & 0 & \dots & 0 & 0 & 0 & 0 \\ I & A_2 & I & 0 & \dots & 0 & 0 & 0 & 0 \\ 0 & I & A_1 & I & \dots & 0 & 0 & 0 & 0 \\ 0 & 0 & I & A_2 & \dots & 0 & 0 & 0 & 0 \\ \dots & \dots & \dots & \dots & \dots & \dots & \dots & \dots & \dots \\ 0 & 0 & 0 & 0 & \dots & A_2 & I & 0 & 0 \\ 0 & 0 & 0 & 0 & \dots & I & A_1 & I & 0 \\ 0 & 0 & 0 & 0 & \dots & 0 & I & A_2 & I \\ 0 & 0 & 0 & 0 & \dots & 0 & 0 & I & A_1 \end{bmatrix}\right) \quad (2.36)$$

Where we define the matrix  $M(\lambda)$  for simplicity in notation. Furthermore,  $A_1 = \lambda I - H_1$  and  $A_2 = \lambda I - H_2$  and the eigenenergies can be expressed as  $E = \lambda t$ . In this form, the transfer matrix method [52] can be used to calculate the determinant (using  $B_i = C_i = I$  and applying the sign change) as:

$$\chi(E) = \det(T(n)_{11}) \det((B_1 \dots B_{n-1})^{-1}) = \det(T_{11}) \quad (2.37)$$

The transfer matrix  $T(n)$  in this equation is the  $2 \times 2$  matrix defined by:

$$\begin{bmatrix} c_{n+1} \\ c_n \end{bmatrix} = T(n) \begin{bmatrix} c_1 \\ c_0 \end{bmatrix} \quad (2.38)$$

The 11 element of  $T(n)$  thus denotes transfer from block 1 to block  $n+1$ . Given the boundary conditions  $c_0 = c_{n+1} = 0$ , this must mean that all valid eigenvectors have  $T(n)_{11} c_1 = 0$ . This implies that  $\det(T(n)_{11}) = 0$  for eigenvectors. It can be seen by multiplying  $M(\lambda)$  with

the coefficient vector  $\vec{c} = \begin{bmatrix} c_1 \\ c_2 \\ \dots \\ c_{n-1} \\ c_n \end{bmatrix}$  : that

$$A_1 c_1 + c_2 = 0 \quad (2.39)$$

$$c_1 + A_2 c_2 + c_3 = 0 \quad (2.40)$$

$$c_2 + A_1 c_3 + c_4 = 0 \quad (2.41)$$

etc.

From this, we find:

$$(T(-1)_{11} + A_1 T(0)_{11} + T(1)_{11})c_1 = 0 \quad (2.42)$$

$$(T(0)_{11} + A_2 T(1)_{11} + T(2)_{11})c_1 = 0 \quad (2.43)$$

$$(T(1)_{11} + A_1 T(2)_{11} + T(3)_{11})c_1 = 0 \quad (2.44)$$

Where we have used  $T(0)_{11} = I$  and  $T(-1)_{11} = 0$ , which hold by the definition of the transfer matrix.

In general, we can deduce that for odd  $n$ :

$$T(n+2)_{11} = -A_1 T(n+1)_{11} - T(n)_{11} \quad (2.45)$$

$$T(n+3)_{11} = -A_2 T(n+2)_{11} - T(n+1)_{11} \quad (2.46)$$

$$T(n+4)_{11} = -A_1 T(n+3)_{11} - T(n+2)_{11} \quad (2.47)$$

Filling the first two equations into the last one, we get:

$$T(n+4)_{11} = -A_1(-A_2 T(n+2)_{11} - T(n+1)_{11}) - T(n+2)_{11} = (A_1 A_2 - 2I)T(n+2)_{11} - T(n)_{11} \quad (2.48)$$

Defining  $\Xi_k(\Lambda) \equiv T(-1+2k)_{11}$ , this defines an equation for a Chebyshev polynomial of  $\Lambda \equiv (\frac{A_1 A_2}{2} - I)$ :

$$\Xi_{k+1}(\Lambda) = 2\Lambda \Xi_k(\Lambda) - \Xi_{k-1}(\Lambda) \quad (2.49)$$

The initial conditions are  $\Xi_0(\Lambda) = T(-1)_{11} = 0$  and  $\Xi_1(\Lambda) = T(1)_{11} = -A_1$

The solution is:

$$\Xi_k(\Lambda) = -(U_k(\Lambda) - T_k(\Lambda))\Lambda^{-1}A_1 \quad (2.50)$$

To solve this, we consider  $\Lambda$  to be nonsingular. Then  $\Lambda$  can be expressed in terms of its eigendecomposition  $\Lambda = PDP^{-1}$ , where  $P$  is a matrix containing the eigenvectors and  $D$  is a diagonal matrix containing the eigenvalues  $\lambda_i$ . For any polynomial function  $f(x)$ , it then holds that:

$$f(\Lambda) = Pf(D)P^{-1} \quad (2.51)$$

And  $f(D)$  is the diagonal matrix containing the elements  $f(\lambda_i)$

Thus, we calculate  $\frac{1}{x}(U_k(x) - T_k(x))$  and fill in  $x = \Lambda$  in post. Consider  $x = \cos(\theta)$ , with  $e^{\theta}$  a complex value confined to the top half of the complex plane to obtain a bijective mapping. Then:

$$f(x) = \frac{1}{x}(U_k(x) - T_k(x)) = \frac{1}{\cos(\theta)}\left(\frac{\sin((k+1)\theta)}{\sin(\theta)} - \cos(k\theta)\right) = \frac{\sin(k\theta)}{\sin(\theta)} \quad (2.52)$$

The zeros can be found at  $\theta = \frac{l\pi}{k}$ ,  $l = 1, \dots, k-1$ .

Thus the polynomial in  $x$  is:

$$f(x) = \prod_{l=1}^{k-1} \left(x - \cos\left(\frac{l\pi}{k}\right)\right) \quad (2.53)$$

Generalizing the expression to the matrix  $\Lambda$ , it follows that:

$$\Xi_k(\Lambda) = - \prod_{l=1}^{k-1} \left(\Lambda - I \cos\left(\frac{l\pi}{k}\right)\right) A_1 \quad (2.54)$$

This effectively solves the Hamiltonian in the zigzag direction, yielding  $W$  effective Hamiltonians for bands in the armchair direction. The objective is to find the eigenvalues, which are found through:

$$\det(\Xi_k) = 0 \quad (2.55)$$

Since the transfer matrix is defined as a product, solutions can be found for each  $l$  separately and for  $A_1$ . The solutions for  $A_1$  are simple, as the Hamiltonian  $H_1$  consists of  $L/2$  pairs of sites coupled by a hopping element  $t$ . This yields two flat bands, one at  $E = +t$  and one at  $E = -t$ . Note that the amount of sites in  $A_1$  is half the amount of sites in  $\Lambda - I \cos(\frac{l\pi}{k})$ . Thus, this results in half the number of states, in agreement with the band cutting picture in Figure 2.4.

The effective determinant for each  $l$  is:

$$\det\left(\Lambda - I \cos\left(\frac{l\pi}{k}\right)\right) = \det\left(\frac{A_1 A_2}{2} - I \lambda_l\right) = \frac{1}{2} \det(A_1 A_2 - 2 \lambda_l I). \quad (2.56)$$

This is the determinant for two chains with Hamiltonians  $H_1$  and  $H_2$  coupled by a hopping element  $t_1^2 = \lambda_l t^2$ , with  $\lambda_l = 2(1 + \cos(\frac{l\pi}{k}))$ . The derived SSH chain is schematically shown in Figure 2.5.

The result is an effective SSH hamiltonian with  $t_1 = \pm \sqrt{\lambda_l} t$  and  $t_2 = t$ . The solution of this Hamiltonian was given in section 2.1.1.4. To get the usual dispersion for graphene, we set

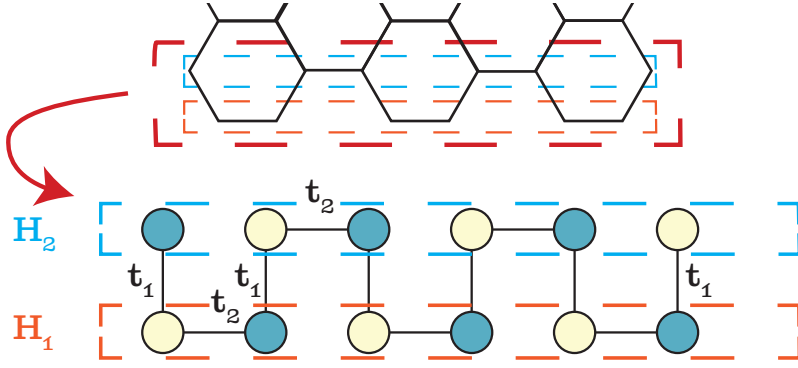


Figure 2.5: Schematic representation of the finite-length SSH chain in an armchair GNR of finite length. The values of the hopping elements are  $t_1 = \sqrt{\lambda_l}t$  (which depends on the band index  $l$ ) and  $t_2 = t$ .

$t_1 = 2\cos(\frac{l\pi}{2k})$ . This avoids the discontinuity in  $\sqrt{\lambda_l} = |\cos(\frac{l\pi}{2k})|$  as  $\lambda_l$  goes through 0 as a function of the index  $l$ .

When  $\lambda_l < 1$ , topological solutions exist, which happens for:

$$\cos(\frac{l\pi}{k}) < -\frac{1}{2}, \quad (2.57)$$

which is equivalent to  $\frac{l\pi}{W} = k_x a > \frac{2\pi}{3}$ .

Thus, in general, the solutions for the eigenvalues/dispersion relation is of the SSH form:

$$E_{\pm}(k_x a, k_y a) = \pm t \sqrt{1 + 4\cos^2(\frac{k_x a}{2}) + 4\cos(\frac{k_x a}{2})\cos(k_y \frac{\sqrt{3}}{2}a)}, \quad (2.58)$$

which is exactly the dispersion relation of graphene. The zero energy edge states at zigzag edges are the result of complex solutions of  $k_y$  (the wavevector in the armchair direction).

This concludes the section on the electronic structure of GNRs. In this section, a simple intuitive understanding of the band structure of graphene was given, based on the SSH model. The band structure of armchair and zigzag GNRs can be obtained by. Finally, an analytical calculation of the characteristic polynomial of the tight binding Hamiltonian for an armchair/zigzag graphene nanoribbon was performed using the transfer matrix method, which allows for calculating the eigenenergies (dispersion relations) of GNRs of arbitrary width and length. The results of this calculation are in agreement with analytical calculations based on a wave-based ansatz with boundary conditions[51]. The analytical calculation justifies the simple SSH picture for armchair graphene nanoribbons and also includes the end-states at the zigzag ends of finite-length armchair graphene nanoribbons.

### Edge states in finite size graphene nanoribbons

At this point, the edge states in the zigzag ends can be understood. Since the graphene lattice behaves as a collection of separate finite-length SSH chains with different  $\frac{t_2}{t_1}$  in the armchair direction, edge states form when the effective hopping integrals at the ends are smaller. For an infinite length GNR, this corresponds to:

$2|t \cos(\frac{k_x a}{2})| < |t|$ , which occurs when  $|\cos(\frac{k_x a}{2})| \leq \frac{1}{2}$ ,  $k_x \geq \frac{2\pi}{3a}$ , which is exactly the condition that  $k_x$  is beyond the Dirac point. This means in the zigzag direction of graphene nanoribbons there is a dispersive band that becomes flat at zero energy. Just past the Dirac point,  $\frac{t_2}{t_1} \approx 1$  and the zero energy state is most delocalized, as opposed to when  $k_x \rightarrow \frac{\pi}{a}$ , where the zero energy state strongly localizes at the edges. In all cases, there is a sign change from unit-cell to unit-cell in the armchair direction.

#### 2.1.2 Magnetism at zigzag edges

The presence of spatially localized zero-energy flat bands at zigzag edges of nanoribbons opens up the possibility of studying the effect of interactions. The absence of curvature in a flat dispersion implies an infinite effective mass. As such, kinetic effects are negligible compared to interactions, such as the Coulomb interaction. An expected result of this is the occurrence of correlations, which can manifest in the form of magnetism or charge density waves[54].

#### 2.1.3 Electronic transport properties of semiconducting graphene nanoribbons

The previous sections on the electronic structure of armchair graphene nanoribbons reveal that their band structure can be mapped to the SSH model. Through this analogy, it is seen that GNRs are semiconducting, unless the criterion  $|t_1| = |t_2|$  is met for some band. Although the exact band gap is related to the width and edge structure, the global trend is for GNRs to exhibit a band gap that is inversely proportional to their width. As a result of this, the on-surface synthesized 9-armchair graphene nanoribbons considered in this thesis are semiconducting in nature, with a predicted band gap of roughly 1 eV. When the GNRs are neutral (meaning not doped), their Fermi energy is predicted to be in the middle of the band gap. Thus, according to this picture, neutral 9-AGNRs should behave as potential/energy barriers to electron and hole excitations, with a barrier size of roughly 0.5 eV. To understand charge transport through them, the conduction mechanisms into the GNRs and through the GNRs needs to be understood. In this section, we will start with transport through the GNRs, assuming no contact effects. Rough estimates will be given for transport through tunneling and through thermally excited carriers. After these considerations, additional charge transport models (Environmental Coulomb blockade/Luttinger liquid/Wigner crystal, Fluctuation induced tunneling) will be presented that have been proven to be useful to describe charge transport in GNRs, CNTs and polyacetylene. In the section following this one, contact limited transport through GNRs will be discussed, which becomes relevant in cases where the barriers at the contacts exceed the channel barrier height. This last case is relevant for GNRs that are back-gated in a field-effect transistor geometry, such that the valence band (or conduction band) is close to the electrochemical

potential.

### Tunneling conduction

To understand conduction through tunneling, we will consider a conductance of  $1 G_0$  through a band if the band is at the Fermi energy. Thus, without the barrier, it would conduct as a perfect single channel conductor. Now, if we include a barrier of width  $W$  and height  $V_0 = 0.5$  V, the tunneling conductance would be

$$G = G_0 e^{-2\kappa W}, \quad (2.59)$$

$$\text{with } \kappa = \sqrt{\frac{2mV_0}{\hbar^2}} \approx 5.01 \text{ nm}^{-1}.$$

From this, one can extract that the tunneling conductance of 9-AGNRS is expected to decay (multiplicatively) at a rate of  $e^{-10} \approx 4.5 \cdot 10^{-5}$  per nanometer.

For a device with a length exceeding a few nanometers, this is a negligible contribution. In reality, the barrier height might be locally reduced by image charge effects close to the metal surface and thus few-nanometer-length GNR channels could still conduct through tunneling. For larger channel lengths, this is not to be expected. Instead, a thermally driven transport mechanism is much more likely.

**Thermally activated charge transport** As was considered for tunneling, the GNR valence and conduction band will be taken to be perfect 1D channels. For thermally activated processes, the carriers can be considered as classical particles. Thermally excited carriers can only enter this channel when their energy exceeds the energy barrier. The amount of electrons at energy  $E$  above the barrier is given by the Boltzmann factor  $N_{\text{thermal}} = \int_{\mu+eV_0}^{\infty} \nu(E) e^{\frac{\mu-E}{k_b T}} dE = \nu k_b T e^{-\frac{eV_0}{k_b T}}$ .

Where we have introduced the density of states  $\nu(E)$ , which is assumed to be energy independent. The validity of this assumption is dubious over energy scales of eV. Metals such as Pd, Pt and Au have d-bands below the Fermi energy, which may lead to excess holes compared to electrons. When a bias voltage is applied, the chemical potential shifts up with respect to the barrier height. Then, as a result, the net imbalance between the two electrodes is:

$$\nu k_b T e^{-\frac{eV_0}{k_b T}} (e^{\frac{eV}{k_b T}} - 1). \quad (2.60)$$

Assuming a low bias  $\frac{eV}{k_b T} \ll 1$  and that all states couple to the channel with equal probability  $\frac{1}{\nu}$ , the low bias conductance is:

$$G = e^{-\frac{eV_0}{k_b T}} G_0. \quad (2.61)$$

For  $V_0 = 0.5$  V and  $k_b T = 25$  meV, this results in  $G = 2 \cdot 10^{-9} G_0 \approx 0.1$  pS. Thus, we may predict that for a density of 2 ribbons per nm, the conductance of a 20 nm wide contact is



1 pS. For a 2  $\mu\text{m}$  wide contact, the expected conductance (assuming an undoped 9-AGNR) is 100 pS.

**High-bias transport** When the applied bias voltage is large, deviations from the picture sketched above may occur. The barrier energy may be effectively lowered by the bias voltage. Furthermore, the potential landscape is tilted, which can result in a thinner energy barrier. As a result, both tunneling conductance and thermally excited carrier conductance is enhanced. A way to take this into account is through

**Fluctuation induced tunneling** A model that combines the tunneling approach with thermal fluctuations is the fluctuation induced tunneling (FIT) model[55]. This model was introduced to explain the conductance properties of highly doped poly-acetylene, but has also seen success in describing other 1D conductors with disorder[56]. At the core of this model is the idea that the material consists of large conductive regions separated by small tunnel barriers. These small tunnel barriers have a small capacitance that can exhibit a relatively large noise voltage, according to

$$\frac{1}{2}CV^2 = k_b T. \quad (2.62)$$

As a result of the small size of the junction, the voltage across it fluctuates. For a capacitance of 1 fF, one obtains a noise voltage of 2 mV at room temperature. The main prediction of this model is a temperature dependent conductance:

$$G = G_0 e^{-\frac{T_1}{T+T_0}(1-\alpha|V|)^2}. \quad (2.63)$$

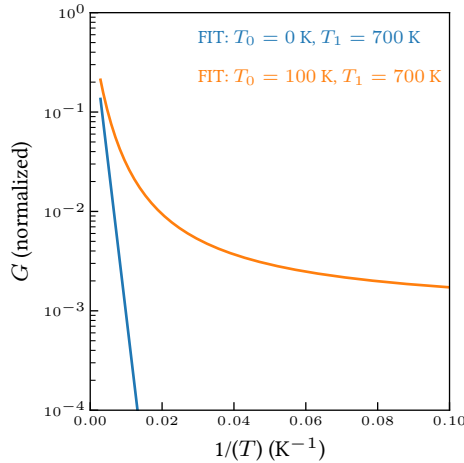


Figure 2.6: Zero-bias conductance versus temperature behavior of the FIT model compared to a simple thermally activated behavior.

At high temperatures, the behavior is thermal, with a temperature scale  $T_1$ , saturating to a value of  $\sigma_0$ . The ratio  $\frac{T_1}{T_0}$  is equal to the exponent for the tunneling probability  $2\kappa w$

(multiplied by a correction factor for the barrier shape). When the temperature is lowered below  $T_0$ , a transition happens to the tunneling regime and the behavior flattens off. This transition is smooth, rather than abrupt. A plot of the zero bias conductance versus inverse temperature in Figure 2.6 illustrates the effect of the parameter  $T_0$ .  $T_0 = 0$  K and  $T_1 = 700$  K results in normal thermally activated behavior. Taking  $T_0 = 100$  K instead results in a smooth transition to a temperature-independent tunneling regime. Furthermore, the bias voltage behavior is exponential for low bias, but flattens off at high bias until  $\alpha V = 1$ . In this limit, the validity of the model becomes questionable. An important feature of this model is a product between the temperature dependence and the bias voltage dependence. As a result, the effective activation energy for high bias voltages is reduced. This also has the consequence of increasing the non-linearity of the IV curves when decreasing the temperature. To perform an analysis with this model as a starting point, it makes sense to consider the logarithm of conductance, which is:

$$\ln(G) = \ln(G_0) - \frac{T_1}{T + T_0}(1 - \alpha V)^2. \quad (2.64)$$

If  $G_0$  is known, the temperature dependence can be extracted by plotting:  $\frac{1}{\ln(G) - \ln(G_0)} = \frac{1}{(1 - \alpha V)^2} \left( \frac{T_0}{T_1} + \frac{T}{T_1} \right)$  versus  $T$  for low bias voltages. A simple linear fit at low bias yields  $\frac{T_0}{T_1}$  as the intercept and  $\frac{1}{T_1}$  as the slope.

The FIT model provides a simple expression for transitioning between thermally activated transport and electron transport through tunneling. The assumption that the material of interest consists of large conductive regions with small barriers is, however, against expectations for undoped GNRs with band gaps on the order of 1 eV. Nevertheless, regardless of the validity of the FIT model and its assumptions, the exponent for the temperature scaling  $\frac{T_1}{T + T_0}$  that it provides gives a simple extension of the thermally excited  $\frac{T_1}{T}$  scaling, where the tunneling contribution can be interpreted as an offset temperature.

An interesting consequence of this scaling is that the temperature dependence at low temperatures  $T < T_0$  can be well approximated by an exponential temperature dependence, with a quadratic correction term. By Taylor expanding the exponent to second order, it is found that:

$$G(T) \approx e^{\ln(G_0)} e^{-\frac{T_1}{T_0}} e^{\frac{T_1}{T_0^2} T} e^{-\frac{T_1}{T_0^3} T^2}. \quad (2.65)$$

A fit of  $\ln(G)$  to a quadratic equation yields  $\ln(G_0) + \frac{T_1}{T_0}$ ,  $\frac{T_1}{T_0^2}$  and  $\frac{T_1}{T_0^3}$ , from which  $T_0$ ,  $T_1$  and  $G_0$  can be obtained. If the quadratic contribution is not (clearly) observed, it is still possible to fit, but not possible to extract  $T_0$ ,  $T_1$  or  $G_0$  independently from the temperature dependence.

### Considerations for matching models with experiments

As the data in chapter 4 will show, the current-voltage characteristic of GNRs possesses two features. Any model that aims to accurately describe transport in GNRs has to at least

match these features. The two main features that any description of GNR transport should match are as follows:

- The current-voltage characteristic is nonlinear and not saturating (up to the high bias voltages (4 V) measured) and becomes increasingly nonlinear as the temperature is decreased.
- The temperature dependence of the conductance flattens off at low temperature at moderate bias voltages. (Measured for  $V > 0.3$  V)

The first feature indicates that any description of transport must include a linear combination of terms which are a function of  $V^a T^b$ , where  $a$  and  $b$  are not equal to 0 for some terms. If this were not the case, the nonlinearity of the IV characteristic can not change with temperature.

The second feature suggests that purely thermally activated transport is insufficient to describe the measured characteristic. Any model that scales as  $I \propto \frac{1}{T^b}$ , with  $b > 0$  at low temperature fails to completely describe the data.

### 2.1.4 Interfaces of graphene nanoribbons and metals

When the 'bulk' of the GNR can be doped, the valence band edge or conduction band edge can lie close to the chemical potential or even cross it. Such doping can potentially be applied by chemicals, such as  $I_2$ , or, as we will consider here, by applying a gate voltage in a field-effect transistor. When a back-gate voltage pulls the bands in the channel down, the GNRs are unaffected at the metal-GNR interface due to electrostatic screening by the metal. As a result of this, the valence band in the channel may cross the electrochemical potential and the transistor reaches the so-called 'on-state', while a barrier for hole transport remains at the interface. This barrier at the metal-GNR interface is called a Schottky barrier, and it limits the on-state conductance. In this section, the properties of Schottky barriers will be discussed. Estimates of Schottky barrier heights will be given to illustrate possible design choices for GNR transistors. Lastly, it will be discussed how Schottky barriers can limit the conductance through the GNR by limiting the injection and extraction probability at the interface.

The height of a Schottky barrier at a metal-GNR interface depends on the degree to which the contact metal dopes the GNRs. The spatial extent, on the other hand, also depends on the local dielectric environment[57]. For a high- $\kappa$  gate dielectric, the spatial extent is reduced compared to low- $\kappa$  gate dielectric. To obtain a GNR FET with a high on-state conductance, equivalent to transparent electrical interfaces, the height and width of the Schottky barrier should be minimized. In an ideal scenario, the Schottky barrier is zero or negative (meaning that the contact is Ohmic). To achieve such a scenario in a device, an estimate of the barrier height needs to be made.

The simplest way to approximate the size of the Schottky barrier is through the Schottky-Mott rule, which states that the Schottky barrier height should be the difference between the metal work function and the electron-affinity of the GNRs for n-type devices, while the Schottky barrier height for p-type devices is the difference between the metal work function and the vacuum ionization energy. In table 2.1, we estimate the band gaps ob-

Table 2.1: Schottky barrier heights calculated using the Schottky-Mott rule for possible metal-GNR combinations. Metals were selected based on their usage with CNTs.

Metal, W	9-AGNR	5-AGNR	17-AGNR
Band gap of GNRs	1.35 eV	2.8 eV	0.19 eV
Au(p), 5.10 eV	0.28	1	-0.30
Pd(p), 5.12 eV	0.26	0.98	-0.32
Pt(p), 5.12 eV	0.26	0.98	-0.32
Mo(p), 4.7 eV	0.68	1.4	0.10
Re(p), 4.72 eV	0.66	1.38	0.10
Ti(n), 4.33 eV	0.31	0.03	-0.27
Al(n), 4.26 eV	0.24	0.96	-0.34
Sc(n), 3.5 eV	- 0.52	0.2	-1.11

tained by the Schottky-Mott rule for a range of contact metals[29, 58]. Here it is assumed that the work function of graphene / mid-gap energy of GNRs is 4.7 eV[59, 60]. Based on this table, it can be seen that 9-AGNRs[61] can only be contacted transparently (with a negative Schottky barrier) by using an n-type contact with Sc. p-type metals, which tend to be noble metals, can form contacts with small, yet non-zero, Schottky barriers. Mo and Re, which are two metals that are known for making good contact to CNTs have remarkably large Schottky barriers according to the Schottky-Mott rule. Furthermore, according to this table, Ti and Al should be competitive with the p-type contacts. For 5-AGNRs[62], the band gap is too large to make an Ohmic contact according to the Schottky-Mott rule. For 17-AGNRs[63], the picture is quite different. Nearly all selected metals do not have a Schottky barrier for these GNRs. Only Mo and Re will exhibit a relatively small ( $\sim 100$  meV) Schottky barrier according to these estimates. Given the fact that different surface terminations of Mo and Re can have different work functions, with a variation of  $\sim 300$  meV, it is likely that Mo and Re can also make an Ohmic contact to 17-AGNRs.

Adding to the previous discussion, it should be noted that when the Schottky barrier is negative, ideally it should not be too far into the negative, as this also implies a large band-bending from the contact to the channel when the band edge in the channel crosses the electrochemical potential. The best contacts have small band bending at resonance without a Schottky barrier. Taking into account the fact that these are rough estimates, this situation could potentially be realized by Pd or Pt for p-type contacts to 9-AGNRs. For n-type contacts to 9-AGNRs, this could potentially be realized by Ti or Al contacts. For 17-AGNRs (and other small band-gap GNRs) a contact electrode made out of Mo, Re or MoRe should be near optimal to realize an on-state situation with little band bending.

The prior discussion around Schottky barriers neglects the fact that doping of the GNRs at the contact relies on a good electrical contact of the GNR to the metal in the first place. If the metal and the GNR are not touching, no band bending is to be expected. Thus, the distance of the GNR  $\pi$ -bond orbitals to the metal orbitals matters. For CNTs, there is an understanding that some metals are weakly interacting (physisorption) and other metals are strongly interacting (chemisorption) with these orbitals. Metals that weakly interact (i.e. Au and Pt) tend to disturb the band structure of CNTs less and have larger

contact length scales. Strongly-interacting contact metals instead significantly hybridize and may result in abrupt contacts, as is the case with Ti-C and Mo-C and Ni-C end bonds for CNTs. In between these two limits are the moderately-interacting metals, of which Pd is an example. Pd is a noble metal that is more chemically reactive than Pt, but less chemically reactive than Ni. As a result, it has been the preferred contact metal for CNTs over the weakly-interacting Pt and the strongly-interacting (but oxidation-sensitive) Ni.

### 2.1.5 Electronic transport through Schottky barriers

For Schottky barriers, the same transport mechanisms (tunneling, thermally excited carriers) as for GNR channels are relevant. However, the relative importance of the different mechanisms differs. Schottky barriers are more localized and, as such, tunneling is more important. We can distinguish different regimes:

**High temperature, low bias voltage** In the limit of barrier limited transport at high temperature and low bias voltages, transport is expected to be dominated by thermal excitations above the barrier energy, called thermionic emission. A characteristic feature of this mechanism is an exponential temperature dependence, as  $I \propto T^{d-1} e^{-\frac{E_a}{k_b T}}$ , where  $d$  is the dimensionality of the channel material.

**Low temperature, low bias voltage** In the limit of a low temperature and a low bias voltage, the carriers can pass through the Schottky barrier by quantum tunneling.

**Low temperature, high bias** When the bias voltage is significantly large, the barrier is deformed and shrinks in size with increasing bias voltages. This leads to Fowler-Nordheim tunneling, also called field emission. A characteristic feature of this is a  $I \propto V^2 e^{-\frac{\Phi}{V}}$  dependence.

**High temperature, moderate to high bias** When both the temperature is high and the bias voltage is moderate to high, a combination of thermionic emission and field emission occurs, which is sometimes called thermionic-field emission. In this regime, either thermionic emission or field emission dominates.

## 2.2 Superconductivity

Superconductivity is a phenomenon in which an electrical conductor loses all electrical resistance below a certain temperature, called the critical temperature[64]. Superconductivity was discovered in mercury by Kamerlingh Onnes[65, 66], who pioneered the liquefaction of helium. Besides the loss of all electrical resistance, it was found by Meissner[8] that superconductors can completely expel the magnetic field, displaying perfect diamagnetism. This effect has been named the Meissner effect. An excellent reference to understanding superconducting phenomena was written by Tinkham[67]. Here, I will give a brief overview of the most important background theory before discussing advanced concepts relating to interfaces between normal metals and superconductors and phenomena relating to superconductivity out of equilibrium.

Motivated by the Meissner effect, the electrodynamics of superconductors is captured by the London theory of superconductivity in a classical manner[68]. The introduction of a

relation between the current density  $\vec{J}_S$  and the vector potential  $\vec{A}$ , given by:

$$\vec{J}_S = -\frac{e^2}{m} n_S \vec{A}, \quad (2.66)$$

and the London gauge:

$$\vec{\nabla} \cdot \vec{A} = 0, \quad (2.67)$$

$$\vec{A} \cdot \hat{n} = 0 \text{ at the boundary of the superconductor and} \quad (2.68)$$

$$\vec{A} = 0 \text{ in the bulk of the superconductor,} \quad (2.69)$$

$$(2.70)$$

reproduces the perfect diamagnetism observed in the Meissner effect. Here  $e$  is the elementary charge,  $m$  is the electron mass,  $n_S$  is the density of superconducting carriers and  $\hat{n}$  denotes the unit normal vector at the superconducting interface. The first and second equation of the London gauge ensure conservation of charge density in the bulk and on the surface, while the third equation explicitly makes the magnetic field in the superconductor equal to zero. By filling this into Ampere's law an equation describing the screening of magnetic fields by a superconductor can be obtained:

$$\vec{\nabla} \times \vec{B} = \vec{\nabla} \times \vec{\nabla} \times \vec{A} = -\nabla^2 \vec{A} = \mu_0 \vec{j} = -\frac{e^2 \mu_0 n_S}{m} \vec{A} = -\frac{1}{\lambda^2} \vec{A}. \quad (2.71)$$

Here, the London penetration depth  $\lambda = \sqrt{\frac{m}{e^2 \mu_0 n_S}}$  was introduced as the characteristic length scale over which magnetic fields are screened by surface Meissner currents. The presence of the electron density in the expression for the London penetration depth indicates that superconductors with a larger electron density screen magnetic fields over a smaller length scale. The response to an electric field  $\vec{E}$  is given by:

$$\vec{v}_S \cdot \vec{\nabla} \vec{J}_S + \frac{\partial \vec{J}_S}{\partial t} = \frac{n_S e^2}{m} \vec{E} \quad (2.72)$$

Here  $v_S$  is the supercurrent velocity, defined as  $\vec{v}_S = \frac{\vec{J}_S}{n_S e}$ . The equation shows that electric fields can be present in superconductors if the left-hand side is finite. The first term on the left-hand side of the equation is a convective derivative of the current[69]. It is often neglected in literature, as uniform superconductors are usually considered. This term can be finite when currents pass through constrictions (Venturi effect)[70] or curved conductors/trajectories (Bernoulli effect)[71], which exist in nanostructures. In a superconductor, this kinetic term can be seen as the equivalent of a Bernoulli term, scaling as  $\nabla(n_S e \frac{\vec{v}_S^2}{2})$ . A spatial variation in the density  $n_S$  at constant  $\vec{v}_S$  will also result in an electric field. If there is no convection term, an electric field will increase the supercurrent until  $\vec{E} = 0$ .

Though the electromagnetism and hydrodynamics of superconductors on a large scale is well described by the London theory, the fact that superconductors are only superconducting below a certain temperature,  $T_c$ , magnetic field,  $H_c$ , and current density,  $J_c$ , is not described by the London theory. This can be described by the Ginzburg-Landau theory for superconductivity[67]. This phenomenological theory introduces constants  $\alpha$ ,  $\beta$  and a complex order parameter  $\psi$ ; the latter of which is similar to the wave function in the Schrödinger equation. The addition of the term  $F_{super} = \alpha|\psi|^2 + \frac{\beta}{2}|\psi|^4$  to the free energy of the normal metal is enough to phenomenologically explain the appearance of superconductivity in the absence of a magnetic field. The Ginzburg-Landau theory also predicts the appearance of a characteristic length over which the superconducting order parameter reacts to a perturbation, called the coherence length,  $\xi$ . In the Ginzburg-Landau theory, it takes on the value:

$$\xi = \sqrt{\frac{\hbar^2}{4m|\alpha|}}. \quad (2.73)$$

In addition, upon taking into account the effect of a magnetic field on the order parameter, the penetration depth also appears in the Ginzburg-landau theory as:

$$\lambda = \sqrt{\frac{m\beta}{\mu_0 e^2 |\alpha|}}. \quad (2.74)$$

Comparison with the London theory allows one to interpret  $\frac{|\alpha|}{\beta}$  as the superfluid density in the Ginzburg-Landau theory. The Ginzburg-landau theory also predicts the existence of two different types of behavior with magnetic field. If  $\kappa = \frac{\lambda}{\xi} < \frac{1}{\sqrt{2}}$ , the superconducting order parameter will be perturbed on a length scale that is longer than the magnetic penetration depth. As a result, when the penetration of magnetism into the bulk becomes favorable, it will occur all at once. If on the other hand  $\kappa > \frac{1}{\sqrt{2}}$ , it becomes possible for the magnetic field to penetrate the superconductor only locally, without destroying the order parameter across the entire superconductor, resulting in so-called vortices[].

With the Bardeen-Cooper-Schrieffer (BCS) theory[72] came the first proposed microscopic mechanism for superconductivity. The BCS theory proposes that repulsive interaction between electrons with opposite spins and momenta by lattice phonons results in a pair potential  $\Delta$  and a corresponding energy gap,  $E_{gap} = 2|\Delta|$ , for single quasiparticles that reduces scattering/dissipation. The energy gap decreases with increasing temperature and magnetic field. In the mean-field approach,  $\Delta = \langle \sum_{\vec{k}, \sigma} V_{\vec{k}, \sigma} \hat{c}_{-\vec{k}, -\sigma} \hat{c}_{\vec{k}, \sigma} \rangle$ , where  $V_{\vec{k}, \sigma}$  is the interaction potential and  $\hat{c}_{\vec{k}, \sigma}$  is the annihilation operator of an electron with wavevector  $\vec{k}$  and spin  $\sigma$ . The resulting BCS term in the Hamiltonian is then  $\sum_{\vec{k}, \sigma} \Delta \hat{c}_{\vec{k}, \sigma}^\dagger \hat{c}_{-\vec{k}, -\sigma}^\dagger + h.c.$ , where  $h.c.$  represents the hermitian conjugate. This term can be interpreted as a term for creation/annihilation of a pair, but also as a single particle scattering term annihilating holes at  $(-\vec{k}, -\sigma)$  and creating electrons at  $(\vec{k}, \sigma)$ . This motivates the definition of a  $2 \times 2$

particle-hole (Nambu) space of electron and hole states. The single quasiparticle annihilation operators correspond to Bogoliubov quasiparticles[73]. They are of the form:

$$\hat{\gamma}_+ = u_{\vec{k},\sigma} \hat{c}_{\vec{k},\sigma} + v_{\vec{k},\sigma} \hat{c}_{-\vec{k},-\sigma}^\dagger, \quad (2.75)$$

$$\hat{\gamma}_- = v_{\vec{k},\sigma}^* \hat{c}_{\vec{k},\sigma} - u_{\vec{k},\sigma}^* \hat{c}_{-\vec{k},-\sigma}^\dagger. \quad (2.76)$$

These are the electron- and hole-like quasiparticles with eigenenergy  $E_\pm = \pm \text{sign}(\epsilon_{\vec{k}}) \sqrt{\epsilon_{\vec{k}}^2 + |\Delta|^2}$ , where  $\epsilon_{\vec{k}}$  is the energy of the electrons in the absence of the pair potential. The electron-like component,  $u$ , and the hole-like component,  $v$ , are given by:

$$u(E) = \frac{1}{2} \left( 1 + \frac{\sqrt{E^2 - \Delta^2}}{E} \right), \quad (2.77)$$

$$v(E) = \frac{1}{2} \left( 1 - \frac{\sqrt{E^2 - \Delta^2}}{E} \right), \quad (2.78)$$

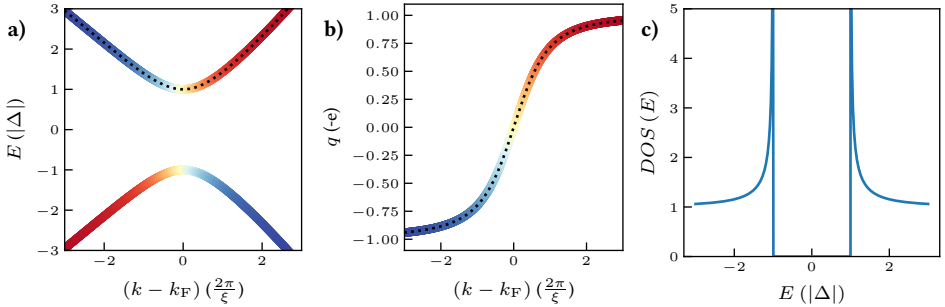


Figure 2.7: a) Quasiparticle dispersion relation versus rescaled wavevector. The color of the line represents the quasiparticle charge, with electrons ( $q = -e$ ) in red and holes ( $q = e$ ) in blue. b) Quasiparticle charge versus the rescaled wavevector. c) Electronic density of states versus energy.

where the index  $\vec{k}$  was suppressed for simplicity. Using these components, the charge of electron-like quasiparticles can be defined as  $q(E) = -e(u(E)^2 - v(E)^2) = -e \frac{\sqrt{E^2 - \Delta^2}}{E}$ . The dispersion relation of electron and hole-like quasiparticle excitations is plotted in Figure 2.7a. The momentum is rescaled to  $\frac{2\pi}{\xi} = \frac{|\Delta|}{\hbar v_F}$ . The dispersion relation is colored to show the quasiparticle charge. Note that the electron-like branch smoothly transitions into the hole-like branch at the Fermi wavevector  $\vec{k}_F$ . To better illustrate the charge versus energy, the quasiparticle charge at positive energy versus momentum at the Fermi surface is also plotted in Figure 2.7b. Since the electron and hole-like branches are related by electron-hole symmetry, the  $E > 0$  excitations suffice to describe superconductivity in the BCS theory.

Finally, the spectral density of states in the BCS theory is given by:



$$\text{DOS}(E) = v(E) \frac{E}{\sqrt{E^2 - \Delta^2}}, \quad (2.79)$$

where  $v(E)$  is the normal state density of states, which is usually well approximated by a constant at the Fermi energy. This is illustrated in Figure 2.7c. The density of states shows an energy gap of size  $2|\Delta|$ , with sharp diverging quasiparticle peaks at the edge. This shape is characteristic of BCS superconductors and can be probed by tunneling spectroscopy of a superconductor.

### 2.2.1 Critical field of superconductors

All currently known superconductors exhibit a critical current and a critical field. Early explorations by Silsbee and Kamerlingh Onnes[74] demonstrated that these two properties are related. According to Silsbee's rule, the relation between critical field and critical current in a macroscopic wire of radius  $r$  is:

$$J_c = \frac{2H_c}{r} \quad (2.80)$$

This statement can be derived through the London equations. At the critical current density, the magnetic field at the surface of the wire is equal to  $H_c$ .

The origin of a critical current or field can be explained by the BCS theory. When the kinetic energy associated with the magnetic field exceeds the potential energy (energy gap) due to the pairing interaction, scattering processes between electrons and holes can occur. The criterion for scattering of quasiparticles from positive velocity  $v_F + v_{\text{drift}}$  to negative velocity  $-v_F + v_{\text{drift}}$  can be written as:

$$\frac{m((v_F + v_{\text{drift}})^2 - (v_F - v_{\text{drift}})^2)}{2} = 2mv_F v_{\text{drift}} = 2|\Delta|. \quad (2.81)$$

This scattering randomizes momentum and results in pair-breaking. The so-called depairing velocity is:

$$v_{\text{depairing}} = \frac{|\Delta|}{mv_F}, \quad (2.82)$$

Which implies a critical current density of:

$$J_c = nev_{\text{depairing}} = \frac{ne|\Delta|}{mv_F}. \quad (2.83)$$

For most metals, the free electron density is on the order of  $10^{28}$  to  $10^{29} \text{ m}^{-3}$  and the Fermi velocity is on the order of  $10^6 \text{ m/s}$ . Assuming  $|\Delta|$  is on the order of 1 meV, and  $m = 9.11 \cdot 10^{-31}$  is the mass of free electrons (no large effective mass), this implies  $J_c$  to be on the order of  $10^{11}$  to  $10^{12} \text{ A/m}^2$ . The associated depairing velocity is on the order of 100 m/s.

### Parallel critical field in a thin film

In a thin film that is thinner than the London penetration depth, the Meissner effect will only partially screen the magnetic field. Here, we describe a thin film centered at  $z = 0$ , with a film thickness,  $d$ , and normal direction oriented in the  $\hat{z}$  direction. Upon applying a magnetic field in the  $\hat{y}$  direction, a Meissner current will run in the  $\hat{x}$  direction. An approximate solution for the vector potential in the London gauge in this case is:

$$\vec{A}(x, y, z) = B_y z \hat{x}. \quad (2.84)$$

The magnetic vector potential at the surface is given by  $\vec{A}(x, y, z = \frac{d}{2}) = \frac{d}{2} B_y \hat{x}$ . To this vector potential a velocity can be associated with:

$$\vec{v}_{\text{field}} = \frac{-e\vec{A}}{m} = \frac{-eB_y d}{2m} \hat{x}. \quad (2.85)$$

Equating the velocity at the surface to the depairing velocity, a thin superconducting film has a parallel critical field scale equal to:

$$B_y = \frac{2|\Delta|}{ev_F d}. \quad (2.86)$$

For a thin film of thickness 13 nm, a Fermi velocity of  $1.4 \cdot 10^6$  m/s (value for niobium and gold) and  $\Delta = 1.3$  meV (value for niobium) this value is 143 mT. The critical field scale found here is related to the depairing at the surface. If the coherence length is smaller than the film thickness, this does not destroy superconductivity in the whole thin film. The critical field will be approximately equal to  $\frac{2|\Delta|}{ev_F \xi}$ .

### Second critical field in type II superconductors

In so-called type II superconductors,  $\lambda > \frac{\xi}{\sqrt{2}}$  holds. As a result, the magnetic field can locally penetrate the superconducting thin film through vortices above the first critical field  $H_{c1}$ . In this case, the critical field necessary to completely destroy superconductivity is larger and a second critical field,  $H_{c2}$ , exists, which is associated with the complete loss of superconductivity in the film. The Landau-Ginzburg result for the second critical field is:

$$H_{c2} = \frac{\Phi_0}{2\pi \xi^2}. \quad (2.87)$$

In dirty superconducting thin films, where the coherence length,  $\xi$ , is smaller than the mean free path,  $l$ , the scattering length changes to:  $\xi^2 = \frac{l}{3} \xi_0$ . Thus, the second critical field can be used as a measure of the mean free path if the coherence length of the clean film is known. For a typical sample in this thesis with a critical field of 2 to 3 T, this

results in an estimated coherence length of 12.8 to 10.5 nm. For niobium with a clean BCS coherence length of  $\xi_0 = 38$  nm, an electronic mean free path of  $l = 13$  to  $l = 8.6$  nm is found.

### 2.2.2 BTK Theory

The conductance of NS interfaces is well-described by Blonder-Tinkham-Klapwijk (BTK) theory[75]. This theory considers scattering of quasiparticles at NS interfaces, which may be transmitted, reflected or Andreev reflected. An Andreev reflection is a process in which two electrons from the normal metal enter the superconductor, forming a Cooper pair[76]. Due to the coherence of the pair, this process can also be considered as a single electron excitation retro-reflecting as a hole excitation in the normal metal. Remarkably, the reflected hole travels along the same trajectory as the incident electron. As a result of this process, the conductance of an NS interface in the superconducting state can exceed its normal state conductance.

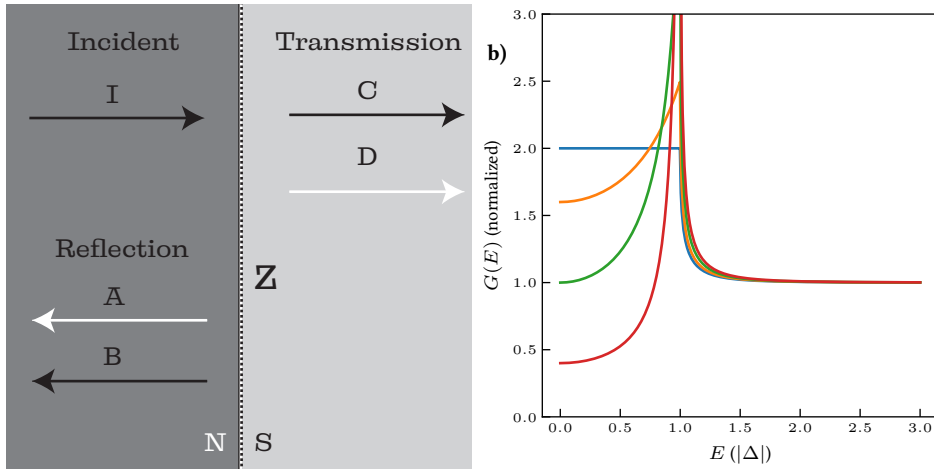


Figure 2.8: a) Schematic representation of scattering processes in BTK theory. I represents incident electrons, A represents the fraction of Andreev reflected holes, B represents the fraction of reflected electrons, C represents the fraction of transmitted electron-like quasiparticles and D represents the fraction on transmitted hole-like quasiparticles. b) NS interface conductance  $G(E)$  versus  $Z$  for  $Z = 0, 0.5, 1.0, 2.0$ .

The BTK theory defines parameters  $A(E)$  and  $B(E)$  as the probability of Andreev and normal reflection as a function of energy, in terms of which the transmission of the interface can be written as  $T(E) = 1 + A(E) - B(E)$ . In calculations, parameters  $C(E)$  and  $D(E)$  for electron- and hole-like transmission are also defined, which are related to  $A$  and  $B$ . In Figure 2.8a these processes are illustrated graphically. The interface in BTK theory is a delta function with dimensionless barrier strength  $Z$ , such that the normal state transparency is  $\frac{1}{1+Z^2}$ . The expressions for  $A(E)$  and  $B(E)$  are:

$$A(E) = \frac{\Delta^2}{E^2 + (\Delta^2 - E^2)(1 + Z^2)^2}, \quad E < \Delta \quad (2.88)$$

$$B(E) = 1 - A(E), \quad E < \Delta \quad (2.89)$$

$$A(E) = \frac{u_0^2 v_0^2}{(u_0^2 + Z^2(u_0^2 - v_0^2))^2}, \quad E > \Delta \quad (2.90)$$

$$B(E) = \frac{(u_0^2 - v_0^2)^2 Z^2 (1 + Z^2)}{(u_0^2 + Z^2(u_0^2 - v_0^2))^2}, \quad E > \Delta \quad (2.91)$$

$$(2.92)$$

where  $u_0$  and  $v_0$  are the electron and hole probability amplitudes of the quasiparticles. The differential conductance versus energy is plotted in Figure 2.8b. For a perfectly transparent barrier, Andreev reflections result in a zero-energy differential conductance that is two times larger than the normal state conductance. As the barrier strength is increased, the zero-bias conductance decreases and a peak in the differential conductance is formed at  $E = |\Delta|$ . For a perfectly transparent barrier, the resulting conductance simplifies to:

$$G(E) = 2G_{\text{NS}}, \quad E < \Delta, \quad (2.93)$$

$$G(E) = G_{\text{NS}} \left(1 + \frac{v_0^2}{u_0^2}\right) = G_{\text{N}} \frac{1 - \sqrt{1 - (\frac{\Delta}{E})^2}}{1 + \sqrt{1 - (\frac{\Delta}{E})^2}}, \quad E > \Delta, \quad (2.94)$$

$$(2.95)$$

where  $G_{\text{NS}} = \lim_{E \rightarrow \inf} G(E)$  is the normal state interface conductance. At zero temperature, this can be integrated to yield:

$$I(V) = 2G_{\text{NS}} V, \quad |V| \leq \frac{\Delta}{e}, \quad (2.96)$$

$$I(V) = G_{\text{NS}} \left( V + \frac{4}{3} \frac{\Delta}{e} \frac{V}{|V|} + \left( \frac{2}{3} \left( \frac{eV}{\Delta} \right)^3 - \frac{2}{3} \left( 1 - \left( \frac{\Delta}{eV} \right)^2 \right)^{\frac{3}{2}} \left( \frac{eV}{\Delta} \right)^3 - \frac{eV}{\Delta} \right) \right), \quad |V| > \frac{\Delta}{e}. \quad (2.97)$$

$$(2.98)$$

This shows that a perfectly transparent NS interface has an excess conductance at low bias and a maximum excess current,  $I_{\text{ex,max}} = \frac{4}{3} \frac{G_{\text{NS}} \Delta}{e}$ , remains at high bias. The excess current can also be considered as a deficit (or insufficient) voltage,  $V_{\text{def,max}} = \frac{4}{3} \frac{\Delta}{e}$ . This property is generally independent of the resistance of the NS interface, only depending on the barrier strength.

In the high-temperature limit ( $k_b T \gg \frac{|\Delta|}{e}$ ), a similar result can be derived. In this case, the excess current is:

$$I_{\text{exc}}(V) = \frac{4\Delta}{3eR_{\text{NS}}} \tanh\left(\frac{eV}{2k_b T}\right), \quad (2.99)$$

with  $R_{\text{NS}} = \frac{1}{G_{\text{NS}}}$ . This function has the same amplitude and a similar shape, but has a voltage scale of  $2k_b T$  instead of  $|\Delta|$ . The maximum excess current is the same. In Figure 2.9, the zero temperature and high temperature deficit voltage  $V_{\text{def}} = I_{\text{exc}} R_{\text{NS}}$  are plotted together. To compare the shape, the high temperature result is plotted for  $k_b T = \frac{|\Delta|}{2}$ .

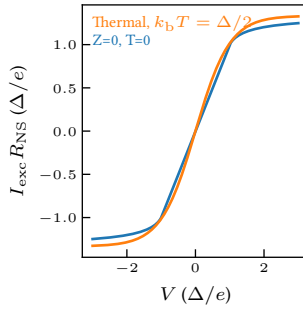


Figure 2.9: Deficit voltage  $I_{\text{exc}} R_{\text{NS}}$  versus bias voltage  $V$ . Comparison between the finite temperature (orange curve) and zero temperature (blue curve) predictions.

With the addition of a finite barrier strength, the low-bias ( $eV < \Delta$ ) junction transmission and, by extension, the differential conductance of NS junctions decreases as Andreev reflection becomes less probable. The differential conductance converges to the BCS density of states with increasing  $Z$  at zero temperature. The deficit voltage approximately scales with junction transparency as  $V_{\text{def}} \approx \frac{\Delta}{2e(1+Z^2)}$ . For an atomic point contact with  $\frac{1}{1+Z^2} = \frac{R_Q}{R_{\text{NS}}}$ , where  $R_Q = \frac{h}{2e^2} \approx 12.9 \text{ k}\Omega$ , this expression results in  $V_{\text{def}} \approx \frac{\Delta}{2e} \frac{R_Q}{R_{\text{NS}}}$ .

The BTK theory can be used to understand the contacting properties of superconductors, as the deficit voltage in particular is a measure of the junction transparency. Also, in superconductor-normal metal-superconductor (SNS) junctions, Andreev reflections play a key role and the deficit voltage profile is related. In SNS junctions, however, multiple Andreev reflections (MAR) can happen sequentially, resulting in a sub-gap structure in the current-voltage relation[77]. This is taken into account by the OTBK theory[78]. As a result of MAR, current-voltage relations have additional features at voltages  $V_n = \frac{2|\Delta|}{ne}$ ,  $n = 1, 2, 3, \dots$ , corresponding to  $n$  Andreev reflections transferring  $n + 1$  electrons. Additional peaks can result if the superconducting gaps of the two superconductors are not equal[79]. Finally, at zero bias voltage, confined cavity modes develop. This process can be viewed as the limit  $n \rightarrow \infty$ , transferring infinite charge (with a speed limit set by the Fermi velocity) without any voltage. The maximum current (for fully transparent NS interfaces) is equal

to  $I = n \frac{V_n}{R_N} = \frac{2|\Delta|}{eR_N}$ , where  $R_N$  is the normal state resistance. The SNS junction can thus carry a supercurrent, also known as a Josephson current for weak superconducting links[80].

Finally, from a conceptual point of view, a question that arises from the presence of a deficit voltage is where this voltage drop is localized. The authors of the BTK theory give an answer to this question. In their paper, they discuss that quasiparticles that are injected from N to S are not instantaneously converted to a pair. Instead, a two-step process occurs. The Andreev quasiparticle current ( $E < \Delta$ ) is converted over a coherence length  $\xi$  into the superconductor, with corresponding wavefunctions behaving as evanescent waves. Quasiparticles injected above the gap instead introduce a charge imbalance,  $Q^*$ , into the superconductor[81]. This imbalance decays into a supercurrent over a timescale of the charge relaxation time,  $\tau_Q$ . The introduced quasiparticle charge is balanced by pairs that flow in response. As a result, charge neutrality in the superconductor is maintained. Thus, both subgap Andreev reflections and injected quasiparticles can introduce a deficit voltage. In the following parts of the theory, the spatial extent of Andreev processes will be discussed further in terms of the quasi-classical diffusive Usadel theory of superconductivity to describe NS interfaces and SNS junctions. Following this, charge imbalance and non-equilibrium superconducting effects will be elaborated further.

### 2.2.3 Diffusive electronic transport

To understand superconducting transport in diffusive structures, it is instructive to first consider normal electronic transport in diffusive structures at low temperatures. In a polycrystalline material, such as a thin film, at low temperature, transport is often limited by elastic scattering at grain boundaries and surfaces. On average, the thin film structure results in a mean free path,  $l$ , which is independent of energy. Using this scattering length and the Fermi velocity,  $v_F$ , the diffusion coefficient due to scattering can be defined as:

$$D = \frac{v_F l}{3}. \quad (2.100)$$

This diffusion constant is relevant for understanding the transport properties of conductors and, in particular, superconducting thin films. The conductivity,  $\sigma$ , of disordered conductors can be expressed in terms of the diffusion coefficient and the volumetric electronic density of states at the Fermi energy,  $N(E_F)$ , using the Einstein relation (which can be derived from combining Ohm's law and Fick's law)

$$\sigma = 2e^2 DN(E_F) = G_0 2\pi \hbar DN(E_F), \quad (2.101)$$

where  $G_0 = \frac{2e^2}{h}$  is the conductance quantum and the factor 2 accounts for spin degeneracy.

From this, the dimensionless conductance can be written in terms of the Thouless energy  $E_{Th} = \frac{\hbar D}{L^2}$  as:

$$\frac{G}{G_0} = 2\pi \hbar DN(E_F) \frac{A}{L} = 2\pi N(E_F) V \frac{\hbar D}{L^2} = 2\pi N(E_F) V E_{Th} = 2\pi \frac{E_{Th}}{\delta}. \quad (2.102)$$

The Thouless energy is the effective energy scale for diffusion across the film and  $\delta = \frac{1}{N(E_F)V}$  is the average level spacing. Given a material and a geometry,  $N(E_F)$ ,  $v_F$ ,  $V$  and  $L$  are fixed. Thus, the conductance of a sample with a given geometry only depends on the Thouless energy through the mean free path.

### 2.2.4 Diffusive superconductivity: Proximity effect

When a superconductor is interfaced with another conductor, the superconducting order parameter can delocalize into the normal metal. This effect is known as the proximity effect. The Josephson effect in SNS junctions discussed in the context of MAR in subsection 2.2.2 on BTK theory is a manifestation of this. The leakage of the superconducting order parameter into the normal metal can be understood as a result of the minimization of the total energy of the quasiparticles. The inverse effect, pair breaking in the superconductor, also occurs. This can locally result in a pair potential condensate in the superconductor and a reduced  $T_c$ . This problem was originally discussed by de Gennes using the Bogoliubov-de Gennes formalism[82]. This formalism works quite well for ballistic/clean samples.

A formalism that is simpler for diffusive transport is the Green's function formalism by Gor'kov[83]. This formalism considers a  $2 \times 2$  matrix Green's function in Nambu space, where the diagonal elements  $G_{ee}$  and  $G_{hh}$  are electron- and hole-like and the off-diagonal elements (called the anomalous Green's function  $F_{eh} = F_{he}^*$ ) corresponds to electron-hole coherence. A full description using the Gor'kov theory is, however, impractical, as it considers interactions between all quasiparticles at positions  $\vec{r}_1$  and  $\vec{r}_2$  and times  $t_1$  and  $t_2$ . A significant simplification occurs by considering the quasiclassical limit, where  $E_F \gg |\Delta|$ , which results in the Eilenberger equations[84]. This limit is nearly always valid and eliminates spatial dependence at the length-scale,  $\lambda_F$ , which is on the order of the radius of an atom in metal thin films. In the quasiclassical limit, only the excitations at the Fermi surface contribute and superconductivity has an intrinsic length-scale  $\xi$ . The equilibrium Eilenberger Green's functions depend only on the center of mass coordinate  $\vec{r}$ , the time difference,  $\Delta t = t_2 - t_1$ , (or energy  $E$ ) and the momentum direction,  $\hat{v}$ , on the Fermi surface.

A further simplification can be made based on the scattering in the thin film. The films is considered clean if  $l \gg \xi$  and dirty if  $l \ll \xi$ . One can define effective coherence lengths  $\xi_{\text{clean}} \approx \xi$  and  $\xi_{\text{dirty}} \approx \sqrt{\frac{l\xi}{3}}$ . In the dirty limit, the Usadel equation[35] describes the proximity effect well. In this limit, the Green's function can be taken to be nearly isotropic over the Fermi surface and the dependence is only on the position  $\vec{r}$  and time difference  $\Delta t$  / energy  $E$ . In the coming discussion, the Usadel equation will be considered. To simplify the equations, the  $2 \times 2$  Nambu Green's function can be parametrized by the polar angle  $\theta$  and the azimuthal angle  $\phi$  on a Bloch sphere. Then it can be expressed as:

$$G^R(E) = \begin{bmatrix} \cos(\theta(E)) & \sin(\theta(E))e^{-i\phi(E)} \\ \sin(\theta(E))e^{i\phi(E)} & -\cos(\theta(E)) \end{bmatrix}, \quad (2.103)$$

which is a unitary matrix. Here, it should be noted that the pairing angle  $\theta$  can be a complex function of energy, with  $0 < \text{Re}(\theta) < \frac{\pi}{2}$ . The latter constraint is necessary to obtain

a positive value for the density of states.  $\phi$  is a real number, representing the phase of the superconducting pairing. In 1D, the Usadel equations for longitudinal ( $\theta$ ) and latitudinal ( $\phi$ ) changes on the Bloch sphere can then be expressed as:

2

$$\frac{\hbar D}{2} \frac{d^2 \theta}{dx^2} = -iE \sin(\theta) - \Delta \cos(\theta) - \left( \frac{\hbar}{\tau_{SF}} + \frac{\hbar D}{2} \left( \frac{d\phi}{dx} + \frac{2e}{\hbar} A_x \right)^2 \right) \sin(\theta) \cos(\theta), \quad (2.104)$$

$$\frac{d}{dx} \left( \left( \frac{d\phi}{dx} + \frac{2e}{\hbar} A_x \right) \sin^2(\theta) \right) = 0, \quad (2.105)$$

where  $\tau_{SF}$  is the spin-flip scattering time and  $A_x$  is the x component of the vector potential  $\vec{A}$ . The second equilibrium Usadel equation is equivalent to conservation of supercurrent. The first equation, which we will focus on, describes the diffusion of the pairing angle  $\theta$ . This angle is driven to  $\theta = 0$  by the energy term  $-iE \sin(\theta)$  and driven to  $\theta = \frac{\pi}{2}$  by the pairing term  $-\Delta \cos(\theta)$ . The final term, related to spin-flip scattering and supercurrent density is called the pair-breaking term, which is largest at the pairing angle  $\theta = \frac{\pi}{4}$ , representing states that behave 50/50 as superconducting ( $|u| = |v|$ ) and normal quasiparticles ( $|u| = 1$  or  $|v| = 1$ ).

In the absence of phase gradients (currents), magnetic fields and spin flip scattering, the Usadel equation reads:

$$\hbar D \frac{d^2 \theta}{dx^2} = -2iE \sin(\theta) - 2\Delta \cos(\theta), \quad (2.106)$$

In the bulk of a superconductor, the condition  $\frac{d\theta}{dx} = 0$  holds and  $\theta = \arctan(i\frac{\Delta}{E})$ , which is approximately  $\frac{\pi}{2}$  for  $E \ll |\Delta|$ . In the bulk of a normal metal, the proximity effect can be studied by taking  $\Delta = 0$  and assuming  $\theta$  is small. Then the following equation results:

$$\hbar D \frac{d^2 \theta}{dx^2} = -2iE\theta. \quad (2.107)$$

The natural length scale in this case is  $L_N = \sqrt{\frac{\hbar D}{2E}}$ , which diverges to infinity as  $E \rightarrow 0$ . In this case the solution can be expressed as:

$$\theta = Ae^{\frac{1-i}{\sqrt{2}} \frac{x}{L_N}} + Be^{-\frac{1-i}{\sqrt{2}} \frac{x}{L_N}}. \quad (2.108)$$

These are exponentially decaying, oscillating solutions, indicating decay towards the normal state accompanied by spatial oscillations in the density and pairing interaction. Going away from a superconducting interface  $\theta$  can only decrease to zero, unless it approaches another superconducting interface. At the middle of an SNS junction  $|A| = |B|$  should be



taken, as  $\frac{d\theta}{dx} = 0$  should hold by inversion symmetry. Considering a length  $L$ , the theta parameter at the center scales as  $e^{-\frac{L}{2\sqrt{2}L_N}} = e^{-\frac{1}{2}\sqrt{\frac{EL^2}{hD}}} = e^{-\frac{1}{2}\sqrt{\frac{E}{E_{Th}}}}$ .

In the center of the wire, the normal metal is most weakly proximitized. For this reason, the maximum Josephson current (the switching current) of an SNS junction is determined by the Thouless energy as  $I_{sw}R_N = \alpha\left(\frac{E_{Th}}{\Delta}\right)\frac{E_{Th}}{e}$  [85, 86], where  $\alpha$  is a function that interpolates between the short junction limit ( $L \ll \xi$ ), where  $eI_{sw}R_N \propto \Delta$  and the long junction limit ( $L \gg \xi$ ), where  $eI_{sw}R_N \propto E_{Th}$  and  $\alpha \approx 10$ .

The local density of states in the center of the wire also exhibits a so-called minigap. For wire lengths on the order of one to two times the coherence length and a transparent NS interface, the energy gap at the center of this wire roughly scales as  $E_{gap} \approx \frac{L}{\xi}E_{Th} = \frac{\hbar D}{L\xi}$  [87]. At long lengths, the energy gap is approximately equal to  $E_{gap} \approx 3.1E_{Th}$ .

### 3D/2D structures

In most of the experiments done in this thesis, the relevant case is not one dimensional, but rather a 3D structure. These structures are made of layered metal thin films. In Figure 2.10 a realistic 2D cross-section of an SNS junction is illustrated, consisting of a normal metal bottom layer with two superconducting layers on top, one on the left and one on the right. This SNS structure will be the focus of the coming subsections. There are two distinct regions in this structure, the NS bilayer part and the single N layer bridge, which forms a constriction. The structure can thus be considered as an SN-N-NS structure. In the coming sections it will be assumed that the inverse proximity effect of the N bridge on the NS bilayer is negligible. Thus, the NS bilayer is considered to be a boundary condition for the bridge. The geometrical effect of the constriction on diffusion will be neglected in the discussion. The geometric effect on diffusion would yield a correction factor for the Thouless energy. The constriction does have a large effect on the current density. Since the current density scales as the inverse of the cross-sectional area  $\frac{1}{A}$ , current densities in constricted geometries are largest at the narrowest point. This results in pair-breaking at the center of the constriction becoming more dominant compared to the pair-breaking in a wire of constant area.

### NS bilayer

The NS bilayer can be considered as a 1D system, as the superconducting properties should be independent of the in-plane dimensions. In the NS bilayer, the relevant parameters are film parameters (densities of states and diffusion constants/conductivity), film thicknesses and the interface parameters. Boundary conditions must be implemented for the Usadel equation at the NS interface, which is beyond the scope of this thesis. Nevertheless, the extreme cases of perfect and poor transparency can be discussed. In the case of perfect transparency,  $\theta$  and  $\phi$  are expected to be continuous across the interface. In this case, the normal metal can also display a Meissner current. In the poorly transparent case, however,  $\theta$  is not continuous.

The static properties of the NS bilayers are determined by the film thicknesses  $d_N$ ,  $d_S$ ,

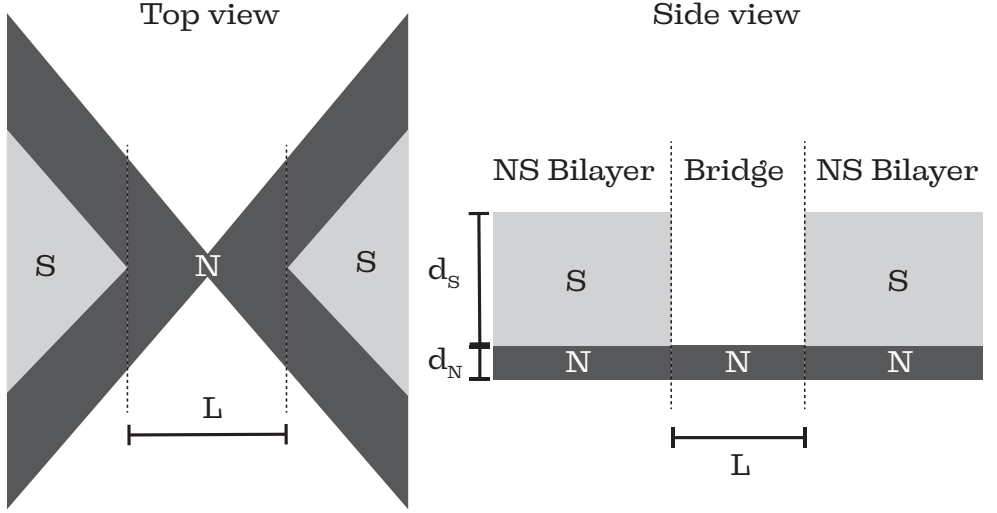


Figure 2.10: Top and side view schematic of a variable thickness constriction SNS junction.

densities of states  $n_N$ ,  $n_S$ , mean free paths  $l_N$ ,  $l_S$  and interface transparency  $\tilde{t}$ . The  $T_c$  has been given by Martinis[88] for thin bilayer NS films. It was found that:

$$T_c = T_{c0} \left( \frac{d_S}{d_0} \frac{1}{1.13(1 + \frac{1}{\alpha})} \frac{1}{\tilde{t}} \right)^\alpha \quad (2.109)$$

with  $T_{c0}$  the critical temperature of the bulk superconductor,  $\frac{1}{d_0} = \frac{\pi}{2} k_B T_{c0} \lambda_F^2 n_S$  the inverse of the coherence length and  $\alpha = \frac{d_N n_N}{d_S n_S}$  a measure for the number of carriers in the films that are mixing. Martinis discussed that this formula could be extended to thicker films by taking:

$$\frac{1}{\tilde{t}_{\text{eff}}} = \frac{1}{\tilde{t}} + A \frac{d_N}{\sigma_N} + B \frac{d_S}{\sigma_S} \quad (2.110)$$

Where  $A$  and  $B$  are constant. This indicates that for thick films, the interface transparency is effectively reduced, with the effective transparency being  $\tilde{t}_{\text{eff}} = \frac{\tilde{t} \tilde{t}_{\text{proximity}}}{\tilde{t} + \tilde{t}_{\text{proximity}}}$ , where  $\tilde{t}_{\text{proximity}}$  is the correction due to the inverse proximity effect. This value tends towards the smallest of the two values. Thus, the interface transparency sets an upper bound for the effective transparency. From the point of view of the proximity effect in the normal metal, the energy gap in the N part of the NS bilayer is expected to be proportional to  $\tilde{t}_{\text{eff}}$ .

The bilayer  $T_c$  is a meaningful quantity that can be measured, as it gives insight into the effective interface transparency. For poor transparency, this value tends to  $T_{c0}$  and is

independent of normal metal thickness. A similar situation occurs if the density of states is small ( $\alpha$  small) or the normal metal is poorly conductive. If the normal metal has more charge carriers or is more conductive in comparison to the superconductor, a reduction of  $T_c$  is expected. Thus, the dependence of  $T_c$  on film thickness can be used to characterize the combination of interface and material properties.

## N bridge

In the normal metal bridge, the static properties of the Usadel equation can be described by just the diffusion constant and the length. As a result, the only relevant parameter for the bridge is the Thouless energy  $E_{Th} = \frac{\hbar D}{L^2}$ . Due to the presence of the NS bilayer, the effective length of the bridge can be longer than the geometric length. A limited interface transparency at the NS interface will scale the effective Thouless energy and reduce the energy gap in the junction. In the highly transparent case, the inverse proximity effect from the bridge, which was neglected until now, can also increase the effective length by approximately one coherence length.

### Estimate of the energy gap at the center of the bridge in an SN-N-NS structure

In the previous two sections, it was found that the pair coherence decays at the NS bilayers and in the bridge. Since the boundary conditions of the bridge for the Usadel equation should be given by the NS bilayer, an effective Thouless energy can be defined for the structure, which is roughly  $\min(t_{eff}\Delta, E_{Th})$ . For a realistic/clean disordered interface transparency of  $t = 0.46$  was found for Pd and Nb[89]. The energy gap in the normal metal is  $E_{gap} = \frac{|\Delta|}{2}$  at best in this scenario. With Nb as the superconductor, this means  $E_{gap} = \frac{1.3 \text{ meV}}{2} \approx 650 \text{ } \mu\text{eV}$  in the center of the junction is a reasonable upper bound. On top of this optimal behavior comes the length scaling as  $(\frac{\xi_N}{L})$ . For most junctions in this thesis, the geometric bridge length is 50 or 60 nm and the coherence length in the normal metal is roughly 20 nm (for gold as N and niobium as S). Following Hammer[87], the geometric length results in energy gaps of  $E_{gap} = 2.5E_{Th} \approx 2.5\frac{\xi^2}{L^2}\Delta = \frac{2.5}{9}1.3 \text{ meV} \approx 360 \text{ } \mu\text{eV}$  with ideal interfaces. An energy gap of 250  $\mu\text{eV}$ , corresponding to the observed gaps in this thesis, corresponds to an effective length of roughly 72 nm. This is in good agreement with predictions, exceeding the geometric length by roughly a coherence length.

The smallest spacings achieved with aluminium as the superconductor during fabrication of SNS junctions were 30 nm, which would give a gap of roughly  $\frac{\xi}{L}\Delta \approx 860 \text{ } \mu\text{eV}$  if done with niobium and gold. Realistically, the effective length is longer by at least 6 nm per side (coherence length in dirty niobium found in this thesis), resulting in a gap of 610  $\mu\text{eV}$ .

With this, the equilibrium proximity effect is described. The next section will briefly focus on the physics of Josephson junctions, after which non-equilibrium effects will be discussed.

### 2.2.5 RCSJ model for SNS junctions

A common model for describing Josephson junctions in circuits is the resistive and capacitive shunted junction (RCSJ) model. This model considers a Josephson junction that is shunted by a parallel resistor  $R$  and capacitor  $C$ . The Josephson junction has a characteristic energy scale that is called the Josephson energy. The Josephson energy is proportional to the critical current and given by:

$$E_J = \frac{\Phi_0}{2\pi} I_c = \frac{\hbar}{2e} I_c. \quad (2.111)$$

In SNS junctions, the resistive shunt is made by the normal metal bridge, whereas the geometric capacitance tends to be negligible. As a result, the capacitance,  $C$ , can be neglected and the SNS junction can be described by the simpler Resistive Shunted Junction (RSJ) model. Besides the Josephson energy, another measure for the quality of SNS junctions is the characteristic Thouless energy. The Josephson energy can be expressed in terms of the Thouless energy. The relation between the Josephson and Thouless energies is:

$$E_J = \frac{\hbar}{2e^2} \frac{\alpha E_{\text{Th}}}{R_N} = \frac{G_N}{G_0} \alpha E_{\text{Th}} \quad (2.112)$$

Whereas  $E_J$  is related to the kinetic impedance of the Josephson junction.

In the RCSJ model approach, the total current across the junction can thus be written as:

$$I = \frac{V}{R_N} + I_c \sin(\phi) + C \frac{dV}{dt}. \quad (2.113)$$

Including the relationship  $\frac{d\phi}{dt} = \frac{2eV}{\hbar}$ , this equation is a differential equation that resembles the equation of motion of particle on a tilted washboard potential, where the position of the particle is  $\phi$ , the washboard potential is  $-I_c \cos(\phi)$ , the mass is  $\frac{\hbar C}{2e}$  and the friction parameter is  $\frac{\hbar}{2eR_N}$ . When the tilting of the washboard potential is sufficient (i.e. when the critical current is reached), the particle will run the potential landscape, resulting in a finite voltage. In the case of an SNS junction, the mass term is insignificant and thus the resistance/friction term dominates. Multiplying equation (2.113) by the normal state resistance and neglecting the capacitance, the RSJ model equation can be rewritten in terms of the Thouless energy:

$$IR_N = V + \frac{\alpha E_{\text{Th}}}{e} \sin(\phi). \quad (2.114)$$

In this equation, the driving term is the normal state voltage  $IR_N$ . In a current-biased measurement, one measures the average voltage  $\langle V \rangle = IR_N - \frac{\alpha E_{\text{Th}}}{e} \langle \sin(\phi) \rangle$ . Importantly, in this formulation, the RSJ model is expressed in terms of a critical voltage  $\frac{\alpha E_{\text{Th}}}{e} = V_c \approx 10 V_{\text{Th}}$ . This critical voltage is independent of the junction resistance.

According to the RSJ model, SNS junctions should be in an overdamped regime. Below the critical current, the phase is constant and there is no voltage across the junction. In this case, the Josephson current-voltage relation is not hysteretic and follows the relation:

$$I(V)R_N = \text{sign}(V)\sqrt{V_c^2 + V^2} \quad (2.115)$$

In experiments, however, SNS junctions can be hysteretic, having a critical current  $I_c$  upon sweeping the current from the S to N state and a retrapping current  $I_r$  for sweeping from N to S.

The ideal RCSJ Josephson junction model presented above ignores two important experimental details. The first being the experimental temperature, which introduces a Johnson noise current and thermally excited quasiparticles. As a result of this, the transition from S to N happens at a current below the ideal critical current, called the switching current  $I_{sw}$ , which is random and can depend on the measurement speed. When the junction is in the normal state, dissipation can also lead to heating, which results in an elevated electronic temperature. As a result, the retrapping current  $I_r$  can be significantly lower than  $I_{sw}$ . Second, the external circuitry can play a role. Noise in this circuitry plays a similar role as temperature does. The impedance of the current source can also significantly influence the junction dynamics[90]. While the source impedance is usually much larger than the junction impedance at low frequency, the same does not hold true at the Josephson and Thouless frequencies, which are on the order of GHz. At these frequencies, the impedance of the external circuitry can be reduced to the characteristic impedance of free space ( $377 \Omega$ ), which increases damping in the junction.

By relating the thermal energy and the Josephson energy, the current-scale related to thermal fluctuations can be calculated. This current-scale only depends on the temperature. The thermal current fluctuations in a Josephson junction at  $T = 100$  mK are of magnitude  $\frac{2ek_b T}{\hbar} \approx 4$  nA.

In the event that the thermal energy  $k_b T$  becomes comparable to the Josephson energy  $\frac{\hbar}{2e} I_c$ , the phase  $\phi$  significantly diffuses due to temperature and the regime of thermally activated phase diffusion is reached. This regime is described by the Ivanchenko-Zilberman (IZ) model[91]. Important features of this model are the appearance of a finite resistance at zero bias current and the reduction of the switching current by  $\frac{E_J}{k_b T}$ . In the limit that  $k_b T \gg E_J$ , the IZ model predicts

$$I(V) = I_c \frac{I_c R_N V}{V^2 + V_{c,IZ}^2}, \quad (2.116)$$

$$\text{with } V_{c,IZ} = \frac{2ek_b T R_N}{\hbar}.$$

### 2.2.6 Nonequilibrium superconductivity: charge and branch imbalance

When normal quasiparticles are injected into a superconductor, the quasiparticle occupancy in the superconductor changes. An example of this can be found in tunnel junctions between superconductors and normal metals. Injection of electrons under application of a finite bias voltage results in an excess of electron-like quasiparticles in the superconductor. An excess positive or negative charge is also called a charge imbalance  $Q^*$  [81, 92]. This results in a measurable voltage and an electrochemical potential difference between the injected quasiparticles and extracted cooper pairs in an SN contact. In response to the injected charge imbalance, pairs will flow to make the superconductor charge neutral.

There are two kinds of processes that result in relaxation of charge imbalance relaxation. A quasiparticle can either scatter inelastically, which decreases its energy,  $E$ , and charge,  $q$ , or recombine with another quasiparticle to form a Cooper pair. Both processes transfer charge from the quasiparticle to the condensate. The timescale for these processes is called the charge imbalance relaxation time  $\tau_Q$ , which roughly scales as the inelastic scattering time  $\frac{k_B T}{\Delta} \tau_E$  in the limit  $|\Delta| \ll k_B T$ . More generally, it has been demonstrated that charge imbalance relaxation rates are equal to pair breaking rates[93]. In the low temperature limit, this is reduced, and elastic scattering can also dominate charge imbalance relaxation in the presence of gap anisotropy[94], magnetic impurities[95], supercurrents[96] and magnetic fields[81]. Charge imbalance relaxation explains how an injected normal current can be converted into a dissipationless superconducting current.

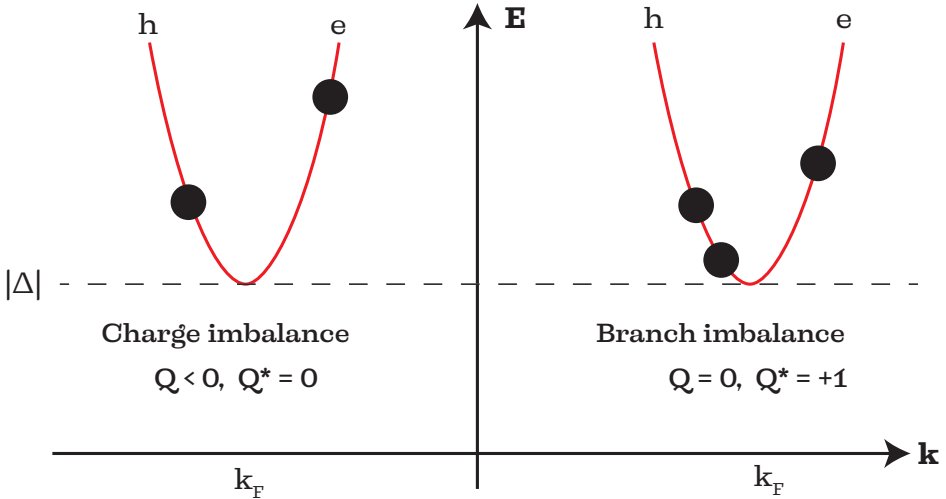


Figure 2.11: Diagram showing charge and branch imbalance. On the left, charge imbalance without branch imbalance is illustrated. There are an equal number of electron and hole-like excitations, but the net charge is negative. On the right, branch imbalance without charge imbalance is illustrated. The two hole-like excitations balance on electron-like excitation in charge.

Even more fundamentally linked to pair-breaking than the concept of charge imbalance is branch imbalance. Branch imbalance (or number imbalance)  $Q$  is a difference between the number of electron-like and hole-like quasiparticles. Because of the energy dependent charge of quasiparticles in superconductors, a charge imbalance does not need to produce branch imbalance and vice versa. To understand this, consider the diagram in Figure 2.11. On the left side, one hole-like quasiparticles with charge  $q = +0.6e$  and one electron-like quasiparticle with charge  $q = -e$  result in a charge imbalance of  $Q^* = -0.4e$  without branch imbalance. This excitation can be considered a combination of a charge mode (In the context of non-equilibrium superconductivity, this is a transverse mode[97]) and an energy/thermal mode (Longitudinal mode) and results in a measurable voltage. On the right side, an additional hole-like quasiparticle with a charge of  $q = +0.4e$  was added. In this case there is no charge imbalance and a branch imbalance of  $Q = +1$ . This excitation is a non-equilibrium energy mode (Longitudinal mode).

As noted in subsection 2.2.2 on BTK theory, the charge imbalance relaxation induced potential difference results in an observable excess current. Branch imbalance relaxation, on the other hand, is related to pair breaking and local heating. In most transport experiments, a combination of charge and branch imbalance is induced in the superconductor.

Related to charge and branch imbalance are the longitudinal and transverse occupancy functions  $f^L(E)$  and  $f^T(E)$ , which are generally odd and even in energy respectively.

Dynamics of the occupancy functions are driven by terms of the form[97]:

$$\hat{\partial} = \hat{I}\vec{\nabla} + i\hat{\tau}_3 m\vec{v}_S \frac{\partial}{\partial E} \quad (2.117)$$

The longitudinal and transverse modes couple together only in the presence of superfluid velocity  $\vec{v}_S$ , as the partial derivative to energy makes odd functions of energy even and vice versa.

For time independent problems, terms of the form  $f^T \propto \frac{Dm\vec{v}_S \cdot \nabla f^L}{\Delta}$  are added.

### 2.2.7 Nonequilibrium: Finite lifetime effects

Quasiparticles in superconductors experience not only a pairing interaction, but also inelastic pair-breaking mechanisms. In contrast to single particle theories, quasiparticles in many-body theories have a lifetime  $\tau_E$ . One way to account for inelastic effects in a single-particle picture is by incorporating a Dynes parameter[98]  $\Gamma = \frac{\hbar}{\tau_E}$ . The Dynes parameter is added to the energy as  $E \rightarrow E + i\Gamma$ , as a result of which the quasiparticles amplitudes get a time dependence  $e^{-\Gamma \frac{\Gamma}{\hbar} t} = e^{-\frac{t}{\tau_E}}$ . In a normal metal, quasiparticle excitations simply decay to other quasiparticle excitations and, as such, the density of states is minimally affected. For a superconductor however, pair coherence is broken as correlated particles become uncorrelated. Thus, the quasiparticle peaks in the density of states broaden and the energy gap can reduce or fill up. Thus, if inelastic effects are taken into account consistently,  $|\Delta|$  will also decrease due to the reduction in coherence.

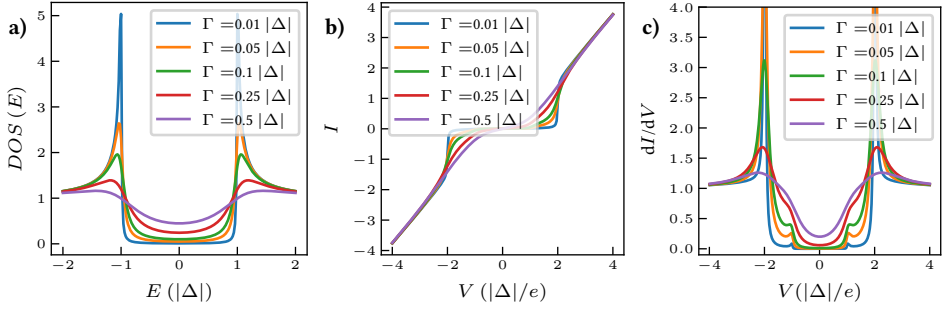


Figure 2.12: Effect of a finite quasiparticle lifetime/Dynes parameter  $\Gamma$  on the a) Electronic density of states versus energy b) Current versus voltage curve of a superconducting tunnel junction c) Differential conductance versus voltage curve of a superconducting-insulator-superconductor tunnel junction.

In the tight binding simulations made using Kwant[99] of NS contacts in the following sections, the Dynes parameter has been added to tight binding simulations by adding  $-i\Gamma\sigma_0$  to the on-site energy, where  $\sigma_0$  is the identity matrix.

### 2.2.8 Effect of a Meissner current on SNS junctions

Besides the phase difference, supercurrent can also be driven by magnetic fields through the Meissner effect. In SNS junctions, the Meissner current flows at the NS interface and can potentially be transmitted into the normal metal. When a magnetic field is applied in the in-plane  $\hat{y}$  direction, the Meissner current runs in the  $\hat{x}$  direction along the NS interface. Assuming zero current bias and finite supercurrent density at the NS interface due to the Meissner effect, a finite current could thus flow across the SNS junction. The flow of a current through the normal metal, however, contradicts a steady-state. If the device were to be left floating, a continuously increasing electric field would establish across the SNS junction due to the movement of charge. This can be resolved in at least two ways:

1. A phase difference develops to counteract the Meissner effect, resulting in no supercurrent.
2. A supercurrent does flow through the junction. To compensate the supercurrent, a dissipative current flows in the opposite direction that is driven by a voltage.

In the first scenario, no supercurrent flow through the junction at all, but the junction is phase-biased. As a result, the junction can behave as a Josephson diode, exhibiting a different critical current for forward and backward currents. This possibility is calculated by Davydova et al.[100]. In the second scenario, supercurrent does flow into the junction, but is converted to a dissipative quasiparticle current. Thus, a finite voltage develops across the normal metal bridge, which is compensated by the charge imbalance relaxation in the superconductor such that there is a net-zero voltage and current across the entire junction.

In equilibrium, in a dissipationless state, only the first proposed mechanism can be present, as the second one is dissipative. Out of equilibrium, however, the story is different. With-



out external damping, a well-defined phase bias is no longer possible at finite voltages, as  $\frac{d\phi}{dt} = V = \frac{2e}{\hbar}$ . Nevertheless, there is a directional Meissner current at the NS interface due to the magnetic field, which would produce a current in the N layer if transmitted at the interface. Thus, the latter mechanism, which leads to a magnetic field dependent voltage offset should be relevant to Josephson diodes above the switching current. As a result, the current-voltage characteristic becomes non-reciprocal, meaning the differential conductance ( $\frac{dI}{dV}$ ) of the SNS junction becomes asymmetric.

To calculate the effect of finite momentum at finite bias voltages, a modification of the BTK theory will be presented in subsection 2.2.10. Before this, however, the effect of a momentum bias on the density of states will be illustrated using the Eilenberger theory.

### 2.2.9 Eilenberger quasiclassical theory of superconductivity: Finite momentum

The Eilenberger equation is useful in the clean limit, when scattering times are large compared to the coherence time. The Eilenberger equation is written as:

$$(-2iE + v_F \hat{v} \cdot \hat{\Pi})f = 2\Delta g + \frac{1}{\tau}(g\langle f \rangle - f\langle g \rangle), \quad (2.118)$$

with the normalization condition

$$g^2 + f f^\dagger = 1 \quad (2.119)$$

Here  $\tau = \frac{l}{v_F}$  is the scattering time,  $l_E$  is the mean free path and  $v_F$  is the Fermi velocity.

The bracket  $\langle \rangle$  denotes an average over the Fermi surface (thus over  $\hat{v}$ ). The operator  $\hat{\Pi}$  is equal to  $\nabla + i\frac{e}{\hbar}\vec{A}$ . In the absence of gradients in  $f$ , scattering and a vector potential, the equation is:

$$-2iEf = 2\Delta g, \quad (2.120)$$

which can be written out for  $f$ .

$$f = -\frac{\Delta}{iE}g \quad (2.121)$$

The normalization condition then reads:

$$g^2(1 - \frac{\Delta^2}{E^2}) = 1 \quad (2.122)$$

Resulting in:

$$g = \pm \frac{E}{\sqrt{E^2 - \Delta^2}} \quad (2.123)$$

This expression does not depend on velocity or position. This is the normal BCS Green's function, as expected. In the presence of finite momentum  $\vec{p}_S$ , the energy term is modified to  $E' = E + v_F p_S \cos(\nu)$ , with  $\cos(\nu) = \hat{v} \cdot \hat{p}_S$ . The result is a velocity direction dependent energy shift in the density of states.

$$g = \pm \frac{E + v_F p_S \cos(\nu)}{\sqrt{(E + v_F p_S \cos(\nu))^2 - \Delta^2}} \quad (2.124)$$

This shifts the energy gap up in the momentum direction and down in the anti-parallel direction. Here it should be noted that since electrons are negatively charged, the direction of charge current is opposite to the defined momentum direction. As such, the pairs of a momentum-biased superconductor can be considered finite-energy pairs. This should be contrasted with the Fulde-Ferrel and Larkin-Ovchinnikov (FF-LO) states, for which the pairing symmetry acquires finite momentum[101, 102]. These states are only stable at large magnetic fields. In both the finite-energy and FFLO cases, however, finite-energy pairs are expected, which are related to odd-frequency pairing[103, 104].

In the presence of scattering, the solution becomes complicated by the self-consistency condition. Since  $\langle f \rangle$  is proportional to  $\Delta$  and  $\langle g \rangle$  is proportional to  $-iE$ , the additions are roughly  $\frac{1}{\tau} \left( \frac{\Delta g + iE f}{\sqrt{E^2 - \Delta^2}} \right)$ . This addition is proportional to the velocity independent part of the Eilenberger equation with a factor  $\frac{1}{\tau \sqrt{E^2 - \Delta^2}}$ . Thus, disorder tends to increase the isotropic part of the Green's function in the Eilenberger equation. To first order, the energy scale at which velocity effects take place thus reduces by a factor proportional to  $\frac{1}{\tau \Delta}$ . At larger scattering rates, the dispersion becomes isotropic with broadening  $\Gamma = \frac{2}{3} (p_F v_S)^2 \tau$ [94].

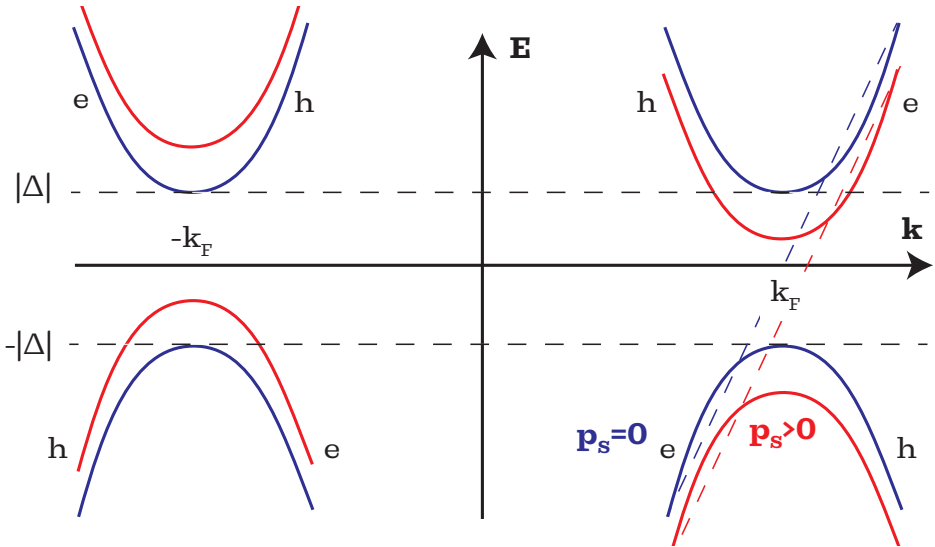


Figure 2.13: Diagram illustrating the low-energy dispersion relation of a normal BCS superconductor (blue) and a finite momentum superconductor in the momentum direction (red). Electron and hole quasiparticle branches are indicated. The dashed blue and red lines indicate the normal electron dispersion with zero momentum and finite momentum. Note that the minimum excitation energy is reduced in the forward direction.

### 2.2.10 Finite momentum BTK theory

The current-voltage relationship of an NS contact is well-described by the BTK theory. Here, a modified BTK theory will be presented where a finite momentum is introduced. Simulations using Kwant will be presented. Before this, the phenomenology will be discussed. The main contribution of finite momentum is an energy shift in the Andreev reflections. As a result of this, the maximum current at which Andreev reflections can occur differs for the forward and backward directions. Naively, this means that for fully transparent interfaces ( $Z = 0$ ) the deficit voltage difference at high bias and momentum  $q$  is equal to  $2v_F|q|$ . This deficit voltage difference saturates at large momentum scales, as for  $v_F|q| > |\Delta|$ , the superconductor becomes gapless at the Fermi energy. This means that either the amount of Andreev reflections is constant or scattering processes start to dominate and  $|q|$  can not exceed  $\frac{|\Delta|}{v_F}$ . At smaller momenta general, one expects to see gap edges at  $|\Delta| \pm v_F|q|$ , dispersing linearly with magnetic field down to zero voltage. At low bias voltages compared to  $\frac{|\Delta|}{e}$  and small momenta  $|q| \leq \frac{|\Delta|}{e}$ , Andreev reflections can happen for positive and negative bias voltages and thus the current-voltage relationship is symmetric in this regime.

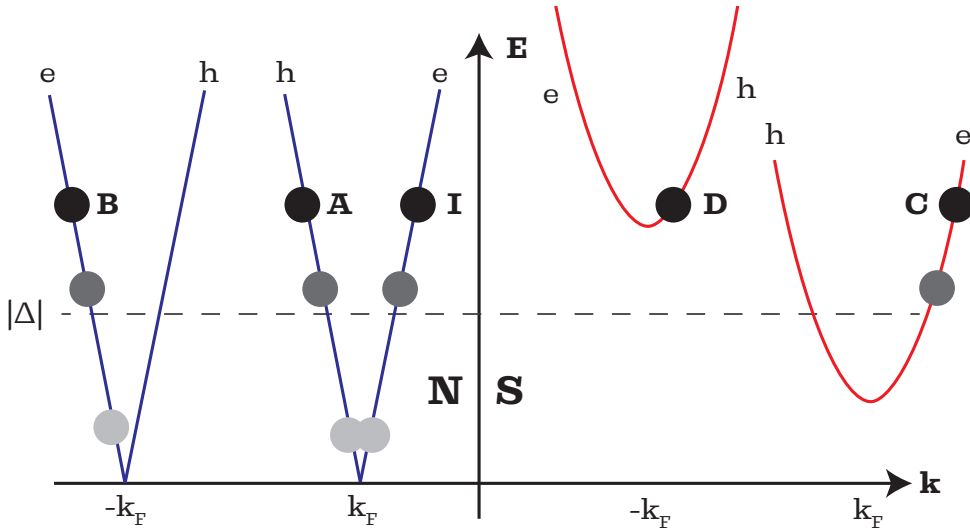


Figure 2.14: Diagram illustrating the scattering processes at an interface between a normal metal (N) and a finite momentum superconductor (S) at three different quasiparticle energies (shades of gray). The different scattering modes indicated are I : incident, A : Andreev reflected, B : normally reflected, C : transmitted into the electron-like branch, D : transmitted into the hole-like branch.

In what follows, it will be assumed that  $|q| = \frac{|\Delta|}{v_F}$ . Since  $|J_S| = n_S e |v_S|$ , we expect that an NS junction can see a gradual change from  $\vec{q} = 0$  to  $\vec{q} = \frac{|\Delta|}{v_F}$  if  $|J_S|$  is conserved and  $n_S$  is decreasing, which happens in a proximity junction.

In the tight-binding model, we simulate a 1D chain of sites (single channel). A finite region

is divided into a normal part, a barrier(2 sites) and a superconducting part. The kinetic energy is included as a hopping term  $-t\hat{\sigma}_z$  to nearest neighbor sites, where  $t$  is the hopping integral and  $\hat{\sigma}_z$  denotes the Pauli Z matrix in electron-hole space. At equilibrium, the on-site energy is  $(2t - \mu)\hat{\sigma}_z = 0$ . Superconductivity is included using an on-site term  $\Delta\hat{\sigma}_x$ . An on-site Dynes parameter is introduced in the superconductor as  $-1i\Gamma\hat{I}$  to incorporate relaxation processes in the superconductor. Finite momentum is introduced by adding a (forward) hopping term  $-iq_S\hat{I}$ , which is a discretized version of  $-i\hbar\frac{d}{dx}$ . Here we note that different dispersions (not finite momentum, but rather different diffusion coefficients) for electrons and holes could be simulated by instead adding a term  $-q_S\hat{I}$ .

Finally, the barrier is introduced using two sites in series. The first site is shifted up in on-site energy by an energy  $|H|\hat{\sigma}_z$  and the second site down in energy by  $-|H|\hat{\sigma}_z$  to maintain electron-hole symmetry.

N and S leads are connected on the left and right side of the 1D wire. The N lead has the same properties as the N part of the finite system. The S lead has the same properties as the S part of the finite system, except for the Dynes parameter, which is taken to be 0 in the extended part of the superconductor.

The system is solved by numerically computing the scattering matrix and taking the conductance through the usual BTK relation  $T = 1 + A - B$ , where  $A$  and  $B$  are the Andreev (e-h) and normal (e-e) reflection coefficients. Resulting plots for the normalized zero-temperature differential conductance at  $p_S = 0$  and  $p_S = \frac{\Delta}{v_F}$  for  $\Delta = 0.1t$ ,  $\Gamma = 0.033t$  and  $H = 0.3t$  using 9 N-sites and 9 S sites are shown in Figure 2.15a. Normalization was performed by dividing by the differential conductance at high bias. The differential conductance at  $p_S = 0$  is symmetric, as expected, while the differential conductance at  $p_S = \frac{\Delta}{v_F}$  is highly asymmetric, with Andreev reflections primarily happening for  $V > 0$ . For  $V < 0$ , the differential conductance decays to its normal state value slower than for  $V > 0$ , where a slight dip in the normalized differential conductance below 1 is observed.

The corresponding product of excess current and the normal state resistance is plotted in Figure 2.15b for  $p_S = -\frac{\Delta}{v_F}$ ,  $0$ ,  $\frac{\Delta}{v_F}$ . This shows that a finite momentum superconducting state in an NS junction results in an asymmetric excess current and deficit voltage versus bias voltage. The asymmetric component of the deficit voltage can be extracted by subtracting the two curves, which we will call  $\Delta I_{\text{excess}, p_S} R_N$ . This is plotted in Figure 2.15c. This function is parabolic at low bias voltages, becoming V-shaped at higher bias voltages. At  $|V| > \frac{2\Delta}{e}$ , the asymmetry saturates and slightly decreases. At  $|V| > \frac{4\Delta}{e}$ , the asymmetric component is roughly constant.

We define the diode efficiency as  $\eta = \frac{\Delta I_{\text{excess}, p_S}}{\Sigma I_{p_S}}$ , where  $\Sigma I_{p_S}$  denotes the field-symmetric part of the current. This is plotted in Figure 2.15d. The efficiency increases linearly around zero bias voltage until saturation at  $V = \frac{2\Delta}{e}$ . Since the excess current saturates at this point, the resulting efficiency then decays roughly as  $\frac{1}{V}$ . For the chosen simulation parameters, the defined diode efficiency is 8%.

In Figure 2.16, the plots of Figure 2.15 are repeated for the fully transparent case, with  $\Gamma = 0$  and  $H = 0$ . Here, the shift in the differential conductance is again visible and asymmetric deficit voltages result with a larger magnitude. In the positive momentum biased case, the maximum excess voltage observed is  $2\frac{\Delta}{e}$  and the minimum excess voltage is roughly  $-\frac{4}{5}\frac{\Delta}{e}$ , resulting in an efficiency of 20.5%

Finally, we note that in an SNS junction, MAR processes are also possible. According to the analysis by Zazunov[105], this could lead to Doppler shifts in the MAR signal. As a result, there are two sets of MAR peaks relating to forward and backward conduction at  $eV = \frac{2(|\Delta| \pm v_F p_S)}{ne}$ . Zazunov suggests that while the Josephson diode efficiency is limited to roughly 40%, the SNS diode efficiency in the voltage biased state can approach the ideal value of  $\eta = 1$ , in contrast to what was found for NS junctions in this section, which appear to saturate at 20%. If the average of the positive and negative excess currents is taken, the efficiency  $\eta' = \frac{\Delta I_{\text{exc}, p_S}}{\Sigma I_{\text{exc}, p_S}}$  can be calculated. This quantity saturates at roughly 40%.

### 2.2.11 Linear response kinetic theory of superconductors

Another way to understand asymmetric charge transport in superconducting junctions at finite bias is through a thermodynamic approach.

In superconductors out of equilibrium, one can consider small perturbations, as was done by A. Schmid[106]. In order to describe non-equilibrium dynamics, a description using a grand-canonical ensemble is taken. In an ordinary conductor, the macrostate can be described by only the electrochemical potential  $\mu$  and the temperature  $T$ . In a superconductor, however, there can also be a finite supercurrent density  $\vec{j}_S$  in equilibrium. Changes in internal energy density can be described by

$$d\epsilon = Tds + \mu dn + \frac{1}{e} \vec{j}_S \cdot d\vec{p}_S, \quad (2.125)$$

where  $\frac{1}{e} \vec{j}_S d\vec{p}_S = nm\vec{v}_S d\vec{v}_S$  is the change in the volumetric density of kinetic energy in the supercurrent. This equation can be rewritten to express changes in entropy density in terms of thermodynamic quantities and generalized forces:

$$dS = \left(\frac{1}{T}\right)d\epsilon + \left(\frac{-\mu}{T}\right)dn + \left(\frac{-\vec{j}_S}{eT}\right) \cdot d\vec{p}_S. \quad (2.126)$$

Thus, in a superconducting junction, the presence of a supercurrent density results in a generalized potential proportional to  $\frac{\vec{j}_S}{T}$ . The potentials can be related to generalized forces, which drive non-equilibrium currents. In the linear regime, Onsager's relations describe how the generalized forces drive the currents. Next, a derivation of these relationships will be given. It will be shown that the addition of a divergence in the supercurrent density results in a deviation from Ohm's law.

Using the continuity relation  $\frac{\partial u}{\partial t} + \nabla \cdot (\vec{j} + \hat{\vec{j}}) = 0$ , where  $u$  denotes the quantity,  $\vec{j}$  denotes the equilibrium flow and  $\hat{\vec{j}}$  denotes the non-equilibrium perturbation, it can be shown that

the entropy production is of the form  $\sigma = \vec{F} \cdot \hat{\vec{j}}$ , with  $\vec{F} = \begin{bmatrix} \nabla \frac{1}{T} \\ \nabla \frac{\mu}{T} \\ \nabla \cdot \frac{-\vec{j}_S}{eT} \end{bmatrix}$  and  $\hat{\vec{j}} = \begin{bmatrix} \hat{j}_\epsilon \\ \hat{j}_n \\ \hat{\mu} \end{bmatrix}$

Where the last relation holds due to the equation of motion  $\frac{\partial \vec{p}_S}{\partial t} + \nabla(\mu + \hat{\mu}) = 0$ . This is the flow equation for the superconducting phase gradient, since  $\vec{p}_S = m\vec{v}_s = m\nabla\phi$ .

The important takeaway at this point is that the divergence of the supercurrent density provides a thermodynamic force, which acts on the energy flow, the particle flow and, most of all, on the electrochemical potential. A divergence of the supercurrent can only happen if the supercurrent is converted to a normal/quasiparticle current. As already seen in the last sections, the process of generating non-equilibrium quasiparticles and shifting the chemical potential results in charge and branch imbalance and the observation of excess currents.

In irreversible systems close to equilibrium, the linear response relation  $\vec{j} = L\vec{F}$  is assumed to hold, where  $L$  is a positive definite (To ensure  $ds > 0$ ) matrix of coefficients. As long as there is no magnetic field, the Onsager reciprocity relations hold.  $\epsilon$  and  $n$  are even functions under time reversal, whereas  $\vec{p}_S$  is odd. As a result,  $L_{12}(\vec{p}_S) = L_{21}(-\vec{p}_S)$  and  $L_{13}(\vec{p}_S) = -L_{31}(-\vec{p}_S)$  (and the same holds for  $L_{23}$ ). However, since  $L_{12}$  is scalar and  $L_{13}$  and  $L_{23}$  are vectors parallel to  $\vec{p}_S$ , the first should be an even function of  $\vec{p}_S$  and the latter two should odd. Thus the matrix  $L$  has the property that  $L_{\alpha\beta}(\vec{p}_S) = L_{\beta\alpha}(\vec{p}_S)$ .

This allows for expressing energy, particle and momentum flow in terms of generalized forces. It can be more convenient to rewrite this such that the force is expressed as

$$\tilde{\vec{f}} = -\nabla \begin{bmatrix} T \\ \mu \\ \vec{j}_S \end{bmatrix}.$$

Such a transformation can be performed by noting that  $\nabla \frac{1}{T} = -\frac{1}{T^2} \nabla T$ ,  $\nabla(\frac{-\mu}{T}) = -\frac{1}{T} \nabla \mu + \frac{\mu}{T^2} \nabla T$  and  $\nabla \cdot (\frac{-\vec{j}_S}{eT}) = -\frac{1}{eT} \nabla \cdot \vec{j}_S + \frac{\vec{j}_S}{eT^2} \cdot \nabla T$

In this case, the thermodynamic current can be expressed as:

$$\tilde{\vec{j}} = \begin{bmatrix} \vec{q} \\ -\frac{T}{e} \hat{\vec{j}}_n \\ -\frac{\hat{\mu}}{e} \end{bmatrix}, \quad (2.127)$$

with  $\vec{q} = \hat{j}_\epsilon + \frac{\mu}{e} \hat{j}_n + \frac{\hat{\mu}}{e} \vec{j}_S$  denoting the heat current.

Introducing  $\tilde{\vec{j}} = M\tilde{\vec{f}}$  with the same properties as  $L$ , the matrix can be expressed as:

$$M = \begin{bmatrix} \kappa & \sigma\alpha & \beta\vec{p}_S \\ \sigma\alpha & \sigma & \gamma\vec{p}_S \\ \beta\vec{p}_S & \gamma\vec{p}_S & \zeta \end{bmatrix} \quad (2.128)$$

Using  $\vec{E}_N = -\frac{1}{e}\nabla\mu$ , we can now express the main result:

$$\vec{q} = \kappa(-\nabla T) + \sigma\alpha T(e\vec{E}_N) + \beta\frac{T}{e}\vec{p}_S\nabla\cdot(-\vec{j}_S), \quad (2.129)$$

$$\hat{j}_n = \sigma\alpha(-\nabla T) + \sigma\vec{E} + \gamma\vec{p}_S\nabla\cdot\vec{j}_S, \quad (2.130)$$

$$\hat{\mu} = \beta\vec{p}_S\cdot(-\nabla T) + e\gamma\vec{p}_S\cdot\vec{E} + \zeta\frac{1}{e}\nabla\cdot\vec{j}_S. \quad (2.131)$$

The interpretation of these equations is as follows. The first equation describes heat transport through thermal conductivity  $\kappa$ , thermoelectric coefficient  $\alpha$  and thermal branch imbalance generation coefficient  $\beta$ . Heat flows from high to low temperatures, in the direction of electric fields and in the direction of conversion of supercurrent to quasiparticle current. The second equation describes the flow of quasiparticle charges due to thermoelectric coefficient  $\alpha$ , electrical conductivity  $\sigma$  and field-driven branch imbalance generation coefficient  $\gamma$ . Finally, the non-equilibrium chemical potential can be changed by branch imbalance generation by thermal gradients, branch imbalance generation by electric fields parallel to supercurrent (related to supercurrent to quasiparticle current conversion) and due to the second viscosity  $\zeta$ , which is related to charge imbalance generation and relaxation by the pairing mechanism.

This phenomenological linear response kinetic theory by A. Schmid highlights the possible transport mechanism close to equilibrium in superconducting systems. Notably, excluding thermal effects, there are three non-equilibrium effects. The first is normal Ohmic conduction. The second is the creation of a voltage by supercurrent to quasiparticle conversion (as occurs in BTK theory). The third effect, which, as far as I am aware, has not been observed or recognized yet, is the creation of voltages and currents at NS interfaces when electric fields and superfluid momentum are large. The non-equilibrium theory reveals an interplay between the driven condensate and driven quasiparticles without resorting to a particular geometry.

As seen in the extended BTK formalism, a finite momentum state created by a magnetic field might produce asymmetric current versus voltage characteristics. The analysis based on Onsager reciprocity does not necessarily hold when a magnetic field is present. In these situations it is expected that the applied vector potential  $\vec{A}$  adds to the condensate momentum. An analysis of Onsager's relations for electrical conduction with magnetic fields results in  $M_{\alpha\beta}(\vec{B}) = M_{\beta\alpha}(-\vec{B})$ , which implies that the symmetric part of the generalized force matrix is even, and the antisymmetric part is odd in  $\vec{B}$ [107]. Anticipating an effect that is linear in  $\vec{B}$  (which is the first order term), we obtain

$$\hat{j}_n = \sigma \vec{E} - e\delta \vec{A} \nabla \cdot \vec{j}_S, \quad (2.132)$$

$$\hat{\mu} = e^2 \delta \vec{A} \cdot \vec{E} + \zeta \frac{1}{e} \nabla \cdot \vec{j}_S, \quad (2.133)$$

where a new constant  $\delta$  (which should be similar to  $\gamma$ ) was introduced for the antisymmetric part. The result is an additional current that is proportional to the applied magnetic field, with  $|\vec{B}| = |\vec{A}|t$ , where  $t$  is a thickness/length scale. It is also proportional to the normal excess current/voltage term  $\nabla \cdot \vec{j}_S$ .

As a final note, we mention that technically, the kinetic energy contribution to the supercurrent  $n_S \frac{mv_S^2}{2}$  is:

$$d\epsilon = n_S m \vec{v}_S \cdot d\vec{v}_S + \frac{m}{2} \vec{v}_S \cdot \vec{v}_S dn_S \quad (2.134)$$

The first term is the term investigated by Schmid and relates to the velocity of the superfluid, while the second term relates to changes in the pair density. This term can be accounted for by replacing  $\mu dn \rightarrow \mu dn_N + (\mu + \frac{mv_S^2}{2}) dn_S$ . Further theoretical work on this term is necessary to understand how it would modify the kinetic equations.

### 2.2.12 Self-field effects

The self-field effect in Josephson junctions arises from the magnetic field produced by the bias current. In order for this effect to be significant, the magnetic flux produced needs to be comparable to the applied magnetic field. Qualitatively, one may understand the self-field effect by considering an SNS sandwich Josephson junction. In such a sandwich, the direction of the return path with respect to the incident path can be chosen. For simplicity, we consider here parallel and anti-parallel current paths.

In the case of a parallel path, the magnetic flux generated by the two superconducting wires adds up to 0. Hence, we expect no self-field effect in this geometry.

On the other hand, for anti-parallel currents, a net magnetic field results in the SNS junction. Hence, we may say that there is an effective magnetic field equal to  $B_{\text{eff}} = B + \alpha I$ . For a loop of current with radius  $r = 50$  nm, the magnetic field scale is roughly  $\alpha = \frac{\mu_0}{r} \approx 25 \frac{\text{T}}{\text{A}}$ . For a current on the order of 1  $\mu\text{A}$ , this is on the order of 25  $\mu\text{T}$ .

Most samples studied in this thesis are planar and could be considered parallel, but can be considered to have a radius of curvature on the order of 50 nm. As such, self-field effects can not be excluded on the basis of geometrical arguments. A way to distinguish self-field effects from the finite momentum explanation caused by the Meissner effect is still possible, however. Self-field effects scale with current, as  $B_{\text{self}} = \alpha I$  and thus tend to result in a constant skewing as a function of current. As a function of voltage, however, the self-field effect should scale as  $\frac{1}{R}$ . Thus measurements at constant voltage in a device where  $R$  can be varied (For example, by electromigration of SNS junctions, as presented in chapters 6 and 7 of this thesis) allow for determining whether asymmetric conductance can potentially be attributed to self-field effects or not.



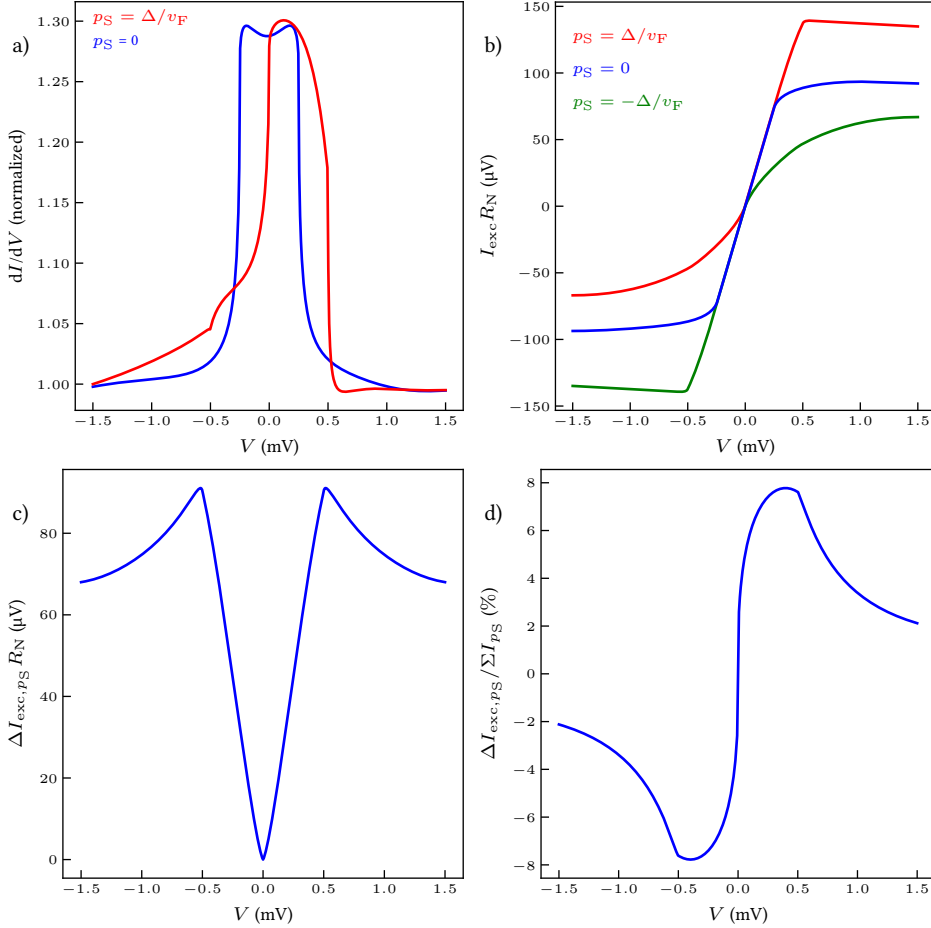


Figure 2.15: Finite momentum BTK simulations run with parameters  $\Delta = 0.1t$ ,  $\Gamma = 0.033t$ ,  $H = 0.3t$ , 9 N-sites and 9 S sites. Voltages and currents were re-scaled such that  $\Delta = 250 \mu\text{eV}$ . a) Normalized differential conductance versus bias voltage at  $p_S = \frac{\Delta}{v_F}$  and  $p_S = 0$ . Normalization is performed at the maximum bias voltage. b) Deficit voltage  $I_{exc} R_N$  versus bias voltage at  $p_S = \frac{\Delta}{v_F}$ , 0,  $-\frac{\Delta}{v_F}$ . c) Difference between the deficit voltage at  $p_S = \frac{\Delta}{v_F}$  and  $p_S = -\frac{\Delta}{v_F}$  plotted as a function of bias voltage. d) Asymmetry of the excess current divided by the average bias current plotted as a function of voltage.

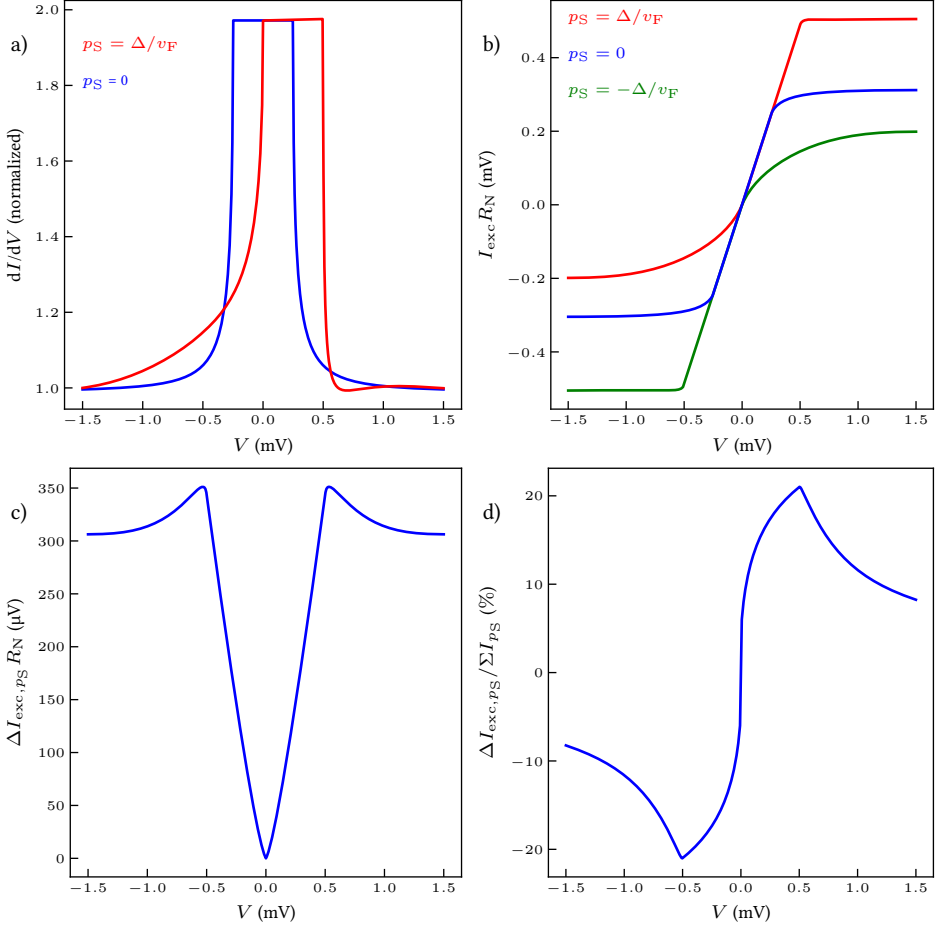


Figure 2.16: Finite momentum BTK simulations run with parameters  $\Delta = 0.1t$ ,  $\Gamma = 0$ ,  $H = 0$ , 9 N-sites and 9 S sites. Voltages and currents were rescaled such that  $\Delta = 250$   $\mu$ eV. a) Normalized differential conductance versus bias voltage at  $p_S = \frac{\Delta}{v_F}$  and  $p_S = 0$ . Normalization is performed at the maximum bias voltage. b) Deficit voltage  $I_{exc}R_N$  versus bias voltage at  $p_S = \frac{\Delta}{v_F}$ , 0,  $-\frac{\Delta}{v_F}$  c) Difference between the deficit voltage at  $p_S = \frac{\Delta}{v_F}$  and  $p_S = -\frac{\Delta}{v_F}$  plotted as a function of bias voltage. d) Asymmetry of the bias current divided by the average bias current plotted as a function of voltage.

## 3

## 3

## Fabrication

*In this chapter, the cleanroom fabrication of the nanogap devices and SNS junctions found in this thesis will be discussed. First, a general discussion will be presented regarding the design considerations for each type of device. After this, a formulaic recipe will be given. Next, a few experimental procedures will be elaborated, such as the transfer of graphene nanoribbons. Lastly, I will discuss symptoms related to imperfections and limitations of the cleanroom recipes.*

### 3.1 Design considerations for nanogap electrodes for graphene nanoribbons

The integration of bottom-up surface synthesized graphene nanoribbons into electrically conductive devices presents a major nanofabrication challenge. There are multiple reasons for this, which are listed below:

- The graphene nanoribbons produced by the atomically precise on surface synthesis method typically have a length of 50 nm or shorter, often being shorter than 20 nm. These length scales are close to the limit of what is possible by e-beam lithography.
- Graphene nanoribbons made on atomically flat surfaces are almost always grown on gold. Because of this, conventional graphene nanoribbon transfer methods use gold etchants, which are harmful to many metal electrodes.
- Atomically precise graphene nanoribbons are limited in width by the synthesis method. For this reason, they generally have band gaps on the order of 1 eV or larger. In devices with metal electrodes, the semiconducting behavior of graphene nanoribbons is expected to result in Schottky barrier limited injection at the metal-GNR interface.

The first two points listed present necessary conditions for the production of any GNR device. Devices should survive the GNR transfer method and the source and drain electrodes should ideally have a separation that is smaller than the average GNR length.

The third point, on the other hand, is important for the improvement of the electronic injection. This is especially important at low temperatures, as a large injection barrier at the metal-GNR interface prevents direct tunneling into or through the GNRs.

A gate electrode and dielectric are also necessary, as GNRs are semiconductors. For efficient electric conduction, the valence or conduction band of the GNR must align with the electrochemical potential of the metal, while the chemical potential of undoped GNRs is expected to lie in the middle of the band gap. Thus, a voltage on the gate electrode needs to be applied to tune bands in the energy of the bands in the GNR to resonance.

In practice, this means that atomically precise graphene nanoribbon devices require electrodes with nanometer-scale separation, which will be referred to as nanogap electrodes. These electrodes should be compatible with GNR transfer protocols.

## 3

### 3.2 Design considerations for nanogap electrodes

To contact nanoscale objects electrically, metallic probes separated by only several nanometers to tens of nanometers are required. Here, the fabrication of nanogap electrodes through direct writing by e-beam lithography and lift-off is described.

Nanogap electrodes are electrodes with a separation,  $d$ , called the gap size, of only several nanometers. Besides the gap size, the geometry and material of nanogaps can be varied. Also, the gap width,  $W$ , can be varied. Depending on the ratio between the gap size and width, a classification between wide nanogaps, with  $W \gg d$ , and narrow/needlelike nanogaps, with  $W \leq d$ , can be made. There are benefits and drawbacks to both geometries. The wide nanogaps have a larger probability of making electrical contact with nanoscale objects by virtue of the large contact area. Hence, even a disperse coverage with nanoscale objects could result in some nanoscale objects being trapped. Needle-like nanogaps, on the other hand, require significantly higher coverage of the surface to obtain the same yield of devices. For GNRs, this means the following: Since GNR growth results in a relatively large coverage, needle-like nanogaps have a larger probability of trapping single ribbons, while wide nanogaps instead are likely to trap multiple in parallel. A minor point to make is that needlelike nanogaps also have favorable electrostatics. Their narrow width results in less screening of the electric field applied by a gate electrode, as the electric field can also wrap around[108]. This improves the gate coupling, making this source-drain electrode geometry more useful for nanoscale field effect transistor (FET) devices.

For the practice of e-beam lithography, a needlelike gap can be made with a significantly smaller separation than a wide gap. For needlelike gaps, the minimum reproducible gap size is on the order of 6 to 10 nm. Meanwhile, for wide nanogaps, this is approximately 20 to 30 nm. But why is this? While the needlelike nanogaps are limited by the e-beam exposure and film structure of the resist, wide nanogaps are instead limited by collapse of the resist mask[109, 110]. Since the gap separation  $d$  is small, the developed resist mask at the gap forms a narrow wall, with width  $d$  and height  $h$ . During drying after development, the resist mask is exposed to a liquid-gas interface. In this process, the surface tension pulls on the resist mask with a force proportional to  $h$ , inducing bending proportional to  $h^2$ . The restorative force/tension in the resist is proportional to  $d$ . For a typical resist film thickness of 60 to 80 nm, this limits the separation to approximately 20 to 30 nm. Dilution

of the resist might allow for a thinner resist film of 30 nm. This could help to resolve this, but should make lift-off trickier. For both the wide and needlelike nanogaps, a thin resist (thickness of 60 to 80 nm) was used.

The distinction between the failure mechanisms determines the strategy which is best to utilize to minimize the gap size. For the needlelike nanogaps, the contrast, how sharply the e-beam dose defines height variations of the resist, is the most important factor. For wide nanogaps, however, while contrast is still important, the strength of the resist (the yield strength for plastic deformation or the elastic modulus if the resist bends and then sticks to the wafer surface) and adhesion of the resist to the substrate could be more important than the contrast. For all nanogap devices in this thesis, the high-resolution/high-contrast and high-sensitivity (low-dose) resist CSAR-62 was used. However, as indicated above, the recipe for the wide nanogaps differs from the recipe for the needlelike gaps.

For needlelike gaps, a cold development strategy was used. By developing at a lower temperature, the contrast of the resist recipe can be enhanced. The development process is the process of dissolving polymer chains that have been cut down by e-beam exposure. The kinetics of this (non-equilibrium) process are temperature ( $T$ ) dependent, approximately scaling with a Boltzmann factor  $e^{-\frac{E_A}{k_b T}}$  [111, 112].  $E_A$  in this formula is an activation energy, which depends on the length distribution of the polymer chains.  $k_b$  is the Boltzmann constant. When the activation energy is positive and the temperature is reduced, the Boltzmann factor decreases. However, the dependence of the Boltzmann factor on the activation energy and hence on size/dose dependence increases. As a result, the development can now only remove smaller polymer chains more selectively. Hence, the contrast is enhanced. For this reason, the developer used for CSAR-62, pentyl acetate, was cooled down to  $-16^\circ\text{C}$  in a freezer. The beaker into which the developer is poured was also pre-cooled in the freezer and the full development process was executed in less than 90 seconds to avoid heating of the developer. The temperature of the developer over time was characterized using a thermometer. After 90 seconds, the developer reached a temperature of approximately  $-6^\circ\text{C}$ . After development, great care should be taken not to let the sample dry. When the sample dries, water vapor may condense and freeze onto the silicon oxide and resist mask, which will deform the resist mask. For this purpose, the sample was sprayed with isopropyl alcohol during removal of the sample from the cold pentyl acetate. It was found that the cold strategy approximately doubles the required doses in e-beam exposure, compared to the conventional development of CSAR-62 with pentyl acetate in standard cleanroom conditions.

The writing strategy for the needlelike nanogaps revolves around creating optimal contrast at the gap region. For this purpose, an overdose-undersize (ODUS, with a dose factor of 2.0) procedure was used with a shape proximity effect correction (shape PEC). The aim behind this is to optimize the exposure such that the dose profile matches the point spread function (PSF) of the beam as closely as possible, which should result in an optimal exposure. The gap size was also slightly increased in the pattern over the desired size and the structure was slightly overexposed.

The wide nanogaps were made using the conventional development process in pentyl acetate, defining the gaps with a distance of 30 nm. The reason for this choice over cold

development, which has better contrast, is that excess e-beam exposure results in more scission, which could hurt the structural integrity of the resist.

### 3.3 Superconductor - normal metal - superconductor junctions

The superconductor - normal metal - superconductor (SNS) junctions in this thesis were designed with two objectives in mind. Firstly, the proximity effect should be optimized. That is, the induced proximity gap in the normal metal should be maximized. Secondly, it should be possible to break the normal metal in the junction through electromigration. Hence, we will refer to these as SNS electromigrated break junction (SNS-EMBJ) devices. Below, I will discuss how the design choice was made in this thesis.

In order to optimize the proximity effect, it is important to optimize three things. Firstly, the superconductor should be 'strong' enough to proximitize the normal metal. The 'strength' of the proximity effect can be viewed as the dilution of superconducting correlations in the boundary region between the superconductor and the normal metal. Beyond the boundary region, the correlations decay into the normal metal. The extent of the boundary region into the superconductor is on the order of the coherence length  $\xi_S$ , which for a dirty film (a film with a mean free path below the BCS coherence length without scattering) scales with the diffusion coefficient (conductivity) of the metal. Within the boundary region, there is a density of superconducting carriers,  $n_S$ . The ideal superconductor has a large boundary region, with many carriers. In this thesis, devices were made with Al and Nb (MoRe and NbTiN are also candidate superconductors). Al has a large BCS coherence length of 1600 nm[39]. Thus, in principle, it could be an ideal superconductor. In practice, however, thin films of Al are in the dirty limit and can have a coherence length that is orders of magnitude smaller, less than 100 nm[113]. Al also has a low carrier density and critical temperature,  $T_{c,Al} \approx 1.2$  K. SNS junctions made with Al as the superconductor and Pd as the normal metal were not found to be superconducting in this thesis. Thus, in this thesis, Nb was used with a coherence length on the order of 10 nm and a relatively large carrier density due its d-orbitals.

Although Au and Pd are chosen in this thesis, the design choice of the normal metal for an optimal SNS junction should follow the same logic as that for the superconductors. Ideally, the normal metal has a low carrier density. This is the case for Au, but not for Pd, which has a carrier density exceeding that of both Al and Nb. Given thin films of Au and Pd with the same mean free path, the proximity effect into the Pd film is expected to be significantly weaker. Following the design logic for the superconductors, the coherence length in the normal metal should be chosen to be small for optimal mixing. Although this is true for the mixing, the decay of correlations into the normal metal is also determined by the coherence length. For this reason, a large coherence length is instead desirable. Improving the propagation of correlations into the normal metal thus always worsens the mixing by increasing the volume of normal metal included in the boundary layer. This problem can be solved by minimizing the volume of the normal metal within a coherence length from the boundary. For a thin film, this implies that the thickness of the normal metal should not be chosen too thick. Since the electronic mean free path of the thin film also depends

on the thickness, there is likely an optimal thickness. In this thesis, a thickness of 13 nm was used for Pd and a thickness of 13 to 15 nm for Au. For Au in particular, a thicker film could improve the diffusivity considerably. Finally, the length-scale of the normal metal,  $L$ , should be chosen as small as possible. Ideally, the length-scale is smaller than the coherence length to minimize the decay. In this thesis,  $L = 50$  nm is chosen, though  $L = 30$  nm was found to be achievable.

Finally, the interface between the superconductor and the normal metal should be electrically transparent in order to allow for efficient mixing of carriers with the normal metal. This motivated using a single step recipe, in which minimal oxidation or contamination would be present at the interface. A double-layer resist mask, consisting of a thin layer of Poly(methyl methacrylate) with a molecular weight of 950K (PMMA-950K) on top of a thicker layer of Poly(methyl methacrylate - methacrylic acid) (p(MMA-MAA)) co-polymer was used, as shown in Figure 3.1a. The more sensitive p(MMA-MAA) layer is fully developed at a lower exposure dose than the PMMA layer. This results in an undercut profile, in which the PMMA forms an overhang where the bottom co-polymer layer is removed. By evaporating at an angle, metal can be deposited below this overhang, in a process known as shadow-mask evaporation, which is illustrated in Figure 3.1b. A full SNS junction can be made by defining a pattern with two closely spaced regions, such that the p(MMA-MAA) fully develops between them, but the PMMA layer does not, as shown in Figure 3.1c. Then, an SNS junction can be made on an  $\text{SiO}_2$  surface by first evaporating an adhesion layer (Ti here) without an angle. Next, the normal metal (Pd here) can be evaporated at an angle  $\theta$  into the undercut. To complete the normal metal layer, the normal metal is next deposited at an angle  $-\theta$ . By finally depositing the superconductor (Nb here) without an angle, a full SNS junction is made. The resulting device is shown schematically in Figure 3.1d. It consists of a constriction in the normal metal (Au/Pd here) and Ti + Au/Pd + Nb banks. Due to the double angle shadow evaporation step, the thickness of the normal metal doubles in the Ti + Au/Pd + Nb banks doubles further into the banks.

For the optimization of electromigration, it is desirable that the junction breaks at a specific point in the normal metal. Since electromigration happens through scattering processes of electrons on atoms in combination with heat, ideally the current density should be large at this point in the normal metal. Furthermore, there should be no other place in the device which dominates the heating. In terms of the design, this leads to the choice of a constricted geometry for the normal metal, where the current ideally converges to a single point. For the shadow evaporation technique described above, this means that the chosen pattern consists of two triangles with vertices facing each other. The evaporation angle and spacing between the triangular patches should be tuned in order to define the constriction as sharp as possible.

Finally, a few final remarks regarding the design choices. Although evaporation in the same step should optimize interfaces, the choice to evaporate Nb on top of the normal metal could lead to implantation of the Nb into the normal metal. This could, as seen in the PhD thesis of Sophie Guéron[42], lead to an energy gap in the normal metal that differs from the expected shape for a normal diffusive NS interface. In addition, alloying of the three deposited layers could locally introduce more scattering. For electromigration, this could lead to electromigration of the normal metal close to the NS interface. An optimal

process should aim to avoid this.

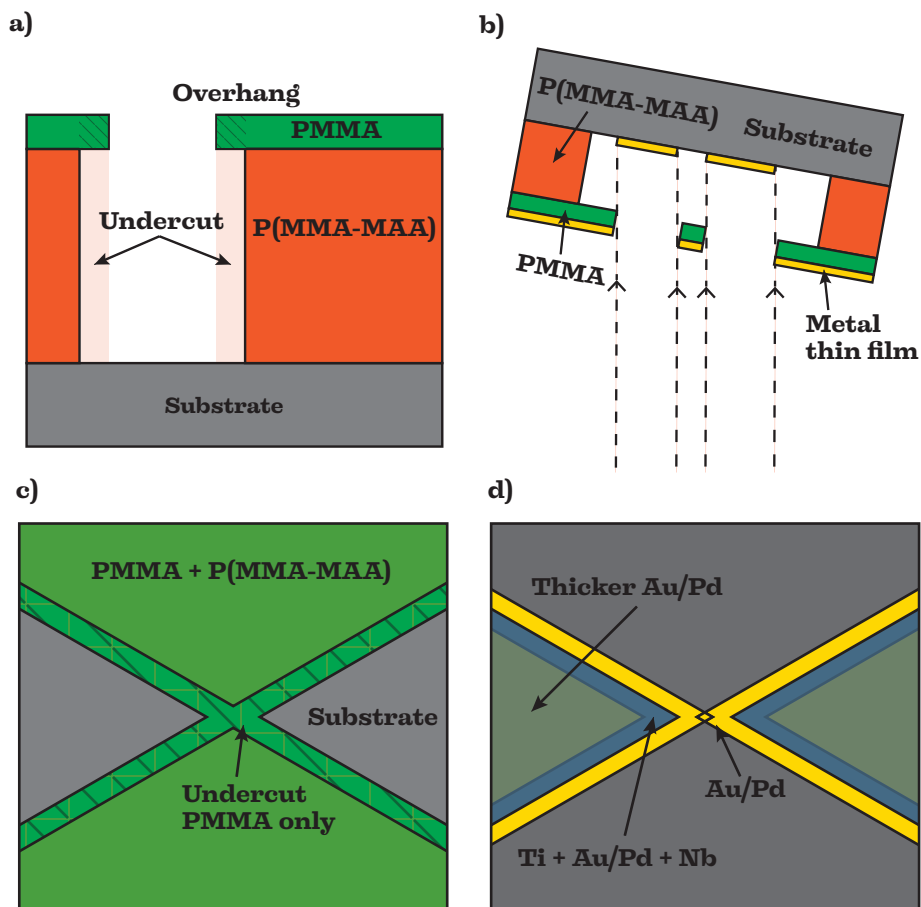


Figure 3.1: a) Schematic of the vertical cross-section of a developed PMMA/P(MMA-MAA) double-layer resist mask. The PMMA (green) top layer defines an overhang (hatched area). Underneath this, the P(MMA-MAA) (orange) is developed away, defining the undercut resist profile. In this region, the substrate (gray) is only shadowed by the PMMA overhang. b) Diagram illustrating the shadow mask angular evaporation technique. By tilting the substrate, the metal thin film (gold/yellow) can be evaporated into the undercut regions. c) Schematic of the top view of the resist prior to evaporation. In the hatched green area, the P(MMA-MAA) co-polymer resist is developed, leaving the substrate shadowed by the PMMA overhang. d) Schematic of the top view of the resulting SNS EMBJ device after lift-off of the resist. The normal metal, Au or Pd, that has been evaporated two times, once at a positive angle and once at a negative angle, is shown in gold color. In the blue regions, a Ti sticking layer is covered by a single layer of Au/Pd, which in turn is covered by a layer of superconductor, Nb. Further away, in the gold-shaded blue areas, the Au/Pd is deposited twice, resulting in a Ti+Au/Pd + Nb layer where the Au/Pd thin film is twice as thick.



## 3.4 Recipes

In this section, formulaic recipes are given for the recipes used in this thesis to fabricate the various devices. The e-beam exposure doses indicated in these recipes are to be used as guidelines. For fine patterns, performing a dose test is recommended.

### 3.4.1 Cleaning of SiO<sub>2</sub> chips prior to processing

For the pre-fabrication cleaning of silicon oxide wafers, cleaning with red fuming nitric acid was performed. This was preferred over solvent cleaning, which might leave polymer residues on the oxide surface. No special care was taken to minimize inorganic residues, such as iron (oxide). Prior to spin coating, stored samples were exposed to an O<sub>2</sub> plasma to clean off organic contamination and improve wetting of the resist during the spin-coating process.

1. Cleaning:
  - Fuming nitric acid cleaning for 5 minutes
2. Cleaning (prior to spin coating):
  - (a) O<sub>2</sub> plasma cleaning in a barrel etcher (Tepla 2) for 5 minutes
    - Power: 600 W
    - Flow: 600 sccm
    - Pressure: 1660  $\mu$ bar

### 3.4.2 Wide nanogap electrodes

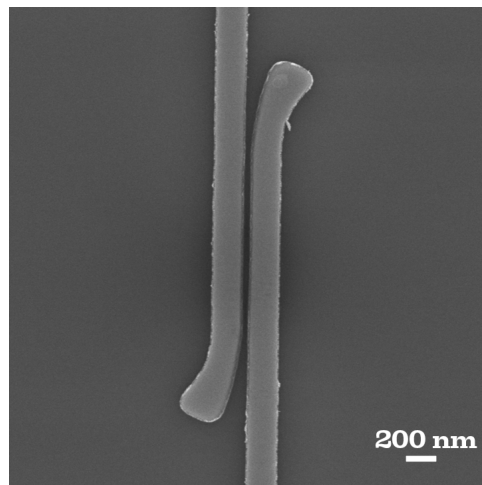


Figure 3.2: SEM image of wide nanogap MoRe electrodes.

The recipe for producing the wide nanogap MoRe electrodes, shown in Figure 3.2, is as follows:

### 3

1. Spin coating of resist CSAR-62/AR-P 6200.04:
  - Spin speed: 4000 rpm (approximately 80 nm)
  - Bake temperature and time: 185 °C for 3 minutes
2. E-beam exposure with Raith EBPG-5200 with an acceleration voltage of 100 kV:
  - (a) Coarse pattern:
    - Aperture: 400  $\mu\text{m}$
    - Beam current: As large as possible  $\sim 100$  nA
    - Dose: 300  $\mu\text{C}/\text{cm}^2$
  - (b) Fine pattern:
    - Aperture: 200  $\mu\text{m}$
    - Beam current:  $\sim 1$  nA (spot size of  $\sim 5$  nm)
    - Dose: 300-350  $\mu\text{C}/\text{cm}^2$
3. Development:
  - 1 minute in Pentyl acetate
  - 5 seconds in Xylene (Descum with a stronger developer. methyl isobutyl ketone (MIBK) could also work); spray with isopropyl alcohol (IPA) while removing the chip.
  - Soak in IPA for 30 seconds; spray with IPA while removing the chip
  - Blow-dry with an  $\text{N}_2$  gun
4. Metal deposition (either sputtering or e-beam evaporation):
  - (a) Sputtering of MoRe in Alliance Metal 2
    - Power: 100 W
    - Pressure: 15  $\mu\text{bar}$  (Pressure can be lowered to 2  $\mu\text{bar}$ )
    - Time: 1 minute and 20 seconds; The time was varied to obtain a thickness of 25 nm
5. Lift off:
  - Soak sample in N-Methyl-2-pyrrolidone (NMP) at 70 °C for approximately 30 minutes (Until the mask and metal on top is removed)
    - Use a holder to place the sample vertically

- Use mild ultrasonication (power 1-4) or blow with a pipette to remove the metal film
- Alternative lift-off solvent to NMP: AR 600.71 at 40 °C
- Let the beaker with NMP cool in room temperature water for ~ 5 minutes
- Move the sample to a second beaker of NMP for cleaning: 15 minutes at 70 °C
- Let the beaker with NMP cool in room temperature water for ~ 5 minutes
- Remove the sample from the NMP while spraying IPA; move the sample to a beaker of IPA
- Remove samples from IPA, spray with IPA upon removal.
- Blow-dry with an N<sub>2</sub> gun

### 3.4.3 Cold development CSAR-62 recipe for needlelike nanogap electrodes

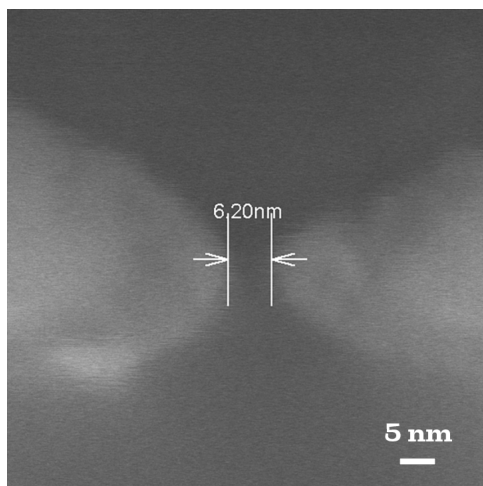


Figure 3.3: SEM image of needlelike MoRe nanogap electrodes.

The recipe for the needlelike nanogaps follows the recipe for the wide nanogaps, with the exception of the cold development step. Here, the recipe that yields the needlelike nanogap MoRe electrodes, shown in Figure 3.3, is detailed.

1. Spin coating of resist CSAR-62/AR-P 6200.04:
  - See wide nanogap recipe

2. E-beam exposure with Raith EBPG-5200 with an acceleration voltage of 100 kV:

(a) Coarse pattern:

- Aperture: 400  $\mu\text{m}$
- Beam current: As large as possible  $\sim 100$  nA
- Dose: 600  $\mu\text{C}/\text{cm}^2$

(b) Fine pattern:

- Aperture: 200  $\mu\text{m}$
- Beam current:  $\sim 1$  nA (spot size of  $\sim 5$  nm)
- Dose: 1000-2000  $\mu\text{C}/\text{cm}^2$  (increasing the dose shrinks the gap size)

3. Development:

- Put a labeled beaker in a  $-16$  °C freezer at least 30 minutes prior to development, ideally before e-beam exposure
- Prepare the wet bench closest to the fridge for the development process
- Take the beaker and cold pentyl acetate from the freezer and fill the beaker with pentyl acetate
- Develop the pattern for 1 minute in the cold pentyl acetate; spray with IPA while removing the chip
- Soak in a beaker of IPA for 30 seconds; Spray with IPA while removing the chip
- Blow-dry with an  $\text{N}_2$  gun

4. Metal deposition:

- See wide nanogap recipe

5. Lift off:

- See wide nanogap recipe

### 3.4.4 TiPt gate electrodes with $\text{HfO}_2$ gate dielectric

The fabrication of the gate electrodes follows the recipe for the wide nanogaps. The only deviation from the recipe is that 5 nm Ti and 10 nm Pt are e-beam evaporated in the AJA MB evaporator. The chosen evaporation rate is 0.5  $\text{\AA}/\text{s}$  for both layers. The gate electrodes in this thesis are considered coarse patterns.

A 12 nm thick  $\text{HfO}_2$  gate oxide is deposited by atomic layer deposition (ALD). Prior to this deposition, the TiPt gate electrodes were exposed to oxygen plasma cleaning in a barrel etcher (Tepla 1).

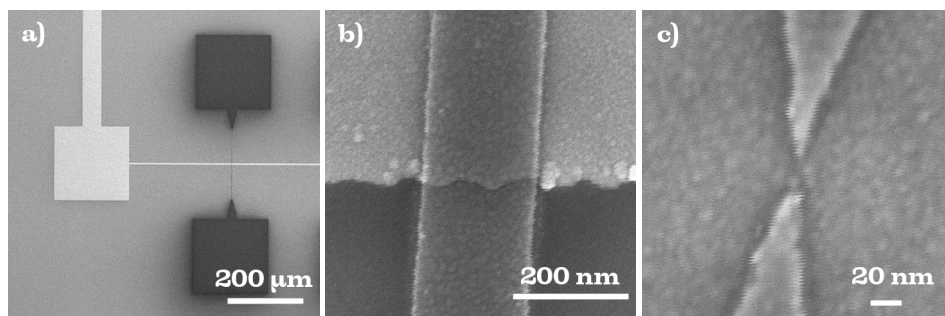


Figure 3.4: a) SEM image of needlelike TiPd (dark) nanogap electrodes on top of TiPt bottom gate electrode (bright) covered by 12 nm  $\text{HfO}_2$  gate dielectric. b) SEM image of the spot where the TiPd electrode (dark) begins to run on top of the TiPt gate electrode (bright). No abrupt topographic feature is observed in the TiPd electrode, which indicates a smooth height variation from the  $\text{SiO}_2$  onto the TiPt gate. c) SEM image of the needlelike nanogap in the TiPd electrodes on top of the TiPt gate electrode.

An example SEM image of a Ti+Pt gate electrode is shown in Figure 3.4a. In this SEM image, the gate electrode shows up bright, while the Ti+Pd needlelike nanogap device shows up as a dark region. At the edge of the gate electrode, a height variation of the substrate is expected. The Ti+Pd layer has to be electrically connected over this height variation. In Figure 3.4b, this region of the sample is shown. No abrupt topographic feature (bright or dark spots in the SEM image) is seen in the Ti+Pd electrode as it crosses the edge of the gate electrode. This is an indication that the height profile after the ALD  $\text{HfO}_2$  deposition is smooth and the Ti+Pd electrode is properly connected over the edge of the gate electrode. The needlelike Ti+Pd nanogap electrode on top of the Ti+Pt gate electrode is shown in Figure 3.4c. Below, we detail the ALD recipe used for depositing the  $\text{HfO}_2$  gate dielectric.

1. ALD of  $\text{HfO}_2$  films in Oxford FlexAL at a temperature of 110 °C:

- 100 cycles of TDMAH +  $\text{H}_2\text{O}$  pulse and purge
  - TDMAH pulse time: 400 milliseconds
  - TDMAH purge time: 59 seconds
  - $\text{H}_2\text{O}$  pulse time: 100 milliseconds
  - $\text{H}_2\text{O}$  purge time: 59 seconds

### 3.4.5 SNS EMBJ devices: Double angle evaporation

The recipe presented here is inspired by the recipe presented by Alvaro Garcia Corral[114] for superconducting aluminium EMBJ devices. An example SNS-EMBJ device, made with 100 nm thick Al evaporated at 5 Å/s as the superconductor and Pd as the normal metal, is shown in Figure 3.5. While devices with Al and Pd were simpler to make, they were not found to be superconducting in this work. Instead, Nb was used for devices in chapters 6

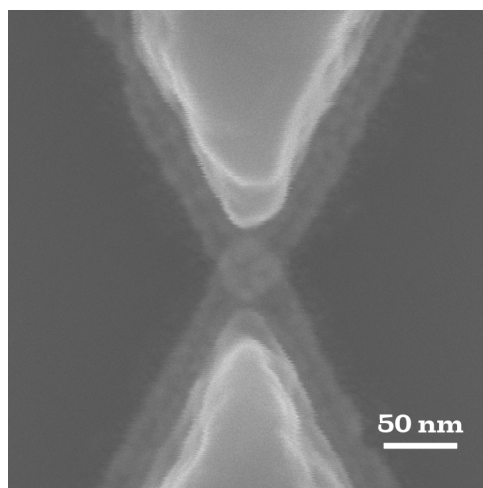


Figure 3.5: SEM image of an SNS EMBJ made with Pd as the normal metal and Al as the superconductor.

and 7. Below, I detail the recipe used when Nb is used as the superconductor:

1. Spin coating of p(MMA-MAA) co-polymer + PMMA 950K double layer resist:
  - (a) Bottom layer of p(MMA-MAA) co-polymer: MMA-MAA EL8
    - Spin speed 2000 rpm ( $\sim 340$  nm)
    - Bake temperature and time:  $180^\circ\text{C}$  for 5 minutes
  - (b) Top layer of PMMA 950K A2 (nota bene: PMMA 950K in ethyl lactate instead of anisole might result in less mixing between the layers)
    - Spin speed 2000 rpm ( $\sim 80$  nm)
    - Bake temperature and time:  $180^\circ\text{C}$  for 5 minutes
2. E-beam exposure with Raith EBPG-5200 with an acceleration voltage of 100 kV:
  - (a) Coarse pattern:
    - Aperture:  $400\ \mu\text{m}$
    - Beam current: As large as possible  $\sim 100$  nA
    - Dose:  $800\ \mu\text{C}/\text{cm}^2$
  - (b) Fine pattern:
    - Aperture:  $200\ \mu\text{m}$
    - Beam current:  $\sim 1$  nA (spot size of  $\sim 5$  nm)

- Dose: 1500-2000  $\mu\text{C}/\text{cm}^2$  (Increasing the dose increases the undercut)

### 3. Development in MIBK:IPA 1:3 :

- Use three beakers and a graduated cylinder to make a 3:1 volumetric mixture of MIBK and IPA
- Develop the chip in the MIBK:IPA mixture for 1 minute and 30 seconds; spray with IPA while removing
- Soak in IPA for 30 seconds; spray with IPA while removing
- Blow-dry with an  $\text{N}_2$  gun

### 4. $\text{O}_2$ plasma descum in Sentech Etchlab 200 (F2) reactive ion etcher:

- Power: 10 W
- Pressure: 70  $\mu\text{Bar}$
- Flow: 45 sccm
- Time: 20 seconds

### 5. Metal deposition For 60 nm electrode spacing:

#### (a) E-beam evaporation in QT AJA (Only if Au is used instead of Pd):

- Align the pattern with the holder
- Vertical evaporation of 5 nm Ti at 0.5  $\text{\AA}/\text{s}$
- Use the tilt controller to modify the tilt angle to  $+6^\circ$ ; note that the tilt angle depends on electrode spacing and resist thickness;  $1^\circ$  per 10 nm works for these resist layers
- Evaporation of 13 nm Au at 0.5  $\text{\AA}/\text{s}$  at an angle of  $+6^\circ$
- Close the shutter and adjust the tilt to  $-6^\circ$  after the previous step; open the shutter and evaporate 13 nm Au
- Finish by vertical evaporation of 50 nm Nb in Plassys

#### (b) E-beam evaporation in Plassys MEB 550S:

- Put the chip on the holder and identify and write down the angle that the pattern makes with respect to the holder by optical microscopy; For evaporation steps where the holder is tilted, correct the rotation angle in the computer program by the measured angle
- Gettering step: Evaporate 20 nm Ti with the shutter closed to reduce the oxygen content in the vacuum chamber
- Vertical evaporation of 5 nm Ti at 0.5  $\text{\AA}/\text{s}$

- Evaporation of 13 nm Pd at 1.0 Å/s at a tilt angle of +6°
- Evaporation of 13 nm Pd at 1.0 Å/s at a tilt angle of +6° and a rotation angle of 180° (effectively -6°)
- Vertical evaporation of 50 nm Nb at 5.0 Å/s

6. Lift off:

- See wide nanogap recipe

### 3.5 Limitations and flaws of fabrication recipes

Although the detailed recipes in the last section produce working devices, a discussion of the limitations and flaws of the recipes is warranted. Understanding the limitations of a recipe is important in order to design better recipes. Similarly, the recipes presented above have flaws that may potentially be removed given proper understanding of the underlying causes. In this section the most important limitations and defects observed during sample fabrication will be briefly discussed. Most of these relate to lift-off processes, as these were primarily used in this thesis.

#### 3.5.1 Large area gaps: Dog-ears and resist collapse

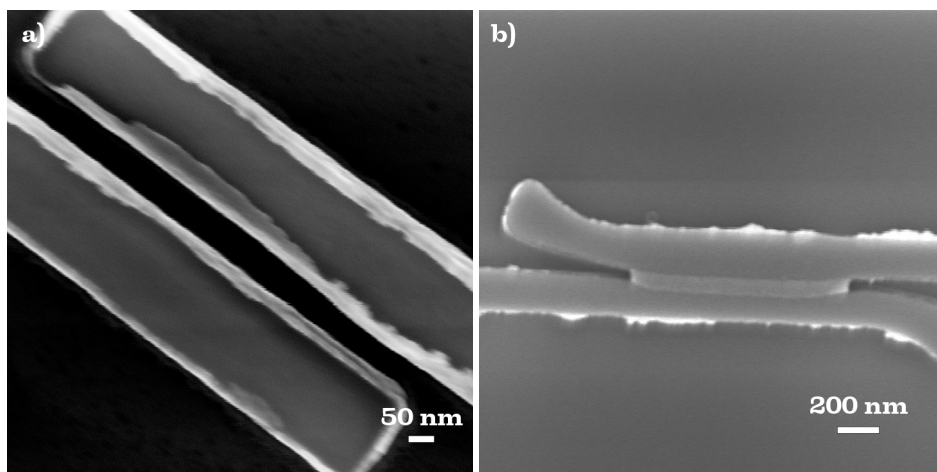


Figure 3.6: a) Wide MoRe nanogap with 'dog-ears'. The use of a 200 nm thick CSAR-62 layer results in large metal fences around the electrodes. b) Wide MoRe nanogap showing resist collapse. An asymmetric metal connection is formed between the MoRe electrodes due to sputtering on top of a collapsed resist wall.

When metal is deposited on the sidewalls of a single layer resist, metal flaps/fences can stay connected to the metal electrode structure after lift-off, sometimes referred to as 'dog-ears'. An example of this is shown in Figure 3.6a, which shows a nanogap electrode made using a 200 nm thick film of MoRe. This is particularly a problem for sputtered MoRe thin films in this thesis. If the dog-ears are thin enough, they may break off during lift-off.



If they only partially tear off, they can potentially short the nanogap electrodes. Worse still, when the dog-ears stay intact, they form a non-ideal surface for contacting graphene nanoribbons and may still break off and short the nanogap electrodes during the GNR transfer. Thus, dog-ears can form a problem. For contacting nanoparticles, such dog-ears may not necessarily be problematic, as long as they fold inwards, away from the opposing electrode. For large-area gaps with sputtered MoRe depositions less than 30 nm in thickness and 30 nm gap sizes, it was observed that dog-ears in the nanogap region often completely tear off during the lift-off.

Resist collapse is the main failure mode that was observed for wide nanogaps. After metal lift-off, the resulting electrodes are electrically shorted. In scanning electron microscopy (SEM) inspection, a metallic connection is seen all across the nanogap, as shown in Figure 3.6b. A telltale sign of resist collapse is a metal connection, which is asymmetric towards one of the two electrodes. Often, the ends of the nanogap pattern are intact, while the parts with the smallest electrode separation are connected. Judging from the SEM image, it looks as though the resist wall has fallen over prior to metal deposition. Such failures have been found before and have been associated with a mechanical collapse of the polymer mask due to capillary forces during rinsing and drying[109]. It is believed that the resist collapse observed in our samples is also of this nature. As resist collapse depends on the mechanical properties of the resist wall, reducing the height of the resist wall reduces the critical gap size at which collapse occurs. Since the first patterns were written in 200 nm thick CSAR-62, a switch to 80 nm thick CSAR-62 was made. This resulted in resist collapse at 25 nm spacings only, comparable to state of the art [110]. Interestingly, cold development recipes with pentyl acetate tended to show resist collapse at 30 nm spacings already, suggesting that the mechanical properties of the resist could be affected by e-beam exposure.

### 3.5.2 Oxides on sputtered MoRe after exposure to (humid) air

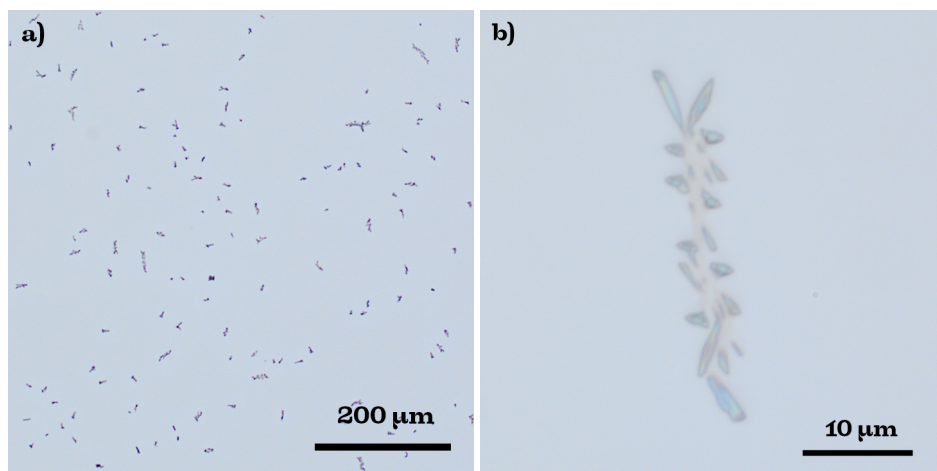


Figure 3.7: a) Optical microscopy image of oxides on the sputtered MoRe surface after overnight exposure to air. b) Optical microscopy image of a single oxide clump/crystallite on MoRe

Immediately after deposition of MoRe films and after lift off of MoRe structures, it was observed in dark field microscopy that there are bright spots on the surface of the metal that appear to grow over time. These have been observed before[115] and are known to be rich in rhenium and oxygen, suggesting the presence of mobile  $\text{Re}_2\text{O}_7$  on the surface, which grows oxide crystallites on the thin film.

Here, I report on a few observations regarding these crystallites. In an experiment, two films of MoRe were left in atmospheric conditions during X-ray diffraction (XRD) characterization. While the aim of the experiment was to investigate the poly-crystalline structure, instead something unexpected happened. One of the MoRe films was left in a gelpak box and the other in the XRD machine. Upon finishing the XRD characterization, the MoRe film that underwent XRD characterization was covered in speckles, as if it had collected a lot of dust. The sample in the gelpak box, on the other hand, was still reflective and shiny. Initially, an attempt was made to remove this 'dust' with a MiraSWAB microfiber swab, without any success. Upon inspection of the MoRe film in the optical microscope it was observed that the surface was completely covered in large crystallites, shown in Figure 3.7a, suggesting that the film in the XRD machine underwent accelerated oxidation compared to the MoRe film in the gelpak box. This could perhaps be explained by a difference in temperature or humidity. A single oxide crystallite is shown in Figure 3.7b.

Finally, an attempt was made to remove these oxide crystals. If they are indeed made of  $\text{Re}_2\text{O}_7$ , they should be volatile and should be fully removed through sublimation above  $350^\circ\text{C}$ [116]. To test this, the oxidized MoRe film was put in a rapid thermal processing machine and annealed at  $400^\circ\text{C}$  in nitrogen gas for 10 minutes. After the annealing process, no more speckles were seen on the MoRe film in optical microscope images, consistent with the idea of sublimation of  $\text{Re}_2\text{O}_7$ . Furthermore, over the next two weeks, no significant oxidation was observed in optical microscope images.

### 3.5.3 Heating effects during evaporation

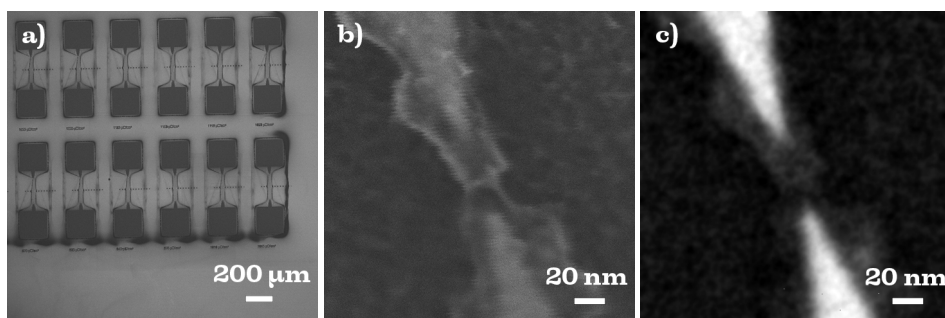


Figure 3.8: a) Large-area secondary electron (SE) SEM image of TiPd nanogaps. The pattern is surrounded by dark lines and areas. b) SE SEM image of a TiPd nanogap with mixed organic-inorganic residue. c) High-angle back-scattered electron (HA-BSE) SEM image of a TiPd nanogap taken together with the SE image in b). Bright areas indicate the presence of metal.

After evaporation and lift-off of palladium and platinum metal structures on 80 nm thick CSAR-62 masks, dark residues were often seen around the electrodes in SEM, shown in

Figure 3.8a. These dark residues are composed of dark lines that tend to follow the pattern. On the nanoscale, a spotty, sometimes web-like, structure can be seen on the surface. There are significantly more residues around the most critical region, the nanogap between the electrodes, which is shown in the SEM image in Figure 3.8b. The high resolution secondary electron (SE) image here mostly shows the topography. While darker regions tend to be associated with light elements, such as carbon in polymer residues, bright regions can be related to edges. To get a better idea of the atomic composition of the residues, a high-angle back-scattered electron (HA-BSE) image was also taken, which is shown in Figure 3.8c. The contrast in this image has been enhanced, and the image was filtered by smart blurring in Adobe Photoshop. Heavier elements, such as metals, result in more backscattered electrons and hence show up brighter. Polymer residues, on the other hand, are mostly made of lighter elements than the Si substrate and hence provide hardly any HA-BSE signal. The residues around the nanogap electrode show up as brighter regions in this image, which clearly indicates the presence of metal.

Notably, the problems described here were observed when evaporating using the Temescal evaporator in the cleanroom in particular, but also sometimes when using the Plassys evaporator. When evaporation was performed using the AJA QT and AJA MB systems, these problems were not experienced. The difference between the two evaporators could potentially be attributed to better heat sinking/thermal management. It was experienced that the stage in the Temescal evaporator can be hot to the touch (60 °C - 80 °C) after evaporation, especially after evaporating thicker (~ 50 nm) layers of Pt or Pd. Using a thick copper stage and thermal paste somewhat mitigated this problem, but not enough to prevent residue formation. When evaporation was instead done in the AJA systems, the stage was never hot to the touch upon unloading. A difference in the lift-off was also observed, with TiPd and TiPt films from the Temescal evaporator lifting off on a timescale of seconds in the remover AR-600.71 at room temperature, while films from the AJA evaporator systems took 15 to 30 minutes to fully lift-off in AR-600.71 (or NMP) at 70 °C.

As suggested by the previous paragraph, a speculative cause of these residues is the high deposition temperature of Pd and Pt, which leads to heating of the sample and stage by infrared radiation. Heating and the related film stress could lead to the formation of cracks and voids in the resist layer starting from weak spots. Pattern edges, corners and exposed resist areas can all be local weak spots in the resist. If the temperature is high enough, the glass transition temperature of the resist could also be reached, which is locally lower in regions that were exposed to back-scattered electrons during the e-beam writing step. A difference in film stress and/or the presence of voids in the resist could also explain the observed difference in the lift-off time. After evaporation into cracks and voids, mixing of the metal and polymer layers results in residues that could not be lifted off using organic solvents.

Although the origin of the residues was not studied further, it was found that, contrary to 80 nm thick CSAR-62 films, 200 nm thick CSAR-62 that were exposed by lower doses ( $\sim 300 \frac{\mu\text{C}}{\text{cm}^2}$ ) did not show residues. Furthermore, the observed different sample outcomes between the two evaporators led to the choice to avoid the use of the Temescal evaporator

in favor of the AJA evaporators for the nanogap patterns.

### 3.5.4 Resist residue

To achieve a high contrast, the developers used in the processing here are 'weak' developers/solvents. Furthermore, the adhesion of the resist to the surface must be good to avoid delamination. As a result, some residue of resist always remains on the surface of the substrate after development. These residues can potentially be problematic, as they could reduce adhesion of subsequently deposited metal thin films. This could make wire bonding of chips difficult, causing them to delaminate[117, 118]. In the case of weak adhesion of a metal thin film, delamination of the metal can also occur in the presence of film stress. Thus, it makes sense to remove resist residues on the surface before deposition, called 'descumming'.

Descumming can be done with a strong developer or with a 'gentle', low-power oxygen plasma. For devices made with CSAR-62 with room temperature development, the first option was chosen, as it had been reported that the loss in contrast was smaller with a descum in xylene[119]. The use of a stronger developer to descum the surface of the substrate will only reduce the amount of residues to a certain extent. For the double-layer PMMA-P(MMA-MAA) recipes an O<sub>2</sub> plasma was instead chosen. Both descumming steps recipes could be further improved. CSAR-62 recipes could be further improved by using MIBK to descum the surface. For the PMMA-P(MMA-MAA) recipe, the time and parameters for the oxygen plasma could be improved. For the CSAR-62 recipes that use cold development, it was found that the solvent descum was not necessary to obtain decent adhesion. This may perhaps be explained by the reduced length of residual polymer chains resulting from the roughly two times larger exposure dose.

### 3.5.5 Metal particles around patterns

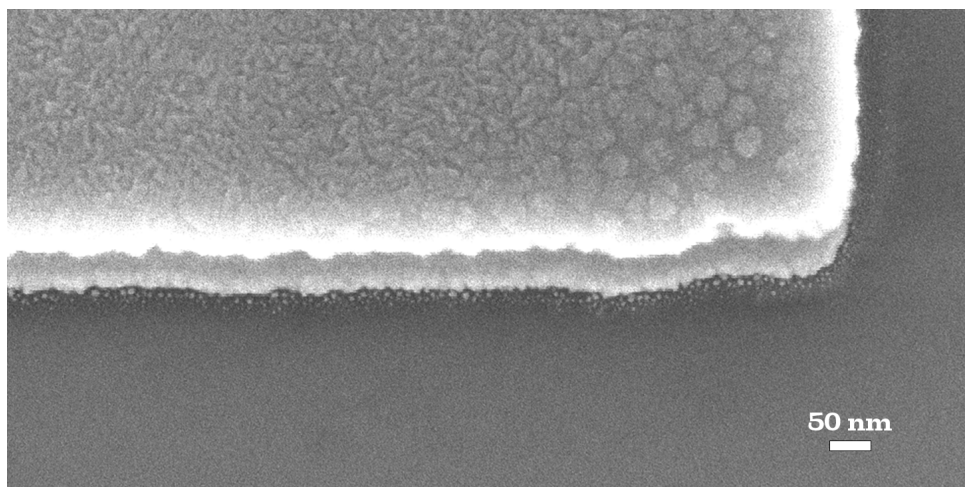


Figure 3.9: SEM image of the edge of a contact pad of an Nb/Au/Nb SNS EMBJ. A halo of gold nanoparticles is seen around the contact pad.

When using double layer resist recipes, it was observed in SEM that the deposited metal layers showed a grainy halo around their edges. These metal grains are deposited outside the intended pattern and possibly mixed with polymer residues. Such metal grains are a problem for defining clean metal nanogaps by e-beam lithography with double layer resist masks. These grains can possibly act as single electron transistors (SETs) in series or in parallel to the nanoscale object of interest. Worse yet, they could be trapped instead of the deposited nanoparticles. Furthermore, they could couple capacitively to other particles, potentially resulting in jumps in offset charges/potentials in SET devices. The metal nanoparticles were found on the  $\text{SiO}_2$  in regions that should have been covered by the top resist layer. There are a few possible explanations for this.

Considering the mean free path of atoms in the high vacuum systems used, which is on the order of 6 km for a pressure of  $2 \cdot 10^{-8}$  mbar, it is unlikely that scattering in the vacuum chamber could produce large metal grains. The metal may simply have scattered on the resist mask. In that case, the question arises why metal grains are not found further away from the metal structures. The resist mask could also have pinholes inside it, resulting from the development and random exposure mechanism. If this is the cause, a single layer resist mask should also show such particles, which is usually not the case. The most likely explanation is that the metal particles are evaporated into the undercut due to the fact that the crucibles in the evaporators have a finite diameter, which is typically about 25 mm to 50 mm. Since the distance from the crucible to the sample is typically around 600 mm for all evaporators in the Kavli Nanolab cleanroom, there can be a considerable angle of around  $2.4^\circ$ . For an undercut of 340 nm, this results in a spread of  $\frac{25 \text{ mm}}{600 \text{ mm}} \cdot 340 \text{ nm} \approx 14 \text{ nm}$ , which is comparable to the observed width of the metal grain halos.

The metal halos could perhaps be removed by a short dip in gold etchants, although this may significantly alter the gold electrodes too. Alternatively, a thin sacrificial layer of  $\text{Al}_2\text{O}_3$  could be deposited underneath the pattern by ALD, which can be partially removed by a wet etchant, such as Transene A or Transene D. Controlled etching should result in lift-off of only the residues, while preserving the device features. The latter technique is not simply compatible with a local bottom gate, unless another protective layer of  $\text{HfO}_2$  is used underneath the  $\text{Al}_2\text{O}_3$ .

### 3.5.6 Importance of rinsing procedure after development

Rinsing and drying are universal in the fabrication process. Thus, understanding the problems that can arise in this process is important. In room temperature development and lift-off/cleaning processes, rinsing should ideally be done while taking samples out of solvents. If this is not done, the developer may dry, depositing polymer residue on the surface of the substrate. It should be mentioned that for cold development processes this procedure is also important for another reason. Since the sample comes out of the developer at a temperature below  $0^\circ\text{C}$ , care should be taken to avoid drying before the sample has warmed up, as water may condense on the sample and freeze, collapsing or distorting the pattern. Rinsing with room temperature isopropyl alcohol for at least 30 seconds and prolonged blow-drying with  $\text{N}_2$  can be used to minimize condensation of water on the sample.



## 3.6 PMMA membrane-assisted graphene nanoribbon transfer

A PMMA-membrane assisted substrate transfer method was developed for graphene nanoribbons. In this process, graphene nanoribbons are picked up from the growth substrate using a Polydimethylsiloxane (PDMS)-supported PMMA membrane. The PMMA membrane can then be deposited onto pre-fabricated electrodes in an aligned manner on a dry-transfer stage with a  $\sim 1\ \mu\text{m}$  precise placement. Crucially, this avoids the contact of more fragile electrodes, such as MoRe, with the liquids that are used in most GNR transfer processes, such as hydrochloric acid, gold etchant and deionized water. Furthermore, since the PMMA membrane is stretched over the PDMS and clamped, wrinkling and folding of the PMMA is likely reduced. Here, we describe the procedure for making the PMMA membranes and the transfer process.

### 3.6.1 Fabrication of PMMA membranes

The procedure for suspension and transfer of the PMMA membranes, based on the technique by Kaverzin et al.[121], is as follows: We start with spin coating a thick layer of a water-soluble polymer, in this case, Elektra 92, onto silicon oxide wafers. Next, a  $1000\ \mu\text{m}$  thick layer of PMMA 950K was spin-coated onto the Elektra 92 layer in two steps, baked at  $180\ ^\circ\text{C}$  for 1 minute after each step. A rectangular hole was cut in a piece of scotch tape, which was subsequently pressed against the PMMA membrane on silicon. The scotch tape was suspended over a beaker filled with deionized water with the silicon piece submerged to dissolve the Elektra 92. After the silicon piece detached from the PMMA membrane, the membrane was rinsed and left to dry in ambient conditions. The dry PMMA membrane was next stretched over a piece of PDMS, placed on a glass slide.<sup>1</sup>

### 3.6.2 GNR transfer using PMMA membranes

The developed transfer procedure will be described, following the steps illustrated in Figure. 3.10. In the first step, the PMMA-PDMS stamp held on a glass slide (ii) is brought in contact with the GNR film, grown on a Au-mica substrate (i), using micromanipulators of a transfer stage, shown in (iii). After the contact of the PMMA membrane and the GNR film, the stage is heated to  $130\ ^\circ\text{C}$  to promote stronger adhesion. The stack of PDMS-PMMA-GNR-Au(111)-mica held on the glass slide is then put into 30% HCl until the mica is delaminated from the Au film, depicted in (iv). The glass slide is then rinsed and soaked in DI water three times, before leaving it to dry in ambient conditions. As shown in (v),  $\text{KI/I}_2$  gold etchant is next drop-casted onto the Au film with a pipette and left for 10 minutes to fully etch the  $200\ \text{nm}$  Au film. The GNR-PMMA-PDMS stack is then rinsed and soaked in DI water overnight to remove residual iodine stains. After drying in ambient conditions(vi), the PMMA membrane is perforated around the PDMS using a needle to allow for its easier detachment from the PDMS stamp in the next step. The PMMA-GNR film is brought into contact with the pre-fabricated electrodes at the transfer stage, heated up to  $150\ ^\circ\text{C}$  to improve adhesion (vii). In the final step, the glass slide-PDMS stamp is

This section is partly based on D. Bouwmeester et al., *MoRe Electrodes with 10 nm Nanogaps for Electrical Contact to Atomically Precise Graphene Nanoribbons*, *ACS Applied Nano Materials* 2023 [120].

<sup>1</sup>Credits for this subsection and Figure 3.10: Talieh Ghiasi

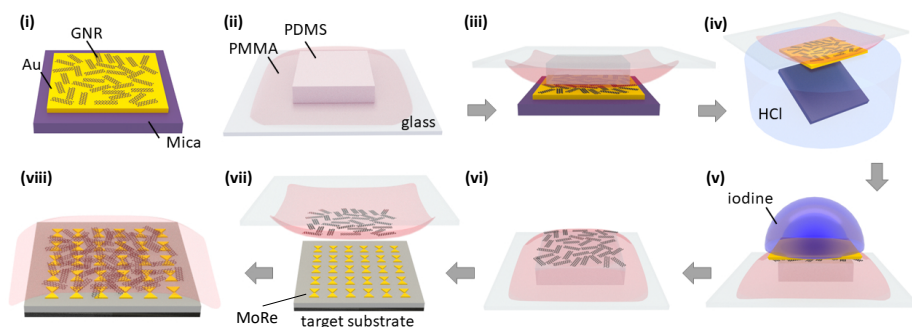


Figure 3.10: PMMA membrane-assisted GNR transfer method. (i) Au(111) on the mica 9-AGNR growth substrate. (ii) PMMA membrane on PDMS placed on a glass slide. (iii) Aligned placement of the PMMA membrane onto the GNR growth substrate. The stage is heated to 130 °C to promote stronger adhesion of the PMMA membrane to the GNR growth substrate. (iv) Delamination of the mica layer in 30% HCl. (v) Gold etching in  $KI/I_2$  for 5 to 10 min followed by rinsing and soaking overnight in DI water. (vi) GNRs on the PMMA membrane after drying in ambient conditions (vii) Stamping of the PMMA membrane onto the target substrate, followed by annealing at 150 °C. (viii) Target substrate with PMMA-covered GNRs after GNR transfer.

retracted, leaving the PMMA-covered GNR film on the electrodes (viii). After the transfer, the devices were post-annealed for 30 minutes at 150 °C to reflow the PMMA layer which would increase the chance of making better contact with the GNR film.





## 4

## MoRe Electrodes with 10 nm Nanogaps for Electrical Contact to Atomically Precise Graphene Nanoribbons

4

*Atomically precise graphene nanoribbons (GNRs) are predicted to exhibit exceptional edge-related properties, such as localized edge states, spin polarization, and half-metallicity. However, the absence of low-resistance nanoscale electrical contacts to the GNRs hinders harnessing their properties in field-effect transistors. In this paper, we make electrical contact with nine-atom-wide armchair GNRs using superconducting alloy MoRe as well as Pd (as a reference), which are two of the metals providing low-resistance contacts to carbon nanotubes. We take a step toward contacting a single GNR by fabricating electrodes with a needlelike geometry, with about 20 nm tip diameter and 10 nm separation. To preserve the nanoscale geometry of the contacts, we develop a PMMA-assisted technique to transfer the GNRs onto the prepatterned electrodes. Our device characterizations as a function of bias voltage and temperature show thermally activated gate-tunable conductance in GNR-MoRe-based transistors.*

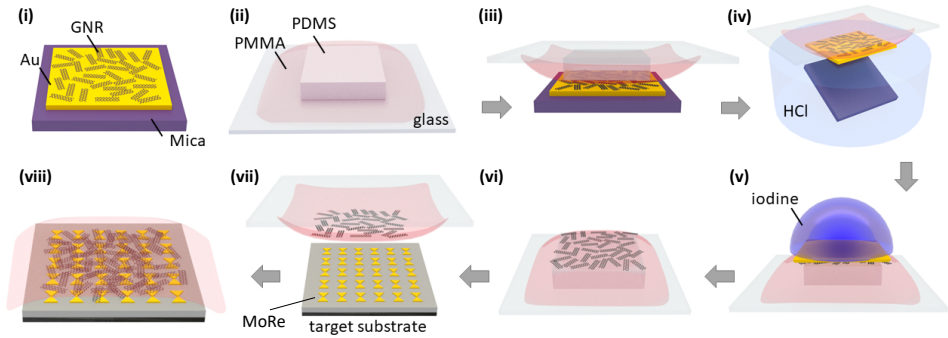


Figure 4.1: PMMA membrane GNR transfer method. (i) Au(111) on the mica 9-AGNR growth substrate. (ii) PMMA membrane on PDMS placed on a glass slide. (iii) Aligned placement of the PMMA membrane onto the GNR growth substrate. The stage is heated to 130 °C to promote stronger adhesion of the PMMA membrane to the GNR growth substrate. (iv) Delamination of the mica layer in 30% HCl. (v) Gold etching in  $\text{KI/I}_2$  for 5 to 10 minutes followed by rinsing and soaking overnight in DI water. (vi) GNRs on the PMMA membrane after drying in ambient conditions (vii) Stamping of the PMMA membrane onto the target substrate, followed by annealing at 150 °C. (viii) Target substrate with PMMA-covered GNRs after GNR transfer.

4

## 4.1 Introduction

Graphene nanoribbons (GNRs) are quasi-1D analogues of graphene. Although graphene is classified as a 2D semimetal, a combination of quantum confinement and electron-electron interaction make GNRs semiconducting [21, 22, 122]. The electronic band gap of GNRs scales inversely with their width and depends on their edge structure [21]. This tunable band gap is a property of interest for field-effect transistors (FETs)[27, 123] and optoelectronics [124]. Moreover, GNRs exhibit edges and ends that can host localized spin-polarized states[122, 125, 126], which is interesting for spintronic applications. Since the electronic properties of GNRs are sensitive to their width and edge structure, edge disorder and width variation at the atomic level result in hopping transport within the ribbon[127], which significantly suppresses their intrinsic electronic/spintronic properties[128].

On-surface, bottom-up chemical approaches have enabled the synthesis of a variety of GNRs from molecular precursors with structural precision at the atomic level[10], such as armchair [10], zigzag [25], chevron[10], staggered/topological [129, 130], metallic[131], and doped GNRs [132]. The electronic properties of these GNRs have mostly been studied by scanning tunneling microscopy. Characterization of the intrinsic electronic properties of the GNRs in electronic circuits has been comparatively limited by high contact resistances, limited chemical stability of the edges, and shorter GNR lengths than typical source-drain contact distances.

Low-resistance Ohmic electrical contacts are important for obtaining large on-state currents in FET devices and for studying the intrinsic transport properties of GNRs. However, making consistent, low-resistance electrical contact to on-surface synthesized atomically precise GNRs is challenging due to their typical 1-nm width scale that leads to large band gaps (of the order of 1 eV). Their typical length scale also results in a small contact area, on the order of 10 nm<sup>2</sup>. Recently, there have been considerable efforts to electrically contact

atomically precise armchair-edge GNRs by electrodes made of graphene[133–136], carbon nanotubes (CNTs)[137], palladium[27, 138–140], and gold[141]. These studies, however, are still limited compared to the detailed characterization of a large variety of contacts to CNTs[28, 142]. Even though CNTs structurally differ from GNRs in the absence of edges, small-diameter (less than 1.0 nm) CNTs are the closest system to atomically precise GNRs due to their similar band structure and considerable band gap (larger than 0.8 eV)[143].

For the case of semiconducting CNTs, Schottky barriers are formed at the metal-CNT interfaces, the size of which depends on the chosen contact metal and the diameter of the nanotube. The presence of Schottky barriers results in a contact resistance that increases as the temperature is decreased. For CNTs, a distinction is often made between physisorption and chemisorption[144, 145] and between p-type (high work function) and n-type (low work function) electrical contacts [28]. Typically, n-type contacts form with metals that are prone to oxidation (Al, Sc, Y, Ti), while p-type contacts can be made with noble metals (Au, Pt, Pd) and Ni, Co, Mo, and W.

Two of the metals that stand out for making low-resistance electrical contacts with small or absent Schottky barriers to CNTs are Pd[146, 147] and Mo [148]/MoRe alloy[149, 150]. Pd contacts to 9- and 13-atom-wide armchair GNRs (9-AGNRs and 13-AGNRs) have already been studied in a short-channel FET geometry by Llinas et al.[27], who found that transport in their devices was limited by tunneling through a Schottky barrier at the contacts. Nevertheless, their Pd-contacted 9-AGNR FETs with a high- $\kappa$   $\text{HfO}_2$  gate dielectric have a large on-state current ( $> 1 \mu\text{A}$ ) and an on-off ratio of  $10^5$ . Mo/MoRe, on the other hand, is of interest as it is a superconducting metal, which may be used to induce superconductivity in GNRs by the superconducting proximity effect[34] at cryogenic temperatures. In a weakly transparent electrical contact, the superconducting energy gap can be used to perform tunneling spectroscopy of the GNRs, while a highly transparent contact would allow for utilizing GNRs in Josephson junctions.

Here, we further explore MoRe and Pd contacts to 9-AGNRs by studying their current-voltage characteristics at various temperatures. In particular, we compare two distinct electrode geometries that have the potential to respectively address many GNRs in parallel and single GNRs. With the aim of contacting single 9-AGNRs, an electrode design is made that minimizes gap width. Here we fabricate needlelike MoRe and Pd nanogap electrodes with a minimum width of  $\sim 20$  nm and spacing of 6–15 nm. The smaller gap spacing achieved by this geometry could also enable addressing shorter GNRs. The polymer-free transfer method is attempted on this geometry, resulting in broken MoRe nanowires due to etching. In order to preserve the more fragile needlelike nanogaps and the contact geometry from etchants used in polymer-free GNR-transfer recipes, here we develop a PMMA-membrane-assisted technique for the transfer of the 9-AGNR films based on the PMMA fishing transfer technique introduced by Martini et al.[133]. This technique keeps the electrodes intact by preventing direct contact with any liquid and allows for controlled handling and  $\sim 1 \mu\text{m}$  precise placement of the GNRs onto the electrical contacts using micromanipulators. Our transfer method offers the additional advantage of using a stretched and clamped PMMA film, which could reduce wrinkling and folding. With this technique, we fabricate 10 nm nanogap MoRe and Pd devices and investigate and compare their performance. We show that the 10 nm Pd nanogap devices have a few orders of magnitude

higher conductance, which suggests that a Pd/MoRe bilayer thin film would be a better contact material for the realization of functional superconducting GNR devices.

## Results

The 9-AGNRs were grown by on-surface synthesis[151], discussed in detail in the methods section. The average length of the 9-AGNRs used in this work is 45 nm.

The two distinct electrode geometries used here to address the GNRs are the wide-nanogap and needle-like geometries. The wide-nanogap geometry consists of a pair of 2  $\mu\text{m}$  long parallel wires, separated by approximately 30 nm. This geometry was made to address transport through many GNRs in parallel. The needle-like nanogap geometry consists of two opposing nanowires that are cusped at a 30° angle, separated by less than 15 nm. This geometry minimizes the contact area and thus, increases the chance of making contact with a single GNR. The fabrication of these two electrode geometries is discussed in detail in the methods section.

Prior to the GNR transfer, the nanogap electrodes were characterized by recording the current versus bias voltage (*IV* characteristic) in the bias range of -1 to 1 V. Only devices that were found to be electrically open (resistance  $\geq 1 \text{ T}\Omega$  at 1 V) were used in this study. The transfer of the GNRs onto wide MoRe nanogaps was performed by a polymer-free method[152]. For the needle-like MoRe and Pd nanogap devices, we resorted to a polymethylmethacrylate (PMMA) membrane-based transfer method, because the gold etchant destroys the MoRe and Pd nanowires. The procedure for making the PMMA membrane for the GNR transfer is detailed in the methods section.

As this PMMA-membrane transfer method has not yet been applied to GNRs, we discuss it in detail, following the steps illustrated in Figure 4.1. In the first step, the PMMA-PDMS stamp held on a glass slide (ii) is brought in contact with the GNR film, grown on a Au-mica substrate (i), using micromanipulators of a transfer stage, shown in (iii). After the contact of the PMMA membrane and the GNR film, the stage is heated to 130 °C to promote stronger adhesion. The stack of PDMS-PMMA-GNR-Au(111)-mica held on the glass slide is then put into 30% HCl until the mica is delaminated from the Au film, depicted in (iv). The glass slide is then rinsed and soaked in DI water three times, before leaving it to dry in ambient conditions. As shown in (v),  $\text{KI/I}_2$  gold etchant is next drop-casted onto the Au film with a pipette and left for 10 minutes to fully etch the 200 nm Au film. The GNR-PMMA-PDMS stack is then rinsed and soaked in DI water overnight to remove residual iodine stains. After drying in ambient conditions(vi), the PMMA membrane is perforated around the PDMS using a needle to allow for its easier detachment from the PDMS stamp in the next step. The PMMA-GNR film is brought into contact with the pre-fabricated electrodes at the transfer stage, heated up to 150 °C to improve adhesion (vii). In the final step, the glass slide-PDMS stamp is retracted, leaving the PMMA-covered GNR film on the electrodes (viii). After the transfer, the devices were post-annealed for 30 minutes at 150 °C to reflow the PMMA layer which would increase the chance of making better contact with the GNR film.

We first discuss the measurements of wide MoRe nanogap 9-AGNR devices at room temperature in vacuum. In Figure 4.2a we show a representative SEM image of the wide MoRe

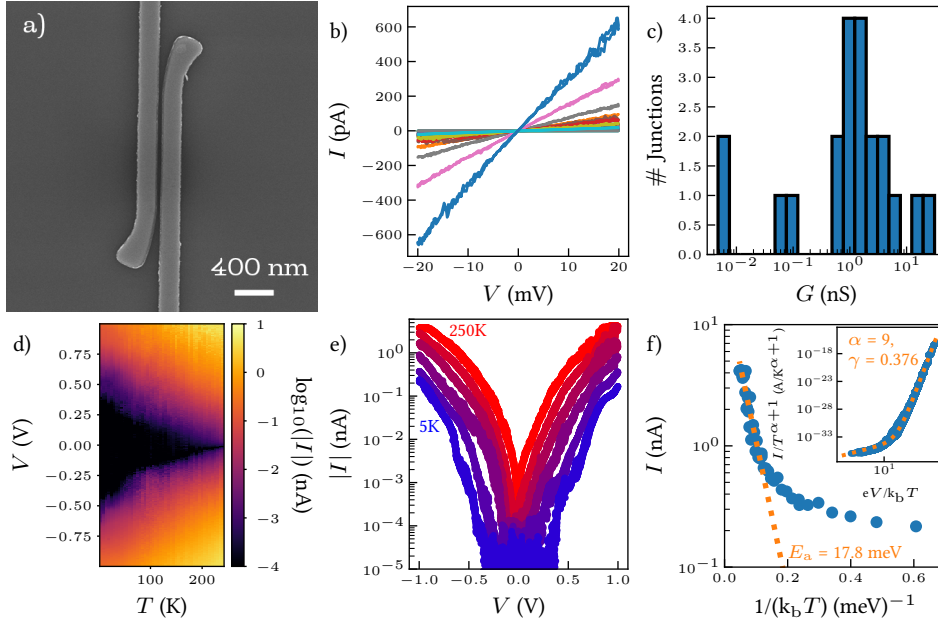


Figure 4.2: Room temperature characterization. a) SEM image of a  $2\ \mu\text{m}$  wide MoRe nanogap contact electrodes; The electrode separation is 30 nm and the scale bar is 400 nm. b)  $IV$  curves of wide MoRe nanogap 9-AGNR devices. Each color corresponds to a measurement performed on a different device. c) Histogram of conductances of wide MoRe nanogap 9-AGNR devices. d) Map of current versus bias voltage and temperature of a selected wide MoRe nanogap 9-AGNR device. e) Corresponding temperature dependence of the  $IV$  characteristic extracted from d) for  $T = 5, 50, 100, 150, 200$ , and  $250\ \text{K}$ . f) Corresponding temperature dependence of the current at  $V = 1\ \text{V}$  extracted from d). The inset shows the rescaled current with a guide to the eye based on the nuclear tunneling model.

nanogap electrodes. For all devices,  $IV$  curves were recorded in the bias range from  $-20$  to  $20\ \text{mV}$ , which we show together in Figure 4.2b. Out of the 22 devices onto which the GNR transfer was performed, 21 were found to be conductive. All  $IV$  curves are linear within the applied bias range, with varying slopes. The electrical conductance ( $G$ ) of the devices was extracted by fitting the slope with a linear fit, resulting in the histogram of Figure 4.2c. The majority of the devices show conductance in the range of  $0.5\text{--}8\ \text{nS}$ , with a median of  $1.3\ \text{nS}$ . The standard deviation of  $\log(G)$  is  $0.95$ , equivalent to a standard deviation in the conductance of  $\sim 1$  order of magnitude. There are, however, also devices with a conductance smaller than  $10\ \text{pS}$  or larger than  $10\ \text{nS}$ , spanning over four orders of magnitude in total.

The temperature dependence of the  $IV$  characteristics of one of the wide MoRe nanogaps-GNR junctions is shown in Figure 4.2d on a logarithmic scale (see Appendix, section 4.4 for measurements of another device. Furthermore, an  $IV$  curve up to  $4\ \text{V}$  taken at  $100\ \text{mK}$  can be found in the Appendix, section 4.4). The measured current at a fixed bias voltage decreases with decreasing temperature, with a kink observed at  $80\ \text{K}$ . In Figure 4.2e, the  $IV$  curves plotted for various temperatures highlight the plateau-like feature at  $T < 100\ \text{K}$ ,

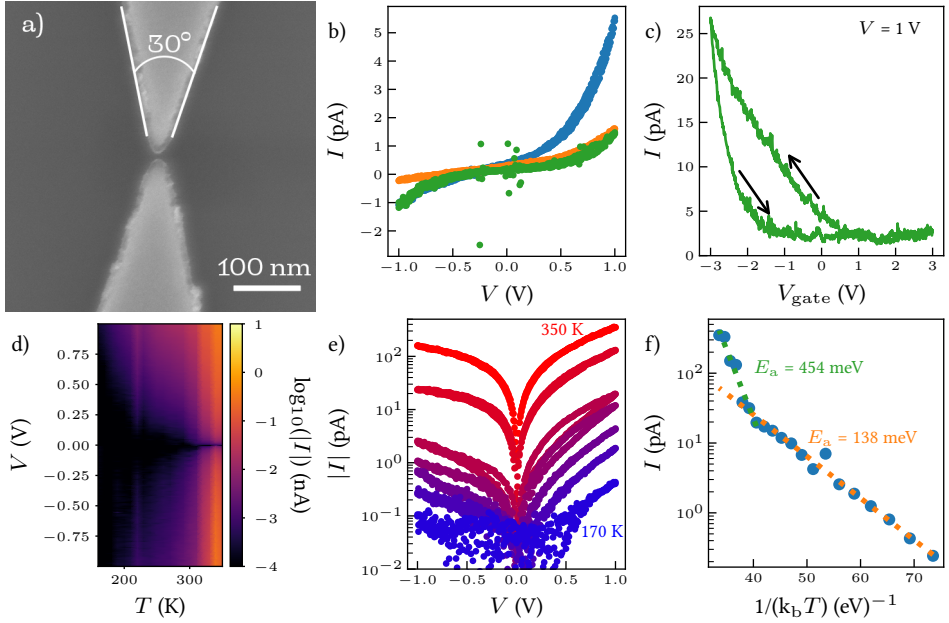


Figure 4.3: a) SEM image of a representative needle-like MoRe 10 nm nanogap electrodes with a separation of roughly 10 nm; The scale bar is 100 nm. b)  $IV$  curves of three MoRe 10 nm nanogap 9-AGNR devices. Each color corresponds to a measurement performed on a different device. c) Gate voltage dependence of the current at  $V = 1$  V of a selected MoRe 10 nm nanogap 9-AGNR device. The arrows indicate the sweep direction of the gate voltage. d) Map of the current versus bias voltage and temperature of the same device as in c) at a fixed gate voltage of -2 V. e) Corresponding temperature dependence of the  $IV$  characteristic extracted from d), shown for  $T = 170, 200, 230, 260, 290, 320$  and  $350$  K. f) Corresponding temperature dependence of the current at  $V = 1$  V extracted from d). The inset shows the rescaled curve with a guide to the eye based on the nuclear tunneling model.

together with an increase in the slope of the logarithm of the  $IV$  curve with decreasing temperature. In Figure 4.2f, the current at a bias voltage of 1 V is plotted versus inverse temperature. In the high-temperature regime, an exponential decay is found, which can be described by:

$$I = C e^{-\frac{E_a}{k_B T}}, \quad (4.1)$$

where  $C$  is a constant,  $k_B$  is the Boltzmann constant and  $E_a$  is an activation energy. Below  $\frac{1}{k_B T} = 0.1$  (meV) $^{-1}$ , equivalent to  $T > 80$  K, the temperature-dependence fit yields  $E_a = 17.8$  meV.

At lower temperatures, the  $\log(\text{current})$ -voltage curve does not follow the exponential decay and instead flattens off. For this part, the scaling analysis done by Richter et al. [141] for charge transport in 9-AGNR networks was followed, which is based on a nuclear tunneling [153–155] model. We note that an analysis based on the Richardson-Schottky and Simmons model was also attempted. The bias voltage dependence could be fit, but we could not simultaneously reproduce the temperature scaling. The nuclear tunneling model

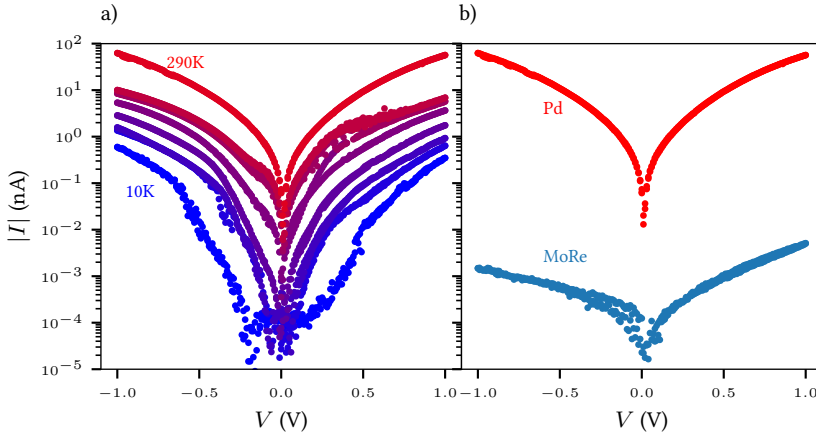


Figure 4.4: a) Temperature dependence of the  $IV$  characteristic of a 10 nm Pd nanogap 9-AGNR device. b) Comparison of the  $IV$  curve of the most conductive 10 nm MoRe nanogap, shown as the blue  $IV$  curve in figure 4.3b, and the  $IV$  curve of the 10 nm Pd nanogap in Figure 4a at room temperature.

instead gives an efficient description of the current versus bias voltage and temperature. The equation describing the  $IV$  characteristic in this model is:

$$I = I_0 T^{\alpha+1} \sinh\left(\frac{\gamma eV}{2k_B T}\right) \left|\Gamma\left(1 + \frac{\alpha}{2} + i\frac{\gamma eV}{2\pi k_B T}\right)\right|^2, \quad (4.2)$$

where  $I_0$  is a constant,  $\alpha$  is a dimensionless dissipation coefficient,  $\gamma < 1$  is the inverse of the number of hopping sites/voltage divisions and  $\Gamma$  is the gamma function. In the inset of Figure 4.2f, a rescaling of the data in Figure 4.2d has been made by plotting  $\frac{I}{T^{\alpha+1}}$  versus  $\frac{eV}{k_B T}$  on a log-log scale.  $\alpha = 9$  was taken as a fixed parameter in the model to compare with the results from Richter et al [141]. When  $\alpha$  is fixed,  $\gamma$  determines the transition from a thermally-activated regime, where  $\frac{I}{T^{\alpha+1}}$  is proportional to  $\frac{eV}{k_B T}$ , to a bias-driven regime, where  $\frac{I}{T^{\alpha+1}}$  scales as  $(\frac{eV}{k_B T})^{\alpha+1}$ . A guide to the eye is plotted for  $\gamma = 0.378$ , which shows reasonable agreement with the data. This corresponds to a voltage division over an average of roughly 3 segments within a distance of 30 nm.

9-AGNR devices with needle-like 10 nm MoRe nanogaps are also characterized at room temperature in vacuum. In Figure 4.3a we show a representative SEM image of the needle-like MoRe electrodes. The GNR film was transferred onto 32 pre-fabricated nanogaps. The current is measured versus the applied bias voltage up to 1 V.  $IV$  curves of the conductive devices are shown together in Figure 4.3b. Three devices are found to have a current above the noise level within this range. The  $IV$  curves are nonlinear with a maximum current of 1 to 5 pA. The electrical characteristics of the two devices shown by the blue and orange curves display an asymmetry in current versus the bias-voltage which is mostly independent of the polarity of the source-drain contacts and can be explained by a capac-



itive coupling of the source and drain electrodes to the GNRs (see Appendix, section 4.4). The current through the junctions was also characterized versus local bottom-gate voltage ( $V_{\text{gate}}$ ) at a fixed bias voltage of  $V = 1$  V. This is shown in Figure 4.3c for the device represented by the green  $IV$  curve in Figure 4.3b. The sweep directions of the gate voltage are indicated by the arrows. The observed hysteresis (additional results on time dependence in Appendix, section 4.4) in the trace and retrace gate-sweeps is similar to what has been reported for 7-AGNR devices at room temperature in air[156], as well as in vacuum for 5-AGNR and 9-AGNR devices for temperatures between 5 and 262 K[157]. Furthermore, the current is the largest at negative gate voltages, which is indicative of p-type behavior of the 9-AGNR FETs.

## 4

Similar to the measurements on the wide-nanogap geometry, the  $IV$  characteristic of the 10 nm nanogaps is measured versus temperature (measurements of another device in Appendix, section 4.4). At a fixed  $V_{\text{gate}} = -2$  V,  $IV$  curves were first measured cooling down from 290 K to 160 K, below which the current gets smaller than the noise floor of 100 fA. To obtain additional information,  $IV$  curves are also measured warming up from 290 K to 350 K. The resulting curves are shown in Figure 4.3d as a colormap, with a few individual traces in Figure 4.3e. As observed in the wide-nanogap MoRe GNR devices, the current decreases by orders of magnitude as the temperature is lowered. In the needle-like MoRe devices, the asymmetry of the current with bias voltage also increases as the temperature is decreased. In contrast to what was observed in the wide-nanogap geometry in Figure 4.2e, the slope of the log(current)-voltage characteristic is smaller in the 10 nm nanogap devices. The temperature dependence of the current at a bias voltage of 1 V versus inverse temperature is plotted in Figure 4.3f. Activation energies are once again extracted by fitting the current versus temperature at  $V = 1$  V using equation 4.1, which results in  $E_a = 138$  meV for  $T < 290$  K and  $E_a = 454$  meV for  $T > 290$  K. The obtained  $E_a$  for the MoRe 9-AGNR devices are an order of magnitude larger in 10 nm nanogap than those found for the wide-nanogap geometry.

Finally, we measured the  $IV$  characteristic of 9-AGNR devices with 10 nm nanogap geometry made of the larger work function noble metal Pd as a function of temperature. Pd is well-known for making low-resistance Ohmic electrical contacts to CNTs, as well as GNRs [27], which makes it an excellent metal to compare with MoRe as a reference. Out of the 32 devices onto which 9-AGNRs were transferred, 2 were found to be electrically conductive. The  $IV$  curves at various temperatures for one device are shown in Figure 4.4a (measurements of another device in Appendix, section 4.4). Furthermore, a nuclear tunneling scaling analysis can be found in the Appendix, section 4.4). The  $IV$  characteristic of the selected Pd device is bias symmetric. The slope of the log(I)-V characteristic is small, but larger than that measured for the MoRe 10 nm nanogaps. The devices with Pd contacts show a weaker temperature dependence of the  $IV$  characteristics than those with MoRe contacts (shown in Figure 4.3e). At  $T = 10$  K, the current is still orders of magnitude above the noise level, with currents up to 300 pA at 1 V bias voltage. In Figure 4.4b the  $IV$  characteristic of the 10 nm Pd nanogap 9-AGNR device is compared with that of the most conductive MoRe nanogap of the same geometry, at room temperature. The conductance of the MoRe devices is four orders of magnitude smaller than the Pd devices at a bias voltage of 1 V.



## 4.2 Discussion

In the *IV* characteristics of wide-nanogap MoRe 9-AGNR devices, one thing that stands out is the variation in conductance by 4 orders of magnitude. Some variation is expected due to inherent uncertainty in the transfer method. The GNRs are not globally aligned and may have lost local alignment during the transfer. The numbers of GNRs present in the different devices varies due to the inherent randomness of GNR film growth and positioning on the devices. Improvements can be made with regard to the effect of GNR alignment by growing and transferring globally aligned GNRs on Au (788) surfaces onto devices. In this case, the alignment can also be monitored by polarized Raman spectroscopy[158]. For 5-AGNR devices, aligned growth on Au (788) has been shown to significantly improve the device yield and conductance[139]. The variation in device conductance over orders of magnitude, however, points toward large variation in GNR conductance. This could possibly be explained by oxidation or inhomogeneity of the sputtered MoRe alloy contact, which would result in additional tunnel barriers and spatially varying work functions. Another possible explanation is that the gold etchant introduces a spatially non-uniform doping profile over the devices, resulting in variable band alignment.

Another peculiarity is the kink at 80 K in Figure 4.2d, which is suggestive of a change in the transport regime. The kink occurs at a voltage of approximately  $\pm 200$  mV, for which  $eV/k_B T \approx 200 \text{ meV} / 6.6 \text{ meV} \approx 30$ . This corresponds to the kink in the nuclear tunneling scaling plot in the inset of Figure 4.2f. In the context of the nuclear tunneling model, this suggests that the kink may be a transition from a thermally dominated regime to a bias voltage-driven regime.

The fact that the temperature and voltage dependence of the wide-nanogap MoRe 9-AGNR devices can be described using a nuclear tunneling model is surprising, considering the fact that the contact spacing is smaller than the average length of the GNRs. The earlier study by Richter et al. [141] described a possible hopping process from ribbon to ribbon. This suggests that either the dominant transport path is through roughly 3 GNRs or that the hopping process occurs within single GNRs with a length scale between  $30 \text{ nm} / 3 = 10 \text{ nm}$  and  $45 \text{ nm} / 3 = 15 \text{ nm}$ . The hopping sites may be local trap states, in which case the subsections in the GNR itself act as the charge transport barrier. Such trap states could be present due to a multitude of possible causes, such as overlapping of the GNRs due to rearrangement during substrate transfer, iodine doping after the conventional wet transfer technique used for the wide-nanogaps, as well as adsorbates or charge puddles [159, 160]. If the transport through our wide-nanogap MoRe devices is dominated by trap sites, that may also explain the large variability in resistances. A sparse trap density with random placement/barrier widths could result in a large variation in conductance.

For the needle-like devices, the expected device yield, based on random angular alignment only, is  $30^\circ / 180^\circ = 1/6 \approx 16\%$ . This is significantly larger than the observed yield, which suggests that there is a mechanism that decreases the observed device yield. We identify two possible mechanisms that could reduce device yield. Firstly, the probability of a GNR to bridge the electrodes could be reduced by rearrangements of the GNR film. Clustering/s-tacking of GNRs, variations in GNR density or the dissolution of GNRs into the PMMA layer and contact defects such as surface oxidation could reduce the device yield (See Ap-

pendix, section 4.4, for the Raman spectra on MoRe). Secondly, the observed device yield can be lower than the number of devices containing GNRs. We suspect the latter could be the case as the measured devices are close to the lower limit of measurable conductances in our setup ( $\sim 0.1$  pS).

The  $IV$  characteristic of the needle-like MoRe nanogap 9-AGNR devices display a significantly smaller slope of the  $\log(\text{current})$ -voltage characteristic. The most likely explanation for this is the gate voltage of  $-2$  V, applied to improve the signal-to-noise ratio. In Appendix section 4.4, we show that the normalized  $IV$  curves get increasingly more linear as the gate voltage goes from 0 to  $-4$  V. Another possible reason for the difference in linearity is that the dominant transport mechanism for these junctions is different, as transport can occur over a source-drain distance of only 6 nm. This distance is smaller than the segment length found for the wide-nanogap MoRe devices.

## 4

From the temperature dependence of the  $IV$  characteristic at 1 V, the extracted  $E_a$  can be related to the band alignment of the contact metal with the valence band of the GNR at p-type contacts. A lower  $E_a$  implies better band alignment and a smaller Schottky barrier. The  $E_a$  extracted for the MoRe-based 9-AGNR devices are an order of magnitude larger in 10 nm nanogaps compared with that in wide nanogaps. Note that for these devices, the used geometry, gate dielectric, and transfer methods are different.

We believe it is unlikely that the geometry itself plays a significant role in the band alignment on the metal surface. It is possible that the high- $\kappa$   $\text{HfO}_2$  and Pt local gate influence the band alignment if the GNR-metal contact is close to the oxide interface. The effective vacuum ( $\epsilon_r = 1$ ) distance between the Pt and the GNR is about 0.5 - 1 nm. For CNTs embedded in Pt, an expected p-doping of 0.75 eV was found by ab-initio calculations using a density functional theory + non-equilibrium Green's function simulation [161]. Assuming a similar doping effect for GNRs over a larger distance than the van der Waals gap of 0.33 nm [162], the expected doping is of the order of  $0.33 \text{ nm} / 1 \text{ nm} \times (0.75 \text{ eV}) = 240 \text{ meV}$ , which is in magnitude comparable to the observed mismatch in activation energies. This would, however, result in a better valence band alignment of the GNRs in the 10 nm nanogap devices and lower activation energies, which is the opposite of what was observed. Thus, this explanation based on geometry can not explain our observations.

The transfer method may also influence the MoRe/GNR contact by means of doping. In particular, the gold etchant step, which produces iodine complexes, is known to result in p-type doping of graphene [163]. Nanoparticle gold residues can also potentially introduce n-doping [164]. In the PMMA-membrane-based transfer technique, no contact of the gold etchant with the electrode was made and a considerably longer rinse and soak time, 8 to 24 hours versus 5 minutes, was used after the gold etchant step. This could have resulted in a lower doping level of the GNRs when compared to the conventional polymer-free wet transfer (used for wide nanogaps) and consequently worsen the band-alignment with MoRe. Besides, the GNRs are covered by PMMA after the membrane-transfer, which may by itself influence the doping of the GNRs.

To get a better understanding of the quality of the MoRe-GNR contact, a comparison with other contact metals is desirable. Activation energies are not as widely reported in the literature as room temperature resistances [27, 133, 135, 141, 165]. Thus, to compare with other

devices, we use the room-temperature resistance per unit of contact width as a benchmark, similar to what is done for 2D materials [166]. The conductance of needle-like MoRe devices with 10 nm nanogaps is around 1 pS for a contact width of around 20 nm, while for the 2  $\mu\text{m}$  wide MoRe contacts an average conductance of approximately 1 nS was found. This translates to a conductance per unit width of 0.05 pS/nm and 0.5 pS/nm, respectively.

For comparison, our Pd 10 nm nanogaps exhibit a current of 1 nA at 0.1 V, resulting in a conductance of 10 nS over the contact width of around 20 nm, which translates to 500 pS/nm. With the sample contact geometry and PMMA-assisted GNR transfer technique, the reference Pd nanogaps show significantly lower resistances than the MoRe ones. Together with the reduced temperature dependence, this suggests that the band alignment of the Pd work function with the 9-AGNR valence band is better. This could have been partially expected based on the fact that the work function of Pd (5.12 eV [29]) is larger than the work function of MoRe (4.6 - 4.96 eV [167, 168]) (See Appendix, section 4.4, for a schematic of the estimated band alignment). Another possible explanation for a larger contact resistance for MoRe contacts is the presence of a thin insulating layer on the MoRe surface. Although MoRe alloys are known to have noble-metal-like properties, surface oxidation is still possible [169].

Recently, 9-AGNR devices with Pt wide-nanogap contacts have been studied at room temperature [165]. It was found that the devices made by PMMA-based GNR transfer have a larger contact resistance than those made by polymer-free GNR transfer. This result suggests that it is well possible that the difference observed between the average conductance of the two types of MoRe devices could similarly in part be an effect of the two different transfer methods. For 1- $\mu\text{m}$  wide Pt contacts with 50 nm spacing, the reported average conductance for the devices made with PMMA-based GNR transfer and with polymer-free GNR transfer is 1.0 pS/nm and 100 pS/nm, respectively.

As a final remark, we note that our MoRe contacts to GNRs show larger contact resistances than expected based on studies on MoRe-CNT junctions, in which resistances smaller than 1 M $\Omega$  per nanotube were obtained [149, 150]. A possible explanation for this difference could be that in studies with CNTs, nanotubes were grown or annealed at temperatures higher than 850  $^{\circ}\text{C}$  on top of the MoRe contacts, resulting in molybdenum-carbon end bonds. Since no such annealing step was performed for our GNR devices, we do not expect chemical bonds between the MoRe and the GNRs. Another possible explanation for the high resistance of our 9-AGNR devices made with MoRe is that the work function of MoRe is too low to achieve a good p-type contact, while it is closer to the work function of graphene (4.62 - 4.7 eV [59, 60]). This explanation is supported by the ambipolar response in the gate dependence of our MoRe devices, which we show in Figure 4.A.10 in the Appendix. This suggests that MoRe could still be a good contact metal for GNRs with smaller bandgaps, such as 17-AGNRs [63], while larger band-gap GNRs are better contacted by high work function metals such as Pd and Pt.

For 9-AGNR devices with superconducting contacts, further advances could be made by doping the 9-AGNRs or modifying the metal/9-AGNR interface by thermal annealing. To reduce the contact resistance with MoRe, GNRs with smaller band gaps could also be considered. In addition, the effective work function of superconductors such as MoRe, Nb

or NbTiN could be increased, and thus brought into better alignment with valence band of GNRs, by applying a thin coating of Pd or Pt to their surface, e.g. in a hybrid Pd/MoRe heterostructure.

### 4.3 Conclusion

9-atom-wide armchair GNRs were transferred onto pre-fabricated wide and 10 nm MoRe nanogap contacts, as well as onto Pd electrodes with 10 nm nanogaps. To facilitate GNR transfer onto chemically fragile electrodes, we introduce a PMMA-membrane assisted transfer technique for the 10 nm MoRe nanogap contacts, which allows for controlled handling and micron-precise placement of the GNR film without exposing the electrodes to any liquid. We characterized the conductance of the devices as a function of bias voltage and temperature. In the devices, the electrical resistance increases with decreasing temperature. The  $T$ -dependence of the  $IV$  characteristics of the wide MoRe nanogap devices can be described by a nuclear tunneling model with a dimensionless dissipation coefficient  $\alpha = 9$  and  $n = 3$  hopping sites. This is despite the average GNR size of 45 nm exceeding the electrode separation of 30 nm. In comparison, the needle-like MoRe 10 nm nanogaps show a stronger  $T$ -dependence of conductance with an order of magnitude larger activation energies. The 10 nm MoRe nanogaps also show field-effect response to the local gate, indicating a p-type metal-semiconductor contact. Pd nanogaps show four orders of magnitude higher conductance for the same bias voltage at room temperature with smaller activation energies than MoRe nanogaps. That suggests the possibility of using Pd/MoRe bilayer thin film electrodes for obtaining low-resistance electrical contacts to GNRs for the realization of superconducting metallic electrodes with a nano-scale geometry down to the limit of addressing a single GNR.

## 4.4 Appendix

### Temperature dependence of other devices

In this section we show the  $IV$  curves of devices which were measured versus temperature, but were not shown in the main text. Figure 4.A.1a shows the  $IV$  characteristic of a wide MoRe nanogap 9-AGNR device versus temperature as a colormap. Individual  $IV$  curves from this map are plotted in Figure 4.A.1b. In Figure 4.A.1c, the same  $E_a$  and nuclear tunneling scaling analysis that was done in the main text is performed on this dataset. The resulting activation energy is  $E_a = 55.8$  meV, which is larger than the value found in the main text, but in the same order of magnitude. The scaling curve with the same parameters,  $\alpha = 9$  and  $\gamma = 3$ , shows reasonable agreement.

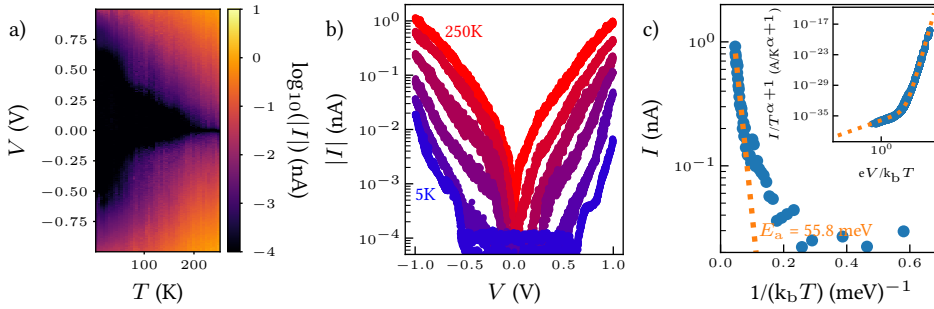


Figure 4.A.1: a) Map of current versus bias voltage and temperature of a selected wide MoRe nanogap 9-AGNR device. b) Corresponding temperature dependence of the current-voltage characteristic extracted from a). c) Corresponding temperature dependence of the current at  $V = 1$  V extracted from a). The inset shows a scaling analysis with a guide to the eye based on the nuclear tunneling model.

$IV$  curves for another 10 nm nanogap MoRe 9-AGNR device (represented by the blue curve in Figure 4.3b in the main text) were taken in the temperature range of 280 K to 170 K at a bottom-gate voltage of  $-2$  V. The data is shown as a colormap in Figure 4.A.2a. The current-voltage curves from this colormap are plotted in Figure 4.A.2b, alongside an  $IV$  curve that was taken at  $T = 350$  K. In Figure 4.A.2c the current at 1 V bias voltage and  $-2$  V gate voltage is plotted versus inverse temperature  $\frac{1}{k_B T}$ . The activation energy fits from Figure 3f are overlaid onto this plot, showing reasonable agreement with the data.

The  $IV$  curve of the other 10 nm nanogap Pd 9-AGNR device was taken at temperatures  $T = 12, 72, 100, 150, 200, 220, 290$  K. The resulting curves are shown in Figure 4.A.3.

### $IV$ to 4 V

In Figure 4.A.4, we show the  $IV$  curve of a wide nanogap MoRe 9-AGNR device up taken up to 4 V bias voltage, taken at a base temperature of 100 mK. The  $IV$  characteristic remains highly nonlinear at higher bias voltages, reaching approximately  $1 \mu A$  at a bias voltage of 4 V.

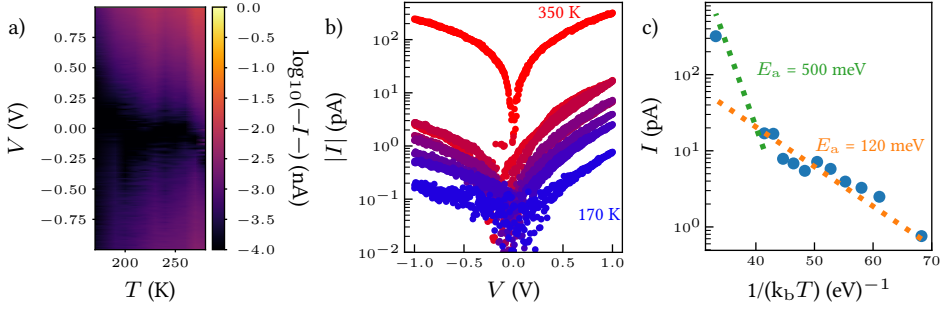


Figure 4.A.2: a) Map of current versus bias voltage and temperature of a selected 10 nm nanogap MoRe 9-AGNR device. b) Corresponding temperature dependence of the current-voltage characteristic extracted from a). c) Corresponding temperature dependence of the current at  $V = 1$  V extracted from b). The inset shows a scaling analysis with a guide to the eye based on the nuclear tunneling model.

4

## Asymmetry of the $IV$ characteristic of 10 nm nanogap MoRe 9-AGNR devices

The asymmetry of the  $IV$  curves of the 10 nm nanogap MoRe nanogap 9-AGNR device discussed in the main text in Figure 3c-f was further studied. The source and drain connections are interchanged (which we denote by ‘Flipped pins’), which reverses the bias direction while preserving the average of the source and drain voltage with respect to the gate voltage. The  $IV$  curve with flipped pins was taken at a gate voltage of  $-2$  V, shown in Figure 4.A.5 together with the  $IV$  curve without the interchanged connections. Both  $IV$  curves are asymmetric, with a larger current at positive bias voltage. This suggests that not just  $V_{\text{source}} - V_{\text{drain}}$ , but also  $(V_{\text{source}} + V_{\text{drain}})/2$  affects the  $IV$  characteristic of the device. A possible explanation for this could be an effective field effect from the voltage bias on the source and drain electrodes. By applying a positive source or drain voltage, the effective back gate voltage  $V_{\text{gate}} - \alpha(V_{\text{source}} + V_{\text{drain}})/2$ , where  $\alpha$  is a constant proportional to the ratio of source and drain capacitance to gate capacitance, becomes more negative. This effectively p-dopes (n-dopes) the GNR channel for positive (negative) bias voltages. Since this effect does not depend on the bias direction, it is unaffected by interchanging the source and drain pins. A small asymmetry remains upon flipping the pins, which could be due to a small asymmetry between source and drain capacitance or possibly due to asymmetry in the electronic coupling.

## Time dependence of hysteresis effect

To investigate the time-dependence of the hysteresis effect, two additional types of measurement were done on the 10 nm nanogap MoRe 9-AGNR device characterized in the main text.

In the first measurement, the current was measured versus gate voltage at a fixed bias voltage of 1 V. The measurement was performed at two different gate voltage ramp speeds; 0.5 V/min and 0.05 V/min. The resulting curves are shown in Figure 4.A.6a. Both curves display hysteresis, with a larger current loop for the faster sweep. The dependence on the sweep rate indicates that the hysteresis loop is time-dependent.

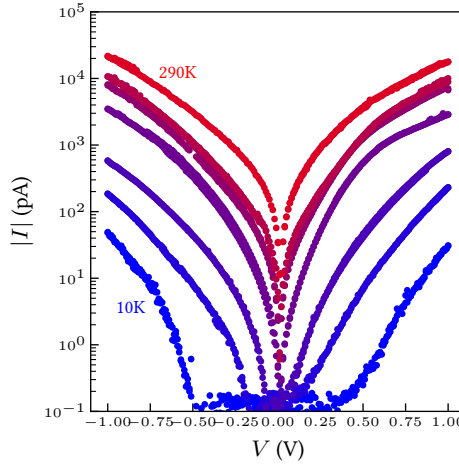


Figure 4.A.3: Current versus bias voltage and temperature of a selected 10 nm nanogap Pd 9-AGNR device at temperatures 10, 70, 100, 150, 200, 220 and 290 K.

A second type of measurement was performed to further characterize this time-dependence. The current was measured versus time during - and after - the ramping of the gate voltage to  $-2$  V at a rate of  $1$  V/min. The resulting data is shown in Figure 4.A.6b. The blue curve in this figure shows the current versus time, while the orange curve shows the gate voltage versus time. The dotted black curve is a guide to the eye, which shows an exponential dependence  $I = I_0 + I_1 e^{-\frac{t}{\tau}}$  with  $\tau = 1$  min. As the gate voltage is ramped, the current increases without a delay. From the end of the gate voltage ramp at 2 minutes onward, the current is well-described by an exponential decay with a timescale of roughly 1 minute. The time-effect thus counteracts the field effect from the back-gate. This suggests a charge-transfer mechanism[170], which may originate from electrochemical reactions with adsorbates, such as water[171, 172], in which silanol groups at the  $\text{SiO}_2$  substrate termination are known to play a role. The hysteresis is opposite to the previously reported hysteresis observed in GNR devices attributed to charge traps in  $\text{SiO}_2$ [157]. Hysteresis due to adsorbates has previously been reduced by passivation of devices with HMDS[156] to make the substrate hydrophobic. For a more detailed discussion on hysteresis effects in graphene nanostructures, we refer to the review article by Lu et al.[173].

### Nuclear tunneling analysis of the 10 nm nanogap Pd 9-AGNR device

In Figure 4.A.7, we show a nuclear tunneling scaling analysis of the data in Figure 4a. By eye, the rescaled  $IV$  curves all fall onto a single curve for  $\alpha = 5$ . A fit was done for  $\gamma$ , which resulted in  $\gamma = 0.145$ , which corresponds to roughly 7 hopping sites. We note that the curve does not fit well for  $\frac{eV}{k_b T} < 10$ . Furthermore, the number of hopping sites is large given the 6 nm contact spacing. This suggests that the nuclear tunneling model is not a satisfactory description of the electronic transport characteristics in this device.



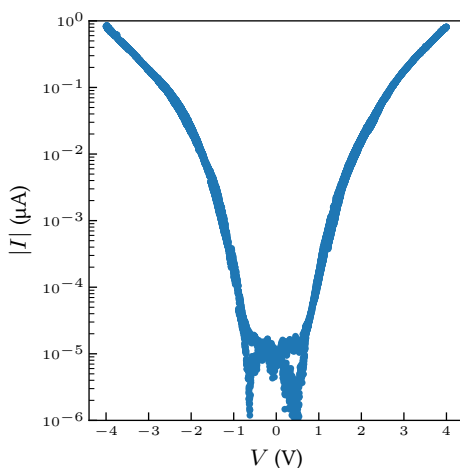


Figure 4.A.4: *IV* curve up to a bias voltage of 4 V of a wide MoRe nanogap 9-AGNR device at a temperature of 100 mK

## Raman Spectroscopy of GNR devices

To confirm the presence and structural integrity of the GNRs, Raman spectroscopy ( $\lambda = 514$  nm) was performed on the GNRs for the wide MoRe nanogap electrodes and the needle-like MoRe nanogap electrodes. In the case of the wide MoRe nanogap electrodes, characterization was performed of GNRs on the 285 nm thick  $\text{SiO}_2$ . For the needle-like MoRe electrodes, the characterization was performed on the 15 nm  $\text{HfO}_2$  covered TiPt bottom gate, which acts as a Raman optimized substrate[158]. The resulting Raman spectra are shown in Figure 4.A.8. The energies of the characteristic G, D and CH peaks for the polymer-free transferred method are  $1595\text{ cm}^{-1}$ ,  $1337\text{ cm}^{-1}$  and  $1230\text{ cm}^{-1}$  respectively. For the PMMA transfer, the G, D and CH peaks are found at  $1593\text{ cm}^{-1}$ ,  $1337\text{ cm}^{-1}$  and  $1234\text{ cm}^{-1}$ . This is similar to the spectra that have been measured before for 9-AGNRs[152, 158]. The presence of the G peak around  $1595\text{ cm}^{-1}$  in both spectra suggests a limited degree of doping in the transferred GNRs and no significant difference between the two substrate transfer methods. Beside the G, D and CH peaks, a sharp peak at  $313\text{ cm}^{-1}$  for the wide nanogap GNR devices and a broad peak at  $311\text{ cm}^{-1}$  for the needle-like GNR devices can be indicative of the radial breathing-like mode (RBLM), which is related to the width of the 9-AGNRs, expected at  $311\text{ cm}^{-1}$ . Although the observed wavenumber matches the expected RBLM wavenumber, it should be noted that Si also has a Raman active vibration TA mode at  $301\text{ cm}^{-1}$ [174]. Thus, we can not with certainty identify the broad peak in the needle-like GNR devices as the RBLM peak. If we suppose that it is the RBLM peak, a possible explanation for the broadening of the RBLM peak could be increased damping of large wavelength vibrations in the GNRs transferred by the PMMA-assisted method. The peaks at  $520\text{ cm}^{-1}$  and  $950\text{ cm}^{-1}$  are related to vibrational modes of the silicon substrate.

To investigate the properties of GNRs on MoRe as well, Raman spectra were taken on the MoRe part of the devices. In Figure 4.A.9, we show Raman spectra on the contact pads of the wide MoRe nanogap devices and the needle-like MoRe nanogap devices. The C-H,



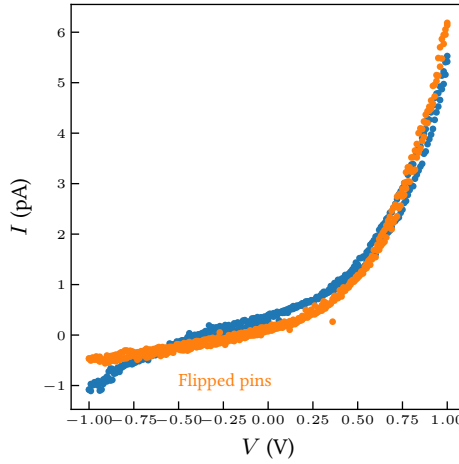


Figure 4.A.5: Current-voltage curve of the 10 nm nanogap MoRe 9-AGNR device studied in the main text. The blue curve is the blue  $IV$  curve shown in Fig. 3b) in the main text. The  $IV$  curve upon interchanging source and drain connections ('Flipped pins') is plotted in orange.

D and G peaks show the presence of the GNRs on the MoRe. The Raman peaks between  $800\text{ cm}^{-1}$  and  $1000\text{ cm}^{-1}$  are characteristic for the vibrational modes of Mo=O bonds[175] and Re=O bonds[176]. In addition, we observe an additional peak below the G peak of the GNRs, at a Raman shift of  $1556\text{ cm}^{-1}$ .

To investigate the new peak on MoRe close to the G-peak, a Raman spectrum was taken on an MoRe contact pad without GNRs. This spectrum is shown in Figure 4.A.9c. In this spectrum, we still observe the presence of the vibrational peak at  $1556\text{ cm}^{-1}$ , which suggests that it should not be attributed to interaction of MoRe and GNRs, but rather to a vibrational mode related to MoRe itself. The peak is rather sharp and appears to correspond to molecular  $\text{O}_2$ [177], suggesting adsorption of  $\text{O}_2$  gas onto the MoRe film or release of  $\text{O}_2$  gas by the MoRe film during the Raman spectroscopy. By comparing the spectrum on bare MoRe to the spectrum with GNRs, we do not observe any obvious peaks that might be related to the formation of Mo-C bonds, which are expected to be found at  $231$  and  $656\text{ cm}^{-1}$ [178]. We do, however, see that the broad peak around  $300\text{ cm}^{-1}$  changes shape between the spectra with and without GNRs, again suggesting the presence of the RBLM mode.

### Gate voltage dependence at $T = 350\text{ K}$

For the 10 nm nanogap MoRe devices, we also studied the gate dependence at a temperature of 350 K. This temperature was chosen because the measured conductance of the devices was larger at this temperature. We measured the current through the devices versus gate and bias voltage. In an attempt to reduce the effect of hysteresis observed in the main text, the data was first taken from a gate voltage of 0 V to a gate voltage of  $-4\text{ V}$  and subsequently ramped back to 0 V. After waiting for 10 minutes at 0 V, another map was taken from 0 V to 4 V. The data is plotted in Figure 4.A.10a as a single color map. The

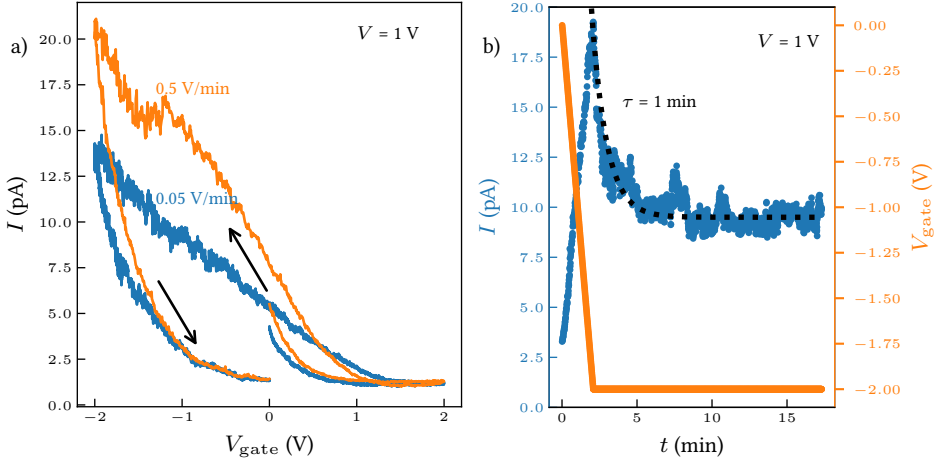


Figure 4.A.6: a) Current versus gate voltage for the 10 nm nanogap MoRe 9-AGNR device in the main text. The curve was taken at two different ramping speeds, 0.5 V/min and 0.05 V/min. The arrows indicate the sweep direction of the gate voltage. b) Measurement of the current versus time during and after ramping the gate-voltage to  $-2$  V at a rate of 1 V/min. The bias voltage was fixed at 1 V. The current (gate voltage) is plotted in blue (orange). As a guide to the eye, an offset exponential decay with time constant  $\tau = 1$  min is plotted (dotted black).

color map does show a discontinuity at zero gate voltage. The device has a much larger current for negative gate voltages than for positive gate voltages. To further illustrate this, in Figure 4.A.10b, we plot a trace at a bias voltage of 1 V, which shows that going from 0 V gate voltage to  $-4$  V, the current increases by 3 orders of magnitude, while an increase of at most 1 order of magnitude is seen going from  $V_{\text{gate}} = 0$  V to  $V_{\text{gate}} = 4$  V. This is in line with the idea that the contact is p-type in nature. At gate voltages lower than  $-3$  V, the increase in  $\log(I)$  starts to flatten off. The shape of the  $IV$  characteristic of the devices also changes as a function of the applied gate voltage.

In Figure 4.A.10c we plot the  $IV$  characteristic at gate voltages of 0 V,  $-2$  V and  $-4$  V. The curves are normalized to  $\max(|I|)$  to illuminate the change in shape. The  $IV$  characteristic becomes more linear as the gate voltage is swept to negative values. At 0 V gate voltage the  $IV$  characteristic is highly non-linear, while at  $-4$  V a nearly linear curve is obtained. In the transition region, the  $IV$  characteristic is more bias voltage asymmetric, with a larger current for positive bias voltages. The increase in linearity could tentatively be explained by a change in the contact to a near-ohmic-regime. A current of only 1 nA at 1 V is, however, orders of magnitude below the conductance of the order of  $G_0 \approx 77 \mu\text{S}$  observed for devices with ohmic contacts to carbon nanotubes [146]. In combination with the large activation energies for 10 nm nanogap MoRe devices, this highlights that the nature of the contact to the GNRs can not be determined solely by the linearity of the current-voltage characteristic.

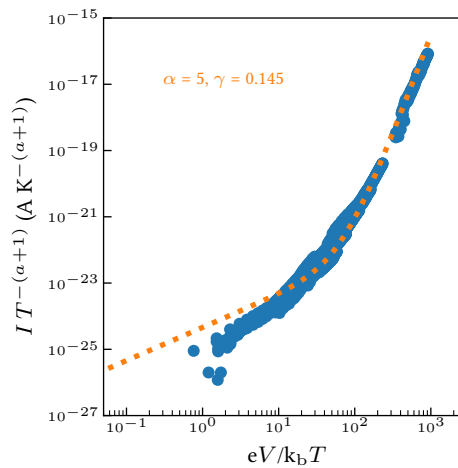


Figure 4.A.7: Nuclear tunneling scaling analysis for the selected 10 nm nanogap Pd 9-AGNR device.

### Band alignment of 9-AGNRs with MoRe

In order to better understand the band alignment of 9-AGNRs with MoRe and Pd, we here illustrate the alignment of the conduction and valence band of 9-AGNRs with the electrochemical potential on MoRe, Pd and SiO<sub>2</sub>, assuming an electronic band gap of 1.4 eV[61] for metal adsorbed GNRs and a chemical potential of 4.6 eV for 9-AGNRs in vacuum. The resulting band alignment is shown in Figure 4.A.11. Following the main text, for MoRe, we take a chemical potential of 4.8 eV and for Pd, we take a chemical potential of 5.1 eV. We apply the Schottky-Mott rule to estimate the band alignment[28], which is known to be valid for 9-AGNRs on Au[61]. For the SiO<sub>2</sub>, we assume no doping here. It should be noted that the actual band alignments could differ due to doping effects at the interfaces. Furthermore, the band gap of GNRs on an insulating substrate such as SiO<sub>2</sub> could differ from the band gap on a metal due to the lack of image charge effects on SiO<sub>2</sub>[61].

### Optical microscopy images of the devices

For completeness, we here add optical microscopy images of the wide MoRe nanogap devices and the needle-like MoRe nanogap devices, which we show in Figure 4.A.12. In the wide MoRe nanogap devices, the 9-AGNR film can be seen as a discoloration on 285 nm thick SiO<sub>2</sub> on Si by optical microscopy images taken with an increased exposure time. The PMMA covered needle-like nanogap 9-AGNR devices, on the other hand, show no clearly visible GNR film.

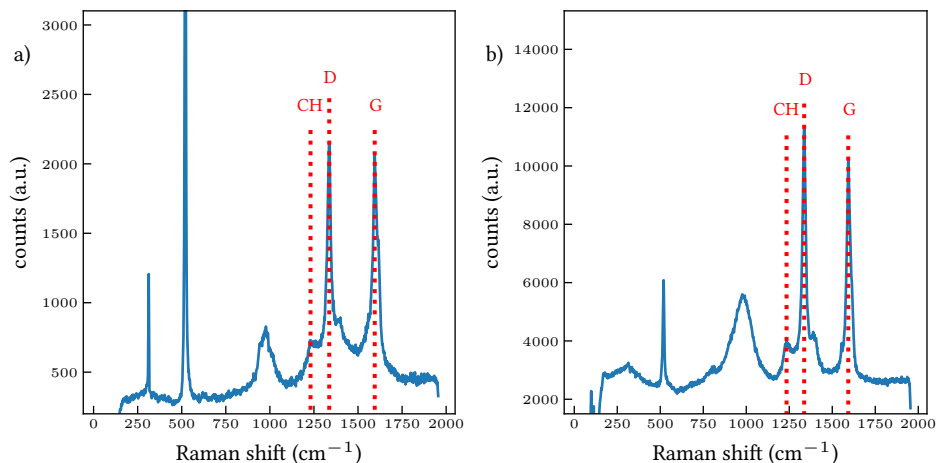


Figure 4.A.8: Raman spectrum taken with a 514 nm laser a) on the SiO<sub>2</sub> near the wide MoRe nanogap 9-AGNR devices. b) on the 15 nm HfO<sub>2</sub> covered TiPt bottom gate near the needle-like MoRe nanogap 9-AGNR devices. The G, D and CH modes are indicated by the red dotted lines.

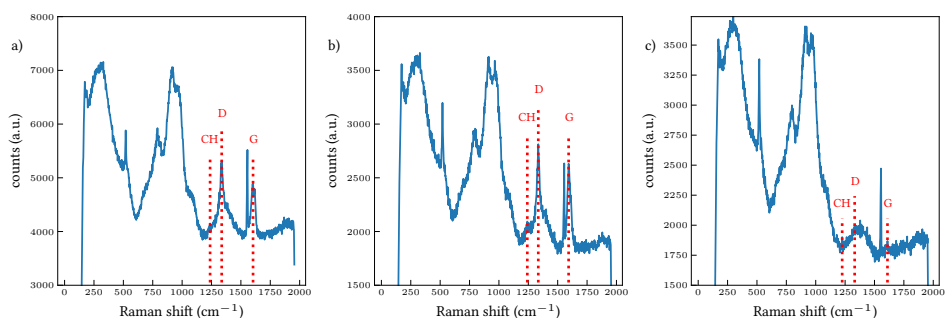


Figure 4.A.9: Raman spectrum taken with a 514 nm laser a) on the contact pad of a wide MoRe nanogap 9-AGNR device b) on the contact pad of a needle-like MoRe nanogap 9-AGNR device. c) on the contact pad of a needle-like MoRe nanogap device that was not covered by GNRs. The identified G, D and CH modes are indicated by the red dotted lines.

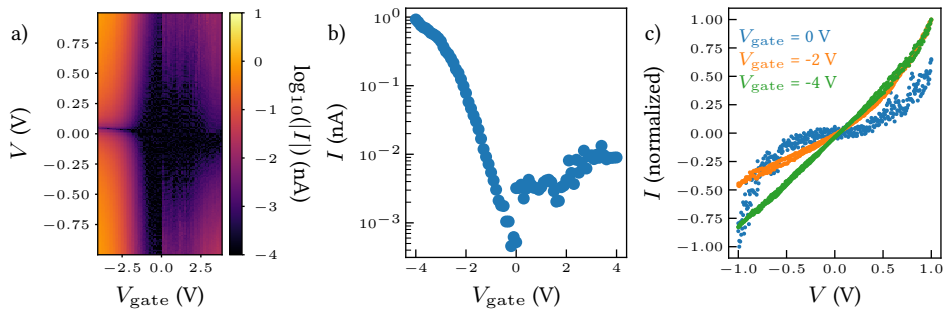


Figure 4.A.10: a) Logarithmic color map of the current versus bias voltage and gate voltage for a 10 nm nanogap MoRe 9-AGNR device at a temperature of 350 K. b) Current versus gate voltage curve at a fixed bias voltage of 1 V; extracted from a). c) Normalized  $IV$  curves of a 10 nm nanogap MoRe 9-AGNR at a temperature of 350 K and gate voltages of 0, -2, and -4 V.

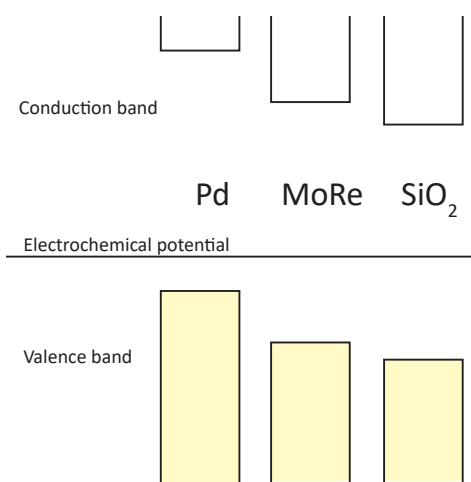


Figure 4.A.11: Graphical representation of the band-alignment between 9-AGNR valence and conduction bands with respect to the chemical potential on MoRe, Pd and SiO<sub>2</sub> estimated by the Schottky-Mott rule.

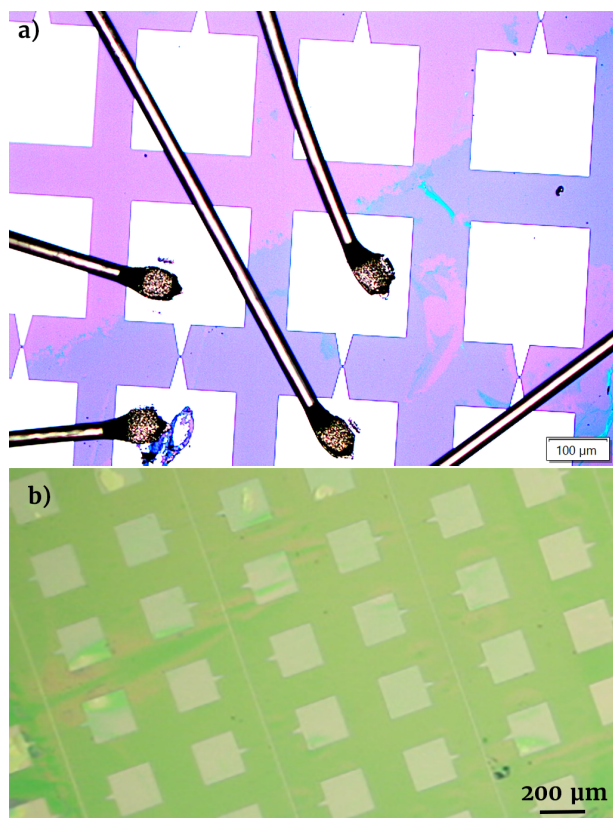


Figure 4.A.12: Optical microscopy image of the 9-AGNR devices. a) Wide nanogap 9-AGNR MoRe devices with wirebonds. The GNR film is visible as a color change in the purposely oversaturated image. b) PMMA covered needle-like MoRe nanogap devices post PMMA-membrane assisted 9-AGNR transfer.

## 5

# Study of MoRe Interfaces to Ligand-Free Gold Nanoparticles Deposited by Aerosol

5

*In this chapter, ligand-free gold nanoparticles were created by spark ablation in aerosol and deposited by impaction from aerosol onto nanogap electrodes made of the superconducting alloy  $\text{Mo}_{62}\text{Re}_{38}$  with a needlelike geometry. To investigate the contact resistance and electrical interface transparency between the MoRe electrode and the Au nanoparticles, two-terminal electrical measurements were performed to characterize the resistance at room temperature and the differential conductance features at a temperature of 40 mK. At room temperature, the resistance of most devices lies in the range of 1 and 100 k $\Omega$ . The low-temperature results are compared to the Blonder-Tinkham-Klapwijk (BTK) model for ballistic normal metal-superconductor interfaces. Comparison to the BTK model suggests a high interface transparency  $\mathcal{T} > 0.5$  at the interface between the MoRe electrode and the Au nanoparticles in low-resistance devices, but also reveals the presence of a series resistance and peaks in the differential conductance that can not be explained by the BTK theory. It is shown that these peaks can be qualitatively understood by a critical current effect and an additional contribution from the diffusive Maxwell resistance. The results demonstrate that the contact resistance of prepatterned MoRe nanogap electrodes to ligand-free gold nanoparticles is not significantly limited by tunnel barriers (i.e., due to oxidation or contamination). Based on this, it is concluded that other nanoparticles or nanostructures could be contacted by MoRe (nanogap) electrodes without a significant contribution of transport barriers originating from the MoRe surface.*

---

I would like to thank VSPARTICLE for their time and effort in providing me with the gold nanoparticles. I also want to thank Thomas Pijls for his contribution during his bachelor thesis project.

## 5.1 Introduction

The surface properties of metals are of key importance for making electrical contacts to nanoscale objects. Any poorly conductive component, such as surface oxides, molecular adsorbates and polymer residues can significantly affect the quality of such interfaces. To gain control over the electrical properties of such interfaces, various techniques can be used to treat the surfaces, such as reactive ion etching, plasma cleaning, ion milling of surfaces and thermal annealing of metal interfaces. Most approaches can be divided into the following three categories:

1. Modification of the surface of the nanoscale object on interest prior to deposition of metal electrodes.
2. Modification of the surface of prefabricated metal electrodes prior to deposition of the nanoscale object.
3. Modification of the interface between the metal and the nanoscale object of interest in a completed device.

### 5

The modification of the surface of the object of study can be acceptable when the surface makes up a small portion of the volume. For nanoscale to atomic scale objects, on the other hand, this is often not desirable. Out of the listed options, only the modification of prefabricated electrodes guarantees that the nanoscale object of interest is intact. However, as the surface of most metals rapidly oxidizes in air, the use of prefabricated electrodes is limited to noble metals, unless deposition of the nanoscale object can be performed without breaking the vacuum after surface cleaning. For noble metals, on the other hand, surface cleaning is often not necessary if devices are properly made, since oxidation is not a problem at all.

For the purpose of making interfaces between a nanoscale object and a superconductor, clean interfaces are crucial. For example, the quality of Josephson junctions, junctions in which the nanoscale object can be incorporated as a 'weak link' between two superconducting electrodes, is strongly dependent on the electrical interface transparency. Unfortunately, nearly all commonly used superconductors such as Al, Sn, Pb and Nb are known to oxidize, which complicates making superconducting-hybrid structures with nanoscale objects. Rhenium is a superconducting element that is close to being a noble metal and sometimes classified as one[179]. It has a positive standard electrode potential of 0.3 V[180], which is close to the standard electrode potential of water 0.41 eV. While this means that rhenium normally oxidizes in water with a pH of 7, it does not corrode in acidic environments below a pH of 5. In air, the oxides that form have been suggested to be hydrates, particularly volatile  $\text{Re}_2\text{O}_7(\text{H}_2\text{O})_2$ [181] crystallites. As a result of this, oxidation depends on humidity and can be kept minimal below 30% humidity.

The superconducting MoRe alloys incorporate both Mo and Re. At a 62:38 ratio, the alloy has a bulk critical temperature of approximately 9 K, which is significantly larger than the critical temperature of the individual elements (0.92 K for Mo[64], 2.4 K for Re[64]). While prefabricated contacts made of MoRe alloy have been successfully used to contact carbon nanotubes[149, 150], annealing above 800 °C was necessary to improve interface transparency. Interestingly, the studies with CNTs do not mention surface oxides, nor



report a change in device performance upon annealing above 300–400 °C, which suggests that the interfaces made with MoRe are not limited by surface oxidation.

To further investigate the surface properties of MoRe, here we study the interfaces between MoRe devices and aerosol deposited ligand-free gold nanoparticles (AuNP). The MoRe devices consist of a pair of 25 nm thick needlelike nanowires separated by a spacing of approximately 10 nm. In the 10 nm gap, nanoparticles can be trapped by chance. The devices have been exposed to approximately 50% relative humidity for approximately 3 hours prior to deposition of gold nanoparticles by impaction. The gold nanoparticles are produced by an early version of the VSP-P1 nanoparticle printer. Importantly, the entire nanoparticle production and deposition process was done in aerosol, resulting in a contaminant-free deposition of gold nanoparticles without an insulating shell.

The electronic interfaces between MoRe and Au nanoparticles are studied in this chapter by means of Andreev reflection spectroscopy. Making use of the fact that normal metal-superconductor interfaces and Josephson junctions display excess conductance in the superconducting state at low bias voltages ( $< 1.3$  mV), measurements of the low-temperature current versus voltage ( $IV$ ) characteristic will be used to estimate the interface scattering parameter,  $Z$ , and the corresponding interface transparency,  $\mathcal{T} = \frac{1}{1+Z^2}$ , through the Blonder-Tinkham-Klapwijk (BTK) theory[75].

## 5.2 Room temperature characterization

Gold nanoparticles were deposited onto needlelike MoRe nanogap electrodes, with an electrode separation of 10 nm. The deposition was performed by the VSParticle nanoparticle printer by spark ablation of gold electrodes in a flow of argon gas. Spark ablation results in a range of charged metal nanoparticles that grow by agglomeration in aerosol. The created gold nanoparticles in aerosol were selected by mass to have the mass of a spherical gold nanoparticle with a diameter of 12 nm. The gold nanoparticles were ejected out of an exhaust nozzle, which is shown retracted from the sample in Figure 5.1a. The sample was mounted onto a motorized stage in a low-vacuum ( $< 1$  mbar) chamber. Driven by the pressure difference between the inside of the nozzle and the vacuum chamber, deposition of nanoparticles occurred by impaction onto the sample. The devices were angularly aligned with respect to the motor axes by optical inspection. To produce similar nanoparticle coverages on a row of devices, the stage was moved back and forth at a constant velocity along a line for a set number of times. The nanoparticle coverage was varied by changing the number of times that the exhaust nozzle was scanned across the devices.

A high coverage deposition and a low coverage deposition were performed, targeting 10% and 1% nanoparticle coverage respectively. Optical microscopy images of these depositions are shown in Figures 5.1b and 5.1c. The high coverage deposition resulted in clearly visible green lines with a redish center on the Si/SiO<sub>2</sub> substrate. The low coverage deposition, on the other hand, resulted in shaded blue/purple lines on the substrate.

Since the nanoparticles were made by spark ablation, the larger particles form due to the agglomeration of smaller charged gold nanoparticles in aerosol[182]. Thus, the larger nanoparticles are not spherical and instead often form chain-like structures. This can be

seen in SEM images after electrical characterization of a separate sample with a coverage of 0.1%, which is shown in Figure 5.1d. Note that the shape and size of the nanoparticles is not well controlled. Most deposited nanoparticles have lengths over 20 nm. For the samples for which electrical characterization is reported in this chapter, it was discovered after electrical characterization that the gold nanoparticle depositions were denser than expected. SEM imaging of the high-coverage deposition resulted in a connected network of clustered Au nanoparticles, forming a nanoporous gold film, shown in Figure 5.1e. The actual coverage exceeded the intended 10% coverage. The 1% low-coverage also showed the formation of clusters of gold nanoparticles, but as opposed to the 10% coverage sample, these clusters are limited in size and do not form micrometer-scale networks. In Figure 5.1f, an SEM image of such gold nanoparticle clusters on an MoRe nanogap is shown. The gold nanoparticles connect the two sides of the nanogap device.

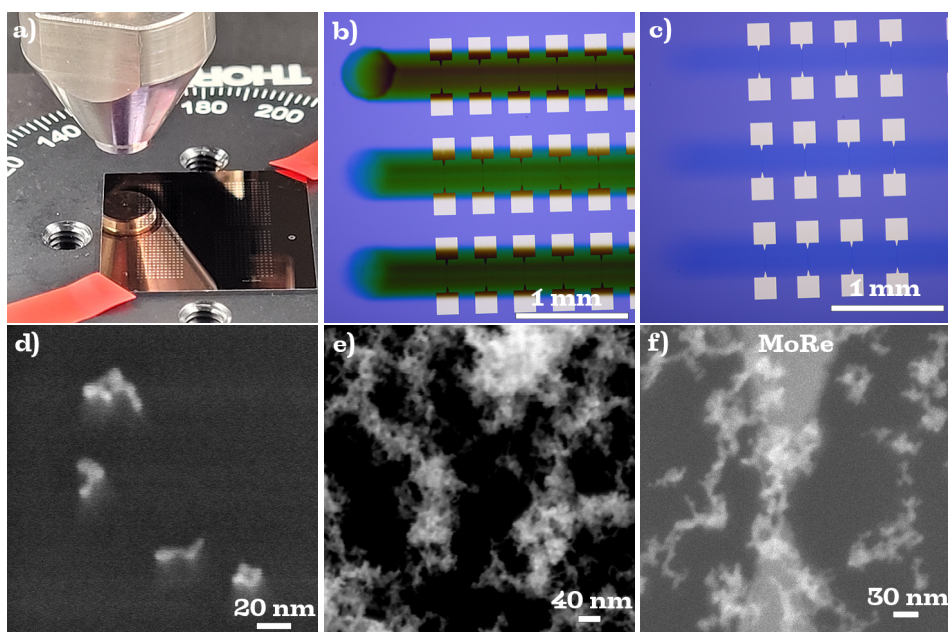


Figure 5.1: a) Photo camera image of the exhaust nozzle of the VSParticle nanoparticle printer and sample after deposition. b) Optical microscopy image of a set of devices with a high coverage of gold nanoparticles deposited. c) Optical microscopy image of a set of devices with a low coverage ( $\sim 1\%$ ) of gold nanoparticles deposited. d) SEM image of individual gold nanoparticles created by spark ablation with 12 nm size selection. e) SEM image of a nanoporous gold network created by deposition of nanoparticles, corresponding to a high coverage. f) SEM image of a nanogap junction with a low density of gold nanoparticles. At low particle density, the deposited gold nanoparticles aggregate and form clusters.

Electrical characterization was performed on the MoRe nanogaps prior to deposition of the nanoparticles to ensure that the nanogap electrodes were not electrically connected. First, MoRe nanogap devices were quickly checked using a Beep-R box (QT designed instrumentation) sample tester that outputs an approximate resistance value. Devices with a resistance larger than  $10\text{ G}\Omega$  (electrically open) at a bias voltage of 10 mV were further characterized by a two-terminal measurement of the electrical current versus the applied

bias voltage (*IV* characteristic). For this measurement, a bias voltage range of  $-1$  to  $1$  V was applied. Devices for which the current exceeded  $1$  pA at  $1$  V were excluded from further characterization. The MoRe nanogaps that were found to have a resistance below  $10$  G $\Omega$  (electrically shorted) were also electrically characterized by *IV* measurements. All shorted devices were found to have a resistance of  $42 \pm 1$  k $\Omega$ . An example *IV* curve of a shorted nanogap device is shown in Figure 5.2a. The *IV* curve is completely linear, which suggests a fully conductive/metallic connection in these devices. This resistance will be referred to and used as the series resistance  $R_{\text{series}}$  of the MoRe nanogap devices.

After the deposition of ligand-free gold nanoparticles, the devices were first pre-characterized with a BEEP-R box. The nanogaps onto which a high-coverage deposition was performed were all electrically shorted, with resistances on the order of  $1$  k $\Omega$  as reported by the BEEP-R box. *IV* characterization of these devices indicated a resistance of approximately  $7.7$  k $\Omega$ . In addition, by connecting the BEEP-R box to contact pads of separate devices, it was found that all devices in a row onto which nanoparticles were deposited were electrically connected. Because of the electrical connection between different devices, low-temperature characterization of these devices was not performed.

Characterization of the low-coverage devices by BEEP-R box measurements showed that 42 out of 53 open nanogap devices onto which nanoparticles were deposited were electrically connected after gold nanoparticle deposition. All devices were also characterized by *IV* measurements, with a bias voltage range of  $-50$  to  $50$  mV, which resulted in the discovery of one additional connected junction, resulting in a yield of 43 electrically connected junctions post nanoparticle deposition out of 53 junctions that were open prior to nanoparticle deposition. In Figure 5.2b, an example of the *IV* curves prior to deposition (blue line) and after nanoparticle deposition (orange line) is given for device A8. Prior to nanoparticle deposition, the *IV* curve has a negligible slope and is dominated by noise on the order of  $1$  pA peak to peak with a resistance larger than  $1$  T $\Omega$ . After nanoparticle deposition, the *IV* curve has a maximum current on the order of  $1$   $\mu$ A at  $50$  mV and resembles the *IV* curve of the shorted MoRe nanogap device in 5.2a. This implies that the majority of the electrical resistance in this representative device originates from the MoRe leads, rather than from the nanoparticle or the electrode-nanoparticle interfaces.

The resistance,  $R$ , of the 43 devices was extracted by fitting the *IV* curve to a linear function,  $I = I_0 + \frac{V}{R}$ , taking into account a small offset current,  $I_0$ . The resulting resistance values are compiled into a histogram in Figure 5.2c. Since this histogram does not take into account the series resistance of the electrodes, a second histogram can be made to account for this. Assuming that the electrical resistance of devices can be modeled by two resistances in series, relating to the nanoparticles in the nanogap and the series resistance of  $42$  k $\Omega$ , a histogram of the MoRe-AuNP-MoRe junction at the nanogap can be extracted by subtracting  $42$  k $\Omega$ . This is plotted in Figure 5.2d. Note that this implicitly assumes that the resistances of the MoRe nanowires leading up to the nanogap are not significantly modified/reduced by parallel conduction paths through the deposited gold nanoparticles. The resulting histogram shows that most devices have resistance between  $1$  and  $100$  k $\Omega$ , while a few devices with a resistance of  $1$  M $\Omega$  to  $1$  G $\Omega$  were also found. The histogram shows a large peak at a resistance of  $10$  k $\Omega$ , where 10 out of 43 devices were found. The

room temperature measurements thus confirm that the surfaces of MoRe are clean enough to make low-resistance (1-100 k $\Omega$ ) electrical contacts to the deposited nanoparticles. This, however, does not necessarily imply highly electrically transparent interfaces. To investigate whether the electrical interface transparency between the MoRe electrodes and the Au nanoparticles is also high, low-temperature electrical characterization was performed next.

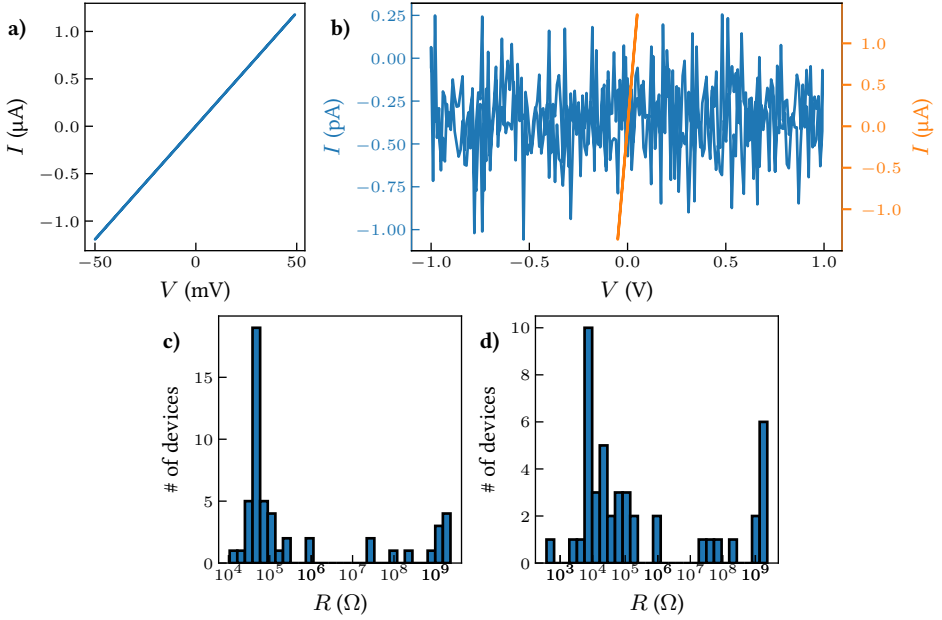


Figure 5.2: a)  $IV$  curve of a shorted needlelike MoRe nanogap device with a resistance of 42 k $\Omega$ . b)  $IV$  curve prior to deposition (in blue) and after gold nanoparticle deposition for device A8. c) Histogram of the device resistances. d) Histogram of the device resistances with a series resistance of 42 k $\Omega$  subtracted.

### 5.3 Low-temperature characterization

The devices were wire bonded and loaded into a He-3/He-4 dilution fridge. After cooling the devices down to a base temperature of 40 mK ( $\sim 100$  mK electronic temperature), electrical  $IV$  characterization was performed. Two distinct types of devices were bonded, namely high-resistance devices, with  $R_N \sim 1$  M $\Omega$  for all bonded devices, and low resistance devices, with  $R_N \leq 20$  k $\Omega$ . High-resistance devices point towards the presence of tunnel barriers and should reflect the superconducting gap of MoRe in transport. Low resistance devices, on the other hand, could either be explained by low transparency interfaces, with many transport channels in parallel, or by a few highly transparent transport channels at the NS interface. The BTK model will be used to extract the effective interface transparency.

### 5.3.1 High-resistance devices

Devices with a large resistance (on the order of 1 M $\Omega$ ) were measured by applying a voltage bias of  $-10$  to  $10$  mV. The  $IV$  curve of such a device, labeled device A4, is shown in Figure 5.3a. The  $IV$  curve of this device is mostly linear, with a region of reduced slope at zero bias voltage. By taking a numerical derivative of the current, the differential conductance,  $dI/dV$ , can be obtained. This is plotted versus bias voltage in Figure 5.3b. Notably, the  $dI/dV$  curve is not flat, as would be expected for an ideal resistor, but instead displays several peaks and dips and is slightly larger for positive bias voltages. The flat region in the  $IV$  curve produces a dip in the  $dI/dV$  at zero bias voltage. In figure 5.3c, a zoomed-in plot of the gap in the differential conductance this peak is shown. At bias voltages of  $\pm 1.18$  mV, indicated by the red lines, peaks that are symmetric in bias voltage can be seen. The observed bias voltage location of these peaks matches the expected voltage scale ( $\pm \frac{|\Delta|}{e} \approx \pm 1.3$  mV, where  $2|\Delta|$  is the energy scale of the gap in the superconducting density of states) for superconductivity in MoRe, which has a critical temperature of approximately 8-9 K, in agreement with the expected presence of superconductivity in the MoRe nanogap electrode. A gap in the  $dI/dV$  was observed in all four high-resistance junctions that were measured. Interpreting such a gap through the BTK theory suggests that at least one of the two NS interfaces between the Au NPs and the MoRe electrodes has a low interface transparency. Here I will assume that a single NS contact dominates the device resistance. Given a differential conductance suppression  $\frac{dI}{dV}(V=0)/\frac{dI}{dV}(V \gg \frac{|\Delta|}{e})$  by a factor of approximately 10, the interface transparency can be calculated using the following expression by Beenakker[183]:  $\frac{dI}{dV}(V=0)/\frac{dI}{dV}(V \gg \frac{|\Delta|}{e}) = \frac{2\mathcal{T}^2}{(2-\mathcal{T})^2} \approx \frac{\mathcal{T}}{2}$ , where the last equality holds at low transparency. This results in a transparency  $\mathcal{T} \approx 0.05$ . Assuming a single conduction channel, this is in disagreement with the observed conductance, which is an order of magnitude lower than  $\mathcal{T} G_0 \approx 0.05 G_0 \approx 4 \mu\text{S}$ . Assuming the presence of more conduction channels will only increase this conductance. Thus, simple BTK theory is not in agreement with the observed differential conductance curve.

By implementing a finite quasiparticle lifetime, using a Dynes parameter  $\Gamma$ , both the conductance suppression and the conductance can be matched. The Dynes parameter modifies the zero-bias density of states, which results in a transparency-independent contribution that is related to the presence of normal quasiparticles below the superconducting gap in the superconductor. Matching the zero-bias conductance, the observed peak locations and the normal state conductance, the parameters  $\Delta = 1.10$  meV,  $Z = 15$  ( $\mathcal{T} = \frac{1}{1+Z^2} = 0.0044$ ),  $\Gamma \approx 0.10|\Delta| \approx 0.10$  meV were taken. The resulting curve is plotted in orange in Figure 5.3c. Even when a finite quasiparticle lifetime, which results in broadening, is included in the BTK model, the model produces a differential conductance curve which overshoots the peaks and undershoots in the gap region. Although the model reproduces the width of the measured peaks, the height and extended tails that the BTK model produces are not observed in the data. In the low bias voltage/sub-gap region, the differential conductance of the sample shows shoulder-like features at  $V \approx \pm 0.55$  mV, which are absent in the BTK model. Tentatively, these might be explained by multiple Andreev reflections (MAR) across the superconducting electrodes. Theoretically, these should have an amplitude on the order of  $\mathcal{T} = 0.0044$  smaller than the normal state conductance, resulting in expected

features on the order of  $0.001 \mu\text{S}$ . This is significantly smaller than the size of the observed shoulder-like features ( $\sim 0.01 \mu\text{S}$ ).

A zero-bias conductance suppression of the same magnitude was observed in three highly resistive devices. One device instead displayed a much larger conductance suppression. This device showed gate voltage tunable Coulomb-blockade features, which will not be explored in this thesis. The  $IV$  characteristics of the highly resistive MoRe-Au NP junctions show the qualitative signatures of a superconducting gap in the differential conductance, thus revealing the presence of poorly transparent NS interfaces. The results from the highly resistive junctions can be used as a baseline for understanding the characteristics of the low-resistance junctions. In the next section, low-temperature measurements of these devices will be analyzed. If the low-resistance junctions also exhibit a low interface transparency, similar behavior is expected.

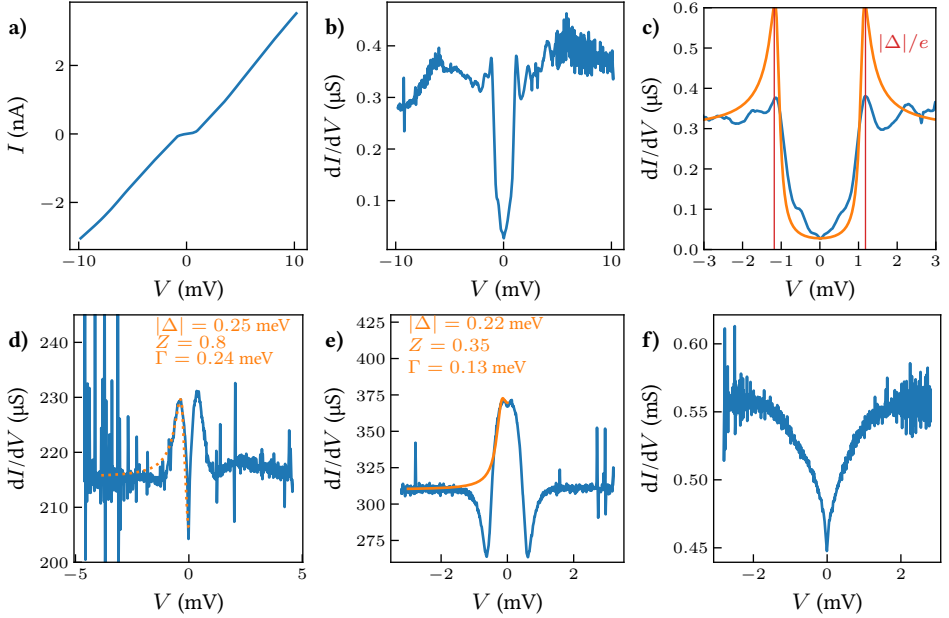


Figure 5.3: a)  $IV$  curve of device A4. b) Differential conductance versus bias voltage curve of device A4. c) Zoomed in differential conductance versus bias voltage curve of device A4 (blue). The orange curve is a BTK curve with  $|\Delta| = 1.10 \text{ meV}$ ,  $Z = 15$ ,  $\Gamma = 0.10 \text{ meV}$ . The red vertical lines indicate the gap voltage scale  $\pm \frac{|\Delta|}{e}$ . d) Differential conductance versus bias voltage curve of device H4. A BTK curve was fitted by eye (orange line, parameters are indicated in the plot). e) Differential conductance versus bias voltage curve of device H8. A BTK curve was fitted by eye (orange line, parameters are indicated in the plot). f) Differential conductance versus bias voltage curve of device A12.

### 5.3.2 Low-resistance devices

Besides the high-resistance devices, also low-resistance devices ( $R < 13 \text{ k}\Omega$ ) were bonded. In these devices, the voltage across the junction was measured upon applying a current bias. The current bias was taken such that the maximum applied bias voltage at least



exceeds  $2 \text{ mV} \approx \frac{2\Delta}{e}$ . In this category of devices, three different types of  $IV$  curves were found. In Figures 5.3d, 5.3e and 5.3f, the corresponding differential conductance curves for devices H4, H8 and A12 are shown. These function as examples of each type of the differential conductance curve.

The differential conductance curve of device H4 shows a V-shaped dip surrounded by two rounded peaks at zero bias voltages, similar to the highly resistive devices. This is one of two devices that show this behavior. To match this to the BTK theory, a gap of  $|\Delta| = 0.25 \text{ meV}$ , a Dynes parameter of  $\Gamma = 0.24 \text{ meV}$  and  $Z = 0.8$  were taken. This is shown as the orange dotted line in Figure 5.3d. The barrier parameter  $Z = 0.8$  implies an interface transparency of  $\mathcal{T} = \frac{1}{1+Z^2} \approx 0.61$ . Notably, this can be considered a high interface transparency. The reduced value of  $|\Delta| = 0.25 \text{ meV}$  is unexpected, given the measurements of the highly resistive devices. This, in combination with the Dynes parameter  $\Gamma = 0.24 \text{ meV}$ , might indicate the presence of a strong pair-breaking mechanism.

Device H8 instead shows a large differential conductance peak at zero bias voltage surrounded by two dips. Again, this is one of two devices that show this behavior. At zero bias voltage, the large peak has a small local minimum. In the context of BTK theory, an enhanced zero bias conductance with a small local minimum can be explained by a high interface transparency ( $Z < 0.55$ ,  $\mathcal{T} > 0.75$ ). The two dips at finite bias, surrounding the peak, however, can not be explained in the context of BTK theory. Since this is the case, a fit by eye was attempted to the zero bias features only, ignoring the dips. This resulted in  $|\Delta| = 0.22 \text{ meV}$ ,  $Z = 0.3$  ( $\mathcal{T} \approx 0.92$ ) and  $\Gamma = 0.14 \text{ meV}$ , which again implies a reduced energy gap, with relaxation and high interface transparency. As shown by Daghero *et al.*[184], within the BTK approach, the dips could potentially be explained if the critical current density of the MoRe is taken into account. This explanation would also explain the absence of extended tails in the  $dI/dV$  curves. Similarly, it could be possible that the NS interface resistances are not dominant in the transport in this device. Additional resistances in the junctions can shift the Andreev reflection features towards higher bias voltages[185]. In this case, the zero bias feature does not need to be related to the interface transparency and might be related to the Josephson effect between the superconducting electrodes. The reduced energy gap  $|\Delta|$  could then correspond to the minigap in the normal metal due to the superconducting proximity effect. We will come back to these issues in the discussion section.

Finally, two devices behaved like device A12 (See Figure 5.3f). These show a V-shaped dip in the differential conductance. A V-shaped dip can not be explained by the conventional BTK theory, which models the tunnel barrier as a delta function potential. Instead, a V-shaped dip could result from a normal tunneling model, such as the Simmons model, an extended potential barrier of small ( $\sim 1 \text{ meV}$ ) height. In such models, an increase in the applied bias voltage reduces the effective barrier height, which increases the conductance until the bias voltage exceeds the characteristic potential barrier height.

In the previous discussion, it has been made evident that the majority of highly conductive junctions show an increased differential conductance around zero bias voltage and no deep dips, as the highly resistive devices show. Within the BTK framework, this could be interpreted as a sign of high interface transparency. From the previous discussion, it is,

however, not clear whether the measured properties are characteristic of the interfaces, as the BTK theory assumes, or result from highly resistive gold nanoparticles. In what follows, the most conductive device that was wire bonded and cooled down will be discussed, in which a spherical gold nanoparticle was found in SEM inspection after measurement, shown in figure 5.4a. The presence of a spherical nanoparticle in only one junction indicates that the junction was modified after deposition. It is suspected that this device was subjected to electrostatic discharge during the room-temperature characterization, melting the gold nanoparticles at the MoRe nanogap into a spherical gold nanoparticle (See the SEM image shown in Figure 5.4a).

The  $IV$  characteristic of the junction with a spherical nanoparticle, plotted in Figure 5.4b, was measured through a two-terminal measurement. Notably, the conductance in this device is enhanced close to zero-bias. At high bias voltages, the junction conducts more current than a normal/linear resistor with the same differential resistance. At a bias voltage of 4 mV, the differential resistance,  $\frac{dV}{dI}$ , is approximately  $R_N = 1023 \Omega$ . For illustrative purposes, the  $IV$  curve of a resistor with the same resistance is plotted as the dotted orange line. The difference between the two curves motivates defining the deficit voltage,  $V_{\text{def}} = IR_N - V$ , the voltage difference between the resistor and the measured junction. This quantity is plotted in Figure 5.4c versus the voltage,  $V$ , across the junction. It can be compared to several voltage scales. Firstly, the gap voltage,  $\frac{|\Delta|}{e}$ , which we take to be 1.3 mV here, indicated by the red line in Figure 5.4c, is clearly exceeded. The maximum deficit voltage for NS interfaces is  $\frac{4}{3} \frac{|\Delta|}{e} \approx 1.73 \text{ mV}$ [75], which is also exceeded. This suggests that transport at a single NS interface alone can not explain the full  $IV$  characteristic. In order to explain the deficit voltage, the device can be considered as an SNS/Josephson junction. This can be a diffusive or a ballistic one. The theoretical upper limit for diffusive SNS junctions is given by  $(\frac{\pi^2}{4} - 1) \frac{|\Delta|}{e} \approx 1.91 \text{ mV}$ . The measured maximum deficit voltage exceeds both these limits, which suggests that the junction could be closer to the clean, ballistic limit. For these junctions, the maximum deficit voltage is given by the Octavio-Tinkham-Blonder-Klapwijk model[78, 186], with an upper limit of  $\frac{8|\Delta|}{3e} \approx 3.46 \text{ mV}$ , which is not exceeded. Within the OTBK framework, the observed deficit voltage can be explained with barrier parameters  $Z_1 = Z_2 \approx 0.4$  for the two NS interfaces.

As before, the differential conductance curve can be used to obtain more understanding about the conduction mechanism of the junction. The differential conductance of device H9 is plotted in Figure 5.4d. Since this data has a sharp peak, the corresponding differential resistance is also plotted in Figure 5.4e. The differential conductance is prominently peaked at zero bias, with small local minima surrounding the peak. As the bias voltage is further increased away from zero bias voltage, the differential conductance decreases, showing a change in slope at  $V \approx 0.65 \text{ meV}$ , below which the differential conductance nearly linearly drops to  $\approx 1 \text{ mS}$ . Notably, the minimum differential resistance is approximately  $167 \Omega$ , about 6 times lower than the normal state resistance. Simple BTK theory can only explain a maximum differential conductance enhancement of a factor 2. Hence, BTK theory can not explain the junction behavior at low bias voltages. At bias voltages larger than  $\frac{|\Delta|}{e} \approx 1.3 \text{ mV}$ , this is not necessarily the case, as the Josephson effect and multiple



Andreev reflections are only expected to be important at voltages lower than  $\frac{|\Delta|}{e}$ .

Thus, the BTK model was fitted by eye to the high bias features, which is shown as the orange curve in Figure 5.4d. The parameters taken are  $|\Delta| = 1.3$  meV,  $\Gamma = 0.15$  meV and  $Z = 0$ . Notably, this fit by eye does not match the shape of the data well. Although the amplitude of the orange curve matches the conductance enhancement at  $V = 1.3$  mV, the slope of the differential conductance data above 1 mV is lower than that of the BTK model curve. As a result, the model undershoots in this regime. Increasing  $\Gamma$  will correct for this, but results in a reduction in the height of the signal. Better agreement between the model and the data can be obtained by accounting for an extra environmental resistance that is unaffected by Andreev processes, called  $R_E$ , and a corresponding resistance ratio,  $r_E = \frac{R_E}{R_N}$  [185]. This is shown by the green curve, labeled BTK +  $r_E$ , in Figure 5.4d. Here  $R_E = 250 \Omega$  and  $R_N = 1024 \Omega$  were chosen. At high bias voltages, this model still slightly overshoots the data above  $V = 3$  mV, similar to the behavior observed in junction H4. To interpret this fit by eye, it is important to note that  $R_E$  can not be interpreted as the series resistance to an NS contact. Notably, a part of  $R_E$  can also originate at the NS contact of interest. Assuming one NS interface is dominant in the resistance,  $R_E$  can be composed of the wiring of the setup ( $\approx 33 \Omega$ ), the resistance of the other NS interface (which may be bias voltage dependent), the resistance of the gold nanoparticle, a series resistance in the MoRe due to critical current effects (which are expected to be bias voltage dependent) and partially from the NS interface itself.

In order to gain more insight into the observed differential conductance/resistance features, dips 1, 2 and 3 are indicated in Figure 5.4e. In the following section, their dependence on an externally applied magnetic field will be measured and discussed.

### 5.3.3 Magnetic field dependence of device H9

The  $IV$  measurements of device H9 demonstrate the presence of a region of high differential conductance at zero bias voltage. In order to better understand what is happening in this region, the magnetic field dependence on an out of plane field,  $B_z$ , was measured. If the junction is indeed superconducting, it is expected that features in the differential conductance related to  $|\Delta|$  decrease in magnitude. Furthermore, these features should also shift to lower bias voltages.

$IV$  measurements were taken at increasing externally applied magnetic fields. The magnetic field was ramped up in steps of 0.5 T from 0 to 6 T and a current biased  $IV$  curve was taken at every magnetic field set-point. In addition, a lock-in amplifier was connected, which applied a sine wave with a root-mean-square output signal of  $dI = 10$  nA at a frequency of 178 Hz. At each current set-point, the resulting signal  $dV$  was measured, from which the differential resistance  $\frac{dV}{dI}$  was calculated. Rather than plotting the differential conductance, the differential resistance will be plotted, as this leads to a clearer color map. The color map of the differential resistance versus bias current and magnetic field is shown in Figure 5.5a. The trace at 0 T corresponds to the same curve as the curve shown in Figure 5.4e, with dips 1, 2 and 3 indicated. Only the sharp differential conductance dip, dip 1, at zero bias current/voltage completely disappears from the color map as the magnetic

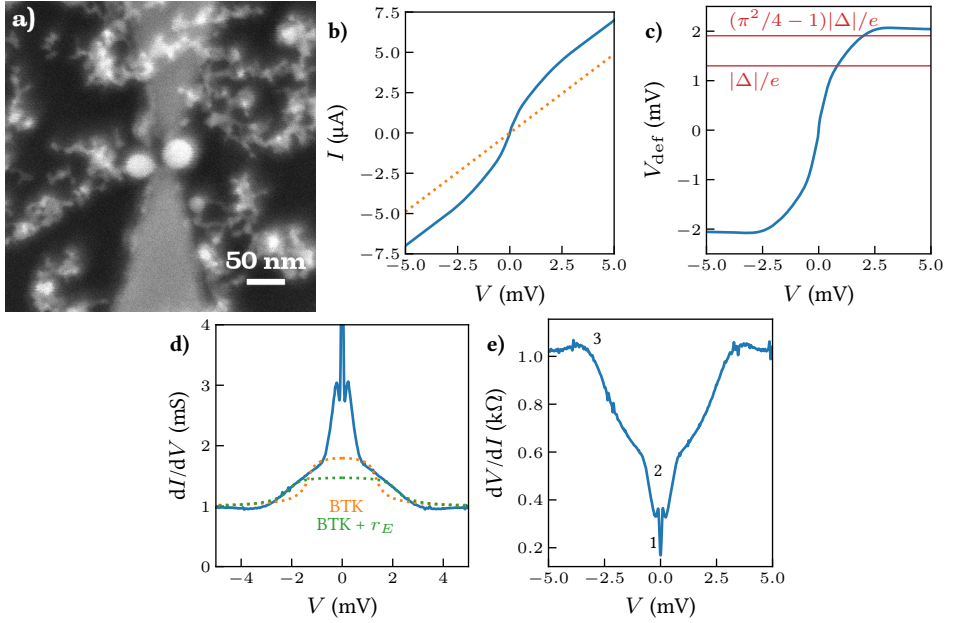


Figure 5.4: Device H9 characterization a) SEM image of device H9. A spherical nanoparticle was found between the needlelike MoRe electrodes. b)  $IV$  curve of device H9. The orange dotted curve is a linear curve with  $R = 1023 \, \Omega$ , matching the differential resistance of the junction at  $V = 4 \, \text{mV}$ . c) Plot of the deficit voltage versus voltage. The deficit voltage is defined as the voltage difference between the blue and orange dotted curve in b). The red lines indicate characteristic voltage scales for NS and SNS junctions in terms of the gap voltage  $\frac{|\Delta|}{e}$ . d) Differential conductance versus voltage curve. The orange dotted curve is a fit by eye to the BTK model ( $|\Delta| = 1.3 \, \text{meV}$ ,  $\Gamma = 0.15 \, \text{meV}$  and  $Z = 0$ ), while the green dotted curve adds an extra resistance  $R_E = 250 \, \Omega$ . e) Differential resistance versus voltage curve. The edges of three dips are indicated, labeled as 1, 2 and 3.

field is increased. This is contrasted by dip 2, which does not visibly shrink or grow with magnetic field. Dip 3, on the other hand, remains approximately constant in size until 1 T. Above 1 T, the current scale of the dip decreases approximately linearly with increasing magnetic field. After the onset of this decrease, several peaks in the differential resistance can be seen above dip 3 and the magnitude of the differential resistance at the edge of dip 3 increases. These peak appear at seemingly random locations in the color map above dip 3. Finally, at high field ( $\sim 6 \, \text{T}$ ) and high current ( $\sim 10 \, \mu\text{A}$ ) in the color map, the differential resistance increases rapidly and the measured voltage saturates. This onset of a large resistance is likely explained by the critical current in the MoRe thin film, which reduces with increasing magnetic field.

In order to investigate the magnetic field dependence of the observed, seemingly random, peaks, a higher resolution measurement was performed. The current range was increased to  $-15$  to  $15 \, \mu\text{A}$  with a step size of  $1 \, \text{nA}$ . The lock-in amplifier was disconnected to avoid smoothing the curve due to an applied AC current. The magnetic field was swept from 0 to 2 T in steps of  $10 \, \text{mT}$ . A color map of the numerically calculated differential resistance is plotted versus the applied magnetic field and bias current in Figure 5.5b. From this color

map, it can be seen that the differential resistance peaks are not random and, in fact, are approximately equally spaced in current at 1.0 to 1.5 T. Their position shifts with the gap edge of dip 3, suggesting a similar origin.

The differential resistance data was measured versus bias current and, hence, also the color maps are most conveniently plotted versus current. A BTK-like analysis, however, is most easily performed as a function of voltage. Hence, in Figure 5.5c, the differential resistance from Figure 5.5a is plotted versus voltage at magnetic fields of 0, 2, 4 and 6 T. From these plots, the disappearance of dip 1 is clearly visible. Furthermore, dip 2 slightly increases in size with increasing magnetic field, as does the differential resistance at high bias voltages ( $V > 5$  mV). As seen from the color map, the voltage-scale of dip 3 decreases and, at the edges of dip 3, peaks develop in the differential resistance. The resistance-scale of dip 3, on the other hand, increases.

#### 5.3.4 High-bias measurements at 1 T magnetic field

Finally, the low-resistance junctions H4, H8 and A12 are revisited. The measurements of device H9 hinted at the possibility of a large effective resistance  $R_E$ , which shifts features related to Andreev reflections at the NS interface up in voltage. Hence, the  $IV$  characteristic of these junctions was measured again with a larger current bias. Measurements were performed with an externally applied magnetic field of 1 T. The differential resistance curves are plotted versus voltage in Figures 5.6a, 5.6b and 5.6c. Junctions H4 and H9 indeed show a suppression in the differential resistance, with a larger voltage scale of approximately 15 mV. To compare these with the BTK model with an effective resistance  $R_E$ , the parameter  $R_E$  was varied such that the voltage scale approximately matches. Fixing the parameters  $|\Delta| = 1.3$  meV,  $\Gamma = 0.6$  meV and  $Z = 0$  to ensure a broadened density of states and high interface transparency, a reasonable fit it found for H4 for parameters  $R_N = 4800 \Omega$  and  $R_E = 3800 \Omega$ . This extended BTK fit, if to be trusted, implies that most of the resistance is not due to Andreev reflections at the NS interface. For device H8, the same parameters were taken, except for  $R_N = 3350 \Omega$  and  $R_E = 2600 \Omega$ .

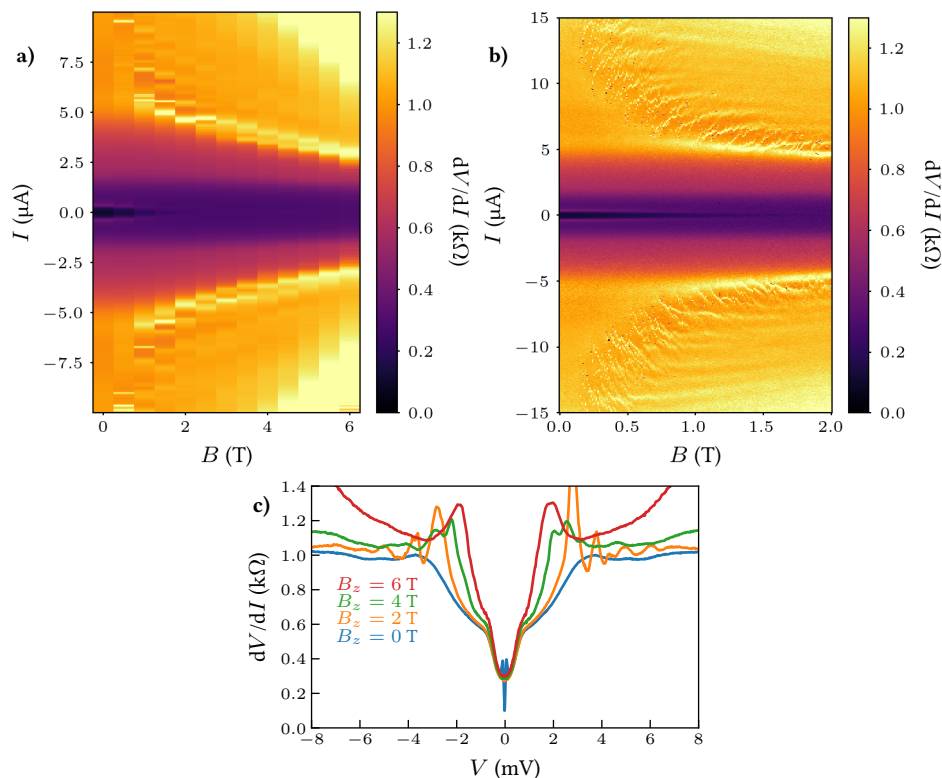


Figure 5.5: a) Color map of the differential resistance (measured by a lock-in amplifier) of device H9 versus externally applied out of plane magnetic field  $B_z$  and bias current  $I$ . A decrease in the field-scale of dips 1 and 3 in the differential resistance can be seen with increasing magnetic field. At bias currents larger than the edge of dip 3, several seemingly random peaks were observed at finite magnetic field ( $\sim 1$  T). b) Color map of the differential resistance (numerically calculated from  $IV$  curves taken at different magnetic field set-points) versus applied out of plane magnetic field  $B_z$  and bias current  $I$ . A higher resolution measurement in magnetic field and bias current was taken to study the random peaks above dip 3 observed in a). The peaks above dip 3 disperse with magnetic field and do not appear at random voltages. c) Differential conductance versus bias voltage curves extracted from the dataset of Figure a). The curves, taken at 0, 2, 4 and 6 T magnetic field show a decrease in the voltage-scale of dips 2 and 3. Dip 1 is only clearly present in the curve at 0 T. The gap edge of dip 3 develops a differential resistance peak with increasing magnetic field. At a magnetic field of 2 T, the dispersing peaks in a) and b) are visible as smooth oscillations in the differential resistance.

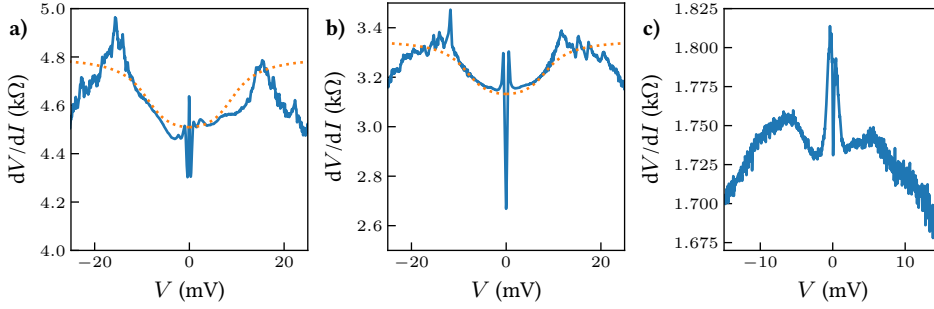


Figure 5.6: Differential conductance versus bias voltage curves at a magnetic field of 1 T. a) High-bias differential conductance versus voltage curve of device H4. The orange dotted curve is a fit by eye to the BTK +  $r_E$  model ( $|\Delta| = 1.3$  meV,  $\Gamma = 0.6$  meV,  $Z = 0$ ,  $R_N = 4800 \Omega$  and  $R_E = 3800 \Omega$ ). b) High-bias differential conductance versus voltage curve of device H8. The orange dotted curve is a fit by eye to the BTK +  $r_E$  model ( $|\Delta| = 1.3$  meV,  $\Gamma = 0.6$  meV,  $Z = 0$ ,  $R_N = 3350 \Omega$  and  $R_E = 2600 \Omega$ ). c) High-bias differential conductance versus voltage curve of device A12.

## 5.4 Discussion

### 5.4.1 Morphology and density of the nanoparticle film

The SEM images of low density deposition, of which an example is given in Figure 5.1d, show that the studied Au nanoparticles are, although similar in mass, irregular in shape. This is a downside for a systematic study of their properties, as every nanoparticle is different. Although the absence of ligands on the nanoparticle surface is necessary for this study, spark ablation with size selection does not result in gold nanoparticles with the same regularity as ligand-stabilized gold nanoparticle suspensions in solvents. Follow-up studies can improve by incorporating a local heater/oven in the gas flow line to melt the nanoparticles into a spherical shape.

The density of nanoparticles on the junctions was optimized with the aim of having a surface nanoparticle coverage of 1 – 10%. Such low-coverage coatings can be identified by color contrast in optical microscopy, as shown in Figure 5.1c. The observed color contrast can thus also be used in future measurements as a guide to produce an optimal nanoparticle coverage. However, with the present coverage, many of the deposited nanoparticles are still connected together, as seen in Figure 5.1f. Thus, although in many junctions only a single or few conduction paths are made between the MoRe electrodes, no junction, except for maybe device H9, shows a measurement of a single nanoparticle. The nanoparticles instead tend to form clusters and high coverage nanoparticle depositions result in nanoporous gold films, as seen in Figure 5.1e. It was not anticipated that at low coverage, this clustering would result from an individually independent deposition of nanoparticles. Whether this effect is related to the elongated and irregular shape of the nanoparticles could be investigated theoretically. Additionally, the clustering could perhaps be caused by the charge on the nanoparticles upon deposition. If this is the case, elongated clusters would be preferentially formed over round ones, as the electric field (and thus the resulting force) at the charged particles is largest at sharp, elongated, points. The effect of nanoparticle charge could potentially also explain the relatively large yield of bridged junctions, as the charged particles should be more strongly attracted to the sharp, needlelike tips of the MoRe electrodes. While the presence of nanoparticle clusters does not hinder the BTK analysis done in this study, it should be addressed in order to study single particles in future studies. In combination with the production of spherical nanoparticles, it can be investigated whether the nanoparticles cluster due to their shape.

### 5.4.2 Room temperature measurements

The measurements at room temperature show that the majority of junctions exhibit a resistance between 1 k $\Omega$  and 100 k $\Omega$ . Although some junctions were found to have a higher resistance, the majority of devices show that a low resistance could be obtained between the nanoparticles and the MoRe electrodes. Thus, for studying nanoscale objects with a resistance larger than 1 M $\Omega$  with MoRe, it is likely that the interface resistance is not dominant.

### 5.4.3 BTK analysis

For most of the presented junction characteristics, a fit was made based on the BTK model. However, although some of qualitative features of the data, such as the presence of peaks

and dips with a voltage scale on the order of 1.3 meV, can be matched with this model, several features of the data were found to be in disagreement with the simple BTK model. The following discrepancies between the data and the model were found:

1. Significantly reduced amplitude of quasiparticle peaks in the differential conductance at  $V = |\Delta|$  for the high-resistance devices;
2. Absence of extended tails in the differential conductance for high voltages ( $V > |\Delta|$ );
3. The presence of dips in the differential conductance at finite bias voltages (H4, H7, H8, H9) in low-resistance devices;
4. A significantly reduced value of  $|\Delta| \approx 0.25$  mV for the low-bias features in the low-resistance devices;
5. The presence of additional dips in the differential resistance (peaks in the differential conductance) at bias voltages exceeding 1.3 mV, which can be fitted by an extended BTK theory with an additional resistance  $R_E$ ;

Furthermore, perhaps related to the points above, a significant Dynes parameter was needed to find good correspondence to the data.

Points 1-3, and potentially point 4, can tentatively be explained by considering the effects of a critical current or local heating in the point contact structures. The presence of heating can result in a loss of superconductivity in the MoRe electrode close to the Au nanoparticle. As a result of this, there is an increase in the differential resistance as the bias current is increased, which, through suppression of  $|\Delta|$ , translates to a dip in the differential conductance (3)[187]. If this is the case, then the validity of the BTK theory at high bias current voltage can not be justified and, rather than an extended tail, the differential conductance will become flat (2). Such heating should also reduce the size of quasiparticle peaks (1). If the critical current is significantly small, the observed voltage scale will be dominated by the critical current of the superconducting electrode, rather than by the gap  $|\Delta|$  (4). The presence of pair-breaking and the associated Dynes parameter  $\Gamma$  might thus be related to the critical current density of the electrode. This raises another interesting question: "How does the heat in these SNS devices flow at low temperatures?" Since the thermal conductivity of a superconductor tends towards zero as  $T \rightarrow 0$ , it appears inevitable that heating in the gold nanoparticle or the MoRe close to the needlelike contact leads to a significant increase in the local electronic temperature. An estimate of the temperature increase can be made assuming an electronic temperature of 100 mK and molybdenum in the normal state as the thermally conductive material. The thermal conductivity of Mo can be estimated from the value at 3 K, which is 45.6 W/mK[188]. Molybdenum is taken as a worst-case scenario for the thermal conductivity of the MoRe alloy. It is worthwhile to mention that the thermal conductivity of rhenium is significantly larger, 1940 W/mK at 3 K. Deposited gold nanoparticles similarly could increase the thermal conductance of the MoRe wires. Assuming a linear temperature dependence of the thermal conductivity, the thermal conductivity at 100 mK is  $1.52$  W/mK =  $1.52$  nW/nmK. For a molybdenum wire that is  $25$  nm x  $200$  nm x  $100$   $\mu$ m in dimensions, this results in heating of the order of  $13$  K/nW. The dissipated power can be estimated by considering that a typical low-resistance junction has a resistance of  $1$  k $\Omega$  and measurements are taken at voltages of the

order of 1 mV. This results in approximately 1 nW of heating power. Ignoring the temperature dependence of the thermal conductivity, this results in 13 K of heating. In reality, the thermal conductivity is temperature dependent, linearly at low temperature, and the substrate can also contribute to cooling. Thus, the actual temperature increase at 1 nW of input power is likely of the order of 1 K. Extrapolating from this, at larger bias voltages the dissipated power can significantly heat up the device to a point where the superconducting wire enters the normal/resistive state. If this is true, future studies could aim to decrease the heating by providing an additional normal metallic connection in proximity to the point contact as a heat sink. The role of local heating by the bias current could also be investigated by means of local thermometry[189].

Finally, point 5, on the other hand, is to be expected, given a series resistance. Since the device contains at least five different conductive components, being the two superconducting MoRe needlelike electrodes, the two NS interfaces and the gold nanoparticles, there are several potentially resistive regions. Thus, the NS interfaces do not necessarily need to be the dominant resistance in the sample and one NS interface can act as a series resistance to another NS interface. The reasonable fits with relatively high values of the extra resistance  $R_E$  suggest that at least one NS interface is highly transparent and not the dominant resistance in the junction. Since the device with the spherical nanoparticle, H9, shows the lowest value of  $R_E$ , it is plausible that the dominant resistance in the other junctions is related to the resistance of the relatively narrower and more irregularly shaped gold nanoparticles.

## 5

#### 5.4.4 Sharvin and Maxwell resistance, critical current effects from the MoRe thin film

The previous discussion on the mismatch of the data can be understood by examining what happens at the point contact regions. In particular, the question of where the resistance of the junction arises is of importance for understanding the data. To do this, we discuss the data from the perspective of point-contact spectroscopy. Typically, three regimes are indicated for both homocontacts and heterocontacts between two metals. The first regime is the classical Maxwell/diffusive limit[190], in which the mean free path,  $l$ , is much larger than the contact diameter,  $a$ . In this case, the resistance scales with the contact area  $R \propto \frac{1}{a^2}$ . In the opposite regime, the contact diameter is much smaller than the mean free path, meaning  $K_n \equiv \frac{l}{a} \gg 1$ , where  $K_n$  is the Knudsen number. This regime is called the Sharvin regime [191] for point contacts, also sometimes referred to as the ballistic or Knudsen regime[192]. Here, the resistance scales with  $R \propto \frac{1}{a}$ . For arbitrary values of  $K_n$ , it was found by Wexler[193] that an interpolation between the Sharvin and Maxwell resistance gives an adequate description of the contact resistance. Finally, a distinction can be made in the diffusive regime based on the inelastic scattering length,  $l_{in}$ . Maxwell contacts with  $l_{in} \ll a$  dissipate heat in the contact region, while Maxwell contacts with  $l_{in} \gg a$  do not. An ideal point-contact spectroscopy measurement is in the Sharvin regime, where the BTK theory is valid, with minimal series resistance. The voltage scale of conductance enhancement observed in this chapter suggests that the Maxwell resistance could be relevant, however. In what follows, the contribution of the Maxwell resistance will be



examined in a phenomenological manner.

The deposition of nanoparticles onto MoRe nanogaps effectively creates multiple contacts with contact diameters on the order of  $a \sim 1 - 10$  nm. The mean free path in the MoRe film on the other hand is presumably small compared to that in the gold nanoparticles. This can be argued based on the resistivity of the MoRe layer. An estimate for the resistivity can be found based on the normal state resistance of the MoRe nanowires,  $R \approx 42$  k $\Omega$ , the length,  $L = 200$   $\mu$ m, the width,  $w = 200$  nm, and thickness,  $t = 20$  nm. The resistivity is  $\rho = \frac{Rwt}{L} \approx 840$   $\Omega$ -nm. An estimate of the mean free path can be extracted from the characteristic  $\rho l$  product of molybdenum,  $\rho l = 599$   $\Omega$ nm<sup>2</sup>[194]. Dividing this by the resistivity of the MoRe thin film results in a mean free path of the order of 0.71 nm. This small mean free path could explain the absence of visible grains in SEM images of MoRe thin films. The mean free path can also be estimated from the high upper critical field of the MoRe alloy, which was above the maximum applied field of 9 T. A critical field of this magnitude implies a coherence length that is smaller than 5 nm and the mean free path is on the order of  $\sim 1$  nm. Thus, the Maxwell resistance related to the MoRe thin film is not necessarily small compared to the Sharvin resistance of the contact. Depending on the MoRe-Au contact area of the studied junction, the ratio of the Sharvin and Maxwell resistance can be quite different.

When the Maxwell resistance is significant, the critical current in the MoRe becomes relevant. To understand the effect of the critical current in superconducting contacts, a phenomenological model was made by Daghero[184], which introduces the differential resistance corresponding to the Maxwell resistance:

$$\frac{dV_M}{dI}(I) = \frac{1}{A((\frac{I_c}{I})^{2n} - (\frac{I_c}{I})^n) + B} + C \int_0^I \frac{1}{1 + e^{-k(1 - \frac{I'}{I_{cut}})}} dI' \quad (5.1)$$

Here,  $A$  and  $B$  are constants that determine the flux creep regime[195, 196].  $\frac{1}{B}$  determines the normal-state resistance and the amplitude of the critical current resistance peak at a fixed value of  $B$  is determined by the combination of  $A$  and  $n$ .  $I_c$  is the critical current and  $n$  determines the width of the critical current peak. The constant  $C$ , on the other hand, adds a contribution that describes thermally assisted flux flow at low bias currents. The parameters  $k$  and  $I_{cut}$  determine the shape of this curve.

In the following paragraphs, we aim to demonstrate that this expression as a series resistance provides a qualitative explanation for the observed features.  $C = 0$  will be assumed to simplify the analysis. We aim to simulate the  $IV$  curve of NS interface as a combination of a Sharvin point contact, which is modeled through the BTK model, in series with a Maxwell point contact, which behaves according to equation 5.1. In order to simulate  $IV$  curves, the BTK model is first solved for the differential conductance at a voltage,  $V_S$ , across the ballistic part of the NS interface. The differential conductance is numerically integrated to the voltage  $V_S$  to find the current  $I$  across the junction. This current is filled into equation 5.1 to obtain  $\frac{dV_M}{dI}(I)$ . Numerically integrating the differential resistance

$\frac{dV_M}{dI}(I)$  to the current  $I$  results in the voltage  $V_M$ . Finally, the voltages across the Sharvin and Maxwell resistances (i.e., across the Au-MoRe interface and the Maxwell resistance of the MoRe electrode) can be added at a fixed current  $I$  to obtain the total voltage,  $V$ . Similarly, the differential resistances of the Maxwell and Sharvin resistance are added. This results in a simulated  $\frac{dV}{dI}$  versus  $V$  curve. The differential conductance can be obtained by  $\frac{dI}{dV}(V) \approx \frac{1}{\frac{dV}{dI}(V)}$ .

The final model contains four parameters: the normal-state resistance of the Sharvin contact,  $R_S$ , the superconducting gap,  $|\Delta|$ , the interface scattering parameter,  $Z$ , and the Dynes parameter,  $\Gamma$ , are used to describe the BTK theory. Five more parameters describe the Maxwell resistance of the superconductor, namely  $A$ ,  $B$ ,  $n$  and  $I_c$ . An additional constant series resistance can be added trivially to  $\frac{dV_M}{dI}(I)$  in 5.1. The use of this many parameters can make a model sufficiently flexible that it can fit many curves. Although the choice of this model can be motivated by the small electronic mean free path in the MoRe films, it could be argued that other models with a similar or smaller number of parameters could potentially also explain the data. Although there are nine free parameters in the model, the degree of freedom in the resulting curve shape is limited. The BTK model (with low values of  $Z$ ) and the phenomenological critical current model are each constrained to a single type of curve. The BTK model only produces a dip in the differential resistivity and the critical current model produces a dip surrounded by peaks. The free parameters in these models only modify the voltage/current scale ( $\Delta$ ,  $I_c$ ), magnitude ( $R_S$ ,  $\Gamma$ ,  $Z$ ,  $A$ ,  $B$ ,  $n$ ) and sharpness ( $\Gamma$ ,  $Z$ ,  $n$ ) of dips and peaks.

In Figure 5.7a, the differential resistance versus bias voltage resulting from such a simulation is plotted as an orange dotted line. An attempt was made to match the model to the differential resistance of device H8 at a magnetic field of 1 T, in blue. The corresponding BTK and Maxwell differential resistances are shown in Figures 5.7b and 5.7c. For the BTK model, the parameters  $R_S = 700 \, \Omega$ ,  $|\Delta| = 1.3 \, \text{meV}$ ,  $Z = 0.0$ ,  $\Gamma = 0.6 \, \text{meV}$  were taken. For the Maxwell resistance,  $R_M = \frac{1}{B} = 480 \, \Omega$ ,  $A = B$ ,  $n = 4$  and  $I_c = 163 \, \text{nA}$  are taken as the parameters. The critical current scale and the Maxwell resistance  $R_M$  can be multiplied to yield an  $I_c R_N$  product of  $I_c R_M \approx 0.06 \frac{|\Delta|}{e} \approx 78 \, \mu\text{V}$ . Finally, a constant series resistance of  $R_{\text{series}} = 2170 \, \Omega$  was added. As discussed for the simpler BTK +  $r_E$  model, this series resistance is necessary to describe the observed dip that is wider than  $\frac{|\Delta|}{e}$  in voltage. The BTK curve with an added Maxwell resistance with a critical current provides a more accurate description of the sharp differential resistance and voltage peaks in this junction than the BTK +  $r_E$  fit in Figure 5.6b. This fit suggests that also in the BTK fit performed in Figure 5.3e, the critical current effect should be considered. Since there are two NS interfaces, the series resistance in Figure 5.7a could be related to resistance of the other NS interface. A barrier value of  $Z \approx 0.55$  might explain the small dip observed at zero bias voltage in Figure 5.3e.

To conclude the discussion of critical current effects, we note that the critical current effect described here could also describe the Josephson effect through the Au nanoparticles, which could potentially explain the presence of dip 1 in junction H9. However, this device

has a finite differential resistance at zero bias voltage, which seems to contradict this idea. We will discuss this in the next section.

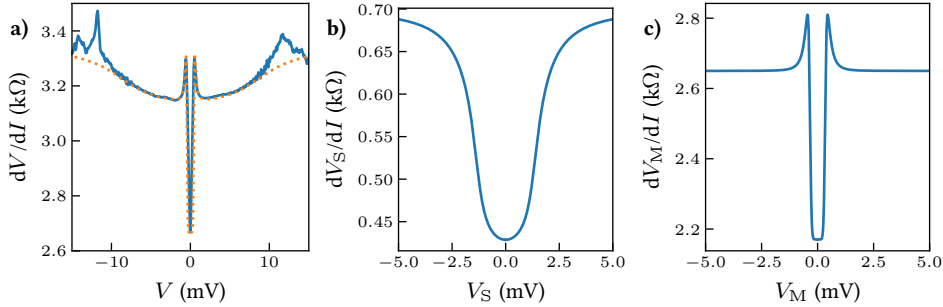


Figure 5.7: a) Differential resistance versus voltage resulting from a BTK model with a superconducting Maxwell resistance in series. The differential resistance versus voltage for the BTK model is shown in b) and the differential resistance versus voltage for the Maxwell resistance is shown in c). The parameters for the BTK model are the normal-state resistance  $R_S = 700 \Omega$ ,  $|\Delta| = 1.3$  meV,  $Z = 0.0$ ,  $\Gamma = 0.2$  meV. The parameters for the Maxwell resistance model are the normal state resistance  $R_M = \frac{1}{B} = 480 \Omega$ ,  $A = B$ ,  $n = 4$  and  $I_c = 163$  nA with an additional series resistance  $R_{\text{series}} = 2170 \Omega$ .

#### 5.4.5 Absence of a dissipation-less Josephson current

In device H9, a large zero bias dip, dip 1, in the differential conductance was discovered, which disappears at a magnetic field of 2 T. This, taken together with the large deficit voltage, predicts the presence of a Josephson current in the short SNS junction. Given  $R_N \approx 1$  k $\Omega$  and  $|\Delta| \approx 1.3$  meV, a critical current on the order of 2  $\mu$ A or lower would be expected for a short/ballistic SNS junction with highly transparent interfaces. The side-peaks of dip 1 are found at 0.4  $\mu$ A, making this feature potentially consistent. However, even with a measurement resolution of 2 nA in Figure 5.5b, the minimum observed resistance is approximately 166  $\Omega$ , of which only 33  $\Omega$  can be attributed to the wiring of the measurement setup. This implies that the effective critical current of the junction is either very low or, perhaps, the junction is affected by external high-frequency noise. This may limit the minimum observable critical current. Since the used measurement setup lacks the necessary filters, such as copper powder filters and RC filters, interference from an external high-frequency signal could suppress the Josephson current. In order to verify this, future samples should be investigated in a dilution fridge with high-frequency filters.

## 5.5 Conclusion

The measurements of ligand-free Au nanoparticles in MoRe nanogaps performed in this chapter were performed to better understand the surface properties of MoRe. The measurements in this chapter show that a significant fraction of junctions is highly conductive ( $R < 1$  M $\Omega$ ) at room temperature. At a temperature of 40 mK, features in the differential conductance were observed, which can be understood through the BTK model as a consequence of Andreev reflections on highly electrically transparent ( $Z < 0.55$ ) NS interfaces. In a significant fraction of the measured junctions, the MoRe electrodes are effectively free from significant transport barriers to the gold nanoparticles, as no large dips in the

differential conductance were identified in highly conductive junctions, which should be visible in tunneling spectroscopy measurements with superconductors. To better describe the differential conductance features in the junctions, the effect of critical currents on the MoRe electrodes or the Josephson current through the nanoparticle was considered, as well as an additional series resistance. The results highlight the potential for making highly-transparent electrical interfaces to other nanoscale objects, such as graphene nanoribbons, by deposition onto prefabricated superconducting MoRe electrodes.

## 6

# Superconducting Proximity Effect in Constricted Variable Thickness SNS Junctions

6

*In this chapter, the superconducting properties of superconductor-normal metal-superconductor (SNS) junctions with a constriction geometry are investigated. In SNS junctions, superconducting correlations and an energy gap in the density of states are induced in the normal metal. As a result, SNS junctions can carry a dissipationless electrical current and exhibit excess current at high bias voltages (an offset current compared to a resistor with the same resistance). To characterize this and compare different devices, the equivalent deficit voltage is investigated. Additionally, the bias voltage dependence of features in the differential conductance is studied. The constricted geometry in these SNS junctions enables the controlled electromigration of the normal metal, which narrows the normal metal connection (Au or Pd) and increases the junction resistance. By gradually narrowing the metal connection, the current-voltage characteristic is studied in the same device at different normal metal resistances. This way, the deficit voltage of the junctions is studied from their initial state to a final state, where the normal metal is broken into two nanometer-spaced electrical contacts; These contacts can be used for studying the electrical conductance of nanoscale objects. In particular, Pd contacts can be promising for the study of graphene nanoribbons. In the broken state, the minigap in the density of states is extracted, which is compared to the voltage scale of features (peaks and bumps) in the differential conductance and the deficit voltage of intact junctions. From this, it is found that the energy gap of the broken junction can be estimated prior to the electromigration.*

---

I want to thank Abel Hutten for his contribution to the work in this chapter during his master thesis project. I also want to thank Serhii Volosheniuk for fabricating the last batch of Nb/Pd/Nb SNS junctions

## 6.1 Introduction

The superconducting proximity effect allows metals that are not intrinsically superconducting to exhibit superconducting properties, such as a spectral energy gap and pair coherence. For the purpose of making Josephson junctions with nanostructures such as molecules, nanoparticles, carbon nanotubes and graphene nanoribbons, the superconducting proximity effect can be exploited to make a good contact metal superconducting[34]. For example, while the surfaces of superconductors such as Al and Nb are prone to surface oxidation, noble metals such as Au, Pt and Pd are far less sensitive. Another aspect where this is beneficial is in contacting semiconducting nanostructures, which may require low or high work function metals to make n- or p-type contacts.

In order to optimize the superconducting properties in the normal metal, a few conditions should be satisfied[197, 198]. Firstly, the superconductor and the normal metal should be in good electrical contact. This requires a high interface transparency, characterized by the parameter  $Z$  in Blonder-Tinkham-Klapwijk(BTK) theory[75], at the boundary between the two metals and sufficiently large interfaces. Second, the suppression parameter,  $\gamma = \frac{\rho_S \xi_S}{\rho_N \xi_N}$ , should be small. Here  $\rho_S$ ,  $\rho_N$ ,  $\xi_S$  and  $\xi_N$  are the resistivity of the superconductor, the resistivity of the normal metal, the coherence length of the superconductor and the coherence length of the normal metal respectively. The requirement that  $\gamma$  should be small intuitively means that the amount of superconducting/correlated charge carriers moving from the superconductor into the normal metal should exceed the number of uncorrelated charge carriers going from the normal metal to the superconductor. Thus, this characterizes the (inverse) proximity effect within a distance scale of a coherence length of the interface. In order to achieve a low suppression parameter, the conductivity of the superconductor should ideally exceed the conductivity of the normal metal. Third, the distance-scale  $L$  from the superconductor to the relevant part of the normal metal should be as small as possible, as the superconducting properties in a diffusive normal metal scale as  $(\frac{\xi_N}{L})^2$ . Finally, the film structure in the normal metal influences the coherence length in the normal metal. Metals with larger electronic diffusion coefficients (larger Fermi velocities and mean-free paths) have a larger Thouless energy,  $E_{Th} = \frac{\hbar D}{L^2}$ , and hence a larger proximity gap at the same length,  $L$ . A large diffusivity, however, also increases the suppression parameter. Thus, unless the length scale of the normal metal is smaller than the coherence length, the simultaneous increase in both Thouless energy and suppression coefficient reduces the scaling with electron diffusivity.

In this chapter, to study the proximity effect in Pd and Au (as a reference metal), the current-voltage ( $IV$ ) characteristic of electromigrated break junction (EMBJ) SNS junctions with superconducting patches will be studied in various devices. EMBJ devices can be broken in a feedback-controlled, step-wise manner by applying a large bias voltage across. When the temperature in the wire exceeds the Hüttig temperature ( $\sim 128$  °C for Au,  $\sim 275$  °C for Pd)[199], surface atoms can diffuse and rearrange. The combination of thermal diffusion and forces exerted by the electric field and scattering of the current on the surface atoms is known to break metal wires[200] In their unbroken form, these devices are SNS junctions, where the normal metal forms a nanoscale constriction. When the junction is broken, a few-atom to a few-nm nanogap results that can be used as a

pair of (superconducting) contact electrodes for nanometer-sized objects. The use of the EMBJ technique offers the advantage of allowing the study of the  $IV$  characteristics at SNS junction resistances between several ohms to kilo-ohms, where only a few atoms remain connected. When the resistance (approximately) exceeds the resistance quantum,  $R_Q \approx 12.9$  kOhms, the junction breaks completely. In this limit, transport is limited by tunneling through vacuum and the spectroscopic energy gap in the normal metal can be probed in the differential conductance versus bias voltage.

Al/Pd/Al, Nb/Pd/Nb and Nb/Au/Nb SNS EMBJs are studied with the aim of obtaining a large proximity gap in the middle of the Pd and Au devices. The junctions are made within a single lithography step using double-angle evaporation, shadow-mask lithography, which is explained in detail in subsection 3.4.5 of the fabrication chapter. The lengths of the SNS junctions studied are relatively small to optimize the Thouless energy, ranging from 30 to 60 nm. With the aim of optimizing the superconducting proximity effect at the NS interfaces, all Pd-based devices were made in a single evaporator (Plassys MEB550S) with a base pressure of  $10^{-8}$  mbar. For Au-based junctions, another evaporator (AJA QT) was used to deposit the normal metal layer.

Besides developing a potentially useful device structure for making superconducting contacts with nanoscale objects, this chapter aims to answer the following question: "Can the  $IV$  characteristic of intact or partially electromigrated EMBJ SNS junctions be used to extract or estimate the superconducting proximity gap of broken EMBJ SNS junctions?" In order to answer this, the  $IV$  characteristic of SNS EMBJ junctions will be measured to verify the presence of superconductivity (switching current and critical temperature), after which experiments follow that aim to establish a link between features (peaks and bumps/slope changes) in the differential conductance and the voltage deviation of the  $IV$  characteristic from linearity, called the deficit voltage, at several junction resistances. In what follows, measurements on these samples will be discussed in chronological order.

## 6.2 Al/Pd/Al

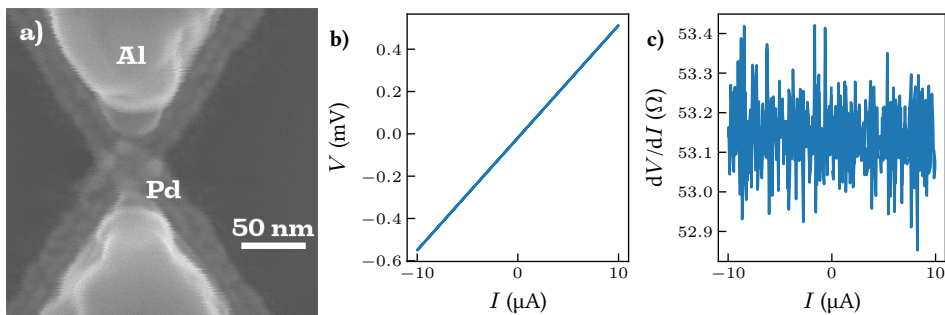


Figure 6.1: a) SEM image of an Al/Pd/Al SNS junction. b) Two-terminal  $IV$  curve at 33 mK. c) Differential resistance calculated from b). Taking into account a  $33 \Omega$  series resistance, the junction has a resistance of approximately  $20 \Omega$ .

The first attempt was made using Al as a superconductor and Pd as the normal metal. In

Figure 6.1a an SEM image of such a junction is shown. In these junctions, 100 nm thick Al patches were spaced apart by 30 nm on top of the 13 nm thick Pd constriction evaporated at an angle of  $4^\circ$ . These junctions were cooled down to a base temperature of 33 mK in a 3-He/4-He dilution fridge. All but one junction were broken by feedback-controlled electromigration in vacuum prior to cooldown.

The junction that was not broken was monitored during cooldown by applying a current bias and measuring the voltage across the junction in a two-terminal measurement with approximately  $33\ \Omega$  series resistance. An example measurement with a current resolution of 100 nA at 33 mK is shown in Figure 6.1b. The differential resistance is plotted in Figure 6.1c. After subtracting the series resistance from the differential resistance curve, the obtained junction resistance is approximately  $20\ \Omega$ . No clear critical current or reduction in low-bias differential resistance was observed in this junction.

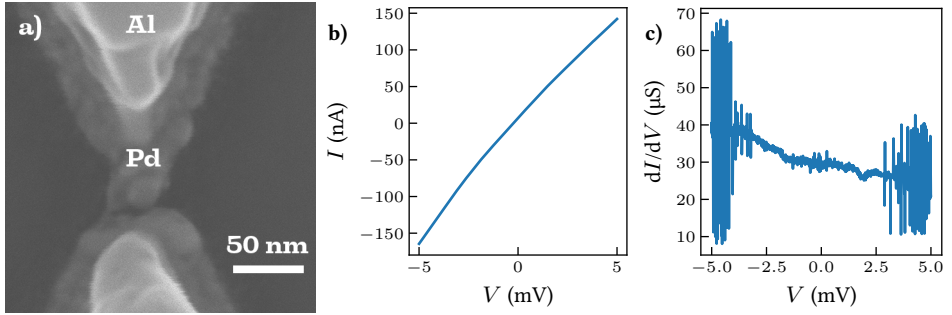


Figure 6.2: a) SEM image of an electromigrated Al/Pd/Al SNS junction. b) Two-terminal  $IV$  curve at 33 mK. The  $IV$  curve of the broken junction is nonlinear. c) Differential conductance calculated from b). In contrast to intact junctions, the differential conductance of the broken junction shows features and voltage dependent current fluctuations. There are no clear peaks or dips related to superconductivity.

The broken junctions, of which an SEM image is shown in Figure 6.2a, were measured by applying a voltage bias and measuring the current. In Figure 6.2b an  $IV$  curve taken at 33 mK with a voltage resolution of  $10\ \mu V$  is plotted. The differential conductance is plotted in Figure 6.2c. There are no gaps or peaks in the differential conductance visible related to superconductivity.

In one junction, an AlSi (1% Si) wirebond was accidentally bonded on top of a constriction. Surprisingly, this junction could be electromigrated to a resistance of  $50\ k\Omega$ . The  $IV$  curve and differential conductance of this junction are plotted in Figures 6.3a and 6.3b. The differential conductance of this junction shows a region of suppressed conductance surrounded by peaks at  $V = \pm 0.56\ mV$ , which corresponds well to double the superconducting gap of nanostructured aluminium[201].

By applying a gate voltage to the p++ doped silicon of the Si/285 nm SiO<sub>2</sub> substrate, the  $IV$  characteristic of this junction could be tuned. The gate voltage was swept from  $-18$  to  $-14\ V$ , taking  $IV$  curves at each gate voltage. The corresponding differential conductance is plotted as a colormap in Figure 6.3c. At a gate voltage of  $-15.8\ V$ , the colormap shows a peak below  $V = \pm 0.56\ mV$  that disperses with gate voltage. This sub-gap peak disperses in



an asymmetric manner as a function of gate voltage, displaying a weaker gate dependence at negative gate voltages. In Figure 6.3d a linecut from the color map is taken at a gate voltage of  $-15.8$  V, which shows that the sub-gap peaks are bias asymmetric, while the peaks at the gap edge are symmetric in amplitude. The presence of asymmetric peaks in the superconducting gap hints at an imbalance in the amount of electron or hole-like excitations in one of the two sides of the broken junction. For a sub-gap peak to appear, a degree of pair breaking must be present, which could be due to a magnetic moment, as is the case for Yu-Shiba-Rusinov bound states[1–3]. There is a tendency for such states to be localized spatially and in energy, which reduces the probability for thermal excitations to other states. This makes the presence of such subgap states potentially interesting for quantum information purposes. Since superconductivity was only found in the junction onto which an AlSi wirebond was accidentally bonded, it could be of further interest to investigate the presence and nature of gate-tunable sub-gap states in electromigrated AlSi (or Al).

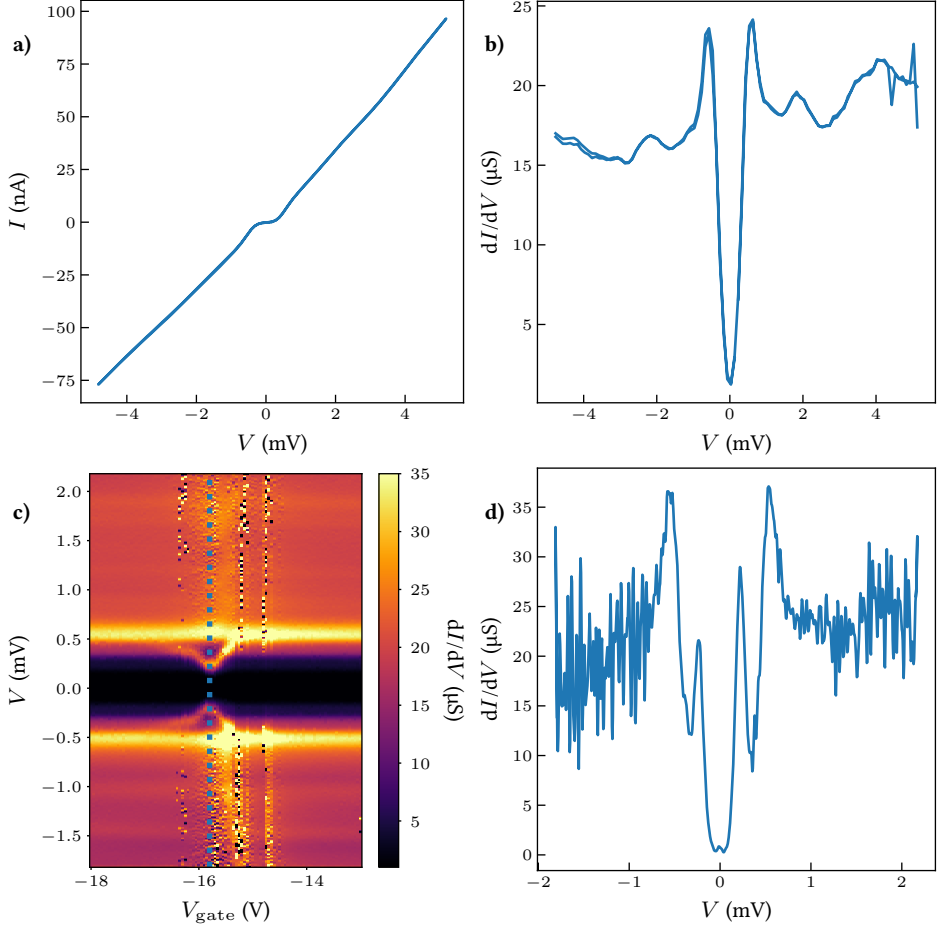


Figure 6.3: Measurements of the electromigrated Al/Pd/Al junction with an AlSi wire bond on top of the constriction a) Two-terminal  $IV$  curve at 33 mK. The  $IV$  curve is nonlinear and flattens at zero bias voltage. b) Differential conductance calculated from a). There is a gap at zero bias voltage, which is surrounded by peaks at  $\pm 0.56$  mV. c) Colormap of the differential conductance versus bias voltage and gate voltage. Two peaks disperse versus gate voltage around  $-15.8$  V in the gap region. d) Linecut of the colormap indicated by the dashed line in c). While the peaks at  $\pm 0.56$  mV are symmetric in magnitude, the in-gap peak at positive bias has a larger amplitude than the in-gap peak at negative bias voltage.

## 6.3 First Nb/Pd/Nb devices

As devices with a 200 nm thick Al layer as a superconductor were found not to successfully induce superconducting properties in 13 nm thick Pd layers, the decision was made to replace e-beam evaporated aluminium by a 100 nm thick thin film of e-beam evaporated Nb. The resulting SEM images of two different devices (A and B) are shown in Figure 6.4. Figure 6.4a and 6.4b show a top and 45° side-view SEM image of device A. While device A is a properly defined SNS junction, the niobium layer clearly exceeds the intended pattern boundaries that the Al layer in Al-based SNS junction devices does follow. Figure 6.4c shows a top view SEM image of device B, in which the Nb layer is connected, which highlights a fabrication issue in these devices.

Despite the fabrication issues, this batch of samples was characterized to investigate whether they do show superconducting properties, such as a critical temperature, a switching current and excess current.

### 6.3.1 *IV* characteristic

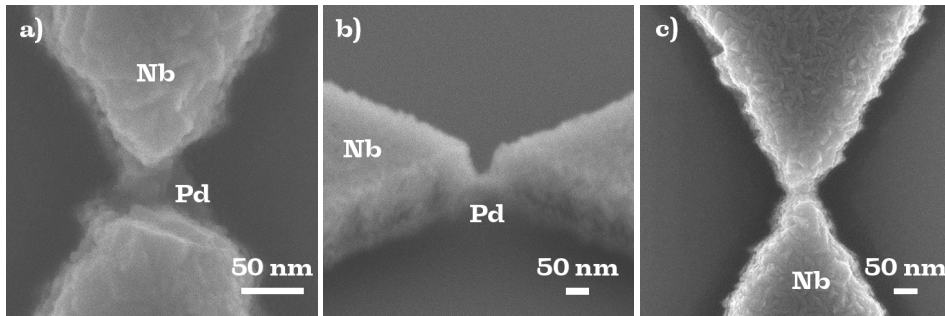


Figure 6.4: a) SEM image of an Nb/Pd/Nb SNS junction (device A). The niobium patches exceed the intended pattern boundaries of the device. b) SEM image at a 45° angle showing a well-defined height profile (device A). c) SEM image of a different Nb/Pd/Nb SNS junction (device B). The poorly defined niobium patches are unintentionally connected.

Several junctions were bonded and loaded into a dilution fridge insert. The junctions were cooled down to a base temperature of 600 mK. The two-terminal *IV* characteristic of the junctions was measured by sourcing current and measuring voltage. The current was swept from  $-30$  to  $30$   $\mu\text{A}$ . The *IV* characteristic of junction A is shown in Figure 6.5a. A change in slope is seen at a current of  $16.5$   $\mu\text{A}$ , which corresponds to the switching current,  $I_{\text{sw}}$ , of the junction. To investigate the junction *IV* characteristic, the series resistance is extracted as the zero-bias differential resistance. The voltage over the junction is calculated by subtracting  $IR_{\text{series}} \approx 34$   $\Omega$ . The resulting *IV* characteristic is plotted as the blue curve in Figure 6.5b. In this plot, the sharp voltage jumps between the superconducting and dissipative branches are more visible. The voltage jump at negative bias current is at a slightly smaller current than the voltage jump at positive bias current. When the sweep direction is reversed, the opposite behavior was seen. The junctions are hysteretic, with a switching current from the superconducting to the dissipative state and a retrapping current from the dissipative state to the superconducting state. The orange dotted curve

plotted in this figure is the  $IV$  characteristic of a resistor with the same resistance as the average differential resistance ( $dV/dI$ ) at high bias current. Here, the average  $dV/dI$  between 28 and 30  $\mu\text{A}$  was taken. A comparison of the blue and orange dotted lines shows that the voltage across the junction is smaller than the voltage across a resistor with the same high-bias differential resistance. Thus, there is a deficit in voltage,  $V_{\text{def}}$ . Plotting the deficit voltage versus the voltage across the junction results in Figure 6.5c. In this junction, the voltage deficit at zero voltage reaches 91.5  $\mu\text{V}$  at the switching current, which is an approximation of the characteristic  $I_{\text{sw}}R_N$ -product of the SNS junction (also called the characteristic voltage  $V_c$ ). At a bias voltage of 200  $\mu\text{V}$ , the deficit voltage is 30  $\mu\text{V}$ .

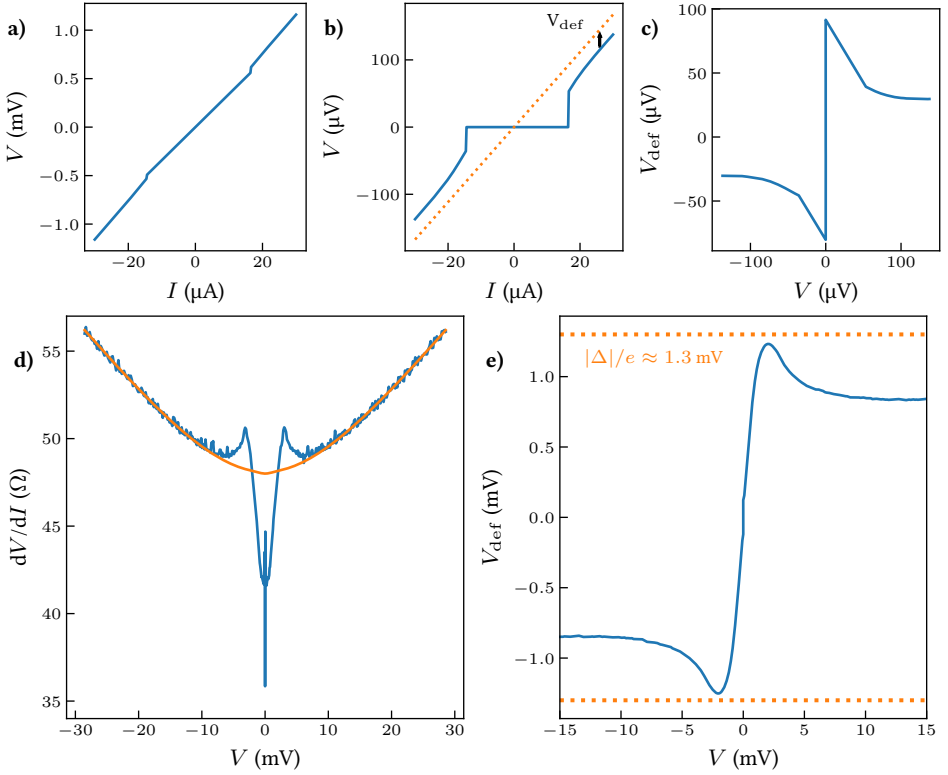


Figure 6.5: a) Two-terminal  $IV$  curve of an Nb/Pd/Nb SNS junction (junction A). b) Two-terminal  $IV$  curve with series resistance of 33  $\Omega$  subtracted (blue). The orange dotted line is a linear  $IV$  curve with a resistance that matches the high-bias differential resistance of the junction. c) Deficit voltage versus the voltage across the junction. d) Differential resistance of the junction versus bias voltage (blue). The differential resistance shows a dip below 5 mV bias voltage, with another dip at zero bias voltage. Furthermore, above 5 mV, the differential resistance can be well-described by a parabola, which is plotted in orange. e) Deficit voltage versus bias voltage calculated from the differential conductance in d). The parabolic background is subtracted and the resistance of 48  $\Omega$  ( $\approx 15 \Omega$  junction resistance + 33  $\Omega$  series resistance). The maximum deficit voltage is close to  $\frac{|\Delta|}{e}$ , plotted as an orange dotted line for comparison.

In order to investigate the voltage deficit with respect to the normal state resistance, the maximum bias voltage applied should be on the order of  $\frac{2\Delta}{e} \approx 2.6$  mV for niobium or larger.

For this purpose, the  $IV$  characteristic was taken up to a bias current of 2 mA. The differential resistance versus bias voltage for this measurement is shown in Figure 6.5d in blue. The switching current is seen as a sharp dip at zero bias voltage. The differential conductance further increases going to higher bias voltages, with a peak at 3 mV. At higher bias voltages, the differential resistance can be described by  $dV/dI \approx R_0 + \alpha V^2$ , which is plotted in orange, with  $R_0 = 48 \, \Omega$  and  $\alpha = 2.06 \cdot 10^6 \, \Omega V^{-2}$ . By subtracting the  $IV$  curve corresponding to this background from the measured  $IV$  curve, the deficit voltage is obtained, shown in Figure 6.5e. The maximum deficit voltage is 1.23 mV, at a bias voltage of 2.6 mV. This deficit voltage is only slightly smaller than the voltage corresponding to the superconducting gap of niobium,  $\frac{\Delta}{e} \approx 1.3$  mV. In the context of the Octavio-Tinkham-Blonder-Klapwijk (OTBK) theory[78], this matches with an SNS junction with  $Z \approx 0.5 - 0.6$ , which is to be expected for a typical disordered NS contact[78, 186, 202–205]. The  $I_{sw}R_N$ -product, on the other hand, is on the order of 180  $\mu V$ , which is comparatively low. A peculiarity of the deficit voltage versus bias voltage is the local maximum, which contrasts the expectations from BTK theory[75] for highly transparent NS interfaces, which predicts a hyperbolic-tangent-like monotonically increasing deficit voltage curve. While the low-bias and high-bias regions do fit with such a curve, understanding the origin of such local maxima requires further theoretical or experimental investigation. A possible explanation for the shape of the curve could be a reduction in heating at low bias voltages. As the bias voltage is increased, Andreev reflections become less important and the resistance increases. Simultaneously, the heating  $I^2R$  should then increase, which could result in an overshoot in the differential resistance.

### 6.3.2 Temperature dependence

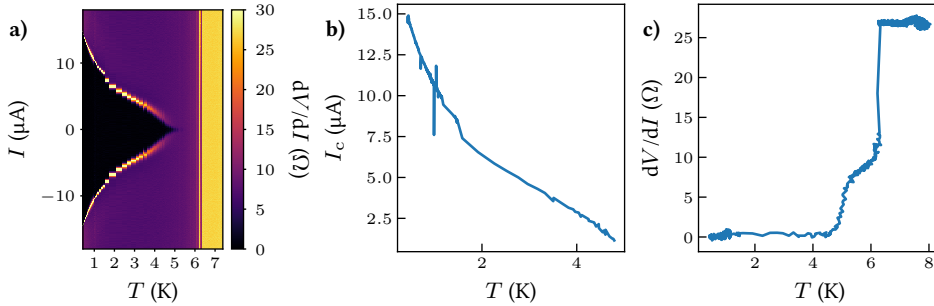


Figure 6.6:  $IV$  characteristic versus temperature while warming up junction B. a) Colormap of differential resistance versus bias current and temperature. b) Switching current versus temperature. c) Zero bias differential resistance versus temperature.

To obtain more information about the superconducting state, the temperature dependence of the  $IV$  characteristic was measured while slowly warming up the sample. The  $IV$  characteristic of a different junction (junction B) versus temperature was measured from 600 mK to 8.0 K. The corresponding differential conductance is plotted as a colormap in Figure 6.6a. This measurement was performed using a  $RuO_2$  thermometer, which has been calibrated below 4.2 K. The high temperature values might therefore deviate from their true value. From the colormap, it can be seen that the critical current decreases mono-

tonically. Furthermore, a transition is seen at 6.25 K, above which the Nb superconductor becomes resistive. By taking the maximum of the differential resistance for each trace, the switching current was extracted for each temperature between 600 mK and 5 K, which is plotted in Figure 6.6b versus temperature. A few spikes at  $T = 1$  K can be seen, which are related to rapid temperature fluctuations. From the slope of the  $I_{sw}$  versus  $T$  curve at 600 mK, the switching current is expected to further increase upon cooling the junctions down to 30 mK, which could not be done with this sample due to failure of the mixture circuit. Besides the switching current, the zero-bias differential resistance can also be used to characterize the SNS junctions. Figure 6.6c shows two steps in the differential resistance versus temperature: One at approximately 5 K, with a width of 1.0 K and another at 6.25 K, with a width of approximately 0.1 K. Comparing to the colormap, these can be interpreted as a  $T_c$  for the SNS junction and a  $T_c$  for superconductivity in the Nb/Pd thin film.

### 6.3.3 Magnetic field dependence

Next, the junctions were characterized versus magnetic field. In Figure 6.7a, the external magnetic field dependence of the differential resistance of junction B is plotted versus the magnetic field in the  $z$  direction,  $B_z$ , swept from  $-0.5$  T to  $0.5$  T and bias current. From the color map, it can be seen that the switching current is asymmetric with respect to magnetic field. Furthermore, the negative and positive switching current show a mirrored behavior. The entire colormap is skew-symmetric (symmetric under flipping  $B_z$  and  $I$ ). The switching current decreases in a monotonic manner as a function of magnetic field, without clear local minima. This is in contrast to the Fraunhofer-like patterns that are expected in larger SNS junctions. An explanation for this could be that the narrow ( $\sim 20$  nm) and constricted shape of the SNS junction produces an energy barrier for trapping Josephson vortices in the center[206], where the current density is largest. This is in contrast to wide SNS junctions. This lack of local minima persists when measuring from 0 to 8 T, as seen in Figure 6.7b. The switching current of the junction decreases more rapidly at low magnetic fields than it does at high magnetic fields. The transition in magnetic field lies at approximately 0.6 to 0.9 T, at which point the critical current is approximately  $7 \mu\text{A}$ , 47% of the maximum switching current. Comparing to the predictions for constricted SNS junctions[206], this suggests that the mean-free path is larger than the junction width.

Beside the switching current of the junction, an increase in differential resistance can be seen between 3 and 4 T. At zero bias current, the middle of this increase is at approximately  $B_{z,c} = 4.3$  T. Using equation 2.87, this yields a coherence length of approximately 8.7 nm. Remarkably, the switching current of the junction persists beyond this transition. This was observed in a subset of all junctions, with many junctions exhibiting a smaller critical field. Above the switching current, peaks in the differential resistance can be seen, which are potentially related to hotspots in the NS bilayer[207], locations where the film locally heats up and loses superconductivity. At a magnetic field of 5.3 T, the switching current appears to split into two peaks, one that decreases more rapidly with magnetic field and one that increases rapidly with magnetic field, before decreasing above 5.7 T. While a possible explanation for the increased critical field of the junction can be sought in increased disorder at the center of the junction, no qualitative explanation has yet been found for the transition at 5.3 T.

Finally, the asymmetry of the switching current was investigated as a function of in-plane magnetic field. The asymmetry as a function of the azimuthal angle of an in-plane magnetic field of 0.2 T is shown in Figure 6.7d. In this plot, the differential resistance is shown as a colormap as a function of the positive bias current and the azimuthal angle, which shows a distinct upside down "angel-like" shape. Here, an azimuthal angle of  $0^\circ$  denotes the magnetic field direction parallel to the current direction in the wire. Furthermore, the vector magnet used is 'left-handed', meaning that the field rotates clockwise. The switching current is asymmetric in the  $90^\circ$  (y) direction. The colormap for negative current is plotted in Figure 6.7d. The negative switching current is similar to the positive switching current rotated by  $180^\circ$  (or mirrored about the origin).

The *IV* measurements of these initial Nb/Pd/Nb devices thus confirm the presence of superconductivity in the junctions through the presence of a switching current and excess current/deficit voltage. Furthermore, the critical field was found to be 4.3 T. To allow proper electromigration and use for contacting GNRs or molecules, the fabrication had to be further optimized to properly define the superconducting patches.

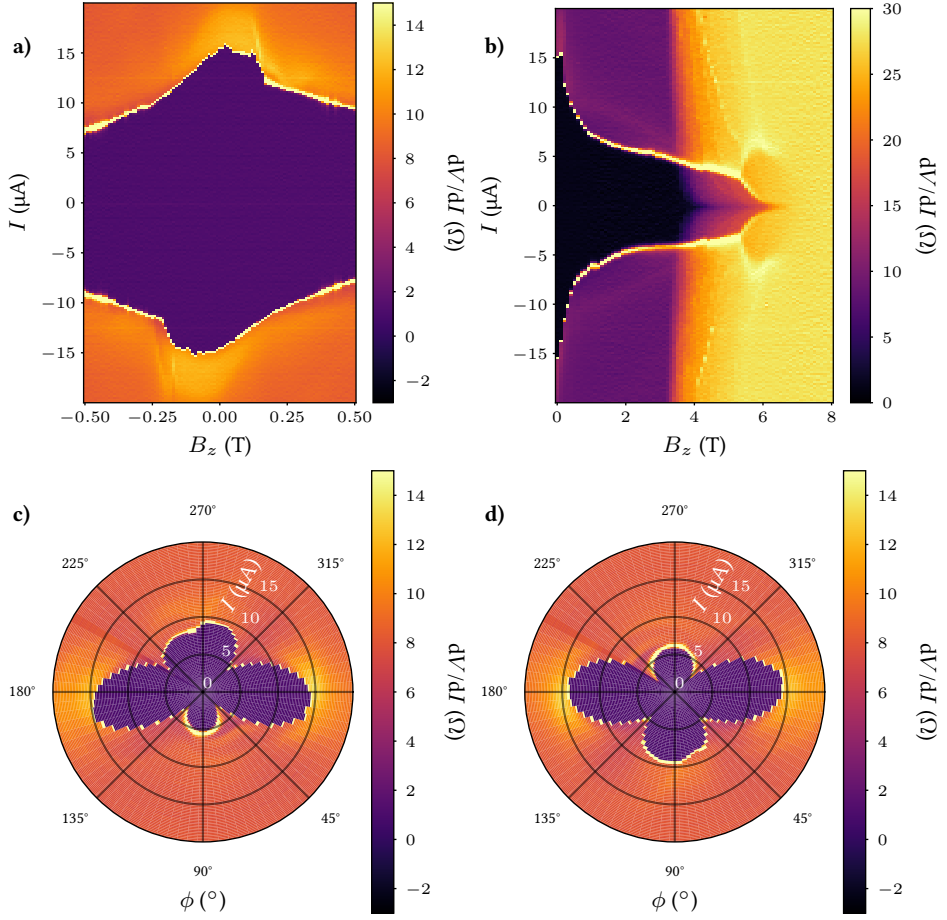


Figure 6.7: Magnetic field dependence of junction B. a) Color map of differential resistance versus magnetic field from -0.5 T to 0.5 T and bias current. b) Color map of differential resistance versus magnetic field from 0 T to 8 T and bias current. c) Polar plot color map of the differential resistance versus in-plane magnetic field angle and positive bias current. The applied magnetic field is 0.2 T. 0° is the direction parallel to the junctions. d) Polar plot color map of the differential resistance versus in-plane magnetic field angle and negative bias current. The applied magnetic field is 0.2 T. 0° is the direction parallel to the junctions.



## 6.4 First Nb/Au/Nb devices

As Nb/Pd/Nb junctions were found to be superconducting, but no clear superconducting gap was yet found in broken junctions, it was decided to change Pd for Au at this stage, since Au has a larger electron diffusion coefficient and has fewer charge carriers[208]. The larger electron diffusivity increases the coherence length in the normal metal but could also increase the importance of the inverse proximity effect. The reduction in the number of charge carriers, on the other hand, reduces the inverse proximity effect. Furthermore, EMBJ devices with Au are a well-characterized device geometry in literature[209] and SNS EMBJ devices with Au as the normal metal have been made before[210, 211], which makes Au a good comparison and testing ground for studying the superconducting proximity effect in break junctions.

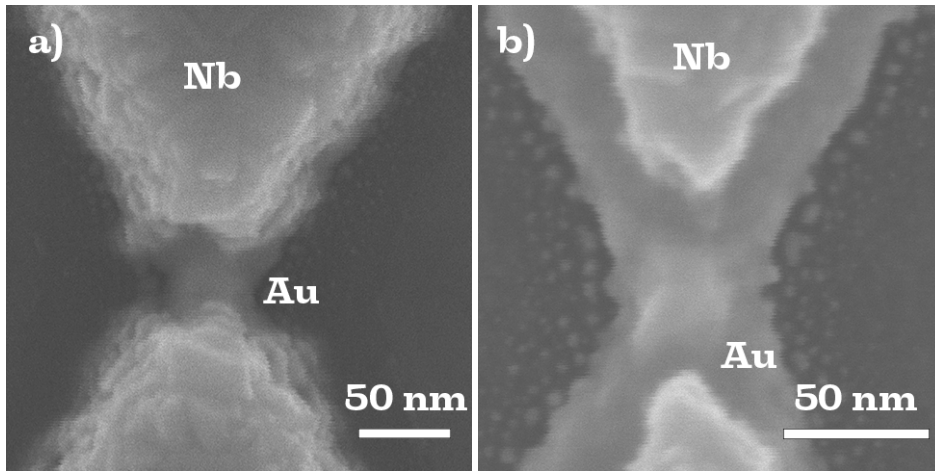


Figure 6.8: a) SEM image of an Nb/Au/Nb junction with 100 nm thick niobium patches. This image was taken by Abel Hutten. b) SEM image of an Nb/Au/Nb junction with 50 nm thick niobium patches. This image was taken by Abel Hutten.

The first Nb/Au/Nb junctions were made using the same recipe as the Pd-based junctions, but with a 50 nm spacing and an evaporation angle of  $6^\circ$ . These again showed connected or nearly connected Nb patches, as shown in Figure 6.8a. It was hypothesized that the cause of the extended Nb patches was due to deformation of the polymer mask during evaporation of the niobium, since Al/Pd junctions did not show this, while Nb/Pd and Nb/Au junctions did. The high melting point of Nb, 2468 K[212], compared to the substrate temperature, means that Nb is an element with a particularly low atomic diffusion coefficient, which results in increasing tensile stress with thickness[213, 214]. With the intention of reducing film stress, the thickness of the Nb layer was reduced to 50 nm in the next batch of junctions, which resulted in Nb patches that were approximately in the correct positions, as seen in Figure 6.8b. It is suspected that tensile stress from the deposition of niobium is responsible for the pattern failure. This can be qualitatively understood by considering that deposited niobium cools on the polymer mask and contracts due to its thermal expansion coefficient. As a result, the edges of the mask pull inwards and upwards, potentially

pulling apart the 30/50 nm wide PMMA strip separating the two niobium patches, thus resulting in the deposition of Nb outside the defined pattern.

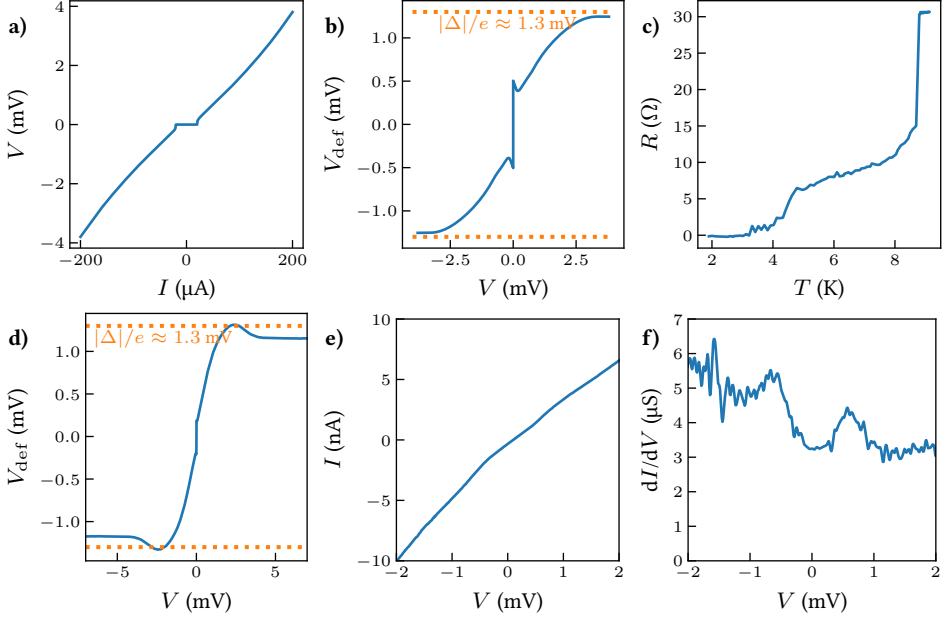


Figure 6.9: a) Sample A: Two-terminal  $IV$  curve with series resistance of  $23 \Omega$  subtracted. b) Sample A: Deficit voltage versus the voltage across the junction. c) Sample A: Zero bias differential resistance versus temperature. d) Sample B: Deficit voltage versus the voltage across the junction. e) Sample B:  $IV$  curve of an electromigrated junction. f) Sample B: differential conductance versus bias voltage calculated from e). A gap in the differential conductance can be seen.

As was done for Pd-based devices, the  $IV$  characteristic of the Au SNS junctions was characterized in order to extract the switching current, junction resistance and deficit voltage. These measurements were performed in a cryogenic dipstick in liquid He-4 at a base temperature of approximately 1.8 K. In Figure 6.9a, the series-resistance ( $24 \Omega$ ) corrected  $IV$  characteristic of an SNS junction with a 100 nm thick Nb layer is shown. The current is swept from  $-200$  to  $200 \mu$ A. The junction displays a switching current of  $20 \mu$ A. The corresponding deficit voltage is plotted in Figure 6.9b. The  $I_{\text{sw}}R_N$ -product is approximately  $500 \mu$ V, which is approximately  $\frac{\Delta}{3}$ . This indicates that the Au SNS junction can be considered to be a relatively high quality Josephson junction compared to its Pd variant. Considering that this measurement was performed at 1.8 K, the zero temperature  $I_c R_N$  can be expected to be even larger. The maximum deficit voltage observed is approximately 1.2 mV, which is similar to the Pd junctions and close to  $\frac{|\Delta|}{e}$ .

Since the dipstick in use was calibrated above 4.2 K,  $IV$  curves were also taken as a function of temperature, from 1.8 K to 9 K. In Figure 6.9c, the zero-bias differential resistance resulting from this measurement is plotted versus temperature. An increase in resistance appears at 4.5 K and a much sharper increase at 8.8 K, which can be interpreted as the  $T_c$

of the junction and the  $T_c$  of the NS bilayer film respectively. A  $T_c$  of 8.8 K for the film is expected for Nb ( $T_{c,bulk} \approx 9$  K) and suggests that the deposited Nb films are of comparable quality to other films in literature[215].

For the junctions with a 50 nm thick Nb layer,  $IV$  curves were taken as well. As can be seen in Figure 6.9d, the deficit voltage is similar to the junction with 100 nm Nb, while the  $I_{sw}R_N$ -product of 190  $\mu V$  is reduced compared to that of the 100 nm junction. This is in line with the expectation of a reduced Thouless energy due to the increased junction length. The 50 nm junctions were electromigrated at cryogenic temperature until resistances exceeded 13 k $\Omega$  with the intention of investigating the resulting superconducting gaps by tunneling spectroscopy. Nearly all junctions did not show a clear gap in the differential conductance. An  $IV$  curve of a junction that did show such a gap is plotted in Figure 6.9e. For this junction, the current was measured as a function of bias voltage. The corresponding differential conductance is plotted in Figure 6.9f. The differential conductance shows broad peaks at approximately  $\pm 600$   $\mu V$ , which indicates a proximity gap of 300  $\mu V$  at the center of the junction, assuming a symmetrically broken junction. The observed peaks form a "soft" gap-like structure, with a differential conductance at zero bias that is of comparable size to the differential conductance above the gap voltage ( $> 1$  mV). Furthermore, the differential conductance of this junction showed large peaks and dips related to fluctuations in the junction conductance and the resulting finite-bias current. This is unusual for Au break-junctions and suggests that the junction might not have broken properly. This could be due to the junction breaking at the Ti of the Ti/Au/Nb layer, alloying with Ti or Nb, or contamination of the gold film.

## 6.5 Final Nb/Au/Nb devices

To improve the electromigration, the spacing between the superconducting patches was increased to 60 nm. As a result, the overlap between the evaporated Au layers decreased and the constriction became more resistive. Current densities and heating were expected to become more localized to the narrower center of the junction, increasing the likelihood of breaking the junction at the center. An example SEM image of the resulting junctions is shown in Figure 6.10. The Nb patches for this particular sample are slightly shifted due to an offset in the mounting between the two evaporators (QT-AJA for Ti+Au, Plassys MEB550S for Nb).

The junctions were measured in a He-3/He-4 dilution fridge, at a base temperature of 33 mK (electronic temperature of approximately 100 mK). Junctions were first measured in their intact state to confirm the presence of a switching current, before breaking them in a step-wise manner to higher resistances. At each resistance, the  $IV$  characteristic was measured to investigate the evolution of the deficit voltage while breaking the junction. In Figure 6.11, the  $IV$  characteristic, deficit voltage and differential conductance of three junctions at resistances of 200  $\Omega$ , 12.7 k $\Omega$  and 67 k $\Omega$  are shown. These are representative curves for a slightly broken junction, a junction broken to an atomic point contact and a tunnel junction. Figures 6.11a, 6.11b and 6.11c show that the  $IV$  characteristic changes from an S shape due to supercurrent and excess current, to an inverted S shape due to a superconducting gap upon breaking the junctions further.

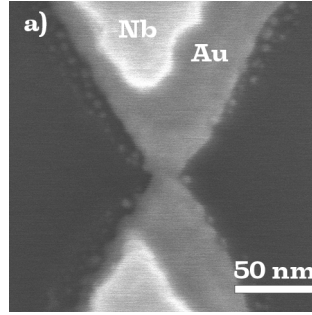


Figure 6.10: a) SEM image of an Nb/Au/Nb SNS junction with a 60 nm defined spacing and a 50 nm thick Nb layer. The Nb layer is shifted with respect to the Ti/Au layer underneath due to a different placement in the two evaporators. The overlap between the two evaporated Au layers in the bridge area is reduced, resulting in a narrower constriction. This image was taken by Abel Hutten.

## 6

The deficit voltage versus bias voltage curves in Figures 6.11d, 6.11e and 6.11f show that the shape of the deficit voltage curve does not drastically change until the junction is broken. A small reduction, approximately a factor  $\frac{2}{3}$ , is observed upon breaking the junction to an atomic point contact. Upon breaking, a negative deficit voltage (or excess voltage) is seen at bias voltages below 0.5 mV. A small positive deficit voltage remains above 1.3 mV bias voltage. The maximum deficit voltages for junctions that are not completely broken appear to coincide with features in the differential conductance, plotted in Figures 6.11g, 6.11h and 6.11i versus the bias voltage.

For the intact junction, Figure 6.11g, a bump/change in the slope of the differential conductance is seen at the maximum deficit voltage, which is marked as  $V_{\text{gap}} \approx 340 \mu\text{V}$ . This coincides with the maximum deficit voltage. The differential conductance also shows a zero-bias peak. Notably, the amplitude of this peak, the slope of the  $IV$  characteristic in Figure 6.11a, is finite, which means that the  $200 \Omega$  junction does not conduct a dissipationless current. This was not expected, as the thermal noise current should be on the order of 4 nA at most, considerably smaller than the expected switching current-scale of  $1 \mu\text{A}$ . As the bias voltage is increased, the peak is followed by symmetrical dips and peaks before decreasing to a constant value above  $\sim 1 \text{ mV}$ . The symmetrical peaks at finite bias could be related to multiple Andreev reflections (MAR). MAR are to be expected in SNS junctions and lead to an enhanced conductance. However, MAR should lead to peaks (or peak-dip structures) in the differential conductance at voltages  $V_n = \frac{2E_{\text{gap}}}{en}$ , with  $n$  and integer. These peaks are not observed in the differential conductance. Considering the lack of a dissipationless current, a possible explanation could be that the MAR signal is smoothed out in voltage by a lack of filtering of GHz frequency interference[216], which excites quasiparticles and induces pair-breaking.

In the differential conductance of the atomic point contact, two sets of peaks are seen. The outer peaks are again marked as  $V_{\text{gap}} \approx 390 \mu\text{V}$ , which corresponds to approximately 2 times the maximum deficit voltage. The inner peaks are slightly asymmetrical towards low bias voltages and located below  $\frac{V_{\text{gap}}}{2}$  in voltage. These peaks are similar to the low-bias

peaks in the  $200\ \Omega$  junction, which shift outwards as the junction resistance is increased. No peak was observed at zero-bias voltage peak for the atomic point contact junction.

Finally, the differential conductance of the tunnel junction shows a dip in the differential conductance, surrounded by peaks, which are at approximately the same voltage as in the atomic point contact. Again, these peaks are labeled with  $V_{\text{gap}} \approx 430\ \mu\text{V}$ . Since the gap voltage scale in the differential conductance corresponds to  $2\frac{E_{\text{gap}}}{e}$ , the superconducting gap in the Nb/Au/Nb contacts is approximately  $215\ \mu\text{eV}$ . In the tunnel junction regime, humps can be seen in the differential conductance at approximately  $\frac{V_{\text{gap}}}{2}$ . These humps could be related to Andreev reflections. However, an alternate explanation can be made based on the presence of a soft gap in the density of states in the normal metal.

A soft gap in the density of states in the normal metal results in a tunneling differential conductance that can be approximately described as  $\frac{dI}{dV}(V) = G_{\text{SS}}(V) + G_{\text{NS}}(V) + G_{\text{SN}}(V) + G_{\text{NN}}(V)$ . Here  $G_{\text{SS}}$  denotes the differential conductance of a superconductor to superconductor tunnel junction. This tunneling process results in peaks at a voltage  $V = 2\frac{|\Delta|}{e}$ . The cross-terms  $G_{\text{NS}}$  and  $G_{\text{SN}}$  are the differential conductance related to a normal metal to superconductor tunnel junction, which result in voltage peaks at  $V = \pm\frac{|\Delta|}{e}$ .  $G_{\text{NN}}$  is the differential conductance of a normal metal to normal metal tunnel junction, which is approximately constant and results in a finite differential conductance at zero bias voltage. When these components are added, the result is an IV curve with peaks at  $V = \pm 2\frac{|\Delta|}{e}$  and peaks or humps at  $V = \pm\frac{|\Delta|}{e}$ , similar to the structure of the data. This alternate explanation shows that only a careful analysis can attribute differential conductance peaks at  $V = \pm\frac{|\Delta|}{e}$  to Andreev reflections. This argument can not explain MAR conductance features at  $V = \pm\frac{2|\Delta|}{ne}$ , with  $n > 2$ .

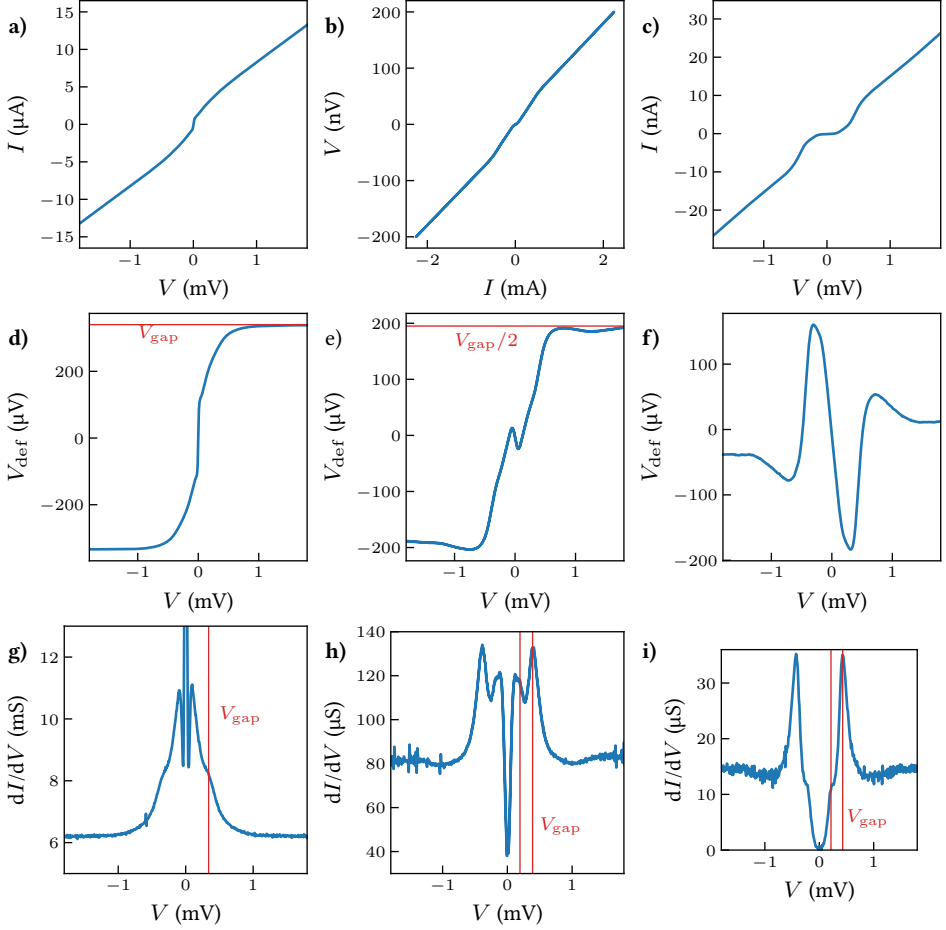


Figure 6.11: a), b), c) Two-terminal  $I$   $V$  curve of  $200\ \Omega$ ,  $12.7\ \text{k}\Omega$ ,  $67\ \text{k}\Omega$  Nb/Au/Nb SNS junctions. d), e), f) Deficit voltage versus bias voltage curves of  $200\ \Omega$ ,  $12.7\ \text{k}\Omega$ ,  $67\ \text{k}\Omega$  Nb/Au/Nb SNS junctions. The red horizontal lines indicate the maximum deficit voltage. g), h), i) Differential conductance versus bias voltage curves of  $200\ \Omega$ ,  $12.7\ \text{k}\Omega$ ,  $67\ \text{k}\Omega$  Nb/Au/Nb SNS junctions. The vertical line in g) is plotted at the maximum deficit voltage. The two red vertical lines in h) are plotted at one and two times the maximum deficit voltage. The red vertical lines in i) are plotted at the voltage corresponding to the peak in the differential conductance ( $V_{\text{gap}}$ ) and half the voltage  $V_{\text{gap}}/2$ .

## 6.6 Final Nb/Pd/Nb devices

The evidence of a gap in the differential conductance of Au-based junctions motivated studying the same geometry with Pd. Matching the changes to the Au-based devices, the Pd devices were changed to have a spacing of 60 nm between superconducting Nb patches of 50 nm thickness. An SEM image of a device is shown in Figure 6.12a. The Nb patches in these devices were again slightly outside the defined pattern. This suggests that the evaporation of Pd instead of Au potentially worsens this fabrication issue, potentially due to increased film stress. Nevertheless, these junctions are SNS junctions that are not shorted through the superconductor. The constriction in these junctions are narrower, with less overlap area between the two Pd evaporation steps that make the bridge, compared to the first Pd devices.

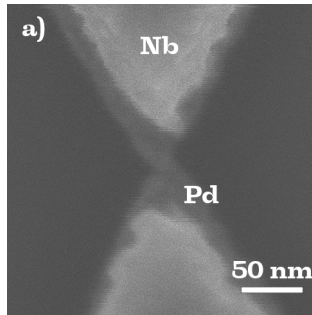


Figure 6.12: a) SEM image of an Nb/Pd/Nb junction with a 60 nm spacing and a 50 nm thick Nb layer.

The junctions were loaded in a He-3/He-4 dilution fridge and measured at a base temperature of 33 mK. Here, the current-voltage characteristic of a single junction will be discussed before and after electromigration. The four-terminal  $IV$  characteristic of the unbroken junction with a resistance of 142  $\Omega$  is shown in Figure 6.13a. It shows a small region of increased differential conductance at low-bias voltages. The corresponding current-scale is 200 nA. As was the case with the broken Au-based junctions, no dissipationless switching current is observed. The deficit voltage versus bias voltage is shown in Figure 6.13b. The  $I_{sw}R_N$ -product is 20  $\mu\text{V}$  and the maximum deficit voltage is 40  $\mu\text{V}$ , labeled as  $\frac{V_{gap}}{2}$ . The differential conductance versus bias voltage, plotted in Figure 6.13c, shows peaks at 40 and 80  $\mu\text{V}$ , indicated by the red lines. In contrast to what was observed for the Au junctions, the inner peaks match with the maximum deficit voltage. This could indicate that only single Andreev reflections dominate in these SNS junctions, as MAR would result in a shift to lower bias voltages.

Upon electromigration of the junction, a tunnel junction was made with a resistance of 63 k $\Omega$ . The  $IV$  characteristic of this junction is plotted in Figure 6.13d. The zero-bias conductance of the  $IV$  characteristic is reduced with respect to the conductance above 50  $\mu\text{V}$ , similar to the gold tunnel junction. The differential conductance, plotted in Figure 6.13e also shows a gap, with peaks at bias voltages of  $\pm 76 \mu\text{V}$ , indicated as  $V_{gap}$ . The corresponding superconducting energy gap, assuming a symmetric junction, is 38  $\mu\text{V}$ .

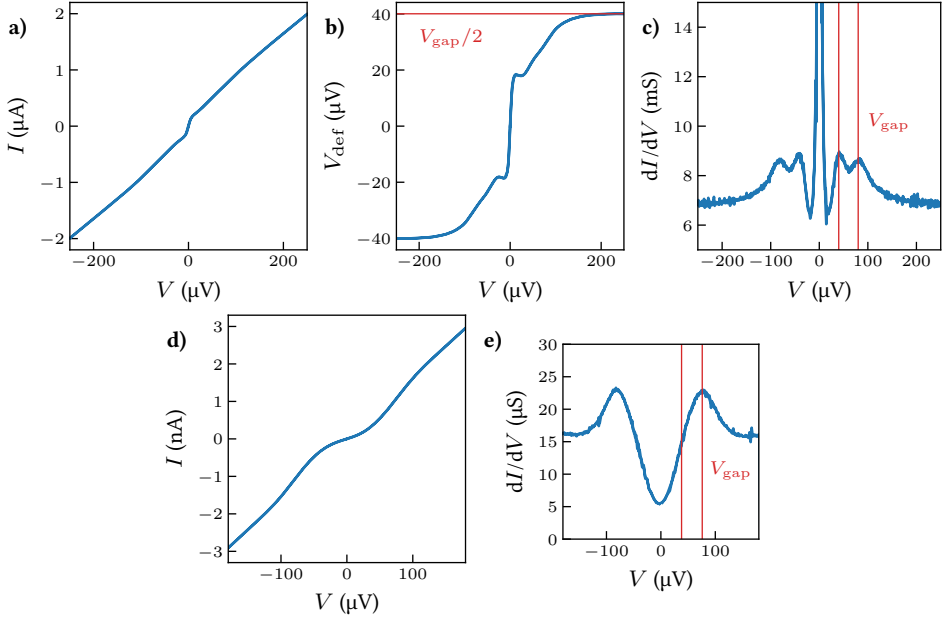


Figure 6.13: Measurements on 60 nm spacing Nb/Pd/Nb SNS junctions with 50 nm thick Nb patches. a) Four-terminal  $IV$  curve of an intact junction. b) Deficit voltage versus bias voltage calculated from a). c) differential conductance versus bias voltage calculated from a). d) Four-terminal  $IV$  curve of an electromigrated junctions (62 k $\Omega$ ). e) Differential conductance calculated from d).

6

## 6.7 Discussion and Conclusion

In this chapter, the current-voltage characteristic of SNS junctions was investigated with the intent of identifying the superconducting gap through the deficit voltage (excess current). The constricted junction geometry allows for electromigration of the SNS junctions.

The deficit voltage of all junctions approximately follows an S shape, matching the expected behavior for NS interface from BTK theory (equations 2.98 and 2.99). On top of this S shape, a region of increased differential conductance is seen at zero bias voltage, which can be related to the Josephson effect. Furthermore, small deviations are observed at finite bias, which can be related to Andreev reflections. Notably, we have shown that in these junctions, the maximum deficit voltage often coincides with bumps or peaks in the differential conductance. These peaks are expected to be found at the voltage corresponding to the energy gap (or two times the energy gap) in the normal metal. Furthermore, the deficit voltage of junctions and the locations of peaks in the differential conductance do not change by more than a factor 2 as the junctions are electromigrated. Hence, the energy gap of the broken junctions can be reasonably estimated from the properties of unbroken or partially electromigrated SNS junctions.

One aspect that has not been characterized yet is the effect of asymmetry on the junctions. Efforts were made to make the junctions break as close to the center between the two niobium patches as possible. It would be of interest to study how the features in the



differential conductance and the deficit voltage change as a function of the position of the breaking point in the junction. In this case, it is expected that the energy gap differs between the source and drain of a tunnel junction. In particular, for the partially broken junctions, it would be of interest to investigate if the differential conductance shows features that reveal the junction asymmetry. Finding a relationship between the differential conductance and the geometrical asymmetry would be useful for tracking whether SNS junctions are breaking symmetrically without post-inspection.

In the broken junctions, a superconducting gap of 215  $\mu\text{eV}$  was extracted from the differential conductance of the Au junctions and a superconducting gap of 40  $\mu\text{eV}$  in Pd junctions with Nb patches. While the induced spectral gap in 60 nm Au devices exceeds the superconducting energy gap of aluminium (176  $\mu\text{eV}$ ) and can be translated in an effective BCS  $T_c$  of 1.36 K, the gap of the Pd devices implies a BCS critical temperature of only 270 mK. Furthermore, the superconducting gap in Pd devices is "soft". The ratio of the minimum differential conductance in this device is  $5.52 \mu\text{S}/16.18 \mu\text{S} \approx 34\%$ . The gap differential conductance gap in the Au device is an order of magnitude "harder". The conductance ratio is approximately  $0.5 \mu\text{S}/15 \mu\text{S} \approx 3.3\%$ . Thus, for purposes such as spectroscopy or to proximitize another material, the spectral gap in the Au devices is both larger and "harder". Further work is necessary to increase the spectral gap in Pd for making useful superconducting contacts to graphene nanoribbons, either by reducing the length-scale of the Pd bridge or by increasing the mean free path in the Pd films, perhaps through annealing or changes to the deposition rate or thickness. Another possibility is to deposit gold underneath the Pd layer to improve carrier diffusivity.

For both Au- and Pd-based devices, the temperature dependence of the  $IV$  characteristic was taken. This revealed that two  $T_c$  values,  $T_{c1} \approx 4.5 - 5 \text{ K}$  and  $T_{c2} \approx 8.8 \text{ K}$ . While the first appears when the switching current of the SNS junction disappears and can thus be related to the junction, the second  $T_c$  is likely related to the NS bilayer film. Since these measurements were performed on junctions where the Nb patches were connected, the effective normal metal length is  $L \approx 0 \text{ nm}$ . Thus, the value of  $T_{c1}$  could be considered as the maximum achievable junction  $T_c$ . The BCS gap related to this critical temperature is approximately 650  $\mu\text{eV}$ . This energy scale can be considered the upper limit for the energy gap in the SNS junctions made in this chapter (with the defined N and S film thicknesses and properties).

Finally, an asymmetry of the switching current, a Josephson diode effect, was discovered in the first Pd junctions as a function of the externally applied magnetic field. A particularly strong effect was seen when the magnetic field was applied in the in-plane perpendicular direction. Although not explicitly shown here, this effect was also present in all other Au and Pd junctions that were investigated with an in-plane perpendicular magnetic field in the dilution fridge. This will be further studied in chapter 7.

In conclusion, the deficit voltage and differential conductance of constricted SNS junctions can be used to estimate the superconducting gap in the center. The maximum deficit voltage stays approximately constant, reducing by a factor of  $2/3$  at most, in the studied junctions as they are electromigrated to an atomic point contact. The energy gap in the normal metal in broken junctions can be estimated from the properties of intact or par-

tially electromigrated junctions. An energy gap of 215  $\mu\text{eV}$  was achieved in Au-based SNS junctions and energy gap of 38  $\mu\text{eV}$  in Pd-based SNS junctions. Further work should be performed to optimize the proximity effect in Nb/Pd devices to obtain larger energy gaps for hybrid devices incorporating graphene nanoribbons or nanoparticles.

## 7

# Josephson Diode Effect and Nonreciprocal Charge Transport in SNS Junctions

7

*The investigation discussed in this chapter started as an unexpected result when studying SNS junctions with the purpose of optimizing the proximity effect in an electromigrated break junction, as discussed in the previous chapter. It was found that samples with fabrication flaws caused by deformation or collapse of the resist mask during the evaporation of a 100 nm thick niobium layer caused the spacing between the superconducting patches to be significantly reduced. In some cases, the Nb patches almost connected, resulting in samples that could effectively be either considered as Dayem bridges or short SNS junctions. These junctions exhibited peculiar features, such as asymmetry in the critical current when a magnetic field was applied in the direction perpendicular to the current in the plane of the sample, as well as critical fields exceeding the critical field of the NS bilayer. In this chapter, further investigation of the critical current asymmetry in well-defined (with a 50 nm thick niobium layer) SNS junctions is presented. The asymmetry of the critical current and excess current/deficit voltage is studied as a function of magnetic field for both Au and Pd SNS junction. An asymmetry in the deficit voltage is found that matches the asymmetry in critical current. Using the feedback-controlled electromigration method, it is found that for a given junction, the effect has a characteristic magnitude, voltage and magnetic field scale that does not show significant dependence on the junction resistance.*

## 7.1 Introduction

A diode is a circuit element that has a different electrical current for a positive bias voltage than for a negative bias voltage of the same magnitude. This asymmetrical electrical conductance has several applications, such as the rectification of alternating current (AC)

---

I want to thank Abel Hutten for his contribution to the work in this chapter during his master thesis project. I also want to thank Serhii Volosheniuk for fabricating the last batch of Nb/Pd/Nb SNS junctions

to direct current (DC). In recent years, it has been discovered that such asymmetrical conductance can also be realized in devices with superconductors, such as bilayer and trilayer thin films involving normal metals[44, 217], and superconducting weak-links/Josephson junctions[46, 50]. In these devices, the critical/switching current above which the devices become resistive is different in the forward and backward directions. This so-called superconducting diode effect, or Josephson diode effect, thus allows for rectification of AC current to DC voltage pulses.

So far, several mechanisms have been put forward to explain the superconducting and Josephson diode effect, such as finite momentum superconductivity and the Meissner effect[100, 218], magnetochiral anisotropy (MCA) in noncentrosymmetric materials[219, 220], asymmetric vortex barriers[217, 221, 222], the Zeeman effect and Rashba or Dresselhaus spin-orbit interaction[47–49], dissipation and breaking of electron-hole symmetry[223] or an electrical polarization in a superconductor-insulator-superconductor (SIS) junction[50]. On the level of the devices studied, there are also differences. Some devices show diode behavior with parallel applied magnetic field, whereas other devices show diode behavior with perpendicular applied magnetic field. This suggests the presence of multiple mechanisms at play. In the case of Josephson junctions made of NbSe<sub>2</sub>/Nb<sub>3</sub>Br<sub>8</sub>/NbSe<sub>2</sub> van der Waals heterostructures, a Josephson diode effect in the absence of magnetic field was found[50]. In addition to mechanisms, general symmetry arguments have been formulated[43, 224]. These theoretical studies highlight the importance of spatial symmetries. In particular, the inversion symmetry (symmetry upon reflection of coordinates with respect to a point,  $\mathcal{I}$ ), mirror symmetry (symmetry upon reflection of coordinates with respect to a plane,  $\mathcal{M}_x$ ,  $\mathcal{M}_y$ , and  $\mathcal{M}_z$ ), twofold rotation symmetries ( $\mathcal{C}_{2x}$ ,  $\mathcal{C}_{2y}$  and  $\mathcal{C}_{2z}$ ), and time reversal symmetry (symmetry upon reversing the time coordinate,  $\mathcal{T}$ ), can all have an impact on the symmetry behavior of the critical current. Depending on the broken coordinate symmetries, Josephson junctions can be categorized based on the resulting symmetry between the positive and negative critical current,  $I_{c+}(\vec{B})$  and  $I_{c-}(\vec{B})$ , where  $\vec{B}$  is the magnetic field. The possible symmetries are the current-reversion symmetry (JR,  $I_{c+}(\vec{B}) = -I_{c-}(\vec{B})$ ), field-reversion symmetry (BR,  $I_{c+}(\vec{B}) = I_{c+}(-\vec{B})$  and  $I_{c-}(\vec{B}) = I_{c-}(-\vec{B})$ ) and field-current reversion symmetry (BJR,  $I_{c+}(\vec{B}) = -I_{c-}(-\vec{B})$ ). Any Josephson diode has to break JR symmetry. Thus, Josephson diodes are of BR type (these can be field-free Josephson diodes), of BJR type or without any critical current symmetry.

To date, most experimental studies of the Josephson diode effect have used materials with strong Rashba spin orbit coupling or a noncentrosymmetric lattice structure. In this chapter, the presence of a Josephson diode effect of the BJR type with perpendicular (to the current) in-plane magnetic field will be investigated in a variable thickness SNS junction made from evaporated metal thin films, with Nb as the superconductor and Au or Pd as the normal metal. The normal metal layer in these SNS junctions is shaped in the form of a constriction, which has the advantage of allowing control over the resistance of the wire using feedback-controlled electromigration. In this way, the scaling of the diode effect with junction resistance (or Josephson energy/critical current) is investigated. As the resistance of junctions increases, it was observed that the critical current disappears in current versus voltage ( $IV$ ) measurements. Thus, a Josephson diode effect could not be observed at all junction resistances. A related asymmetry in the finite bias conductance is

characterized instead.

At finite bias voltages, rather than the Josephson current, it is the excess current,  $I_{\text{exc}} = I - \frac{V}{R_N}$ , where  $R_N$  is the normal state resistance, that is of importance. To compare transport at different resistances, the deficit voltage,  $V_{\text{def}} = I_{\text{exc}} R_N = IR_N - V$ , is defined. Here, with the aim of answering the question: "How does the deficit voltage asymmetry scale with the junction resistance", we investigate the deficit voltage versus bias voltage and magnetic field for various increasing junction resistances. It is found that neither the deficit voltage, nor the asymmetry in deficit voltage, changes significantly as the junction resistance is increased, until the normal metal is broken. In the tunneling regime, both quantities reduce in magnitude.

## 7.2 Methods

The SNS junctions are made within a single lithography step using angular shadow mask evaporation. The fabrication is further explained in chapter 3. The superconducting banks of the SNS junction consist of a 5 nm thick Ti adhesion layer underneath a 13 nm thick Pd (15 nm thick Au for the gold junctions) layer. On top of this, 50 nm Nb was evaporated. The superconducting banks were designed with a spacing of 60 nm. In the N region of the SNS junctions, only Pd (or Au) was evaporated. The Pd-based SNS junctions were made within the same evaporator (Plassys MEB 550<sup>1</sup>) without breaking the vacuum, whereas the Au junctions were made by first evaporating Ti + Au in another evaporator (AJA-QT<sup>2</sup>). Care was taken to align the junctions as well as possible in both cases. For the Pd junctions, an optical microscope was used to obtain angular alignment with an accuracy of 0.1°. In order to perform four-terminal measurements of the devices, extra connections and contact pads were made on the Pd chips.

7

## 7.3 Results

We first discuss the Pd-based junctions. In Figure 7.1a, an SEM image of a Pd-based SNS junction is shown. The bright areas in this image are the regions where Nb was evaporated. At the center of the junction, another brighter region is seen, which corresponds to a thicker Pd region due to the small overlap between the two evaporated Pd layers.

### 7.3.1 Basic characterization

The junctions were measured in a Helium-3/Helium-4 dilution refrigerator with a vector magnet (1/3/9 T in X/Y/Z) at a base temperature of 30 mK. In order to characterize the junctions, a bias current was applied to them using the symmetrical bias mode of an S4c current source module<sup>3</sup>. The voltage across the junction is measured using a low-noise M2i voltage measurement module (<2 nV noise<sup>4</sup>). In Figure 7.1b, we show the voltage

<sup>1</sup><https://www.tudelft.nl/tnw/over-faculteit/afdelingen/quantum-nanoscience/kavli-nanolab-delft/equipment/deposition/plassys>

<sup>2</sup><https://www.tudelft.nl/tnw/over-faculteit/afdelingen/quantum-nanoscience/kavli-nanolab-delft/equipment/deposition/aja-qt>

<sup>3</sup>QT designed instrumentation: <https://qwork.tudelft.nl/schouten/ivvi/doc-mod/docs4c.htm>

<sup>4</sup>QT designed instrumentation: <https://qwork.tudelft.nl/schouten/ivvi/doc-mod/docm2i.htm>

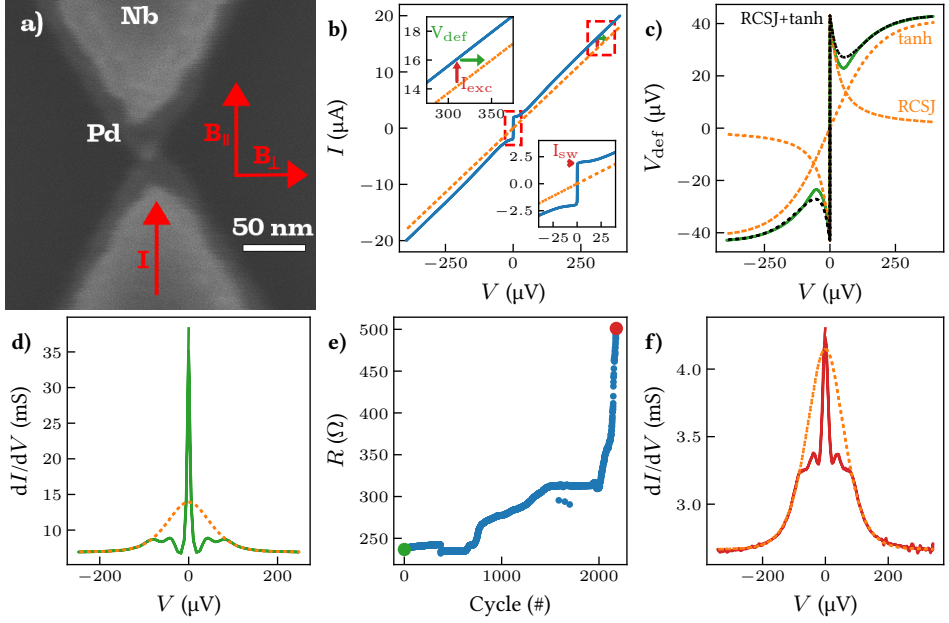


Figure 7.1: Basic characterization of SNS junctions. a) SEM image of a variable thickness Nb/Pd/Nb SNS constriction made by the shadow-mask evaporation technique. b)  $IV$  curves of a device with an initial resistance of 22  $\Omega$ . Measurements were taken by measuring voltage versus bias current in a four-terminal geometry. c) Excess current and voltage  $I_{exc}R_N$  versus voltage (green curve). The orange dotted curves represent RCSJ model and a hyperbolic tangent (tanh) curve. The black dotted line is the sum of the RCSJ and tanh curves. d) Differential conductance of a sample with an initial resistance of 144  $\Omega$  (green curve). The orange dotted line is a fit to an empirical fit function. e) Evolution of the two-terminal resistance during the electromigration process. The green and red dots indicate the initial and final state, for which the four-terminal  $dI/dV$  curves are plotted in Figure 7.1d and Figure 7.1f respectively. f) Differential conductance of a sample after electromigration to a final state resistance of 375  $\Omega$  (red curve). The orange dotted line is a fit to an empirical fit function.

versus bias current curve ( $IV$  curve) of a device with a resistance of 22  $\Omega$  (Junction A) in blue. In order to also record potential hysteresis effects, the voltage was recorded while the current was ramped from 0 to +20 to -20 to 0  $\mu A$ . Since no such effects were found, in the following measurements data points were only taken during sweeps up from 0 to +20  $\mu A$  and from 0 to -20  $\mu A$ . For comparison, a linear  $IV$  curve for a 22  $\Omega$  resistor is plotted (dashed orange line). The SNS junction conducts more current than a normal resistor with the same high-bias differential resistance would at all voltages. The difference between the curves in current at constant voltage is called the excess current ( $I_{exc}$ ), while the deviation in voltage at constant current is the deficit voltage ( $V_{def}$ ). In addition, the current at which the junction switches from superconducting to resistive is denoted as  $I_{sw}$ . Below the switching current, the measured voltage is zero (with  $\sim 1$  nV noise).

In Figure 7.1c the deficit voltage is plotted versus the measured voltage in green. Since no hysteresis was observed, the low bias behavior was fitted by eye using the overdamped resistively capacitance shunted junction (RCSJ) model expression,  $V_{def} = \frac{V}{|V|} \sqrt{V_{sw}^2 + V^2} - V$ .

A switching voltage  $V_{sw}$  of 43  $\mu\text{V}$  was found by comparison to the data. The corresponding curve is plotted as a dotted orange curve. Above approximately 100  $\mu\text{V}$ , the excess current begins to flatten off. In this regime, the deficit voltage was fitted by eye to the empirical formula:

$$V_{\text{def}} = V_0 \tanh\left(\frac{V}{V_1}\right), \quad (7.1)$$

where  $V_0$  and  $V_1$  are fit parameters. This empirical fit can be related to the typical excess current of high transparency NS interfaces in the Blonder-Tinkham-Klapwijk (BTK) model[75]. The found parameters are  $V_0 = 41.4 \mu\text{V}$  and  $V_1 = 180 \mu\text{V}$ . This curve is plotted as an orange dotted curve in Figure 7.1c, labeled as 'tanh'. The sum of the RCSJ model curve and the empirical tanh curve is plotted as the black dotted curve labeled 'RCSJ + tanh'. This curve matches the deficit voltage at zero bias and at high bias, overshooting by 5  $\mu\text{V}$  below bias voltages of 100  $\mu\text{V}$ .

To illustrate the behavior of the deficit voltage better, the differential conductance is plotted. The differential conductance is related to the excess current by  $\frac{dI}{dV} = G_N + \frac{dI_{\text{exc}}}{dV}$ . The excess conductance from the normal state conductance  $G_N = \frac{1}{R_N}$  is the derivative of the excess current. In Figure 7.1d, the differential conductance of a junction with an initial resistance of 144  $\Omega$  (Junction B) is plotted. The empirical tanh formula is again used to fit the high-bias behavior, with  $V_0 = 64.6 \mu\text{V}$  and  $V_1 = 63.9 \mu\text{V}$ . This junction did not show a clear switching current; A finite resistance remained at zero bias current. Instead of carrying a supercurrent, the junction shows a large enhancement of the differential conductance at zero bias voltage. This could be consistent with a phase-diffusive conductance described by Ivanchenko-Zilberman (IZ) theory[91], as described in chapter 2, or by  $P(E)$  theory[225].

This junction was electromigrated using the feedback controlled electromigration described by O'Neill[209]. The bias voltage was repeatedly ramped up from 100 mV until a user-defined maximum voltage was reached or the two-terminal resistance across the junction changes by more than a certain percentage ( $\sim 1\%$ ), monitored every 1  $\mu\text{s}$ . After this condition is reached, the voltage is ramped down to 100 mV. Each ramp up and down constitutes a cycle. The two-terminal resistance versus the cycle number is shown in Figure 7.1e. In the regime where the wire has a low resistance compared to the conductance quantum, the desired sample resistance can be accurately achieved by electromigration. The initial point (green) corresponds to the initial state for which the differential conductance is shown in Figure 7.1d. The differential conductance versus voltage at the final point (red) is plotted in Figure 7.1f. The four-terminal junction resistance at this point is 375  $\Omega$ . A fit to 7.1 was again performed, which gives  $V_0 = 78 \mu\text{V}$  and  $V_1 = 43 \mu\text{V}$ . While the fit parameters of the dissipative tanh component are similar, the excess zero-bias differential conductance peak is significantly reduced in amplitude relative to the normal-state conductance.

### 7.3.2 Josephson diode effect in a magnetic field

In order to characterize the symmetry properties of the switching current of the SNS junctions, a magnetic field was applied. First, the  $IV$  characteristic of sample A was recorded versus magnetic field in the  $z$  direction. The measured voltage is plotted as a color map

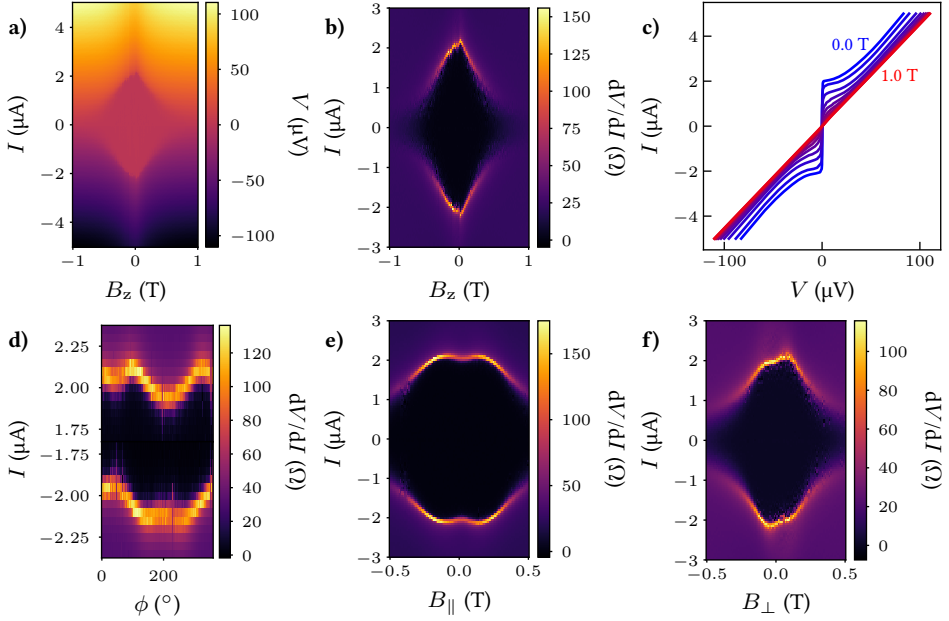


Figure 7.2: Josephson diode effect in a  $22\ \Omega$  junction (junction A). a) Color map of the measured voltage versus bias current and applied magnetic field in the  $z$  direction. b) Differential resistance map calculated from a). The color map is slightly asymmetric as a function of applied magnetic field, but symmetric as a function of current. c)  $IV$  curves at increasing applied magnetic field. The critical current and excess current are suppressed as the magnetic field is increased. d) Color map of the differential resistance versus bias current and the azimuthal angle,  $\phi$ , of the in-plane magnetic field (100 mT). e) Color map of the differential resistance versus bias current and parallel in-plane applied magnetic field. f) Color map of the differential resistance versus bias current and perpendicular in-plane applied magnetic field. The color map for this magnetic field direction shows an additional asymmetry versus current, with a skew-symmetric dependence, such that  $dV(I, B)/dI \approx dV(-I, -B)/dI$ .

in Figure 7.2a. In this color map, a region with zero resistance and a resistive region can be seen. To highlight the transition to the resistive state, the corresponding differential resistance is plotted in Figure 7.2b. This map shows a small asymmetry in magnetic field, with a symmetric behavior in current. Individual  $IV$  traces at magnetic fields of 0.0 to 1.0 T in steps of 0.1 T are plotted in Figure 7.2c. As the magnetic field increases, the  $IV$  characteristic becomes increasingly linear and both the switching current and excess current decrease.

After this, the azimuthal angle of the sample with respect to the vector magnet axes was determined. This is necessary for accurate characterization of diode effects, as the mounting of samples in a chip carrier and insertion into the dilution fridge results in an offset angle of the sample with respect to the vector magnet axes (this value is typically of the order of  $40^\circ \pm 10^\circ$  in the dilution fridge measurement setup). To characterize the offset angle, the in-plane magnetic field was kept at 100 mT and the azimuthal angle,  $\phi$ , was swept. For each angle, an  $IV$  curve was taken. The differential resistance versus the azimuthal angle and bias current is shown in Figure 7.2d. This shows a roughly sinusoidal dependence of the switching current on magnetic field. In addition, it can be seen that



the positive and negative switching currents  $I_{\text{sw}+}$  and  $I_{\text{sw}-}$  at  $\phi = 30^\circ$  are not equal to their values at  $\phi = 210^\circ$ . Instead, the data follows  $I_{\text{sw}+}(\phi) = I_{\text{sw}-}(\phi + 180^\circ)$ . The angular dependence of this measurement was compared to a camera image of the sample. From this it was determined that the azimuthal angle of  $30^\circ$  corresponds to the perpendicular in-plane direction to the SNS junction, as indicated in Figure 7.1a.

After the offset angle was determined, the response of the  $IV$  characteristic to a magnetic field in the perpendicular ( $30^\circ$ ) and parallel ( $120^\circ$ ) in-plane directions were recorded. The color map of the differential resistance versus bias current and magnetic field in the parallel direction is plotted in Figure 7.2e. The dependence of the differential resistance on parallel in-plane field is similar to the dependence on the field in the  $z$  direction, but appears to be more symmetric. Furthermore, the switching current initially increases as the magnitude of the magnetic field is increased from zero field, which is not expected for an ordinary SNS junction. There is no visible asymmetry in the switching current. The color map of the differential resistance versus bias current and magnetic field in the perpendicular direction is plotted in Figure 7.2f. Again, the switching currents are not at their maximum at a magnetic field 0 T. The dependence on perpendicular in-plane field, however, differs from the parallel field dependence.  $I_{\text{sw}+}$  increases as the magnetic field is increased, while  $I_{\text{sw}-}$  increases as the magnetic field is decreased. The differential resistance becomes more asymmetric as the magnetic field is increased and has an apparent skew symmetric component such that  $dV(I, B)/dI \approx dV(-I, -B)/dI$ . A positive magnetic field biases the junction towards conducting in the forward direction and, vice versa, a negative magnetic field biases the junction in the backward direction. The junction behaves as a Josephson diode that is tunable by the perpendicular in-plane magnetic field.

The properties of a more highly resistive SNS junction, junction B at  $375 \Omega$ , was investigated in more detail as well. In Figure 7.3a, a color map of the differential resistance is plotted versus magnetic field in the  $z$  direction. This map is symmetric in current and magnetic field. In Figure 7.3b, the differential conductance corresponding to line cuts at magnetic fields from 0.0 T with steps of 0.1 T to 1.0 T are shown. These show that the magnetic field in the  $z$  direction gradually suppresses the differential conductance, without introducing significant asymmetry in the differential conductance versus voltage curve, similar to the behavior of Junction A. The color map of the differential resistance versus perpendicular in-plane magnetic field in Figure 7.3c shows a distinctly different behavior. Matching the behavior of the switching current in junction A, the differential resistance map is skewed, showing skew symmetry such that  $dV(I, B)/dI \approx dV(-I, -B)/dI$ . To illustrate the extent of the skewing, the differential conductance at  $-0.08$ ,  $0.02$  and  $0.12$  T are plotted in Figure 7.3d in green, blue and red respectively. An offset magnetic field shift of  $+0.02$  T was found and taken into account. From the curves, it can be seen that a positive magnetic field changes the differential conductance to be larger at positive voltages and smaller at negative voltages. Vice versa, a negative field biases the differential conductance to be larger at negative voltages. Moreover, the differential conductance at  $0.12$  T ( $-0.08$  T) exceeds the differential conductance at zero magnetic field at positive (negative) bias voltages. This is in contrast to the behavior observed for an applied magnetic field in the  $z$  direction, for which the differential conductance decreases uniformly with increasing magnetic field.

So far, it has been shown that an asymmetry in the electrical conductance with magnetic

field exists in the switching current of a low-resistance junction ( $20\ \Omega$ , junction A) and in the differential conductance of a high-resistance junction ( $375\ \Omega$ , junction B). To investigate whether the effect persists as the junction resistance is further increased, junction B was electromigrated in a step-wise manner, aiming to double the resistance with each step. This was continued until the junction reached  $11\ \text{k}\Omega$ , close to the resistance quantum. This is an indication that the normal metal in the SNS junction has been broken down to a few-atom point contact [226]. Attempting to electromigrate further, the resistance increased to  $60\ \text{k}\Omega$  and displayed signatures of tunneling between (proximitized) superconductors (shown in the appendix, Figure 7.A.1).

### 7.3.3 Conductance asymmetry in an atomic point contact

In Figure 7.4a, the magnetic field dependence of the junction at  $11\ \text{k}\Omega$  is shown. In contrast to the junction at  $375\ \Omega$ , this junction shows a relative increase, rather than a decrease of the differential resistance at zero bias. In the differential conductance traces from  $0.0$  to  $1.0\ \text{T}$  in  $0.1\ \text{T}$  steps in Figure 7.4b, this appears as a small zero-bias dip. Similar to the behavior at  $375\ \Omega$ , the peaks in the differential conductance are suppressed as the magnetic field is increased. In contrast, however, the differential resistance curves are slightly asymmetric at all magnetic fields. The curve at  $1.0\ \text{T}$  is also not flat as a function of voltage, instead showing residual asymmetry with voltage. Since excess conductance due to superconductivity is suppressed at  $1.0\ \text{T}$ , this residual asymmetry is to be attributed to the presence of the atomic point contact. The color map of differential resistance as a function of magnetic field in the perpendicular in-plane direction in Figure 7.4d again shows skewing that is visually similar in magnetic field scale and symmetry to the color map for the  $375\ \Omega$  junction. This demonstrates that the nonreciprocal conductance as a function of  $B_{\perp}$  remains even when the junction is broken to an atomic point contact. The differential conductance traces at  $-0.08\ \text{T}$ ,  $0.02\ \text{T}$  and  $0.12\ \text{T}$  in Figure 7.4d highlight this fact, showing asymmetry similar to the junction at  $375\ \Omega$ .

7

### 7.3.4 Resistance dependence

Since junction B shows a similar asymmetry at different resistances, a comparative analysis of the nonreciprocal conductance is of interest. For this purpose, the differential conductance was normalized by the differential conductance at the largest measured positive bias current for each resistance. Differential conductance curves at resistances of  $144$ ,  $700$ ,  $3\ \text{k}\Omega$  and  $11\ \text{k}\Omega$  are shown in Figure 7.5a, offset by  $0.1$ . These show that the differential conductance features change significantly at voltages below  $100\ \text{mV}$ , but are similar for the region between  $100$  to  $200\ \text{mV}$ . This makes a comparison based on differential conductance features difficult. Instead, it was found that the deficit voltage for the junction at different resistances is comparable. The deficit voltage is plotted as a function of the measured voltage in Figure 7.5b. The deficit voltage shows a hyperbolic tangent-like profile for all resistances. The voltage scale in measured voltage ( $\sim 100\ \mu\text{V}$ ) and in deficit voltage ( $\sim 40\ \mu\text{V}$ ) is of similar magnitude at all plotted resistances.

In order to compare the nonreciprocal conductance effect in the deficit voltage for different junction resistances, two quantities will be introduced to quantify the asymmetry. These are the asymmetry with respect to magnetic field and the asymmetry with respect

to current. To illustrate the nonreciprocal conductance effect with respect to the magnetic field, the deficit voltage is plotted as a function of bias voltage at magnetic fields of  $-0.08$ ,  $0.02$  and  $0.12$  T in Figure 7.5c. The curves at finite field also qualitatively follow equation 7.1 as a function of bias voltage, but with a smaller amplitude and shifted in  $V$  and  $V_{\text{def}}$ . Notably, the deficit voltage increases uniformly with increasing magnetic field for all voltages. Close to zero bias voltage, the deficit voltage curves overlap. The difference between the deficit voltage at  $0.12$  T and  $-0.08$  T is indicated by an orange arrow as  $\Delta V_{\text{def},B}$ , which will be used as a measure of the asymmetry of the deficit voltage with respect to magnetic field.

The dependence of the deficit voltage on magnetic field is shown in Figure 7.5d, for the maximum positive and negative applied bias currents. The deficit voltages are not symmetric under flipping the sign of the current or magnetic field individually, but are (anti)symmetric upon flipping the sign of both current and magnetic field. The asymmetric part of the deficit voltage with respect to current can be obtained by adding the curves at positive and negative current (adding the red and green curves), which will be called  $\Sigma V_{\text{def},I}$ .

The response of the deficit voltage to magnetic field at different junction resistances was analyzed next.  $\Delta V_{\text{def},B}$  is plotted versus the measured voltage in Figure 7.5e. The excess voltage difference is zero at zero bias voltage and grows with increasing bias voltage until  $100 \mu\text{V}$ , above which the deficit voltage difference starts to plateau. The response versus bias voltage is even. At low bias voltages, the deficit voltage asymmetry is roughly quadratic with voltage. From the plot, it can be extracted that a magnetic field of  $100$  mT results in an induced deficit voltage of  $\frac{\Delta V_{\text{def},B}}{2} \approx \frac{13 \mu\text{V}}{2} = 6.5 \mu\text{V}$  at  $200 \mu\text{V}$ ; This is an effect of approximately 3.5% of the bias voltage. Since the excess voltage difference plateaus at high measured voltage (bias current), the scaling of the measured effect with magnetic field is most easily investigated in this regime.

In Figure 7.5f,  $\Sigma V_{\text{def},I}$  is plotted as a function of applied magnetic field in the perpendicular in-plane direction. Remarkably, the low-field behavior of the deficit voltage asymmetry versus current at all different resistances has the same slope around zero bias voltage of roughly  $150 \mu\text{V}/\text{T}$ . The curve saturates at roughly  $15 \mu\text{V}$  and  $200$  mT and can be described empirically by the formula  $\Delta V = \frac{cb}{1+|b|^3}$ , with  $b = \frac{B_{\perp}}{B_0}$ , plotted as the dotted blue line in Figure 7.5f. Here, the voltage scale  $c = 30 \mu\text{V}$  and the field scale,  $B_0$ , is equal to  $200$  mT. Based on the magnetic field dependence, the maximum effect compared to the voltage scale is:  $\frac{\Delta V_{\text{def}}}{V_+ + V_-} \approx \frac{15 \mu\text{V}}{400 \mu\text{V}} \approx 3.75\%$ . If the asymmetry in deficit voltage is instead compared to the average deficit voltage, the effect scale is roughly  $\frac{\Delta V_{\text{def}}}{V_{\text{def}+} + V_{\text{def}-}} \approx \frac{15 \mu\text{V}}{60 \mu\text{V}} \approx 25\%$ .

### 7.3.5 Asymmetry in Au-based SNS junctions

Finally, to investigate whether the found effect is specific to Pd-based SNS junctions, the non-reciprocity in deficit voltage was investigated in gold-based SNS junctions, for which the same measurements were performed in the same dilution fridge. Here, we discuss the behavior of a gold junction which was electromigrated to a resistance of  $12.2 \text{ k}\Omega$ , which is close to the conductance of a single atom gold contact[227]. A two terminal  $IV$  mea-

surement was performed for perpendicular magnetic fields for every 10 mT from  $-400$  to  $400$  mT. The differential resistance, which was numerically calculated from the bias current and measured voltage, versus perpendicular magnetic field and bias current is plotted as a color map in the appendix, Figure 7.A.2a. Rather than discussing the differential resistance map, here the deficit voltage at constant bias current versus perpendicular in-plane magnetic field will be focused on to allow for comparison with the analysis of the Pd junctions.

The deficit voltage of this junction as a function of perpendicular in-plane magnetic field at various bias currents ( $-190$ ,  $-95$ ,  $0$ ,  $95$ ,  $190$  nA) is plotted in Figure 7.6a. The excess voltage saturates already at  $\pm 95$  nA. The deficit voltage shows similar asymmetry as a function of magnetic field to the results for Nb/Pd/Nb junctions. This asymmetric contribution again depends on the direction of the current. In order to illustrate this, the sum and difference with respect to the bias current (even and odd parts in  $I$ ) are calculated by subtracting and adding the deficit voltage at  $95$  nA and  $-95$  nA and dividing by 2, plotted in Figure 7.6b. The odd part in  $I$  is even in  $\vec{B}_\perp$  and the even part in  $I$  is odd in  $\vec{B}_\perp$ . The shape of the even part in  $I$  matches that of the Pd junction studied, but the deficit voltage scale is larger, reaching a maximum of  $50 \mu\text{V}$  at  $0.16$  T. Dividing the even part in  $I$  by the odd part in  $I$ , the asymmetry of the excess voltage is obtained, shown in Figure 7.6c. This maxes out at roughly 40% at  $\pm 180$  mT.

The deficit voltage versus the measured voltage across the junction is plotted in Figure 7.6d for constant applied perpendicular in-plane magnetic fields of  $0.02$  T (blue),  $0.19$  T (red) and  $-0.15$  T (green). These magnetic field set-points were chosen as they maximize the diode signal, given by the odd part of  $\Delta V_{\text{def},I}$  plotted in 7.6b. Again, an offset field on the order of  $20$  mT is found. As was found for the Pd-based junction, the zero-field curve (at  $0.02$  T applied magnetic field) is symmetric and follows a hyperbolic-tangent-like shape. At finite field, the difference between the maximum and minimum excess voltage decreases and the deficit voltage becomes more asymmetric. As was found for the Pd junctions, a positive applied perpendicular in-plane magnetic field results in a larger deficit voltage in the forward current direction and a negative applied perpendicular in-plane magnetic field results in a larger deficit voltage in the backward current direction. By subtracting the negative field curve (green) from the positive field curve (red), the asymmetric component with respect to magnetic field,  $\Delta V_{\text{def},B}$ , was obtained. This is plotted in Figure 7.6e versus bias voltage, which shows a V-shaped curve that saturates at a deficit voltage of approximately  $90 \mu\text{V}$ . Finally, dividing this by the average of the measured voltage at  $0.19$  T and  $-0.15$  T results in a measure of the efficiency, which is plotted in Figure 7.6f. This efficiency shows that the voltage signal from changing the magnetic field has a local maximum and maxes out at approximately 9% of the average applied voltage.

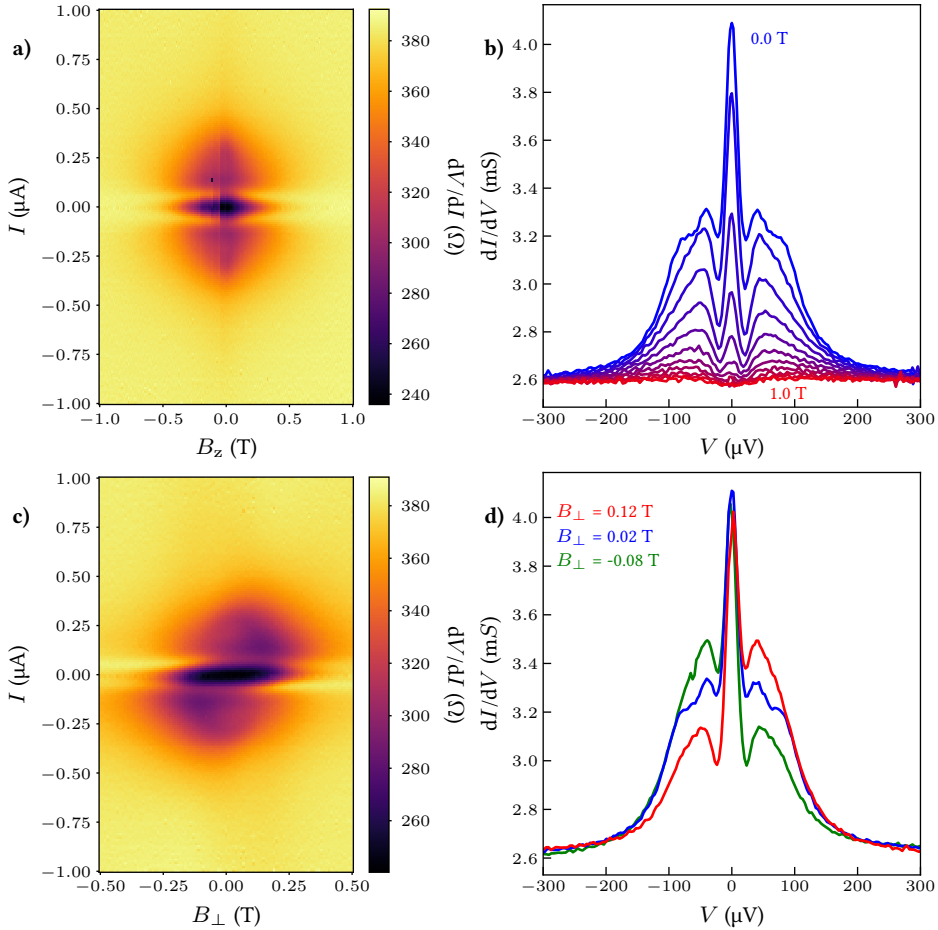


Figure 7.3: Nonreciprocal conductance in a 375 Ω junction (junction B). a) Color map of the differential resistance versus bias current and magnetic field in the  $z$  direction. b) Differential conductance versus bias current curves corresponding to a) for increasing applied magnetic field in the  $z$  direction. The excess conductance is suppressed as the magnetic field is increased. c) Color map of the differential resistance versus bias current and applied magnetic field in the perpendicular in-plane direction. The differential resistance profile is skew-symmetric again. d) Differential conductance curves versus perpendicular in-plane applied magnetic field. Curves for net negative, zero and positive magnetic field are shown. An offset field of 0.02 T was determined by the symmetry of the  $dV/dI$  map.

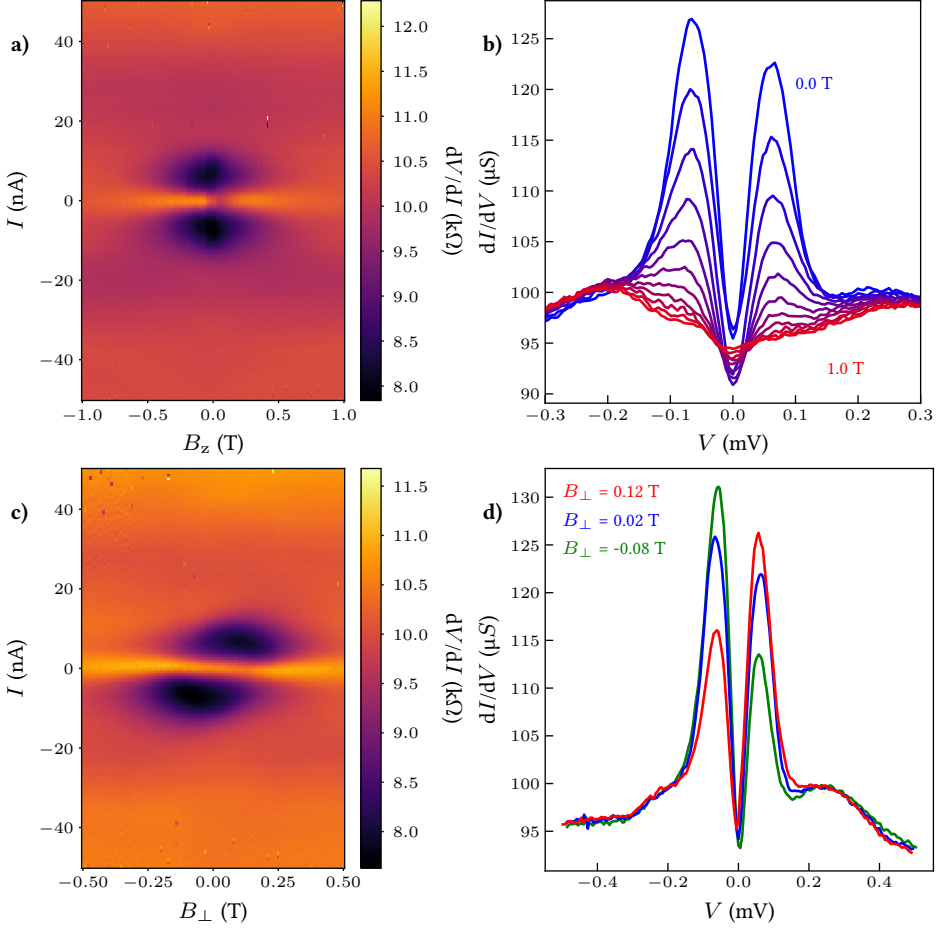


Figure 7.4: Nonreciprocal conductance in a 11 kΩ junction device a) Color map of the differential resistance versus bias current and magnetic field in the z direction. b) Differential conductance versus bias current curves corresponding to a) for increasing applied magnetic field in the z direction. The excess conductance is suppressed as the magnetic field is increased. c) Color map of the differential resistance versus bias current and applied magnetic field in the perpendicular in-plane direction. The differential resistance profile is skew-symmetric again. d) Differential conductance curves versus perpendicular in-plane applied magnetic field. Curves for net negative, zero and positive magnetic field are shown. An offset field of 0.02 T was determined by the symmetry of the  $dV/dI$  map.

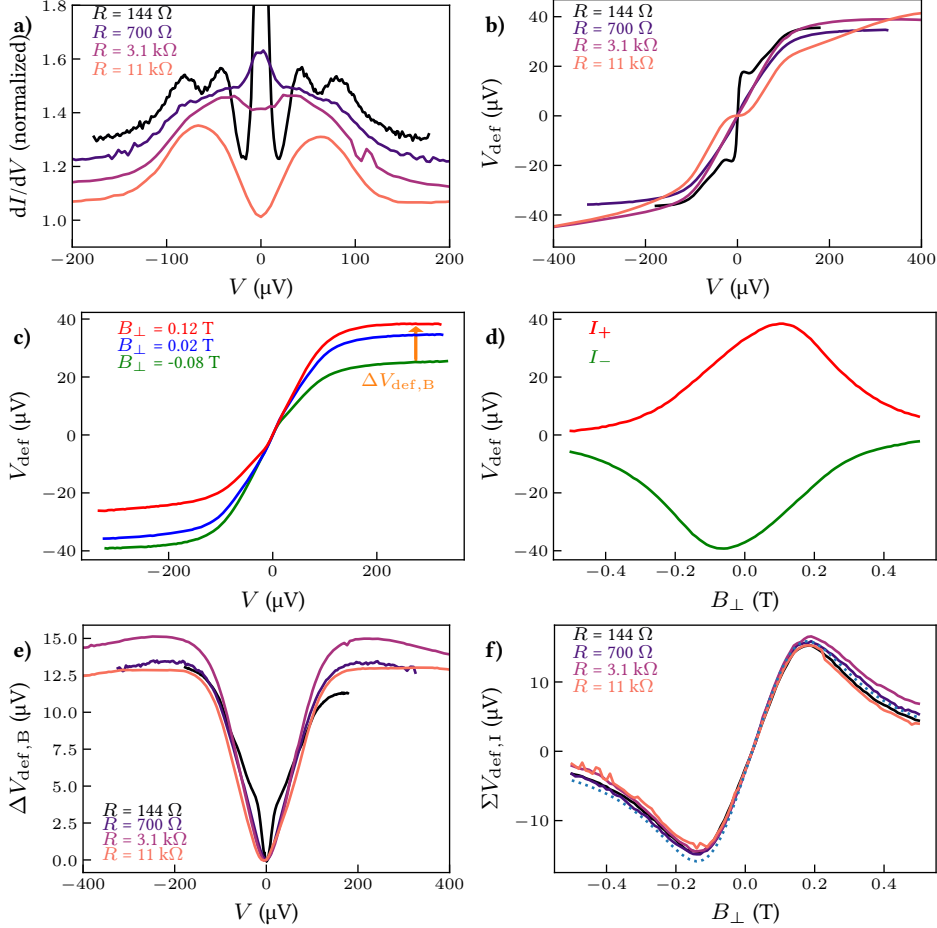


Figure 7.5: Non-reciprocity as a function of device resistance for junction B. a) Differential conductance (normalized to high-bias resistance) versus bias voltage at zero magnetic field. The different curves correspond to different resistance values of the same junction created by feedback-controlled electromigration. b) Deficit voltage difference versus bias voltage. c) Deficit voltage at a junction resistance of  $700 \Omega$  versus bias voltages for perpendicular in-plane magnetic fields of  $-0.08$ ,  $0.02$  and  $0.12$  T. d) The deficit voltage versus perpendicular in-plane magnetic field at a junction resistance of  $700 \Omega$  at maximum positive and negative bias currents. e) Normalized differential conductance difference between  $-0.08$  and  $0.12$  T versus bias voltage. f) Sum of the deficit voltage at the maximum and minimum applied current versus in-plane magnetic field. The dashed blue line corresponds to a fit by eye to the formula  $\Delta V = \frac{cb}{1+|b|^3}$ , with  $b = \frac{B_{\perp}}{B_0}$ .

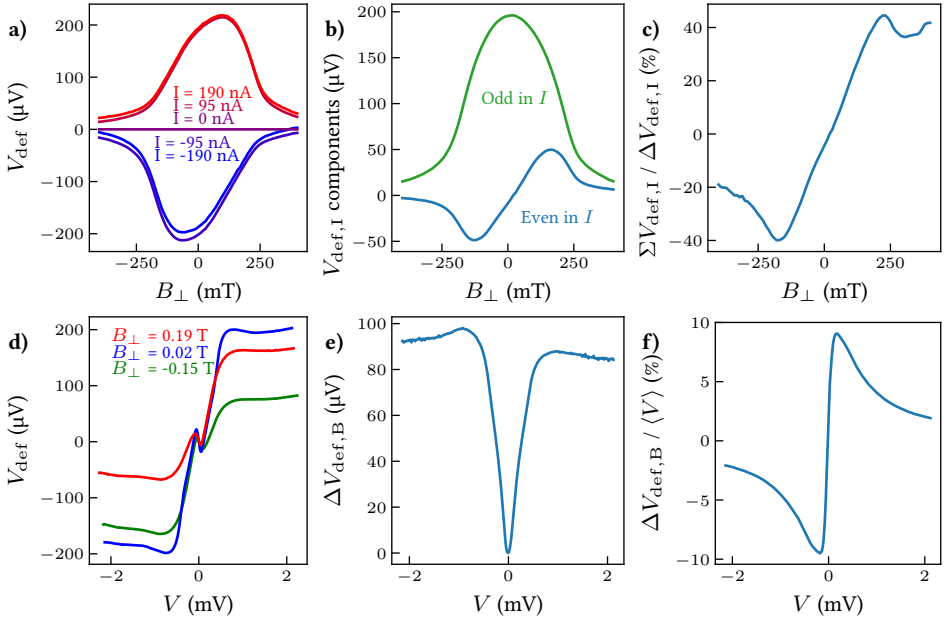


Figure 7.6: Nonreciprocal conductivity in a Nb/Au/Nb SNS junction electromigrated to 12.2 k $\Omega$ . a) Deficit voltage versus perpendicular in-plane magnetic field for several bias currents. b) Even and odd components of the deficit voltage with respect to bias current as a function of perpendicular in-plane magnetic field. The even part (blue curve) in bias current is odd with respect to magnetic field and the odd part (green curve) in bias current is even with respect to magnetic field. c) Ratio of the even and odd parts of the deficit voltage with respect to bias current as a function of magnetic field. d) Deficit voltage as a function of bias current for several net -170 mT, 0 mT and +170 mT applied magnetic field. e) Deficit voltage difference between +170 mT and -170 mT applied magnetic field as a function of bias current. f) Asymmetry of the IV curve as a function of bias current, calculated by taking the ratio of deficit voltage difference to the average voltage.



## 7.4 Discussion

### 7.4.1 Current symmetries and coordinate symmetries

The first finding in this chapter is the presence of an asymmetry in the critical current at finite magnetic field in Nb/Pd/Nb and Nb/Au/Nb SNS junctions. An asymmetry in the critical current is also known as the Josephson diode effect. In order for this to occur, it has been posited that certain symmetries must be broken[224]. According to the theoretical classification, the behavior of the critical current and deficit voltage of the devices is of the BJR type. This translates into breaking inversion symmetry ( $\mathcal{I}$ ), mirror symmetry in the  $z$  direction ( $\mathcal{M}_z$ ), twofold rotation symmetry about the  $x$  axis ( $C_{2x}$ ), and twofold rotation symmetry about the  $y$  axis ( $C_{2y}$ ). Furthermore, at least one symmetry must be obeyed. In the Nb/Pd/Nb and Nb/Au/Nb junctions studied in this chapter,  $\mathcal{I}$ ,  $\mathcal{M}_z$ ,  $C_{2x}$  and  $C_{2y}$  are broken by the height variation in the layered (vertically U-shaped) geometry. Meanwhile, devices obey mirror symmetry in the  $x$  direction,  $\mathcal{M}_x$ . Thus, the broken coordinate symmetries match the symmetry requirements for the BJR-type Josephson diode effect. As seen in Figure 7.2, in order for the magnetic field to produce a Josephson diode effect, the external magnetic field must be applied in the direction perpendicular to the current path and the  $z$  direction, which is the direction in which the mirror symmetry is broken. This way, the rotation of the magnetic vector potential,  $\vec{A}$ , occurs in the plane of the current path and the broken symmetry.

### 7.4.2 Theoretical explanation for diode effects in SNS junctions

The fact that the SNS junctions that were studied are made of only elemental superconductors and noble metals favors a simple explanation. We will here consider three different scenarios that can explain the diode effect.

*Momentum from Meissner screening current:* The observed effect aligns with the theory proposed by Davydova[100]. In this theory, the Meissner current at the surface of the superconductor, which arises when a perpendicular magnetic field is applied, can modify the current-phase relation of a Josephson junction. This mechanism does not depend on specific properties of the superconductor or normal metal and should thus be universal for all Josephson junctions. In this theory, it is the momentum-scale  $e|\vec{A}|$  of the Meissner current that results in a finite-energy, odd frequency component of the pairing[104]. For a uniform magnetic field and no screening, this can be expressed as a momentum boost by  $e|\vec{A}| = e|\vec{B}|w$ , where  $w$  is half the thickness of the superconductor. The momentum boost affects the kinetic energy. When electrons at the Fermi velocity are shifted by a velocity,  $v = \frac{e\vec{A}}{m} = \frac{e|\vec{B}|w}{m}$ , their energy changes to

$$E = \frac{m(v + v_F)^2}{2} = E_F + mv_F v + \frac{mv^2}{2} \approx E_F + eBwv_F. \quad (7.2)$$

The last equality holds because  $v_F \gg v$ . When the velocity term exceeds the gap energy  $\Delta$ , depairing will occur due to the velocity boost. The depairing velocity can be expressed as  $v_{\text{dep}} = \frac{|\Delta|}{mv_F} \approx 163 \text{ m/s}$  and the related depairing magnetic field scale is  $|\vec{B}_{\text{dep}}| = \frac{|\Delta|}{ev_F w} \approx 37 \text{ mT}$ , taking  $|\Delta| = 1.3 \text{ meV}$ ,  $v_F = 1.37 \cdot 10^6 \text{ m/s}$  (Estimate for the Fermi velocity of s-orbital elec-

trons in niobium) and  $w = 25$  nm. The value obtained here is lower than the experimentally observed magnetic field scale of approximately 170 mT. This could be due to overestimation of the Fermi velocity, as niobium contains both s and d orbitals. In order to achieve better agreement, the magnetic screening by the superconductor should also be taken into account properly, rather than assuming  $\vec{A} = \vec{B}w$ , as is the case for a uniform magnetic field inside the superconductor. This matters only when the London penetration depth ( $\sim 39$  nm for niobium[228]) of the superconductor is on the order of  $w$  or smaller.

*Self-field effect:* Aside from the Josephson diode explanation, tentative explanations can be sought in the self-field of the device. The self-field of the device is the magnetic field that is produced by the current in the device itself. Since this adds up with the externally applied magnetic field, the total magnetic field at positive and negative bias current and finite magnetic field will differ. The self-field can be estimated by assuming the device is half a loop of wire with a radius of  $r = 25$  nm. Then, the magnetic field at the center of half a loop is approximately  $\frac{\mu_0 I}{4r}$  by the Biot-Savart law, where  $\mu_0 = 1.256 \cdot 10^{-6}$  N/A<sup>2</sup> is the vacuum magnetic permeability. At a bias current of 2  $\mu$ A, this results in a magnetic field of 25 mT. This is not negligible. The simplified estimate of the self-field, however, does assume that the current runs in a single loop-like path. In a more realistic picture, the current is distributed across the thin film, mostly flowing in the regions of highest conductivity. Thus, the calculation above is an overestimate of the self-field.

The experiments in which the normal metal in the junction was electromigrated allow for testing the self-field hypothesis. Rather than a Josephson diode effect in the switching current, in these experiments, an asymmetry was found in the deficit voltage versus magnetic field when the resistance of the wire increases, as was shown in Figures 7.3 and 7.4. Since the deficit voltage relates to the presence of a supercurrent (or excess current) in the junctions in non-equilibrium conditions, I will refer to this as the non-equilibrium Josephson diode effect. If the Josephson diode effect results due to the self-field effect, it would be expected that the total field is  $B_{\text{total}} = B_{\text{external}} + c_0 I_c \approx B_{\text{external}} + c_0 \frac{V_c}{R}$ , where  $c_0$  is a constant that defines the magnitude of the self-field effect. Assuming that the critical voltage scale  $V_c$  is constant, when the resistance is increased, this implies that the critical current will decrease as  $\frac{1}{R}$ . Hence, the Josephson diode effect would scale as  $\frac{1}{R}$  if the effect arises due to the self-field. In Figure 7.4, the deficit voltage scale and the critical voltage scale were both found to be approximately constant as a function of the junction resistance, in contrast with the expected behavior for a self-field effect. Hence, the self-field effect can not explain the observed diode effect.

*Vortices:* Next, we consider the effect of vortices, which have been proposed to explain the supercurrent diode effect in thin films[217]. This explanation also involves screening current, but instead suggests that because the barrier to vortex entry (or vortex pinning) in the superconductor is different at the two edges, the critical current becomes asymmetric at finite field[229, 230]. In the devices fabricated, the top surface is oxidized niobium, while the bottom surface is niobium in contact with palladium or gold. The barrier to vortex entry is likely reduced on the normal metal side due to the inverse proximity effect compared to the niobium side. While for the supercurrent diode effect, the effect has been shown to exist due to a difference in the vortex barrier at the two edges, in the SNS

junctions, the switching current is coupled to one edge (the bottom of the superconducting Nb film in contact with the normal metal). At a finite externally applied magnetic field, this means that a diode effect is to be expected due the addition of the bias current to the Meissner screening current at the NS interface. In terms of current densities  $\vec{j}$ , this can be expressed as:  $\vec{j} = \vec{j}_{\text{Meissner}} + \vec{j}_{\text{bias}}$ . If the currents are in the same direction, the vortex barrier will be broken earlier. Notably, this effect again relies on the magnitude of the bias current with respect to the Meissner current. This implies that if the diode effect arises due to the vortex barrier, it should be suppressed as the resistance of the normal metal wire increases due to electromigration. Since this is not the case, we exclude the vortex surface barrier.

### 7.4.3 Non-reciprocity at finite bias voltages

Although the Josephson diode effect can potentially be explained by the theory of Davydova, the non-equilibrium version of the effect in SNS junctions is not captured by the theory. The extension to the non-equilibrium case has been performed by Zazunov[105]. In SNS junctions, it is proposed that the multiple Andreev reflection (MAR) signal splits into a red-shifted and blue-shifted variant in the case of helical superconductors, with finite Cooper pair momentum. This approach assumes that the pairing order parameter oscillates in space as  $\Delta = \Delta e^{i\vec{q}\cdot\vec{r}}$ , where  $\vec{q}$  is the Cooper pair momentum. For NS junctions, they report that this approach results in no non-reciprocity. However, there are reasons to assume that the analysis by Zazunov does not accurately describe the situation of the samples. The assumption that the superconductor enters a finite momentum state, such as the Fulde-Ferrel state[101], should not hold at small magnetic fields. The finite momentum order parameter should only be the ground state/stable close to the depairing field [231]. Rather than finite momentum pairing, in the Meissner state, Cooper pairs are composed of momentum-shifted quasiparticles that pair up with equal and opposite momentum[104]. As a result, the electron and hole quasiparticles that form the Cooper pairs no longer have equal energies, resulting in finite energy Cooper pairs. Only when the energy shift approaches  $|\Delta|$ , a finite momentum order parameter could be justified.

Here, I will calculate the non-reciprocity related to the presence of a finite energy Meissner state. Assuming only BCS-like pairing and a momentum (vector potential) term in the Hamiltonian, a 1D tight binding simulation in Kwant[99] was performed to investigate the  $IV$  characteristic of an NS junction where a Meissner current flows in the superconductor. In the absence of a momentum term, this simulation produces the expected BTK model results. The momentum was implemented as an imaginary hopping term by discretizing the momentum operator  $\hat{p}|\psi\rangle(x) = -i\hbar \frac{d}{dx}|\psi\rangle(x) \rightarrow -i\hbar \frac{1}{2a}(|\psi\rangle_{k+1} - |\psi\rangle_{k-1}) = -i\frac{mv_F}{2}(|\psi\rangle_{k+1} - |\psi\rangle_{k-1})$ , where  $a$  is the lattice spacing and  $k$  is the site index. The added momentum boost term is  $\frac{p_S}{m}\hat{p}$ . The calculation was performed in Nambu space, using a hopping-scale  $-t$ , on-site pairing term  $\Delta = 0.1t$ , a Dynes parameter  $\Gamma = 0.033t$  and a two-site potential barrier between the normal metal and the superconductor of size  $H = 0.3t$  ( $Z \approx 0.15$ ).  $IV$  curves were calculated for momenta  $p_S = -\frac{|\Delta|}{v_F}, 0, \frac{|\Delta|}{v_F}$ . The resulting  $I_{\text{exc}}R_N$  (equivalent to deficit voltage) curves for different momenta are plotted in Figure 7.7a. Notably, the finite momentum term results in a diode effect, with positive momentum en-

hancing forward conduction and negative momentum enhancing backward conduction. The deficit voltage curve for positive momentum follows the zero momentum deficit voltage curve between 0 mV and 0.25 mV, but not between  $-0.25$  mV and 0 mV. Similarly, the curve for negative momentum follows the curve for negative voltages, but not for positive voltages. This is in agreement with the data in Figure 7.6d. One disagreement that can be found between the data from the Au SNS junctions and the simulations is that for finite momentum the deficit voltage in the simulations exceeds the deficit voltage at zero momentum. In the measurement, this is not the case. Part of the reason for this could be that  $|\Delta|$  is suppressed as  $|\vec{B}|$  is increased in the experiment, which was not taken into account in the simulation. A few other points that could be improved in the simulation are the inclusion of elastic scattering, a 2D sample geometry and the inverse proximity effect. Nevertheless, with the addition of only a momentum/vector potential term, the model produces a qualitatively good explanation of the data. This confirms that a Meissner current running on the NS interface can produce an asymmetry in the excess current. The asymmetry in this model arises due to quasiparticle momentum (a Doppler shift). The Doppler shift in quasiparticle momentum results in a momentum resolved energy shift of the superconducting gap. As an example, a constant shift of the quasiparticle branch in momentum  $k$  results in the energy gap shifting down at the Fermi momentum  $k_F$  and up at  $-k_F$ . The energy shift produces an asymmetry in the Andreev reflection of carriers at  $k_F$  and  $-k_F$ . This effectively shifts the conductance enhancement in voltage. It is noteworthy that this explanation can not be captured by the Usadel formalism, which is conventionally used to describe the proximity effect at diffusive NS interfaces, as this effect relies on a momentum-resolved dispersion at the NS interface. The Usadel formalism instead assumes the superconductor to be isotropic due to scattering. This also suggests that the effect should scale with the dimensions of the junction, becoming more prevalent for shorter (or cleaner) junctions.

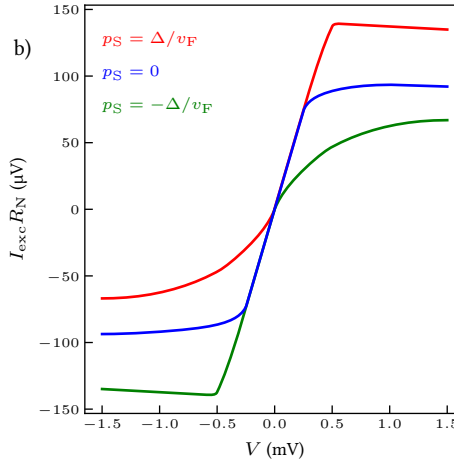


Figure 7.7: Finite momentum simulations of an NS interface with parameters  $\Delta = 250 \mu\text{eV}$ ,  $t = 10\Delta$ ,  $\Gamma = 0.33\Delta$ ,  $H = 0.3t$ , 9 N-sites and 9 S sites. The voltage  $I_{\text{exc}} R_N$  is plotted versus bias voltage  $V$  for different momentum values  $p_S = -\frac{\Delta}{v_F}, 0, \frac{\Delta}{v_F}$ .

The non-equilibrium Josephson diode effect that was discovered here allows for the conversion of an applied magnetic field to a voltage on the order of  $50 \mu\text{V}$  per  $200 \text{ mT}$  in Nb/Au/Nb SNS junctions. Furthermore, the effect is almost linear at low magnetic fields. Hence, the devices made can find a potential use as magnetic field sensors with a sensitivity of  $250 \mu\text{V/T}$ . With a voltage measurement accuracy of approximately  $2 \text{ nV}$ , this device could thus read magnetic fields on the order of  $10 \mu\text{T}$ . This resolution could potentially be improved by making multiple Josephson junctions in series, or by increasing the maximum deficit voltage of the junctions through improvements in the fabrication.

Finally, we discuss a peculiarity in the data. That is, the enhancement of the switching current in the Pd junctions around zero magnetic field. This could indicate that the amount of pair breaking reduces with increasing magnetic field in this regime. An enhancement was only observed for in-plane magnetic field, and was most clearly seen for the parallel field direction. This was not observed for all Pd-based devices, but only for this particular batch of junctions. A possible explanation could be the presence of localized magnetic moments in the Pd film. If these are oriented in random orientations or in the out of plane direction, they effectively provide a field in the  $z$  direction. Applying a magnetic field in the parallel direction will then align these moments to the parallel direction, in which the superconducting film is less sensitive to magnetic field.

## 7.5 Conclusion

In conclusion, a Josephson diode effect was discovered in variable thickness SNS junctions made with Nb as the superconductor and Pd or Au as the normal metal. By applying an in-plane magnetic field on the order of  $100 \text{ mT}$  perpendicular to the bias current direction, the switching current was biased in the forward or backward direction. Additionally, when the normal metal wire was gradually slimmed down by feedback controlled electromigration, an asymmetry in the deficit voltage (equivalently, the excess current) was revealed. The deficit voltage asymmetry is related to the perpendicular in-plane magnetic field and, similarly to the Josephson diode effect, has a characteristic magnetic field scale on the order of  $100 \text{ mT}$ . Neither the deficit voltage scale nor the deficit voltage asymmetry changed significantly upon increasing the resistance of the normal wire by electromigration of the SNS junctions below  $12 \text{ k}\Omega$ .

Both the Josephson diode effect and deficit voltage asymmetry can both be classified as nonreciprocal charge transport mechanisms in SNS junctions. The independence of these effects on the current scale allows us to exclude self-inductance as a trivial mechanism by which this could occur. Instead, an explanation based on the Meissner effect at the NS interface gives a satisfactory description of both the Josephson diode effect and the observed deficit voltage asymmetry. In this explanation, the asymmetry results from a Doppler shift of the electron quasiparticle momentum. As a result, Cooper pairs and Bogoliubov quasiparticles are formed by electron and hole excitations with unequal energies. Electrons going in the forward direction are shifted down in energy and electrons going in the backward direction are shifted up in energy. Due to this, zero momentum Cooper pairs have finite energy and the Bogoliubov quasiparticle energies shift with respect to the Fermi energy. As a result, Andreev reflections at the NS interface are direction dependent.

The Josephson diode and deficit voltage asymmetry discovered in these conventional SNS junctions motivates further investigation. In particular, it is of interest to understand what determines the magnitude of the asymmetry. The proposed explanation for the nonreciprocity in these junctions relies on the Doppler shift of Andreev reflections. This is a momentum-based effect, which is largest in the ballistic case and decreases with an increase in elastic scattering. Junctions with a shorter length should show a larger diode efficiency and a larger deficit voltage asymmetry with respect to the maximum deficit voltage. Studies of the nonreciprocal effect as a function of the spacing between the superconducting electrodes should be done to verify this.

## 7.6 Appendix

### Magnetic field dependence of a tunnel junction

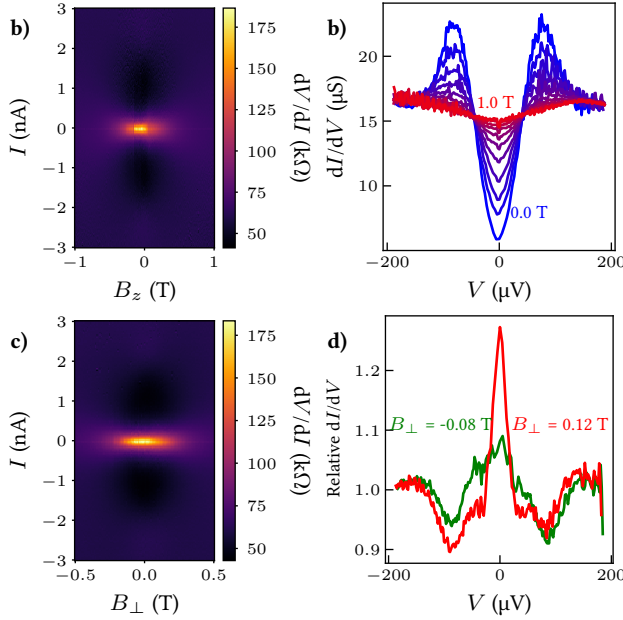


Figure 7.A.1: Nonreciprocal conductance in a 60 kΩ junction device a) Color map of the differential resistance versus magnetic field in the  $z$  direction. b) Differential conductance versus voltage curve for magnetic fields ranging from 0 T to 1 T in steps of 0.1 T. c) Color map of the differential resistance versus magnetic field in the perpendicular in-plane direction d) Normalized differential conductance versus voltage curves for  $-0.08$  and  $0.12$  T ( $-0.1$  and  $0.1$  T effective) magnetic field in the perpendicular in-plane direction. Normalization was performed by dividing the differential resistance curves by the differential resistance curve at  $0.02$  T

Junction B was further electromigrated to a resistance of 60 kΩ. At this resistance, the dependence of the  $IV$  characteristic was measured versus out of plane and perpendicular in-plane magnetic field. The color map of the differential resistance versus bias current and magnetic field in the  $z$  direction is shown in Figure 7.A.1a. Corresponding differential conductance versus voltage curves from 0 to 1 T with steps of 0.1 T are shown in Figure 7.A.1b. The differential conductance curves show a gap structure at zero voltage, surrounded by peaks at low magnetic field. This is the expected behavior of a superconducting tunnel contact; the gap in the quasiparticle density of states appears in the differential conductance. As the magnetic field is increased, the gap in the differential conductance gradually disappears. The color map of the differential resistance versus current and perpendicular in-plane magnetic field is shown in Figure 7.A.1c. In contrast to the behavior of the junction at lower resistances, there is no clear skewing of the differential resistance in the color map. To see the effect of the magnetic field, I examine the normalized differential conductance versus voltage curves at  $-0.08$  T and  $0.12$  T, shown in Figure 7.A.1d. Here normalization was performed by dividing the differential resistance curves by the curve at  $0.02$  T. This however reveals that the differential conductance curves are still skewed.

The normalized curves show that at 0.12 T, the junction is relatively more conductive in the forward bias direction and at  $-0.08$  T, the junction is relatively more conductive in the backward bias direction. This shows that even in the tunnel junction, a diode effect remains.

### Color map of the magnetic field dependence of the $12.7 \text{ k}\Omega$ Nb/Au/Nb SNS junction

In Figure 7.A.2, the color map of the differential resistance versus bias current and perpendicular in-plane magnetic field is shown for the Nb/Au/Nb SNS junction electromigrated to a resistance of  $12.7 \text{ k}\Omega$  in the main text.<sup>5</sup> This color map shows skew symmetry (BJR-type behavior) and an approximately constant background differential resistance.

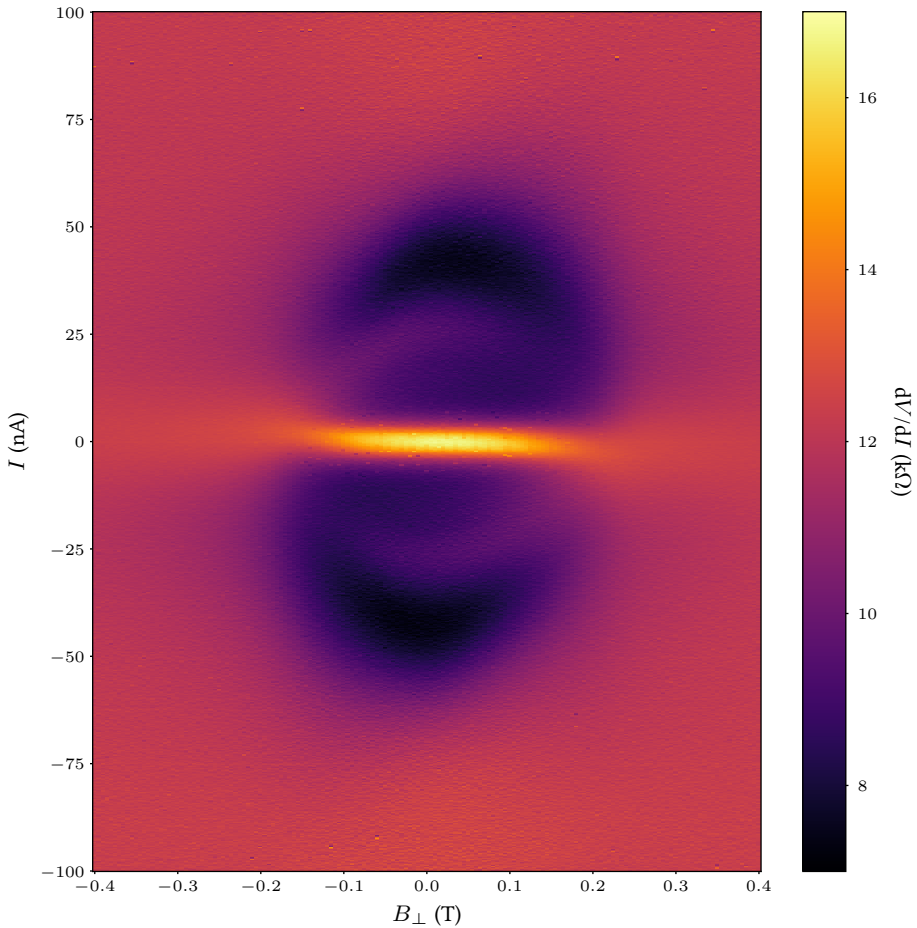


Figure 7.A.2: Nonreciprocal conductance in a  $12.7 \text{ k}\Omega$  Nb/Au/Nb SNS junction. Color map of the differential conductance versus bias current and perpendicular in-plane magnetic field.

<sup>5</sup>This color map was used as the cover image for this thesis



## 8

## Conclusion and outlook

The core focus of this thesis is making superconducting contacts to graphene nanoribbons. Thus, this thesis started out with making such contacts out of MoRe. However, it was found that such devices made with 9-atom-wide armchair graphene nanoribbons contacted by electrodes made out of molybdenum-rhenium alloy in fact do not conduct electricity at low temperatures and low bias voltages. It was initially not known whether this issue was due to the surface quality of MoRe or due to the inherent Schottky barriers at the metal-semiconductor interfaces; hence studies were performed with ligand-free gold nanoparticles to characterize the surface of the MoRe contacts. Here, it was found that the electrical interface between the MoRe electrodes and the Au nanoparticles appeared to be highly transparent. Since the surface of MoRe was found to make good contacts to Au nanoparticles and thus sufficiently clean from oxides and contaminants, the focus for graphene nanoribbons shifted towards making optimal electrical interfaces, rather than just making superconducting contacts.

8

As a strategy toward making transparent electrical contacts to narrow armchair graphene nanoribbons, a focus was put on palladium contacts. Palladium is known to be an excellent (p-type) contact metal for carbon nanotubes. By utilizing the superconducting proximity effect, superconducting correlations could be induced in this material, provided that it is in good electrical contact with a superconductor. This motivated the study of Nb/Pd/Nb (and Nb/Au/Nb) SNS junctions, with the aim of studying the proximity effect. These junctions were made in a constriction, such that they can be gradually narrowed down and eventually broken by feedback-controlled electromigration. By breaking the Pd or Au wire, the induced energy gap in the normal metal could be characterized. A superconducting gap of 50  $\mu\text{V}$  could be induced in the Pd constrictions, significantly smaller than the gap of 250  $\mu\text{V}$  in Au. Unexpectedly, a Josephson diode effect and nonreciprocal Andreev conductance was identified in the SNS junction upon applying an external magnetic field in the direction perpendicular to the current direction and parallel to the NS interface. Such an effect could be qualitatively understood within the Blonder-Tinkham-Klapwijk theory by considering the contribution of the Meissner screening current in the superconductor on

the quasiparticle dispersion relations. Within the next few paragraphs, a brief overview of the conclusions and outlook is given per chapter.

Chapter 4 describes a series of measurements done to characterize the electrical interfaces of electrodes made out of MoRe alloy to 9-atom-wide armchair graphene nanoribbons. This is done with the express purpose of making GNR devices that are electrically conductive at cryogenic temperatures and low bias voltages, where the MoRe alloy is superconducting. Although MoRe had been shown to make excellent contacts to carbon nanotubes[149, 150] at low temperature, the measurements with graphene nanoribbons showed current on the order of 1 pA at voltage of 500 mV at a temperature of approximately 100 mK. A bit more success was found with Pd electrodes, which exhibited a  $10^4$  better conductance at room temperature. Yet, all devices continued to show thermally activated behavior and consequently high electrical resistance at low temperatures. In this regard, the behavior of the GNR devices studied thus deviates from the carbon nanotubes devices studied before. Most likely, the band gap of the GNRs studied here is significantly larger than the band gap of the carbon nanotubes for which highly conductive interfaces were found. This could be explained if the width of the GNRs ( $\sim 1$  nm) is presumably quite narrow compared to the circumference (or diameter) of the carbon nanotubes. Assuming this is true, a massive improvement on the current devices can be made by replacing the 9-atom-wide armchair GNRs with a band gap of 1.4 eV by 17-atom-wide armchair GNRs, which have a theoretically predicted band gap of only 660  $\mu$ eV[63] and a measured band gap of only 190 meV in scanning tunneling spectroscopy. The theoretically predicted band gap makes the 17-AGNRs comparable to carbon nanotubes with a 1.3 nm diameter (instead of an 0.6 nm diameter for 9-AGNRs). For a carbon nanotube of this diameter, a significantly smaller Schottky barrier to Pd is to be anticipated[142]. If experience with carbon nanotubes translates to GNRs, wider GNRs could be necessary to make Josephson junctions with GNRs. Indeed, while further engineering of the contacts to improve the interface resistance is, in principle, possible by using metals with very high or very low work functions, i.e., by making n-type contacts with scandium, device fabrication with such metals is impractical due to oxidation of n-type contacts or impossible due to a lack of high enough work function for p-type contacts. For the purpose of making superconducting circuits with GNRs, I expect that engineering of the GNRs to produce smaller band gaps, rather than engineering of the contact area, is necessary to produce a breakthrough.

In chapter 5, it was revealed by Andreev spectroscopy that the interfaces of MoRe with ligand-free gold nanoparticles have a high electrical interface transparency. This is an important conclusion, as it shows the potential to use prepatterned MoRe electrodes as superconducting electrodes for making superconducting contacts with a material of interest without directly sputtering or evaporating on top. For the purpose of studying graphene nanoribbons, this confirms that the interfaces of MoRe are likely not limited by barriers inherent to the MoRe electrodes. Although studies of MoRe - carbon nanotube - MoRe devices performed by Kaikkönen et al.[150] suggested that prepatterned MoRe electrodes can make highly transparent electrical interfaces to carbon nanotubes, the interface transparency of prepatterned MoRe electrodes to nanostructures was never characterized before. To my knowledge, this study thus provides the first experimental confirmation of the highly transparent interface properties of MoRe. Future experiments could utilize

this special property of MoRe alloys to study nanoparticles or 2D materials, as has already been done with monolayer MoS<sub>2</sub>[232], with superconducting contacts.

Furthermore, for studying individual nanoparticles, there are a few possible directions to take. An improvement on the current study should aim to study ligand-free nanoparticle with a defined shape and size, rather than just a defined mass. In order to achieve this for nanoparticles created by spark ablation, a heater could be installed in the gas line. Heating the particles prior to size selection should melt the nanoparticles, which, by minimization of surface energy, is expected to lead to a spherical shape. Another direction that could be taken is the study of different nanoparticles made out of different metals or perhaps alloys. Since the spark ablation technique used in this thesis allows for the production of nanoparticles out of arbitrary metals and can even make thermodynamically unstable alloys ("impossible" alloys)[233], this technique could be used to investigate unique materials. In the context of Josephson junctions with (anti)ferromagnetic nanoparticles, i.e., by mixing a noble metal such as Au with Cr, Mn, Fe, Co or Ni, would be of interest.

Beyond studying individual nanoparticles, it could be of interest to study the properties of the nanoporous films created by the thicker nanoparticle depositions. The gold nanoparticles studied in this thesis have a typical diameter of approximately 5 nm, which is significantly smaller than the mean-free path in bulk gold ( $\sim 38$  nm [194]). This is smaller than the thinnest conductive film that can be created by e-beam evaporation ( $\sim 13$  nm) and comparable to the smallest filament diameter of nanoporous gold structures[234]. It is to be expected that boundary scattering is dominant in such nanostructures and dominates the electronic transport properties. As the particles forming the film get smaller, the surface area to volume ratio also changes. Thus, the influence of electronic states related to the surface of the gold should be much more important in such nanoporous films. If the nanoparticle diameter or the degree of porosity can be controlled by tuning deposition parameters, this might allow for an investigation of the contribution of the predicted topological surface states in gold[235, 236] on the transport characteristics.

In chapter 6, SNS junction made using the superconductor Nb and the normal metals Au and Pd were studied. With the purpose of creating junctions that could be electromigrated to form superconducting contacts with nanoparticles or GNRs, a constricted geometry was chosen. This, ideally, makes the normal metal the most resistive element. Through tuning the deposition of Nb and the pattern, such that the constriction was narrow enough, junctions were successfully electromigrated in a symmetric manner. Such devices could be used to study nanoparticles or GNRs. The observed proximity effect in Pd was small, with an induced gap of  $\sim 50$   $\mu$ V. Although this can be improved by further scaling down the junction length, the significant thickness of the Nb layer would make deposition of GNRs into the nanogap difficult. Thus, for Pd, an N/S bilayer with Pd, or AuPd on top of Nb might provide a better device structure, provided the interface between the Pd and the Nb can be made and kept clean.

In chapter 7, the observation of a Josephson diode effect and a non-reciprocal Andreev conductance was observed in the SNS junctions made in chapter 6. Through electromigration of the junctions, it was found that the observed deficit voltage scale and its non-reciprocity do not scale with the resistance of the normal metal. A qualitative model was made, which

explains the effect on the basis of quasiparticle momentum due to a Meissner current at a highly transparent NS interface. Various characterizations can still be done in order to better understand the behavior of such a junction. The theory by Davydova[100] for the Josephson diode effect, for example, suggests that the effect is quasi-ballistic, decreasing with an increase in scattering. This can be characterized by studying the maximum deficit voltage as a function of the length of the normal metal bridge (the spacing between the niobium patches). Furthermore, it is still not fully understood how the thickness of the superconductor and the normal metal affects the diode effect in these junctions. Another idea is to investigate whether the diode effect is also present when the normal metal is replaced by a (highly conductive) superconductor, such as aluminium. Since the critical field of aluminium ( $H_c = 10$  mT[237]) is small, such measurements should be done at a low magnetic field.

Finally, I will make a remark on a pervasive technical issue within this thesis, which was found in the MoRe devices with gold nanoparticles, but also in the Nb/Pd/Nb and Nb/Au/Nb SNS junctions: The absence of an observable critical current in SNS junctions below approximately  $1 \mu\text{A}$ . Since the gold nanoparticle SNS junctions had resistances larger than  $1 \text{ k}\Omega$ , their critical current was expected to be below  $1 \mu\text{A}$ . Indeed, for such junctions, a critical current-like effect was observed, but not without dissipation/resistance. For the SNS junctions, on the other hand, a dissipationless current was observed, but only for  $R \sim 10 \Omega$ . Upon electromigration of the normal metal constriction, the junction became resistive at all bias currents, while a partially resistive critical current feature remained. The approximate critical current scale of  $1 \mu\text{A}$  is alarming, since the associated Josephson energy,  $E_J = \frac{eI_c}{2\pi G_0}$ , where  $G_0$  is the conductance quantum and  $I_c$  is the critical current, is approximately  $2 \text{ meV}$ . This is orders of magnitude above the thermal energy at  $100 \text{ mK}$ , ( $k_B T \sim 10 \mu\text{V}$ )! It is suspected that a lack of (high frequency) filtering at milli-Kelvin cryogenic temperatures in the dilution fridge is to blame for this. Careful consideration of filtering should be performed in order to observe a dissipationless Josephson current in more resistive devices ( $R_N \geq 1 \text{ k}\Omega$ ).

# References

## References

- [1] Y. Luh, *Acta Physica Sinica* **21**, 75 (1965).
- [2] H. Shiba, *Progress of Theoretical Physics* **40**, 435 (1968), <https://academic.oup.com/ptp/article-pdf/40/3/435/5185550/40-3-435.pdf>.
- [3] A. I. Rusinov, *Sov. Phys. JETP* **29**, 1101 (1969).
- [4] A. V. Balatsky, I. Vekhter, and J.-X. Zhu, *Reviews of Modern Physics* **78**, 373 (2006).
- [5] M. Ruby, F. Pientka, Y. Peng, F. Von Oppen, B. W. Heinrich, and K. J. Franke, *Physical review letters* **115**, 197204 (2015).
- [6] L. Schneider, P. Beck, T. Posske, D. Crawford, E. Mascot, S. Rachel, R. Wiesendanger, and J. Wiebe, *Nature Physics* **17**, 943 (2021).
- [7] M. Slota, A. Keerthi, W. K. Myers, E. Tretyakov, M. Baumgarten, A. Ardavan, H. Sadeghi, C. J. Lambert, A. Narita, K. Müllen, and L. Bogani, *Nature* **557**, 691 (2018).
- [8] W. Meissner and R. Ochsenfeld, *Naturwissenschaften* **21**, 787 (1933).
- [9] E. Liebhaber, L. M. Rütten, G. Reece, J. F. Steiner, S. Rohlf, K. Rosnagel, F. von Oppen, and K. J. Franke, *Nature Communications* **13**, 2160 (2022).
- [10] J. Cai, P. Ruffieux, R. Jaafar, M. Bieri, T. Braun, S. Blankenburg, M. Muoth, A. P. Seitsonen, M. Saleh, X. Feng, K. Müllen, and R. Fasel, *Nature* **466**, 470 (2010).
- [11] R. E. Blackwell, F. Zhao, E. Brooks, J. Zhu, I. Piskun, S. Wang, A. Delgado, Y.-L. Lee, S. G. Louie, and F. R. Fischer, *Nature* **600**, 647 (2021).
- [12] S. Mishra, G. Catarina, F. Wu, R. Ortiz, D. Jacob, K. Eimre, J. Ma, C. A. Pignedoli, X. Feng, P. Ruffieux, J. Fernández-Rossier, and R. Fasel, *Nature* **598**, 287 (2021).
- [13] Q. Sun, X. Yao, O. Gröning, K. Eimre, C. A. Pignedoli, K. Müllen, A. Narita, R. Fasel, and P. Ruffieux, *Nano Letters* **20**, 6429 (2020), pMID: 32787158, <https://doi.org/10.1021/acs.nanolett.0c02077>.
- [14] N. Friedrich, R. E. Menchón, I. Pozo, J. Hieulle, A. Vegliante, J. Li, D. Sánchez-Portal, D. Peña, A. García-Lekue, and J. I. Pascual, *ACS Nano* **16**, 14819 (2022), pMID: 36037149, <https://doi.org/10.1021/acsnano.2c05673>.
- [15] W. P. Su, J. R. Schrieffer, and A. J. Heeger, *Phys. Rev. Lett.* **42**, 1698 (1979).

- [16] A. G. MacDiarmid, R. J. Mammone, R. B. Kaner, L. Porter, R. Pethig, A. J. Heeger, D. R. Rosseinsky, R. J. Gillespie, and P. Day, *Philosophical Transactions of the Royal Society of London. Series A, Mathematical and Physical Sciences* **314**, 3 (1985), <https://royalsocietypublishing.org/doi/pdf/10.1098/rsta.1985.0004>.
- [17] K. S. Novoselov, A. K. Geim, S. V. Morozov, D. Jiang, M. I. Katsnelson, I. V. Grigorieva, S. V. Dubonos, and A. A. Firsov, *Nature* **438**, 197 (2005).
- [18] G. Lu, K. Yu, Z. Wen, and J. Chen, *Nanoscale* **5**, 1353 (2013).
- [19] L. Lin, J. Li, Q. Yuan, Q. Li, J. Zhang, L. Sun, D. Rui, Z. Chen, K. Jia, M. Wang, Y. Zhang, M. H. Rummeli, N. Kang, H. Q. Xu, F. Ding, H. Peng, and Z. Liu, *Science Advances* **5**, eaaw8337 (2019), <https://www.science.org/doi/pdf/10.1126/sciadv.aaw8337>.
- [20] K. Wakabayashi, K. ichi Sasaki, T. Nakanishi, and T. Enoki, *Science and Technology of Advanced Materials* **11**, 054504 (2010).
- [21] Y.-W. Son, M. L. Cohen, and S. G. Louie, *Phys. Rev. Lett.* **97**, 216803 (2006).
- [22] L. Yang, C.-H. Park, Y.-W. Son, M. L. Cohen, and S. G. Louie, *Phys. Rev. Lett.* **99**, 186801 (2007).
- [23] M. Golor, T. C. Lang, and S. Wessel, *Phys. Rev. B* **87**, 155441 (2013).
- [24] R. Meena, G. Li, and M. Casula, *The Journal of Chemical Physics* **156**, 084112 (2022), [https://pubs.aip.org/aip/jcp/article-pdf/doi/10.1063/5.0078234/16537254/084112\\_1\\_online.pdf](https://pubs.aip.org/aip/jcp/article-pdf/doi/10.1063/5.0078234/16537254/084112_1_online.pdf).
- [25] P. Ruffieux, S. Wang, B. Yang, C. Sánchez-Sánchez, J. Liu, T. Dienel, L. Talirz, P. Shinde, C. A. Pignedoli, D. Passerone, T. Dumlaff, X. Feng, K. Müllen, and R. Fasel, *Nature* **531**, 489 (2016).
- [26] H. Shirakawa, E. J. Louis, A. G. dd, C. K. Chiang, and A. J. Heeger, *J. Chem. Soc., Chem. Commun.*, 578 (1977).
- [27] J. P. Llinas, A. Fairbrother, G. Borin Barin, W. Shi, K. Lee, S. Wu, B. Yong Choi, R. Braganza, J. Lear, N. Kau, W. Choi, C. Chen, Z. Pedramrazi, T. Dumlaff, A. Narita, X. Feng, K. Müllen, F. Fischer, A. Zettl, P. Ruffieux, E. Yablonovitch, M. Crommie, R. Fasel, and J. Bokor, *Nature Communications* **8**, 633 (2017).
- [28] J. Svensson and E. E. B. Campbell, *J. Appl. Phys.* **110**, 111101 (2011), <https://doi.org/10.1063/1.3664139>.
- [29] H. B. Michaelson, *J. Appl. Phys.* **48**, 4729 (1977), <https://doi.org/10.1063/1.323539>.
- [30] H. B. Michaelson, *IBM Journal of Research and Development* **22**, 72 (1978).
- [31] J. Adjizian, P. De Marco, I. Suarez-Martinez, A. El Mel, R. Snyders, R. Gengler, P. Rudolf, X. Ke, G. Van Tendeloo, C. Bittencourt, and C. Ewels, *Chemical Physics Letters* **571**, 44 (2013).

- [32] J. C. Phillips, Phys. Rev. Lett. **10**, 96 (1963).
- [33] C. Caroli, P. G. de Gennes, and J. Matricon, Physik Kondensierten Materie **1** (1963), 10.1007/BF02422468.
- [34] H. Meissner, Phys. Rev. **117**, 672 (1960).
- [35] K. D. Usadel, Phys. Rev. Lett. **25**, 507 (1970).
- [36] W. Belzig, C. Bruder, and G. Schön, Phys. Rev. B **54**, 9443 (1996).
- [37] G. R. Stewart, Review of Scientific Instruments **54**, 1 (1983), [https://pubs.aip.org/aip/rsi/article-pdf/54/1/1/8372715/1\\_1\\_online.pdf](https://pubs.aip.org/aip/rsi/article-pdf/54/1/1/8372715/1_1_online.pdf).
- [38] C. N. Singman, Journal of Chemical Education **61**, 137 (1984), <https://doi.org/10.1021/ed061p137>.
- [39] C. Kittel, *Introduction to Solid State Physics*, 8th ed. (Wiley, 2004).
- [40] M. Zarea, H. Ueki, and J. A. Sauls, Frontiers in Physics **11** (2023), 10.3389/fphy.2023.1269872.
- [41] S. Samaddar, D. van Zanten, A. Fay, B. Sacépé, H. Courtois, and C. B. Winkelmann, Nanotechnology **24**, 375304 (2013).
- [42] S. Guéron, *Quasiparticles in a Diffusive Conductor: Interaction and Pairing*, Ph.D. thesis, CEA-Saclay (1997).
- [43] D. Wang, Q.-H. Wang, and C. Wu, “Symmetry constraints on direct-current josephson diodes,” (2022), arXiv:2209.12646 [cond-mat.supr-con] .
- [44] F. Ando, Y. Miyasaka, T. Li, J. Ishizuka, T. Arakawa, Y. Shiota, T. Moriyama, Y. Yanase, and T. Ono, Nature **584**, 373 (2020).
- [45] J. Yun, S. Son, J. Shin, G. Park, K. Zhang, Y. J. Shin, J.-G. Park, and D. Kim, Phys. Rev. Res. **5**, L022064 (2023).
- [46] B. Pal, A. Chakraborty, P. K. Sivakumar, M. Davydova, A. K. Gopi, A. K. Pandeya, J. A. Krieger, Y. Zhang, M. Date, S. Ju, N. Yuan, N. B. M. Schröter, L. Fu, and S. S. P. Parkin, Nature Physics **18**, 1228 (2022).
- [47] C. Baumgartner, L. Fuchs, A. Costa, S. Reinhardt, S. Gronin, G. C. Gardner, T. Lindemann, M. J. Manfra, P. E. Faria Junior, D. Kochan, J. Fabian, N. Paradiso, and C. Strunk, Nature Nanotechnology **17**, 39 (2022).
- [48] B. Turini, S. Salimian, M. Carrega, A. Iorio, E. Strambini, F. Giazotto, V. Zannier, L. Sorba, and S. Heun, Nano Letters **22**, 8502 (2022), pMID: 36285780, <https://doi.org/10.1021/acs.nanolett.2c02899>.
- [49] D. Z. Haxell, M. Coraiola, D. Sabonis, M. Hinderling, S. C. ten Kate, E. Cheah, F. Krizek, R. Schott, W. Wegscheider, and F. Nichele, ACS Nano **17**, 18139 (2023), pMID: 37694539, <https://doi.org/10.1021/acsnano.3c04957>.

- [50] H. Wu, Y. Wang, Y. Xu, P. K. Sivakumar, C. Pasco, U. Filippozzi, S. S. P. Parkin, Y.-J. Zeng, T. McQueen, and M. N. Ali, *Nature* **604**, 653 (2022).
- [51] A. García-Fuente, D. Carrascal, G. Ross, and J. Ferrer, *Phys. Rev. B* **107**, 115403 (2023).
- [52] L. Molinari, *Journal of Physics A: Mathematical and General* **31**, 8553 (1998).
- [53] A. M. Marques and R. G. Dias, *Journal of Physics A: Mathematical and Theoretical* **53**, 075303 (2020).
- [54] M. Raczkowski and F. F. Assaad, *Phys. Rev. B* **96**, 115155 (2017).
- [55] P. Sheng, *Phys. Rev. B* **21**, 2180 (1980).
- [56] S. J. Konezny, C. Richter, R. C. I. Snoeberger, A. R. Parent, G. W. Brudvig, C. A. Schmuttenmaer, and V. S. Batista, *The Journal of Physical Chemistry Letters* **2**, 1931 (2011), <https://doi.org/10.1021/jz200853v>.
- [57] M. Brahma, M. L. Van de Put, E. Chen, M. V. Fischetti, and W. G. Vandenberghe, *npj 2D Materials and Applications* **7**, 14 (2023).
- [58] W. Schottky, *Annalen der Physik* **424**, 195 (1938), <https://onlinelibrary.wiley.com/doi/pdf/10.1002/andp.19384240122>.
- [59] S. M. Song, J. K. Park, O. J. Sul, and B. J. Cho, *Nano. Lett.* **12**, 3887 (2012).
- [60] E. Rut'kov, E. Afanas'eva, and N. Gall, *Diam. Relat. Mater.* **101**, 107576 (2020).
- [61] L. Talirz, H. Söde, T. Dumsloff, S. Wang, J. R. Sanchez-Valencia, J. Liu, P. Shinde, C. A. Pignedoli, L. Liang, V. Meunier, N. C. Plumb, M. Shi, X. Feng, A. Narita, K. Müllen, R. Fasel, and P. Ruffieux, *ACS Nano* **11**, 1380 (2017), pMID: 28129507, <https://doi.org/10.1021/acsnano.6b06405>.
- [62] H. Zhang, H. Lin, K. Sun, L. Chen, Y. Zaganyarski, N. Aghdassi, S. Duhm, Q. Li, D. Zhong, Y. Li, K. Müllen, H. Fuchs, and L. Chi, *Journal of the American Chemical Society* **137**, 4022 (2015), pMID: 25775004, <https://doi.org/10.1021/ja511995r>.
- [63] J. Yamaguchi, H. Hayashi, H. Jippo, A. Shiotari, M. Ohtomo, M. Sakakura, N. Hieda, N. Aratani, M. Ohfuchi, Y. Sugimoto, H. Yamada, and S. Sato, *Commun. Mater.* **1**, 36 (2020).
- [64] B. T. Matthias, T. H. Geballe, and V. B. Compton, *Rev. Mod. Phys.* **35**, 1 (1963).
- [65] D. van Delft, *Physica C: Superconductivity* **479**, 30 (2012), proceedings of VORTEX VII Conference.
- [66] H. K. Onnes, *Leiden Comm.* , 120b, 122b, 124c (1911).
- [67] M. Tinkham, *Introduction to Superconductivity*, 2nd ed. (Dover Publications, 2004).
- [68] F. London and H. London, *Proceedings of the Royal Society of London Series A* **149**, 71 (1935).



- [69] P. Mangin and R. Kahn, *Superconductivity : An Introduction* (Springer International Publishing AG, Cham, Switserland, 2017).
- [70] T. Morris and J. Brown, *Physica* **55**, 760 (1971).
- [71] F. London, *Superfluids*, Vol. 1 (Wiley, 1950).
- [72] J. Bardeen, L. N. Cooper, and J. R. Schrieffer, *Phys. Rev.* **108**, 1175 (1957).
- [73] N. N. Bogolyubov, *Sov. Phys. JETP* **7**, 41 (1958).
- [74] D. Dew-Hughes, *Low Temperature Physics* **27**, 713 (2001), [https://pubs.aip.org/aip/ltp/article-pdf/27/9/713/7438953/713\\_1\\_online.pdf](https://pubs.aip.org/aip/ltp/article-pdf/27/9/713/7438953/713_1_online.pdf).
- [75] G. E. Blonder, M. Tinkham, and T. M. Klapwijk, *Phys. Rev. B* **25**, 4515 (1982).
- [76] A. F. Andreev, *Zh. Eksperim. i Teor. Fiz.* **Vol: 46** (1964).
- [77] T. Klapwijk, G. Blonder, and M. Tinkham, *Physica B+C* **109-110**, 1657 (1982), 16th International Conference on Low Temperature Physics, Part 3.
- [78] M. Octavio, M. Tinkham, G. E. Blonder, and T. M. Klapwijk, *Phys. Rev. B* **27**, 6739 (1983).
- [79] M. Ternes, W.-D. Schneider, J.-C. Cuevas, C. P. Lutz, C. F. Hirjibehedin, and A. J. Heinrich, *Phys. Rev. B* **74**, 132501 (2006).
- [80] B. Josephson, *Physics Letters* **1**, 251 (1962).
- [81] J. Clarke, "Charge imbalance," in *Nonequilibrium Superconductivity, Phonons, and Kapitza Boundaries* (Springer US, Boston, MA, 1981) pp. 353–422.
- [82] P. G. de Gennes and D. Saint-James, *Phys. Letters* **Vol: 4** (1963), 10.1016/0031-9163(63)90148-3.
- [83] L. P. Gor'kov, "Theory of superconducting alloys," in *Superconductivity: Conventional and Unconventional Superconductors* (Springer Berlin Heidelberg, Berlin, Heidelberg, 2008) pp. 201–224.
- [84] G. Eilenberger, *Zeitschrift für Physik A Hadrons and nuclei* **214**, 195 (1968).
- [85] P. Dubos, H. Courtois, B. Pannetier, F. K. Wilhelm, A. D. Zaikin, and G. Schön, *Phys. Rev. B* **63**, 064502 (2001).
- [86] J. Freericks, A. Tahvildar-Zadeh, and B. Nikolic, *IEEE Transactions on Applied Superconductivity* **15**, 896 (2005).
- [87] J. C. Hammer, J. C. Cuevas, F. S. Bergeret, and W. Belzig, *Phys. Rev. B* **76**, 064514 (2007).
- [88] J. M. Martinis, G. Hilton, K. Irwin, and D. Wollman, *Nuclear Instruments and Methods in Physics Research Section A: Accelerators, Spectrometers, Detectors and Associated Equipment* **444**, 23 (2000).

- [89] C. Cirillo, S. L. Prischepa, M. Salvato, and C. Attanasio, *The European Physical Journal B - Condensed Matter and Complex Systems* **38**, 59 (2004).
- [90] R. L. Kautz and J. M. Martinis, *Phys. Rev. B* **42**, 9903 (1990).
- [91] Y. M. Ivanchenko and L. A. Zilberman, *Zh. Eksp. Teor. Fiz.*, 55: 2395-2402(Dec. 1968). (1968).
- [92] C. J. Pethick and H. Smith, "Charge imbalance: Its relaxation, diffusion and oscillation," in *Nonequilibrium Superconductivity, Phonons, and Kapitza Boundaries* (Springer US, Boston, MA, 1981) pp. 481–520.
- [93] T. R. Lemberger, *Phys. Rev. B* **29**, 4946 (1984).
- [94] G. Schön, *Physica B+C* **107**, 171 (1981).
- [95] T. R. Lemberger and J. Clarke, *Phys. Rev. B* **23**, 1088 (1981).
- [96] T. R. Lemberger and J. Clarke, *Phys. Rev. B* **23**, 1100 (1981).
- [97] A. Schmid, "Kinetic equations for dirty superconductors," in *Nonequilibrium Superconductivity, Phonons, and Kapitza Boundaries* (Springer US, Boston, MA, 1981) pp. 423–480.
- [98] R. C. Dynes, V. Narayanamurti, and J. P. Garno, *Phys. Rev. Lett.* **41**, 1509 (1978).
- [99] C. W. Groth, M. Wimmer, A. R. Akhmerov, and X. Waintal, *New Journal of Physics* **16**, 063065 (2014).
- [100] M. Davydova, S. Prembabu, and L. Fu, *Science Advances* **8**, eabo0309 (2022), <https://www.science.org/doi/pdf/10.1126/sciadv.abo0309> .
- [101] P. Fulde and R. A. Ferrell, *Phys. Rev.* **135**, A550 (1964).
- [102] A. I. Larkin and Y. N. Ovchinnikov, *Zh. Eksperim. i Teor. Fiz.* **Vol: 47** (1964).
- [103] J. Linder and A. V. Balatsky, *Rev. Mod. Phys.* **91**, 045005 (2019).
- [104] D. Chakraborty and A. M. Black-Schaffer, *Phys. Rev. B* **106**, 024511 (2022).
- [105] A. Zazunov, J. Rech, T. Jonckheere, B. Grémaud, T. Martin, and R. Egger, "Nonreciprocal charge transport and subharmonic structure in voltage-biased josephson diodes," (2023), arXiv:2307.15386 [cond-mat.supr-con] .
- [106] A. Schmid, *Journal of Low Temperature Physics* **41**, 37 (1980).
- [107] P. Mazur and S. de Groot, *Physica* **19**, 961 (1953).
- [108] S. S. Datta, D. R. Strachan, and A. T. C. Johnson, *Phys. Rev. B* **79**, 205404 (2009).
- [109] T. Tanaka, M. M. M. Morigami, and N. A. N. Atoda, *Japanese Journal of Applied Physics* **32**, 6059 (1993).

- [110] C. Vieu, F. Carcenac, A. Pépin, Y. Chen, M. Mejias, A. Lebib, L. Manin-Ferlazzo, L. Couraud, and H. Launois, *Applied Surface Science* **164**, 111 (2000), *surface Science in Micro & Nanotechnology*.
- [111] L. E. Ocola and A. Stein, *J. Vac. Sci. Technol. B Nanotechnol. Microelectron.* **24**, 3061 (2006), <https://avs.scitation.org/doi/pdf/10.1116/1.2366698>.
- [112] M. A. Mohammad, K. Koshelev, T. Fito, D. A. Z. Zheng, M. Stepanova, and S. Dew, *Japanese Journal of Applied Physics* **51**, 06FC05 (2012).
- [113] K. Steinberg, M. Scheffler, and M. Dressel, *Phys. Rev. B* **77**, 214517 (2008).
- [114] A. G. Corral, *Yu-Shiba-Rusinov states in superconductor-quantum dot transistors made by electromigration.*, Ph.D. thesis, CEA-Saclay (2020).
- [115] F. E. Schmidt, *Josephson junctions in superconducting coplanar DC bias cavities.*, Ph.D. thesis, Delft University of Technology (2020).
- [116] M. T. Greiner, T. C. R. Rocha, B. Johnson, A. Klyushin, A. Knop-Gericke, and R. Schlögl, *Zeitschrift für Physikalische Chemie* **228**, 521 (2014).
- [117] A. Shah, *Mechanical and Tribological Aspects of Microelectronic Wire Bonding*, Ph.D. thesis, University of Waterloo (2010).
- [118] E. Spaan, E. Ooms, W. van Driel, C. Yuan, D. Yang, and G. Zhang, in *2010 11th International Thermal, Mechanical & Multi-Physics Simulation, and Experiments in Microelectronics and Microsystems (EuroSimE)* (2010) pp. 1–4.
- [119] M. Schirmer, B. Büttner, F. Syrowatka, G. Schmidt, T. Köpnick, and C. Kaiser, *Proc. SPIE* **88860**, 88860D (2013).
- [120] D. Bouwmeester, T. S. Ghiasi, G. Borin Barin, K. Müllen, P. Ruffieux, R. Fasel, and H. S. J. van der Zant, *ACS Applied Nano Materials* **6**, 13935 (2023), <https://doi.org/10.1021/acsanm.3c01630>.
- [121] A. A. Kaverzin, T. S. Ghiasi, A. H. Dismukes, X. Roy, and B. J. van Wees, *2D Mater.* **9**, 045003 (2022).
- [122] K. Nakada, M. Fujita, G. Dresselhaus, and M. S. Dresselhaus, *Phys. Rev. B* **54**, 17954 (1996).
- [123] F. Schwierz, *Nat. Nanotechnol.* **5**, 487 (2010).
- [124] W. Miao, L. Wang, X. Mu, and J. Wang, *J. Mater. Chem. C* **9**, 13600 (2021).
- [125] Y.-W. Son, M. L. Cohen, and S. G. Louie, *Nature* **444**, 347 (2006).
- [126] C. Tao, L. Jiao, O. V. Yazyev, Y.-C. Chen, J. Feng, X. Zhang, R. B. Capaz, J. M. Tour, A. Zettl, S. G. Louie, H. Dai, and M. F. Crommie, *Nat. Phys.* **7**, 616 (2011).
- [127] I. Martin and Y. M. Blanter, *Phys. Rev. B* **79**, 235132 (2009).

- [128] J. Brede, N. Merino-Díez, A. Berdonces, S. Sanz, A. Domínguez-Celorrio, J. Lobo-Checa, M. Vilas-Varela, D. Peña, T. Frederiksen, J. I. Pascual, D. G. de Oteyza, and D. Serrate, “Detecting the spin-polarization of edge states in graphene nanoribbons,” (2023).
- [129] O. Gröning, S. Wang, X. Yao, C. A. Pignedoli, G. Borin Barin, C. Daniels, A. Cupo, V. Meunier, X. Feng, A. Narita, K. Müllen, P. Ruffieux, and R. Fasel, *Nature* **560**, 209 (2018).
- [130] D. J. Rizzo, G. Veber, T. Cao, C. Bronner, T. Chen, F. Zhao, H. Rodriguez, S. G. Louie, M. F. Crommie, and F. R. Fischer, *Nature* **560**, 204 (2018).
- [131] D. J. Rizzo, G. Veber, J. Jiang, R. McCurdy, T. Cao, C. Bronner, T. Chen, S. G. Louie, F. R. Fischer, and M. F. Crommie, *Science* **369**, 1597 (2020), <https://www.science.org/doi/pdf/10.1126/science.aay3588>.
- [132] C. Bronner, S. Stremlau, M. Gille, F. Brauße, A. Haase, S. Hecht, and P. Tegeder, *Angew. Chem. Int. Ed. Engl.* **52**, 4422 (2013), <https://onlinelibrary.wiley.com/doi/pdf/10.1002/anie.201209735>.
- [133] L. Martini, Z. Chen, N. Mishra, G. B. Barin, P. Fantuzzi, P. Ruffieux, R. Fasel, X. Feng, A. Narita, C. Coletti, K. Müllen, and A. Candini, *Carbon* **146**, 36 (2019).
- [134] M. El Abbassi, M. L. Perrin, G. B. Barin, S. Sangtarash, J. Overbeck, O. Braun, C. J. Lambert, Q. Sun, T. Prechtel, A. Narita, K. Müllen, P. Ruffieux, H. Sadeghi, R. Fasel, and M. Calame, *ACS Nano* **14**, 5754 (2020), pMID: 32223259, <https://doi.org/10.1021/acsnano.0c00604>.
- [135] O. Braun, J. Overbeck, M. El Abbassi, S. Käser, R. Furrer, A. Olziersky, A. Flasby, G. Borin Barin, Q. Sun, R. Darawish, K. Müllen, P. Ruffieux, R. Fasel, I. Shorubalko, M. L. Perrin, and M. Calame, *Carbon* **184**, 331 (2021).
- [136] J. Zhang, O. Braun, G. B. Barin, S. Sangtarash, J. Overbeck, R. Darawish, M. Stiefel, R. Furrer, A. Olziersky, K. Müllen, I. Shorubalko, A. H. S. Daaoub, P. Ruffieux, R. Fasel, H. Sadeghi, M. L. Perrin, and M. Calame, *Adv. Electron. Mater.* **9**, 2201204 (2023), <https://onlinelibrary.wiley.com/doi/pdf/10.1002/aelm.202201204>.
- [137] J. Zhang, L. Qian, G. B. Barin, A. H. S. Daaoub, P. Chen, K. Müllen, S. Sangtarash, P. Ruffieux, R. Fasel, H. Sadeghi, J. Zhang, M. Calame, and M. L. Perrin, “Ultimately-scaled electrodes for contacting individual atomically-precise graphene nanoribbons,” (2022).
- [138] Z. Mutlu, Y. Lin, G. B. Barin, Z. Zhang, G. Pitner, S. Wang, R. Darawish, M. D. Giovannantonio, H. Wang, J. Cai, M. Passlack, C. H. Diaz, A. Narita, K. Müllen, F. R. Fischer, P. Bandaru, A. C. Kummel, P. Ruffieux, R. Fasel, and J. Bokor, in *2021 IEEE International Electron Devices Meeting (IEDM)* (2021) pp. 37.4.1–37.4.4.
- [139] G. Borin Barin, Q. Sun, M. Di Giovannantonio, C.-Z. Du, X.-Y. Wang, J. P. Llinas, Z. Mutlu, Y. Lin, J. Wilhelm, J. Overbeck, C. Daniels, M. Lamparski,

- H. Sahabudeen, M. L. Perrin, J. I. Urgel, S. Mishra, A. Kinikar, R. Widmer, S. Stolz, M. Bommert, C. Pignedoli, X. Feng, M. Calame, K. Müllen, A. Narita, V. Meunier, J. Bokor, R. Fasel, and P. Ruffieux, *Small* **18**, 2202301 (2022), <https://onlinelibrary.wiley.com/doi/pdf/10.1002/sml.202202301> .
- [140] Y. C. Lin, Z. Mutlu, G. Borin Barin, Y. Hong, J. P. Llinas, A. Narita, H. Singh, K. Müllen, P. Ruffieux, R. Fasel, and J. Bokor, *Carbon* **205**, 519 (2023).
- [141] N. Richter, Z. Chen, A. Tries, T. Pechtl, A. Narita, K. Müllen, K. Asadi, M. Bonn, and M. Kläui, *Sci. Rep.* **10**, 1988 (2020).
- [142] Z. Chen, J. Appenzeller, J. Knoch, Y.-m. Lin, and P. Avouris, *Nano. Lett.* **5**, 1497 (2005).
- [143] Y. Matsuda, J. Tahir-Kheli, and W. A. I. Goddard, *J. Phys. Chem. Lett.* **1**, 2946 (2010), <https://doi.org/10.1021/jz100889u> .
- [144] Y. Zhang, N. W. Franklin, R. J. Chen, and H. Dai, *Chem. Phys. Lett.* **331**, 35 (2000).
- [145] S. Sarkar, M. L. Moser, X. Tian, X. Zhang, Y. F. Al-Hadeethi, and R. C. Haddon, *Chem. Mater.* **26**, 184 (2014).
- [146] A. Javey, J. Guo, Q. Wang, M. Lundstrom, and H. Dai, *Nature* **424**, 654 (2003).
- [147] D. Mann, A. Javey, J. Kong, Q. Wang, and H. Dai, *Nano. Lett.* **3**, 1541 (2003), <https://doi.org/10.1021/nl034700o> .
- [148] Q. Cao, S. J. Han, J. Tersoff, Y. Zhu, Z. Zhang, G. S. Tulevski, J. Tang, and W. Haensch, *Science* **350**, 68 (2015).
- [149] B. H. Schneider, S. Etaki, H. S. J. van der Zant, and G. A. Steele, *Sci. Rep.* **2**, 599 (2012).
- [150] J.-P. Kaikkonen, A. T. Sebastian, P. Laiho, N. Wei, M. Will, Y. Liao, E. I. Kauppinen, and P. J. Hakonen, *Nano Res.* **13**, 3433 (2020).
- [151] M. Di Giovannantonio, O. Deniz, J. I. Urgel, R. Widmer, T. Dienel, S. Stolz, C. Sánchez-Sánchez, M. Muntwiler, T. Dumsclaff, R. Berger, A. Narita, X. Feng, K. Müllen, P. Ruffieux, and R. Fasel, *ACS Nano* **12**, 74 (2018), pMID: 29200262, <https://doi.org/10.1021/acsnano.7b07077> .
- [152] G. Borin Barin, A. Fairbrother, L. Rotach, M. Bayle, M. Paillet, L. Liang, V. Meunier, R. Hauert, T. Dumsclaff, A. Narita, K. Müllen, H. Sahabudeen, R. Berger, X. Feng, R. Fasel, and P. Ruffieux, *ACS Appl. Nano. Mater.* **2**, 2184 (2019).
- [153] M. P. A. Fisher and A. T. Dorsey, *Phys. Rev. Lett.* **54**, 1609 (1985).
- [154] H. Grabert and U. Weiss, *Phys. Rev. Lett.* **54**, 1605 (1985).
- [155] M. Bockrath, D. H. Cobden, J. Lu, A. G. Rinzler, R. E. Smalley, L. Balents, and P. L. McEuen, *Nature* **397**, 598 (1999).

- [156] P. B. Bennett, Z. Pedramrazi, A. Madani, Y.-C. Chen, D. G. de Oteyza, C. Chen, F. R. Fischer, M. F. Crommie, and J. Bokor, *Appl. Phys. Lett.* **103**, 253114 (2013), <https://doi.org/10.1063/1.4855116>.
- [157] A. Tries, N. Richter, Z. Chen, A. Narita, K. Müllen, H. I. Wang, M. Bonn, and M. Kläui, *Phys. Chem. Chem. Phys.* **22**, 5667 (2020).
- [158] J. Overbeck, G. Borin Barin, C. Daniels, M. L. Perrin, L. Liang, O. Braun, R. Darawish, B. Burkhardt, T. Dumsclaff, X.-Y. Wang, A. Narita, K. Müllen, V. Meunier, R. Fasel, M. Calame, and P. Ruffieux, *Phys. Status Solidi B* **256**, 1900343 (2019), <https://onlinelibrary.wiley.com/doi/pdf/10.1002/pssb.201900343>.
- [159] Y. Zhang, V. W. Brar, C. Girit, A. Zettl, and M. F. Crommie, *Nat. Phys.* **5**, 722 (2009).
- [160] Y. Mayamei, J. C. Shin, K. Watanabe, T. Taniguchi, and M.-H. Bae, *Phys. Status Solidi B* **257**, 2000317 (2020), <https://onlinelibrary.wiley.com/doi/pdf/10.1002/pssb.202000317>.
- [161] A. Fediai, D. A. Ryndyk, G. Seifert, S. Mothes, M. Claus, M. Schröter, and G. Cuniberti, *Nanoscale* **8**, 10240 (2016).
- [162] P. Sutter, J. T. Sadowski, and E. Sutter, *Phys. Rev. B* **80**, 245411 (2009).
- [163] Y. Yao, S. ang Peng, X. nan Huang, D. yong Zhang, J. yuan Shi, and Z. Jin, *Nanotechnology* **30**, 405205 (2019).
- [164] Y. Wu, W. Jiang, Y. Ren, W. Cai, W. H. Lee, H. Li, R. D. Piner, C. W. Pope, Y. Hao, H. Ji, J. Kang, and R. S. Ruoff, *Small* **8**, 3129 (2012), <https://onlinelibrary.wiley.com/doi/pdf/10.1002/sml.201200520>.
- [165] C. Hsu, M. Rohde, G. Borin Barin, G. Gandus, D. Passerone, M. Luisier, P. Ruffieux, R. Fasel, H. S. J. van der Zant, and M. E. Abbassi, *Appl. Phys. Lett.* **122** (2023), 10.1063/5.0143663, 173104, [https://pubs.aip.org/aip/apl/article-pdf/doi/10.1063/5.0143663/17051333/173104\\_1\\_5.0143663.pdf](https://pubs.aip.org/aip/apl/article-pdf/doi/10.1063/5.0143663/17051333/173104_1_5.0143663.pdf).
- [166] A. Allain, J. Kang, K. Banerjee, and A. Kis, *Nat. Mater.* **14**, 1195 (2015).
- [167] S. Berge, P. Gartland, and B. Slagvold, *Surf. Sci.* **43**, 275 (1974).
- [168] Y. Liang, J. Curless, C. J. Tracy, D. C. Gilmer, J. K. Schaeffer, D. H. Triyoso, and P. J. Tobin, *Appl. Phys. Lett.* **88**, 072907 (2006), <https://doi.org/10.1063/1.2175488>.
- [169] S. Hoekje, R. Outlaw, and S. Sankaran, *NASA Tech. Pap.* 3402 (1993).
- [170] H. Wang, Y. Wu, C. Cong, J. Shang, and T. Yu, *ACS Nano* **4**, 7221 (2010).
- [171] W. Kim, A. Javey, O. Vermesh, Q. Wang, Y. Li, and H. Dai, *Nano. Lett.* **3**, 193 (2003).
- [172] H. Xu, Y. Chen, J. Zhang, and H. Zhang, *Small* **8**, 2833 (2012), <https://onlinelibrary.wiley.com/doi/pdf/10.1002/sml.201102468>.

- [173] Y.-X. Lu, C.-T. Lin, M.-H. Tsai, and K.-C. Lin, *Micromachines* **13** (2022), 10.3390/mi13040509.
- [174] W.-J. Lee and Y.-H. Chang, *Coatings* **8** (2018), 10.3390/coatings8120431.
- [175] M. Dieterle, G. Weinberg, and G. Mestl, *Phys. Chem. Chem. Phys.* **4**, 812 (2002).
- [176] F. D. Hardcastle, I. E. Wachs, J. A. Horsley, and G. H. Via, *Journal of Molecular Catalysis* **46**, 15 (1988).
- [177] A. Weber and E. A. McGinnis, *Journal of Molecular Spectroscopy* **4**, 195 (1960).
- [178] O. R. Caylan and G. Cambaz Buke, *Sci. Rep.* **11**, 8247 (2021).
- [179] K. P. Kepp, *ChemPhysChem* **21**, 360 (2020), <https://chemistry-europe.onlinelibrary.wiley.com/doi/pdf/10.1002/cphc.202000013>.
- [180] P. A. Nikolaychuk, *Chemical Thermodynamics and Thermal Analysis* **7**, 100068 (2022).
- [181] J. M. Mannion, C. R. Shick, Jr., G. A. Fugate, M. S. Wellons, B. A. Powell, and S. M. Husson, *Talanta* **168**, 183 (2017).
- [182] J. Feng, G. Biskos, and A. Schmidt-Ott, *Scientific Reports* **5**, 15788 (2015).
- [183] C. W. J. Beenakker, *Phys. Rev. B* **46**, 12841 (1992).
- [184] D. Daghero, E. Piatti, N. D. Zhigadlo, and R. S. Gonnelli, *Low Temperature Physics* **49**, 886 (2023), [https://pubs.aip.org/aip/ltp/article-pdf/49/7/886/18040361/886\\_1\\_10.0019702.pdf](https://pubs.aip.org/aip/ltp/article-pdf/49/7/886/18040361/886_1_10.0019702.pdf).
- [185] T. Y. Chen, S. X. Huang, and C. L. Chien, *Phys. Rev. B* **81**, 214444 (2010).
- [186] G. Niebler, G. Cuniberti, and T. Novotný, *Superconductor Science and Technology* **22**, 085016 (2009).
- [187] G. Sheet, S. Mukhopadhyay, and P. Raychaudhuri, *Phys. Rev. B* **69**, 134507 (2004).
- [188] C. Y. Ho, R. W. Powell, and P. E. Liley, *Journal of Physical and Chemical Reference Data* **1**, 279 (1972), [https://pubs.aip.org/aip/jpr/article-pdf/1/2/279/19140486/279\\_1\\_online.pdf](https://pubs.aip.org/aip/jpr/article-pdf/1/2/279/19140486/279_1_online.pdf).
- [189] S. Volosheniuk, D. Bouwmeester, C. Hsu, H. S. J. van der Zant, and P. Gehring, *Applied Physics Letters* **122**, 103501 (2023), [https://pubs.aip.org/aip/apl/article-pdf/doi/10.1063/5.0137392/16774287/103501\\_1\\_online.pdf](https://pubs.aip.org/aip/apl/article-pdf/doi/10.1063/5.0137392/16774287/103501_1_online.pdf).
- [190] J. C. Maxwell, “Resistance and conductivity in three dimensions,” in *A Treatise on Electricity and Magnetism*, Cambridge Library Collection - Physical Sciences, Vol. 1 (Cambridge University Press, 2010) p. 345–359.
- [191] Y. V. Sharvin, *JETP* **21**, 655 (1965).

- [192] M. Knudsen, *Nature* **80**, 491 (1909).
- [193] G. Wexler, *Proceedings of the Physical Society* **89**, 927 (1966).
- [194] D. Gall, *Journal of Applied Physics* **119**, 085101 (2016), [https://pubs.aip.org/aip/jap/article-pdf/doi/10.1063/1.4942216/15177542/085101\\_1\\_online.pdf](https://pubs.aip.org/aip/jap/article-pdf/doi/10.1063/1.4942216/15177542/085101_1_online.pdf).
- [195] P. W. Anderson, *Phys. Rev. Lett.* **9**, 309 (1962).
- [196] Y. B. Kim, C. F. Hempstead, and A. R. Strnad, *Phys. Rev.* **131**, 2486 (1963).
- [197] I. Soloviev, S. Bakurskiy, V. Ruzhickiy, N. Klenov, M. Kupriyanov, A. Golubov, O. Skryabina, and V. Stolyarov, *Phys. Rev. Appl.* **16**, 044060 (2021).
- [198] V. Ruzhickiy, S. Bakurskiy, M. Kupriyanov, N. Klenov, I. Soloviev, V. Stolyarov, and A. Golubov, *Nanomaterials* **13** (2023), 10.3390/nano13121873.
- [199] J. Moulijn, A. van Diepen, and F. Kapteijn, *Applied Catalysis A: General* **212**, 3 (2001), catalyst Deactivation.
- [200] T. Taychatanapat, K. I. Bolotin, F. Kuemmeth, and D. C. Ralph, *Nano Letters* **7**, 652 (2007), pMID: 17305400, <https://doi.org/10.1021/nl062631i>.
- [201] N. A. Court, A. J. Ferguson, and R. G. Clark, *Superconductor Science and Technology* **21**, 015013 (2007).
- [202] N. A. Mortensen, K. Flensberg, and A.-P. Jauho, *Phys. Rev. B* **59**, 10176 (1999).
- [203] G. Rubio-Bollinger, C. de las Heras, E. Bascones, N. Agraït, F. Guinea, and S. Vieira, *Phys. Rev. B* **67**, 121407 (2003).
- [204] K. Gloos and E. Tuuli, *Low Temperature Physics* **40**, 902 (2014), [https://pubs.aip.org/aip/ltp/article-pdf/40/10/902/15724538/902\\_1\\_online.pdf](https://pubs.aip.org/aip/ltp/article-pdf/40/10/902/15724538/902_1_online.pdf).
- [205] S. Artemenko, A. Volkov, and A. Zaitsev, *Solid State Communications* **30**, 771 (1979).
- [206] M. Irfan and A. R. Akhmerov, “Geometric focusing of supercurrent in hourglass-shaped ballistic josephson junctions,” (2018), arXiv:1810.04588 [cond-mat.mes-hall].
- [207] W. J. Skocpol, M. R. Beasley, and M. Tinkham, *Journal of Applied Physics* **45**, 4054 (1974), [https://pubs.aip.org/aip/jap/article-pdf/45/9/4054/7953478/4054\\_1\\_online.pdf](https://pubs.aip.org/aip/jap/article-pdf/45/9/4054/7953478/4054_1_online.pdf).
- [208] M. Wolz, C. Debuschewitz, W. Belzig, and E. Scheer, *Phys. Rev. B* **84**, 104516 (2011).
- [209] K. O’Neill, E. A. Osorio, and H. S. J. van der Zant, *Applied Physics Letters* **90**, 133109 (2007), [https://pubs.aip.org/aip/apl/article-pdf/doi/10.1063/1.2716989/14372433/133109\\_1\\_online.pdf](https://pubs.aip.org/aip/apl/article-pdf/doi/10.1063/1.2716989/14372433/133109_1_online.pdf).



- [210] R. Gaudenzi, J. O. Island, J. de Bruijkere, E. Burzurí, T. M. Klapwijk, and H. S. J. van der Zant, *Applied Physics Letters* **106**, 222602 (2015), [https://pubs.aip.org/aip/apl/article-pdf/doi/10.1063/1.4922042/14315360/222602\\_1\\_online.pdf](https://pubs.aip.org/aip/apl/article-pdf/doi/10.1063/1.4922042/14315360/222602_1_online.pdf).
- [211] J. O. Island, R. Gaudenzi, J. de Bruijkere, E. Burzurí, C. Franco, M. Mas-Torrent, C. Rovira, J. Veciana, T. M. Klapwijk, R. Aguado, and H. S. J. van der Zant, *Phys. Rev. Lett.* **118**, 117001 (2017).
- [212] F. Habashi, “Niobium, physical and chemical properties,” in *Encyclopedia of Metalloproteins*, edited by R. H. Kretsinger, V. N. Uversky, and E. A. Permyakov (Springer New York, New York, NY, 2013) pp. 1552–1554.
- [213] G. Abadias and R. Daniel, in *Handbook of Modern Coating Technologies*, edited by M. Aliofkhazraei, N. Ali, M. Chipara, N. Bensaada Laidani, and J. T. De Hosson (Elsevier, Amsterdam, 2021) pp. 359–436.
- [214] M. Murakami and T. Yogi, *Journal of Applied Physics* **57**, 211 (1985), [https://pubs.aip.org/aip/jap/article-pdf/57/2/211/14675675/211\\_1\\_online.pdf](https://pubs.aip.org/aip/jap/article-pdf/57/2/211/14675675/211_1_online.pdf).
- [215] A. I. Gubin, K. S. Il’in, S. A. Vitusevich, M. Siegel, and N. Klein, *Phys. Rev. B* **72**, 064503 (2005).
- [216] J. M. Martinis, M. H. Devoret, and J. Clarke, *Phys. Rev. B* **35**, 4682 (1987).
- [217] Y. Hou, F. Nichele, H. Chi, A. Lodesani, Y. Wu, M. F. Ritter, D. Z. Haxell, M. Davydova, S. Ilić, O. Glezakou-Elbert, A. Varambally, F. S. Bergeret, A. Kamra, L. Fu, P. A. Lee, and J. S. Moodera, *Phys. Rev. Lett.* **131**, 027001 (2023).
- [218] N. F. Q. Yuan and L. Fu, *Proceedings of the National Academy of Sciences* **119**, e2119548119 (2022), <https://www.pnas.org/doi/pdf/10.1073/pnas.2119548119>.
- [219] R. Wakatsuki, Y. Saito, S. Hoshino, Y. M. Itahashi, T. Ideue, M. Ezawa, Y. Iwasa, and N. Nagaosa, *Science Advances* **3**, e1602390 (2017), <https://www.science.org/doi/pdf/10.1126/sciadv.1602390>.
- [220] A. Daido, Y. Ikeda, and Y. Yanase, *Phys. Rev. Lett.* **128**, 037001 (2022).
- [221] D. Y. Vodolazov and F. M. Peeters, *Phys. Rev. B* **72**, 172508 (2005).
- [222] D. Suri, A. Kamra, T. N. G. Meier, M. Kronseder, W. Belzig, C. H. Back, and C. Strunk, *Applied Physics Letters* **121**, 102601 (2022), [https://pubs.aip.org/aip/apl/article-pdf/doi/10.1063/5.0109753/16450522/102601\\_1\\_online.pdf](https://pubs.aip.org/aip/apl/article-pdf/doi/10.1063/5.0109753/16450522/102601_1_online.pdf).
- [223] M. Trahms, L. Melischek, J. F. Steiner, B. Mahendru, I. Tamir, N. Bogdanoff, O. Peters, G. Reece, C. B. Winkelmann, F. von Oppen, and K. J. Franke, *Nature* **615**, 628 (2023).
- [224] Y. Zhang, Y. Gu, P. Li, J. Hu, and K. Jiang, *Phys. Rev. X* **12**, 041013 (2022).
- [225] P. Joyez, *Phys. Rev. Lett.* **110**, 217003 (2013).

- [226] S. Csonka, A. Halbritter, G. Mihály, O. I. Shklyarevskii, S. Speller, and H. van Kempen, *Phys. Rev. Lett.* **93**, 016802 (2004).
- [227] J. N. Armstrong, R. M. Schaub, S. Z. Hua, and H. D. Chopra, *Phys. Rev. B* **82**, 195416 (2010).
- [228] N. Pinto, S. J. Rezvani, A. Perali, L. Flammia, M. V. Milošević, M. Fretto, C. Cassiago, and N. De Leo, *Scientific Reports* **8**, 4710 (2018).
- [229] C. P. Bean, *Rev. Mod. Phys.* **36**, 31 (1964).
- [230] D. Y. Vodolazov, B. A. Gribkov, S. A. Gusev, A. Y. Klimov, Y. N. Nozdrin, V. V. Rogov, and S. N. Vdovichev, *Phys. Rev. B* **72**, 064509 (2005).
- [231] Q. Cui, C.-R. Hu, J. Y. T. Wei, and K. Yang, *Phys. Rev. B* **73**, 214514 (2006).
- [232] M. Ramezani, I. C. Sampaio, K. Watanabe, T. Taniguchi, C. Schönenberger, and A. Baumgartner, *Nano Letters* **21**, 5614 (2021), pMID: 34161104, <https://doi.org/10.1021/acs.nanolett.1c00615>.
- [233] G. B. Jicheng Feng, Nabil Ramlawi and A. Schmidt-Ott, *Aerosol Science and Technology* **52**, 505 (2018), <https://doi.org/10.1080/02786826.2018.1427852>.
- [234] G. Wittstock, M. Bäumer, W. Dononelli, T. Klüner, L. Lühns, C. Mahr, L. V. Moskalova, M. Oezaslan, T. Risse, A. Rosenauer, A. Staubitz, J. Weissmüller, and A. Wittstock, *Chemical Reviews* **123**, 6716 (2023), pMID: 37133401, <https://doi.org/10.1021/acs.chemrev.2c00751>.
- [235] B. Yan, B. Stadtmüller, N. Haag, S. Jakobs, J. Seidel, D. Jungkenn, S. Mathias, M. Cinchetti, M. Aeschlimann, and C. Felser, *Nature Communications* **6**, 10167 (2015).
- [236] H. Zheng, A. Weismann, and R. Berndt, *The Journal of Physical Chemistry C* **125**, 25327 (2021), <https://doi.org/10.1021/acs.jpcc.1c08061>.
- [237] S. Caplan and G. Chanin, *Phys. Rev.* **138**, A1428 (1965).

## Acknowledgments

I would like to thank everyone that I have happened to cross paths with in the past 4 years. First of all, I would like to thank my first promotor, Herre, for guiding me through the writing of my dissertation. I would also like to thank Anton, my second promotor. I was not entirely guided by my supervisors alone, as I also remember, and enjoyed discussions with Gary, Yaroslav, Jos, Yuli and Maz. I would also like to thank Diana for bringing a unique cheerfulness to the lab every year.

I would also like to thank other staff in the department. This, of course, includes Tino and Tom, our dependable in-house technicians. Whenever a pump broke down or chemicals needed to be ordered, they would always assist us in a cheerful manner. I want to thank DEMO and Raymond Schouten for their quick help with our electronics modules. The top-notch modular IVVI-rack made by DEMO has been absolutely amazing to use during my PhD. Lastly, but certainly not least, my PhD project heavily relied on the tools in the Kavli cleanroom. Despite the many complaints I have heard over the years, I hardly had any gripes with the facilities or staff. I would like to thank all the cleanroom staff, including Bas, Roald, Marinus, Eugene, Paulien, Lodi, Hozanna, Arnold, Charles, Marc, Anja, Ewan and Brian. A special thanks goes to Bas and Roald for their commitment and engagement with me and the needs of my project. I really enjoyed my time in the Kavli cleanroom and I hope that the future of the cleanroom is as bright as the evaporating niobium in the Plassys evaporator.

It goes without saying that I would like to thank all the people I have directly or indirectly collaborated with, including Gabriela Borin Barin, Pascal Ruffieux, Roman Fasel, Andres Castellanos Gomez and Mazhar Ali. A special thanks goes to VSPARTICLE and Coosje Pothoven for their willingness to facilitate experiments on ligand-free gold nanoparticles. I am glad to have had the opportunity to use the VSP-P1 nanoparticle printer for my research. The fact that this experiment resulted in a thesis chapter is a testament to the versatility of the nanoparticle printer.

Next, I would like to thank the many PhDs and Postdocs I have met during my PhD<sup>1</sup>. I will fondly remember my time spent with Chunwei and Luca, who have been around from the start of my PhD. Chunwei, I will remember you as a close friend, who was open in communication, taught me lots during my PhD and was an excellent sparring partner whenever we would play Switch on Friday afternoons. You were quite productive and ambitious and thus always had a lot of balls in the air, be it master students or projects. Whatever you do, I know you will be successful. Just make sure to also take your time to rest. Luca, I was always impressed by how incredibly rigorous and ordered you are. I really admire that whilst you are precise and self-critical, you were also very considerate and kind to

---

<sup>1</sup>et al.

others. You were hardly ever judgmental. Of course, I will cherish the Friday afternoons, funny/silly and also deeper (lunch break) conversations, your dark humor and of course chatting about Formula 1. Serhii, I was glad to be a part of many interesting conversations with you. It was also a pleasure to collaborate on projects with you. We should go cycling again sometime soon! Maria, you were my first mentor. We've had our misunderstandings and it wasn't always smooth sailing, but I also cherish lots of happy moments. I will remember the picnic that we had with the lab in summer and the Moroccan cookies, mint tea and sweets that you often brought. I wish you good health and that you'll put a little less sugar in your tea in the future. Tristan, I hope your nanoparticles will start conducting electricity sometime soon. You deserve a little luck! You're connected with the people around you in an attentive manner and I hope others will appreciate this even more in the future. Sebastiaan, you are the gentle giant of the lab. You always brought with you a calm and collected atmosphere, even when you were under pressure. Thomas, I hope you will find your future wife soon and that she appreciates your delicious (not Italian?!) tiramisu. Talieh, I am incredibly grateful for all the support you have given me. Clever and humorous, you always manage to find the right thing to say or do and the right place to be. I hope Harvard treats you well and that you will move on to even bigger things soon. Josep, you were an incredibly kind and intelligent postdoc. I enjoyed having deep discussions about the physics going on in your devices. I found it amazing that - in only two years - you managed to make bilayer graphene devices that qualitatively rival those from the Ensslin lab! I wish you lots of luck in your career. Jacqueline, you were always laser-focused on exactly what you needed to do. That is a very valuable trait to have in your future career, which I wish you lots of luck with. Jasper, we didn't interact all that much, but it was quite fun to image your bacterial nanowires in the SEM. In the end, the physics in our devices was not all that dissimilar, and it was nice to be able to discuss the theoretical approaches with you. Álvaro, you were here, you were there, you are everywhere! You've got a great sense of humor and helped in making the social outings a lot of fun. You've got a whole PhD ahead of you and with your smarts and attitude, I'm sure you will do something fascinating. Maurits, may your drums have many phase transitions. It was nice to have you around for interesting lunch break conversations. Linde, I hope you make big drums. The biggest. The deepest. The best. In all seriousness, you're capable of a lot, and you might be a little frustrated with progress so far. With your entrepreneurial attitude, I'm sure you'll find success and interesting results soon enough. Riccardo, I regrettably heard that Darth Baum converted you to the dark side of the lab and you have started measuring MCBJs. Knowing you will succeed despite this outrageous misfortune, I wish you the best of luck. Yongqing, you're taking over the baton in the relay race to integrate atomically precise graphene nanoribbons into functional devices. You're making some excellent progress, but know that there are many challenges ahead of you. Cherish the successes you get and don't let yourself be discouraged when the going gets tough.

I also met many other PhDs and Postdocs, who in one way or another played a role in my experiences here at TU Delft. Thank you, Thierry, Martin, Makars, Yaojia, Heng, Patrick, Ulderico, Evert, Ivan, Moritz, Robin, Jean-Paul, Matteo, Artem, Sonakshi, Kars, Marc, Samer, Gabriele, Samuel, Arjan et al.

I would also like to thank the C & C committee for their incredible efforts to make the

years memorable with many events.

I have had the pleasure of guiding some wonderful students, many of whom have made direct or indirect contributions to this thesis. These include Pablo, Kiri, Roel, Thomas and Abel. Every one of you managed to survive being guided by me, which is admirable. From my side, it was a pleasure to supervise your projects. As you might notice while reading this thesis, many of your contributions have directly or indirectly impacted my research. I wish you lots of success and I hope you are living fulfilling lives. In addition, I would like to acknowledge my 'adopted' master students Jorien and Jesse. It was fun to teach you what I could in the short time that I was still around. I was impressed by how quickly you two managed to pick up on techniques in the lab and in the cleanroom. I wish you lots of success in finishing your master's thesis projects.

I want to thank Dahlia for all the conversations and moments we have had in these past years. It was wonderful to finally go back to Malaysia and to see you in person again. Finally, I would like to thank my brother and parents for being there for me these four years. These years were very busy and stressful, no less so due to the coronavirus pandemic. Through these trying times, you still always managed to put a smile on my face. The various trips we made to the Ardennes, the Black Forest and Rhodes were all really enjoyable and much-needed moments to rest. Thank you, Justin, Ron and Lucienne for always listening and supporting me through the toughest of times.



# Curriculum Vitæ

## Damian Bouwmeester

1996/04/24      Date of birth in Leiderdorp, Zuid Holland, The Netherlands

### Education

2008-2014      **Secondary school**  
Visser 't Hooft Lyceum, Leiden, The Netherlands (2008-2012)  
The International School of Kuala Lumpur, Kuala Lumpur,  
Malaysia (2012-2014)  
International Baccalaureate + High School Diploma

2014-2019      **BSc and MSc Applied Physics (Cum Laude)**  
Delft University of Technology, Delft, The Netherlands  
*BSc Thesis:* Graphene gas pumps  
*Supervisor:* Prof. Dr. P.G. Steeneken  
*MSc Thesis:* Electronic transport through Yu-Shiba-Rusinov  
states in S-QD-S junctions  
*Supervisor:* Prof. Dr. Ir. H.S.J. van der Zant

2019-2024      **PhD in Physics**  
Delft University of Technology, Delft, The Netherlands  
*Thesis:* Superconducting contacts for atomically precise  
graphene nanoribbons  
*Promotors:* Prof. Dr. Ir. H.S.J. van der Zant and Dr. A.  
Akhmerov





## List of Publications

7. **D. Bouwmeester**, S. Volosheniuk, A. S. Hutten and H. S. J. van der Zant, *Josephson diode effect and nonreciprocal Andreev conductance in metallic SNS junctions*, in preparation.
6. S. Volosheniuk, **D. Bouwmeester**, C. Hsu, P. Gehring and H. S. J. van der Zant, *Yu-Shiba-Rusinov states revealed by thermocurrent spectroscopy*, in preparation.
5. **D. Bouwmeester**, T. S. Ghiasi, G. Borin Barin, K. Müllen, P. Ruffieux, R. Fasel and H. S. J. van der Zant, *MoRe Electrodes with 10 nm Nanogaps for Electrical Contact to Atomically Precise Graphene Nanoribbons*, ACS Applied Nano Materials **6** (15), 13935-13944 (2023)
4. S. Volosheniuk, **D. Bouwmeester**, C. Hsu, H. S. J. van der Zant and P. Gehring, *Implementation of SNS thermometers into molecular devices for cryogenic thermoelectric experiments*, Appl. Phys. Lett. **122**, 103501 (2023)
3. Y. Wang, G. McCandless, X. Wang, K. Thanabalasingam, H. Wu, **D. Bouwmeester**, H. S. J. van der Zant, M. Ali and J. Chan, *Electronic Properties and Phase Transition in the Kagome Metal  $\text{Yb}_{0.5}\text{Co}_3\text{Ge}_3$* , Chemistry of Materials **34**, (2022).
2. J. Azpeitia, R. Frisenda, M. Lee, **D. Bouwmeester**, W. Zhang, F. Mompean, H. S. J. van der Zant, M. García-Hernández and A. Castellanos-Gomez, *Integrating superconducting van der Waals materials on paper substrates*, Mater. Adv. **2**, 3274-3281 (2021)
1. D. Chatzopoulos, D. Cho, K.M. Bastiaans, G. O. Steffensen, **D. Bouwmeester**, A. Akbari, G. Gu, J. Paaske, B. M. Andersen and M. P. Allan, *Spatially dispersing Yu-Shiba-Rusinov states in the unconventional superconductor  $\text{FeTe}_{0.55}\text{Se}_{0.45}$* , Nat. Commun. **12**, 298 (2021).